Lebanese American University

Development of Seed Variables Prediction Models for Use in Dynamic Backcalculation of FWD Data

By
Cynthia Michel Nasr

A thesis Submitted in partial fulfillment of the requirements for the degree of Master of Science in Engineering

School of Engineering
April 2022

LAU
الجامعة اللبنانية الأميركية
Lebanese American University

THESIS APPROVAL FORM

Student Name: Cynthia Michel Nasr I.D. #: 201502137

Thesis Title: Development of Seed Variables Prediction Models for Use in Dynamic Backcalculation of FWD Data

Program: Graduate Program Scholarships

Department: Civil Engineering

School: of Engineering

The undersigned certify that they have examined the final electronic copy of this thesis and approved it in Partial Fulfillment of the requirements for the degree of:

MS in the major of Civil and Environmental Engineering

Thesis Advisor's Name Jean Chatila | Signature [redacted] | DATE: 27 / 04 / 2022 (Day Month Year)

Committee Member's Name JOHN KHOURY | Signature [redacted] | DATE: 27 / 04 / 2022 (Day Month Year)

Committee Member's Name F. Jordan SRour | Signature [redacted] | DATE: 27 / 04 / 2022 (Day Month Year)

LAU
الجامعة اللبنانية الأميركية
Lebanese American University

THESIS COPYRIGHT RELEASE FORM

LEBANESE AMERICAN UNIVERSITY NON-EXCLUSIVE DISTRIBUTION LICENSE

By signing and submitting this license, you (the author(s) or copyright owner) grants the Lebanese American University (LAU) the non-exclusive right to reproduce, translate (as defined below), and/or distribute your submission (including the abstract) worldwide in print and electronic formats and in any medium, including but not limited to audio or video. You agree that LAU may, without changing the content, translate the submission to any medium or format for the purpose of preservation. You also agree that LAU may keep more than one copy of this submission for purposes of security, backup and preservation. You represent that the submission is your original work, and that you have the right to grant the rights contained in this license. You also represent that your submission does not, to the best of your knowledge, infringe upon anyone's copyright. If the submission contains material for which you do not hold copyright, you represent that you have obtained the unrestricted permission of the copyright owner to grant LAU the rights required by this license, and that such third-party owned material is clearly identified and acknowledged within the text or content of the submission. IF THE SUBMISSION IS BASED UPON WORK THAT HAS BEEN SPONSORED OR SUPPORTED BY AN AGENCY OR ORGANIZATION OTHER THAN LAU, YOU REPRESENT THAT YOU HAVE FULFILLED ANY RIGHT OF REVIEW OR OTHER OBLIGATIONS REQUIRED BY SUCH CONTRACT OR AGREEMENT. LAU will clearly identify your name(s) as the author(s) or owner(s) of the submission, and will not make any alteration, other than as allowed by this license, to your submission.

Name: Cynthia Michel Nasr

Signature: [redacted]

Date: 27/4/2022

LAU
الجامعة اللبنانية الأميركية
Lebanese American University

PLAGIARISM POLICY COMPLIANCE STATEMENT

I certify that:

1. I have read and understood LAU's Plagiarism Policy.
2. I understand that failure to comply with this Policy can lead to academic and disciplinary actions against me.
3. This work is substantially my own, and to the extent that any part of this work is not my own I have indicated that by acknowledging its sources.

Name: Cynthia Michel Nasr

Signature: [redacted]

Date: 27/4/2022

Acknowledgment

The author would like to acknowledge the US Federal Aviation Administration (FAA) for making available several tools that were developed under research project ARAP0005 “Update Backcalculation Software (BAKFAA)”. Those tools were critical for this research and include, but are not limited to, Pulse_FE and Pulse_Analyzer.

Development of Seed Variables Prediction Models for Use in Dynamic Backcalculation of FWD Data

Cynthia Michel Nasr

Abstract

Understanding the material properties of a pavement structure is crucial for evaluating the pavement's performance and assessing its damage level. Generally, the backcalculation process is extensively used to analyze the Falling Weight Deflectometer (FWD) data for estimating the layer moduli of a pavement structure. It is mainly an iterative process that starts with a set of seed (initial) variables, calculates the theoretical pavement surface deflections, and compares them to the measured deflections. Yet, this process is most likely unstable and is prone to numerous errors including the selection of relevant seed variables. The selected seed variables hold significant consequences on the final backcalculated results. This research project aims to develop models through classification analysis to predict the seed variables. This involves (1) calculating theoretical surface deflections through a finite element model that simulates different pavement structures and properties, (2) calculating FWD parameters and indices for each structure and (3) using those parameters to build Random Forest models that predict the seed variables with low OOB error and high accuracy. The dynamic approach is adopted to perform the analysis on 3-layered rigid and flexible pavements. The AC layer is modeled as an LVE material while the PCC and the unbound layers are modeled as linear elastic materials with damping. The OOB-Estimate of error rate and the overall accuracy values obtained dictate that the predictor variables selected to build the RF models are efficiently trained and generate accurate predictions for all seed variables except for the Rayleigh Damping Parameter of the PCC layer "α_{RPCC}". The developed models can be considered as an effective guidance for pavement engineers to select the seed variables that are closer to the actual values to initiate the backcalculation process.

Keywords: Seed Variables, Backcalculation, Random Forests, FWD Data, Finite Element Methods, Classification Analysis

TABLE OF CONTENTS

Chapter **Page**

I-Introduction and Background 1

1.1 Introduction..1

1.2 Literature Review..4

II-Finite Element Method 8

2.1 FEM Definition..8

2.2 Structural Mechanics...9

2.3 Axisymmetry...9

   2.3.1 Displacement.Field...11

   2.3.2 Strain Field...11

   2.3.3 Stress Field...12

   2.3.4 Relationship between the Strains and the Stresses...........................13

2.4 Formulating the Finite Elements...14

   2.4.1 Structure Discretization and Element Types 14

   2.4.2 Axisymmetric Triangle with Three Nodes 16

   2.4.3 Stress-Strain and Strain-Displacement Relationships 18

2.5 Linear Viscoelasticity...19

   2.5.1 Viscoelastic-Properties 19

2.6 FE Equations..25

   2.6.1 Development of Governing Equations 25

   2.6.2 Dynamic Response Equilibrium Equations 26

   2.6.3 Element Stiffness Matrix Development 27

   2.6.4 Element Mass Matrix Development...27

   2.6.5 Element Damping Matrix Development...28

   2.6.6 Global Matrix Development 29

   2.6.7 Applied Surface Forces 29

2.7 Dynamic Analysis 30

   2.7.1 Newmark's Method...31

Ⅲ-LOESS Regression Analysis 34
3.1 Locally Weighted Regression 34
    3.1.1 LOESS Model Description 34
    3.1.2 Data's Localized Subsets and Smoothing Parameter 35
    3.1.3 Local Polynomials Degree 35
    3.1.4 Weight Function 36
3.2 LOESS Procedure 36
    3.2.1 LOESS Advantages and Disadvantages 39

Ⅳ-FWD Indices and FWD Parameters 41
4.1 Maximum Deflection (Do) 41
4.2 Radius of Curvature (RoC) 42
4.3 Surface Curvature Index (SCI) 44
4.4 Base Damage Index (BDI) 44
4.5 Base Curvature Index (BCI) 45
4.6 The AREA Parameter 46
4.7 Area Under Pavement Profile (AUPP) 48
4.8 Area Indices 48
4.9 Shape Factors 49
4.10 Deflection Ratio (Q_R) 49
4.11 Bending Index (BI) 50
4.12 Radius of Influence (RI) 51
4.13 Slope of Deflection 51
4.14 Normalized Area Ratio (A_r') 52
4.15 Surface Modulus 53
4.16 FWD Parameters 54
4.17 Difference Variables 56

Ⅴ-Machine Learning Algorithms and Variable Selection 60
5.1 Neural Networks 60
5.2 Decision Trees 61
5.3 Random Forests 63

5.4 Reasons Behind Adopting the Random Forest Algorithm 65
5.5 Random Forests Variable-Importance-Measures (VIMs) 66
    5.5.1 Random Forest Model 66
    5.5.2 Variable Selection 67

VI-Methodology 71
6.1 Research Program 71
    6.1.1 Software Used 73
    6.1.2 Combinations 73
6.2 Model Development and Optimal Mesh Selection 84
6.3 Output Generation for Rigid and Flexible Pavement Structures 93
6.4 Extracting FWD Parameters 94
6.5 Initial Steps: Building Neural Networks and Decision Trees through Regression Analysis ..96
6.6 Building Random Forests through Classification Analysis 97

VII-Results 99
7.1 Seed Variables for the Asphalt Concrete (AC) Layer 100
    7.1.1 AC Master Curve Sigmoidal Coefficient “Alpha (α)” 100
    7.1.2 AC Master Curve Sigmoidal Coefficient “Beta_prime (β')” 103
    7.1.3 AC Master Curve Sigmoidal Coefficient “Delta (δ)” 105
    7.1.4 AC Master Curve Sigmoidal Coefficient “Gamma (γ)” 107
7.2 Seed Variables for the Portland Cement Concrete (PCC) Layer 110
    7.2.1 Modulus of Elasticity ($E1$) 110
    7.2.2 Rayleigh Damping Parameters ($\alpha RPCC$) 112
    7.2.3 Rayleigh Damping Parameters ($\beta RPCC$) 115
7.3 Seed Variables for Unbound Layers 117
    7.3.1 Base Layer Modulus of Elasticity ($E2$) 117
    7.3.2 Subgrade Layer Modulus of Elasticity ($E3$) 120
    7.3.3 Stiff Layer Modulus of Elasticity ($E4$) 122
    7.3.4 Rayleigh Damping Parameters (αR) 125
    7.3.5 Rayleigh Damping Parameters (βR) 130
    7.3.6 Stiff Layer Thickness measured from Surface ($h3$) 134

Ⅷ-Discussion and Conclusion..137
8.1 Building Neural Networks (NN) and Decision Trees (DT)..137
8.2 Building Random Forests 137
8.3 Validation 147
8.3.1 Original Combinations 147
8.3.2 Synthetic Data_2 148
8.3.3 Synthetic Data_3 at 3 Different Temperatures (68,104 and 392˚F)...........................151
8.3.4 Synthetic Data Including Random Errors...152
8.3.5 Real-Life Data...153
8.3.6 General Observations and Deductions 156
8.4 Summary...157
8.5 Conclusion 158

References 160

LIST OF TABLES

Table **Page**

Table 1: Structural Condition Rating for DBPs (Horak 2007) 45
Table 2: Typical Area and Do values for a 4-Sensor Configuration, Pierce et. al (2017) 47
Table 3: General Trends and Guides of AREA and Do Values, Pierce et. al (2017) 47
Table 4 : Structural Condition Rating for DBPs (Hoffman and Thompson 1981, Horak 2015)...49
Table 5: Deflection Ratio (Q_R) Values and Indications (Saleh 2016) 50
Table 6: Structural Capacity Classification based on the Normalized Area Ratio (Saleh 2016) ..53
Table 7:Combinations for the Flexible and Rigid Pavement Structures......................................74
Table 8:Sigmoidal Function and Shift Factor Coefficients Comparison (Mix25) 76
Table 9: Sigmoidal Function and Shift Factor Coefficients Comparison (Mix37) 76
Table 10: ESTAR_LINK 1 Sample Data 78
Table 11: Lower and Upper Outlier Limit- First Trial...79
Table 12:Lower and Upper Outlier Limit- Last Trial 80
Table 13: Statistics Values for the Sigmoidal Coefficients from the 344 Sets............................82
Table 14: Maximum Modulus Values..82
Table 15:Sigmoidal Coefficients Selected for FE Modeling...82
Table 16: The 12 Sets Resulting after the Sigmoidal Coefficients' Selection..............................83
Table 17: AC Master Curve Sigmoidal Coefficients Classes 84
Table 18: Combinations used for Sensitivity Analysis 85
Table 19:Percentage Error in Minimum Deflection Relative to Densest Mesh 92
Table 20: Testing 25,383 Elements using Different Combinations...92
Table 21: Testing the Optimal Mesh with 29,462 Elements 93
Table 22: Distribution of the Rigid Pavement Combinations 94
Table 23: Distribution of the Flexible Pavement Combinations 94
Table 24: Layer Properties for Combination R036109...95
Table 25: Time taken to Build RF-Model and to Predict the Seed Variables..............................99
Table 26: Optimal Model Characteristics for each Seed Variable 100
Table 27: Number of Observations for AC Layer in Flexible Pavements 141
Table 28: Number of Observations for PCC Layer in Rigid Pavements 141
Table 29:Number of Observations for Unbound Layer Underlying AC and PCC Layers 141
Table 30: The Parameters Defined to Build an RF Model for each Seed Variable....................143
Table 31: Rigid Pavement Combinations with Varying "$\alpha RPCC$" 145
Table 32: Prediction Vs. Original for Combination 1 – Flexible Pavement 147
Table 33: Prediction Vs. Original for Combination 10,200 – Flexible Pavement......................147
Table 34: Prediction Vs. Original for Combination 36,619 – Flexible Pavement......................148
Table 35:Prediction Vs. Original for Combination 1 – Rigid Pavement 148
Table 36: Prediction Vs. Original for Combination 413,343 – Rigid Pavement.......................148
Table 37: New Accuracy Vs. Original Accuracy 149
Table 38: Number of Predictor Variables Corresponding to Offsets 84 through 120-inches in the Optimal Model 149
Table 39: Predictions Vs. Target Values for the 4 Methods 150
Table 40: Predictions for A10, A15, A20 & A35 Vs. Target Values..150

Table 41: Predictions Using Classifier & Average Vs. Target for Temp. 68˚F 151
Table 42: Predictions Using Classifier & Average Vs. Target for Temp. 104˚F 151
Table 43: Predictions Using Classifier & Average Vs. Target for Temp. 392˚F 151
Table 44: Predictions from RF Classifier Vs. Average Predictions for Combination 1 – Flexible Pavement 152
Table 45: Predictions from RF Classifier Vs. Average Predictions for Combination 36,619 152
Table 46: Predictions from RF Classifier Vs. Average Predictions for Combination 1 – Rigid Pavement 153
Table 47: Predictions from RF Classifier Vs. Average Predictions for Combination 413,343 ..153
Table 48: RF Classifier Predictions using Strategy 1 154
Table 49: “$E1$” Values from Sigmoidal Coefficients predicted by RF Classifier in Strategy 1 .154
Table 50: Average Predictions using Strategy 1...154
Table 51: “$E1$” Values from Sigmoidal Coefficients using Average Predictions in Strategy 1 .155
Table 52: RF Classifier Predictions using Strategy 2 155
Table 53: “$E1$” Values from Sigmoidal Coefficients predicted by RF Classifier in Strategy 2 .155
Table 54: Average Predictions using Strategy 2...155
Table 55: “$E1$” Values from Sigmoidal Coefficients using Average Predictions in Strategy 2 156
Table 56: Actual Values for the Moduli of Elasticity 156

LIST OF FIGURES

Figure **Page**

Figure 1: Deflection Basin resulting from FWD Testing, Choi et al. (2010)................................2
Figure 2: Backcalculation Process 3
Figure 3: Axisymmetric-Solid (Oñate 2009)...10
Figure 4: Axisymmetric/Element "ijm" (Logan 2017) 10
Figure 5: Axisymmetric Engineering Problem (Bazi et al. 2020) 10
Figure 6 : Axisymmetric Element (Logan 2017)..11
Figure 7: Plane Cross Section (Logan 2017)...11
Figure 8: Element Displacement in the r-z Plane (Logan 2017) 12
Figure 9: Element Displacement in the r-z Plane, (Logan 2017) 13
Figure 10: Stresses in an Axisymmetric Structure, (Logan 2017)..13
Figure 11: Structured Mesh 14
Figure 12:Unstructured Mesh 14
Figure 13: Linear, Quadratic Triangular and Quadrilateral Elements, (Logan 2017) 15
Figure 14: Axisymmetric Structure discretized into Triangular Elements (Logan 2017)............16
Figure 15: Ni Variation over the X-Y surface for a certain Element (Logan 2017)....................18
Figure 16: Storage and Loss Moduli Concept (Saba et al., 2016) 20
Figure 17: Hooke Element (Elastic Component)..21
Figure 18: Newton Element (Viscous Component)...21
Figure 19: Maxwell Element in Series...21
Figure 20: Kelvin-Voight Element 21
Figure 21: Generalized Maxwell Element..22
Figure 22: Maxwell Element Relaxation Experiment...22
Figure 23: Discretization by Four Triangular Elements 29
Figure 24: Degrees of Freedom Distribution...29
Figure 25: Linear Triangular Element Shape Functions 30
Figure 26: Nodal Forces Surface Traction 30
Figure 27: Average Acceleration Method (Left) , Linear Acceleration Method (Right).............32
Figure 28: Artificial Data Scatterplot with Smoothed Points (Cleveland 1979) 37
Figure 29: Artificial Data Scatterplot (Cleveland 1979)...37
Figure 30: Deflection Basin...43
Figure 31: Curvature Zones of the Deflection Basin 43
Figure 32: A Typical FWD Deflection Time History, Bazi, Brynick, Bou Assi, and Gagnon (2021) 55
Figure 33: A Typical FWD Velocity Time History, Bazi, Brynick, Bou Assi, and Gagnon (2021) 56
Figure 34:Neural Network Structure..60
Figure 35: Functioning of a Data-Processing-Unit (Neuron)..61
Figure 36: Radom Forest Model...64
Figure 37: Multi-Layer Flexible Pavement 72
Figure 38: Multi-Layer Rigid Pavement 72
Figure 39: Steps for Developing RF Models..73

Figure 40: Boxplot Explanation....79
Figure 41: Box Plots for (δ, α ,β and γ) after First Trial....80
Figure 42: Box Plots for after (δ, α ,β and γ) Last Trial....81
Figure 43: Master Curve showing the 12 Sets, each at 3 Temperatures....83
Figure 44: Model Development Initial Steps on AUTOCAD....85
Figure 45 : Optimal Model Generation by Gmsh....86
Figure 46: Finite Element Sensitivity Analysis at Offset (0,0)....88
Figure 47: Percent Difference in Deflection Relative to the Densest Mesh at Offset (0,0)....88
Figure 48: Finite Element Sensitivity Analysis at Offset (24,0)....89
Figure 49 : Percent Difference in Deflection Relative to the Densest Mesh at Offset (24,0)....89
Figure 50 : Finite Element Sensitivity Analysis at Offset (48,0)....90
Figure 51: Percent Difference in Deflection Relative to the Densest Mesh at Offset (48,0)....90
Figure 52: Finite Element Sensitivity Analysis at Offset (72,0)....91
Figure 53: Percent Difference in Deflection Relative to the Densest Mesh at Offset (72,0)....91
Figure 54: FWD Surface Deflection Time Histories for Combination R036109 under the FWD Load....95
Figure 55: FWD Surface Deflection Time Histories for Combination R036109 at Offset 8-inches....96
Figure 56: MDA and MDG Plots for “Alpha (α)”....101
Figure 57: MDA and MDG Plots for “Alpha (α)”....101
Figure 58: Importance of each Predictor Variable for Predicting “Alpha (α)” based on MDA and MDG Total Score....102
Figure 59: Training Data Confusion Matrix and OOB Estimate for “Alpha (α)”....102
Figure 60: Testing Data Confusion Matrix and Statistics for “Alpha (α)”....102
Figure 61:MDA and MDG Plots for “Beta_prime (β')”....103
Figure 62: Importance of each Predictor Variable for Predicting “Beta_prime (β')” based on MDA and MDG Total Score....104
Figure 63: Training Data Confusion Matrix and OOB Estimate for “Beta_prime (β')”....104
Figure 64: Testing Data Confusion Matrix and Statistics for “Beta_prime (β')”....105
Figure 65: MDA and MDG Plots for “Delta (δ)”....106
Figure 66: MDA and MDG Total Score for “Delta (δ)”....106
Figure 67: Training Data Confusion Matrix and OOB Estimate for “Delta (δ)”....107
Figure 68: Testing Data Confusion Matrix and Statistics for “Delta (δ)”....107
Figure 69: MDA and MDG Plots for “Gamma γ”....108
Figure 70: Importance of each Predictor Variable for Predicting “Gamma γ” based on MDA and MDG Total Score....109
Figure 71: Training Data Confusion Matrix and OOB Estimate for “Gamma γ”....109
Figure 72: Testing Data Confusion Matrix and Statistics for “Gamma γ”....110
Figure 73: MDA and MDG Plots for “$E1$”....111
Figure 74: MDA and MDG Plots for “$E1$”....111
Figure 75: Training Data Confusion Matrix and OOB Estimate for “$E1$”....112
Figure 76: Testing Data Confusion Matrix and Statistics for “$E1$”....112
Figure 77: MDA and MDG Plots for “$\alpha RPCC$”....113
Figure 78: Importance of each Predictor Variable for Predicting “$\alpha RPCC$” based on MDA and MDG Total Score....113
Figure 79: Training Data Confusion Matrix and OOB Estimate for “$\alpha RPCC$”....114

Figure 80:Testing Data Confusion Matrix and Statistics for “$\alpha RPCC$” 114
Figure 81: MDA and MDG Plots for “$\beta RPCC$”..115
Figure 82: Importance of each Predictor Variable for Predicting “$\beta RPCC$” based on MDA and MDG Total Score..116
Figure 83: Training Data Confusion Matrix and OOB Estimate for “$\beta RPCC$”........................116
Figure 84: Testing Data Confusion Matrix and Statistics for “$\beta RPCC$” 117
Figure 85: MDA and MDG Plots for “$E2$” 118
Figure 86: Importance of each Predictor Variable for Predicting “$E2$” based on MDA and MDG Total Score..119
Figure 87: Training Data Confusion Matrix and OOB Estimate for “$E2$” 119
Figure 88: Testing Data Confusion Matrix and Statistics for “$E2$”..120
Figure 89: MDA and MDG Plots for “$E3$” 121
Figure 90: Importance of each Predictor Variable for Predicting “$E3$” based on MDA and MDG Total Score..121
Figure 91: Training Data Confusion Matrix and OOB Estimate for “$E3$” 122
Figure 92: Testing Data Confusion Matrix and Statistics “$E3$” 122
Figure 93: MDA and MDG Plots for “$E4$” 123
Figure 94: Importance of each Predictor Variable for Predicting “$E4$” based on MDA and MDG Total Score (2 Sections) 124
Figure 95: Training Data Confusion Matrix and OOB Estimate for “$E4$” 125
Figure 96: Testing Data Confusion Matrix and Statistics “$E4$” 125
Figure 97: MDA and MDG Plots for “αR”...127
Figure 98: Importance of each Predictor Variable for Predicting “αR” based on MDA and MDG Total Score (4 Sections) 128
Figure 99: Training Data Confusion Matrix and OOB Estimate for “αR”...............................129
Figure 100:Testing Data Confusion Matrix and Statistics for “αR” 129
Figure 101:MDA and MDG Plots for “βR”...131
Figure 102:Importance of each Predictor Variable for Predicting “βR” based on MDA and MDG Total Score (3 Sections) 132
Figure 103: Training Data Confusion Matrix and OOB Estimate for “βR”.............................133
Figure 104:Testing Data Confusion Matrix and Statistics for “βR” 133
Figure 105: MDA and MDG Plots for “$h3$”...134
Figure 106: Importance of each Predictor Variable for Predicting “h_3” based on MDA and MDG Total Score..135
Figure 107: Training Data Confusion Matrix and OOB Estimate for “$h3$”..............................135
Figure 108: Testing Data Confusion Matrix and Statistics for “$h3$” 136
Figure 109: Variation of OOB-Estimate of Error Rate versus Number of Trees for rf_Delta Model 142
Figure 110: Variation of OOB-Estimate of Error Rate versus Number of Trees for rf_$E3$ Model 142
Figure 111: A Sample Code from R-Studio used to Build an RF-Model for “Delta (δ)”..........143
Figure 112: Density Plot for three Combinations...146
Figure 113: Deflection Plots for three Combinations 146

Chapter One

Introduction and Background

1.1 Introduction

It is crucial to have an elaborate understanding of all the material properties that constitute a pavement structure for reliably predicting their performance. The accurate estimation of such properties is a key element in determining adequate maintenance strategies and precisely assessing the damage level and the pavement's remaining life. The surface pavement deflection or displacement has been recognized to represent the sum of the vertical deflections in the subgrade and the pavement structure (Horak 1987b). Globally, the vertical deflections, among many others, are one of the mostly used measures to assess the pavements' structural condition for several reasons including: (1) cost efficiency, (2) the relative ease of measurements, (3) availability of historical data in large amounts, (4) historical correlation existing between the performance of the pavement and the deflection data (Solanki et al. 2014 as cited in Fuentes et al. 2020). Two approaches are considered to evaluate the structural condition of an existing pavement structure; Non-Destructive Testing (NDT) and Destructive Testing (DT). However, the road agencies mainly encourage using NDT devices for assessing the pavement's structural conditions to avoid any intrusive testing that might cause further destruction to the pavement structure. The Falling Weight Deflectometer (FWD) is considered the most common NDT device as it better simulates the actual field conditions when compared to laboratory testing. Figure 1 illustrates the general effect of an FWD load applied on a certain pavement structure. The pavement structure undergoes deflection under the wheel load. Consequently, it is important to note that the impact of the FWD load will generally extend over a certain radial distance from the point of load application. According to Horak (2008), the deflection bowl/deflection basin refers to the area of the pavement deflection under and close to the point of load application.

The FWD drops an impulse load having a duration of about 20 to 30 milliseconds. This test is used to assess the layer properties and evaluate the structural capacity of the pavement under study. The loading provokes an extensive range of frequency mechanisms and simulates the weight effect of a truck or an aircraft moving wheel. Therefore, the pavement surface deflections induced are measured using sensors located at different offsets from the applied load (Sebaaly et al. 1985). In a typical FWD equipment, one sensor is directly placed under the loading plate along with a minimum of six other sensors placed every 300mm. The aforementioned sensors are also referred as geophones and are mainly velocity transducers. Using the FWD device, the structural strength of a pavement structure, whether flexible or rigid, can be quantified using the backcalculation analysis of the elastic moduli for each layer.

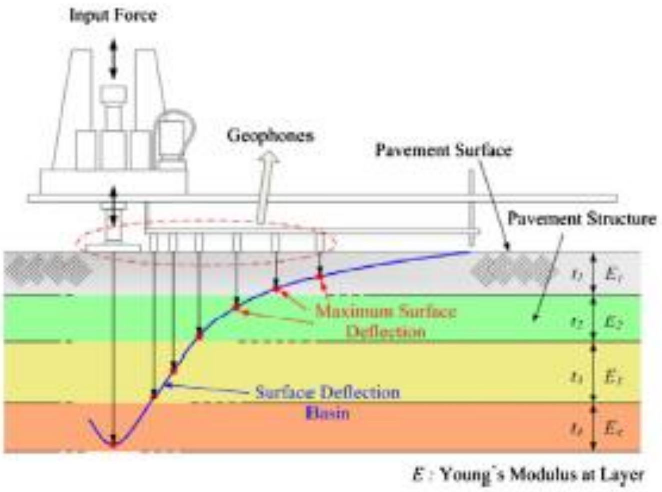

Figure 1: Deflection Basin resulting from FWD Testing, Choi et al. (2010)

For an effective analysis, the estimation of each layer modulus is required. As previously mentioned, the latter is obtained by a process known as the backcalculation. This method analyzes the FWD results and estimates the layer moduli for the pavement structure. It is based on an iterative process initiated by assuming a seed layer moduli (initial assumed) values for each layer. Following an optimization or root-solving algorithm, a forward calculation method generates new surface deflections that match – to a certain extent – the actual response of the pavement structure. Therefore, after several iterations, the assumed layer moduli obtained from the analytical pavement model are varied and adjusted until they generate a response that converges or strictly matches the measured FWD surface deflections. In other words, the analysis is validated once the measured and the theoretical deflection basins coincide and reliable results are obtained. Figure 2 illustrates the backcalculation process and the steps performed to reach the optimal results. Note that the seed moduli are consecutively adjusted for the upper pavement layers moving towards the lower ones. This approach is necessary to further improve the convergence between the measured and the calculated deflection basins.The seed moduli values tend to affect the convergence speed in almost all backcalculation software (Chou and Lytton 1991 , Uzan 1994, Fwa et al. 1997).

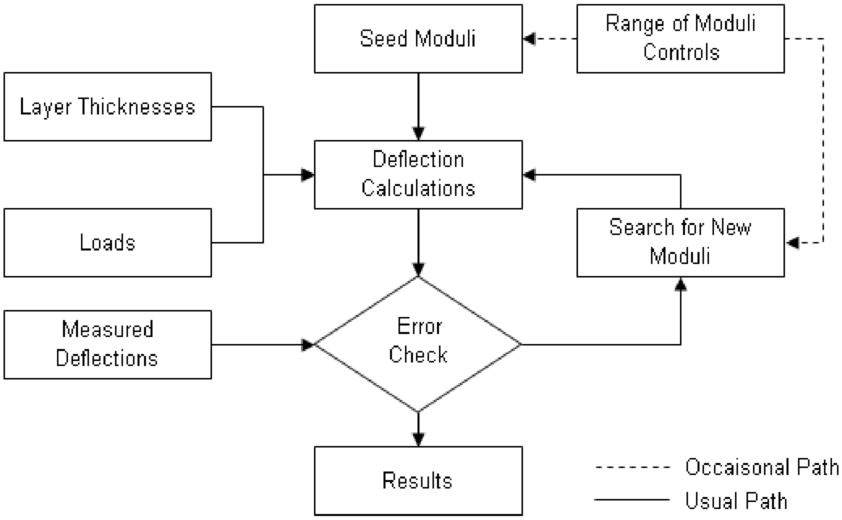

Figure 2: Backcalculation Process

Conventional static backcalculation models are based on peak FWD deflection values. Yet, several progressions have been adopted while using the dynamic models to address the full-time histories of the FWD load applied and the recorded/measured surface deflections, (Li and Wang 2019, Bazi and Assi 2020). Static analysis may be suitable for moderately thin pavements, though it holds substantial constraints for stiff and thick flexible or rigid structures which are mainly constructed for the airports, (Bazi et al. 2020). The use of dynamic modeling for backcalculation is endorsed over static modeling as the viscoelastic properties of asphalt concrete (AC) layers, inertial effects, damping and the resonance of the subgrade materials can be taken into account, (Bazi and Assi 2020). Thus, the dynamic modeling better reflects the pavement's real-life behavior and generates more reliable results that are suitable to the characteristics of the FWD analysis assuming the model is robust.

Initiating the dynamic backcalculation procedure with seed layer variables that represent the actual material properties rather than just guessing some arbitrary values, tends to lessen the computational-time required to achieve an adequate match between the calculated and measured deflection basins. Thus, developing prediction models for the seed variables will assist and guide pavement engineers in the seed variables estimation process. It further tends to generate more reliable backcalculation results which are critical for the structural evaluation of any pavement structure.

In this research , the dynamic approach is adopted to perform the analysis on both rigid and flexible pavements. Pavement structures with three and four layers are considered and modeled using Gmsh software. For flexible pavements, the Asphalt Concrete layer is modeled as linear viscoelastic (LVE). As for the Portland Cement Concrete layer and all unbound layers underlying flexible and rigid pavements are modeled as linear elastic (LE) with damping. A study is performed using the axisymmetric finite element modelling to quantify the effect of the FWD parameters on the pavement properties (variables). The models that predict the seed values are built using machine learning algorithms, specifically using random forests, while following a classification analysis. In other words, this research project aims to develop and validate an accurate solution that tends to serve as the starting point for the initiation of dynamic backcalculation. Therefore, leading to an efficient structural evaluation for both, flexible and rigid pavement structures.

1.2 Literature Review

Dynamic backcalculation methods are subject to several constraints. The backcalculated modulus does not constantly ensure a precise estimate in which a seed modulus is essential for all the individual pavement layers. Thus, this method does not generate a unique solution but rather a user dependent one. The backcalculation analysis remains unstable under the effect of several error corresponding to either the modeling of the forward approach, numerical computations or deflection measurements. As the mathematical expressions used for the backcalculation process consider several algorithms, the results will vary from one software to another. It is obligatory to identify beforehand the Poison ratios and the thicknesses of each layer within the pavement structure. Such parameters are typically assumed for the road agencies that lack databases. The accuracy of the backcalculation procedure is further assessed based on a specific tolerance degree between the measured FWD deflections and the calculated deflection values (Noureldin 1993). Because of the initially assumed seed variables, the convergence to the local optima may lead to erroneous and subjective final moduli results. Researchers studied the effect of the Root Mean Sqaure Error (RSME) on the backcalculation procedure and the impact of the seed estimation on such RSME values, (Seeds et al. 2000). It was noticed that RSME may be used as a mean to regulate the convergence of the calculated and measured deflection basins, yet this approach does not secure a precise layer moduli backcalculation. Realistic moduli values may not be generated from a backcalculation procedure having the least RSME value. Seeds et al. (2000) advocated the cautious use of the recommended RSME thresholds with the aid of engineering judgement to validate the reasonability of the backcalculated moduli. Similar findings were reported by Mehta and Roque (2003) in which a good match between the measured and the calculated deflections in terms of moderately minute RSME values might not certainly produce logical moduli.

Over the years, studies emphasized the importance of selecting relevant seed variables for the layer properties and acknowledged its major impact on the backcalculation software performance and on the final backcalculated results. As the subgrade layer can largely contribute to the surface deflection under the effect of the applied load, any error associated to the subgrade elastic modulus estimate will result in errors in the backcalculated moduli of the remaining pavement layers. The backcalulation results tends to converge to the accurate parameter solutions as long as the seed values are relatively closer to the real parameters (Fwa and Rani 2005). Several methods were followed by researchers and engineers to select the appropriate seed variables for the individual pavement layers and are stated as follows:

- Regression equations based on previous records
- Engineering judgments based on personal experiences
- Empirical models
- Internally produced seed variables in backcalculation software. For example, ELMOD uses the radius of curvature method for estimating the seed values.

Due to the nature of such strategies, their applicability has been limited to certain pavement structural design, material types and climate states (Fwa and Rani 2005). Rationally, backcalculation software provide embedded seed variables to initiate the analysis. Yet, these values do not always generate satisfactory and rational results. For this reason, the convention of “user-input” seed variables was recommended in most cases. Fwa and Rani (2005) developed an algorithm, 2L-BACK, as a guidance to select the appropriate seed moduli for two-layered flexible pavement structure. The algorithm depends on a closed form solution for the backcalculation of the moduli. Two different backcalculation programs, EVERCALC and MICHBACK, were used to evaluate the effeciency of the proposed process. The authors found that the proposed algorithm has improved the MISHBACK performance more than that of EVERCALC in terms of the convergence features and the precision of the backcalculation results. This indicated that the 2L-Back program lacks consistency among different backcaluclation software. Though, the study proved that the proposed algorithm showed no transferability constrictions and can be considered – to a certain extent – as an effective guidance (Fwa and Rani 2005). Additionally, an approach based on the Constrained Extended Kalman Filter (CEKF) was introduced for backcalculation (Choi et al. 2010). It makes use of a tranformation to limit the search for the domains required to obtain the optimial estimations for the material properties. The approach's sensitivity was tested with respect to the initial seed layer moduli values and the number of the pavement layers. The results showed that the EKF method allowed a quick convergence to the actual moduli irrespective of the seed values selected (Choi et al. 2010). However, for pavement structures having a stabalized base/subbase layer ,the efficiency of the algorithm in terms of the seed value dependency and the convergence achievment is not quite confirmed and requires additional research.

New algorithms are further developed to assist with the fast convergence of the deflection basins and to reduce the effect of the seed variables selected on the latter. Genetic algorithm technique (GA) is recently presented as an advanced robust method and a highly effective optimization tool, capable of conveying various parameters and features that have an impact on the backcalculation procedure (Plati et al. 2017). Instead of having a seed value, the optimized-unknown in GA can have a certain range. Thus, making the quest for an optimal solution tends to be more potent than other approaches as the overall solution can be attained and the divergence is proscribed (Plati et al. 2017). Additionally, Li and Wang (2019) combined GA with Artificial Neural Networks (ANN) to enhance the solution optimizations. With the aid of finite element models, synthetic database was generated to comprehend all the disparities in the pavement structure, material properties, temperature and the loading magnitude. The ANN-GA model had more advantages when compared to the conventional backcalculation software such as the exclusion of the seed variables and the use of complex properties. Yet, the accuracy and the applicability of this model presented limitations related to the parameter range used in the simulated database (Li and Wang 2019). Moreover, Abd El-Raof et al, (2018) developed a simplified closed form procedure which achieved success in the estimation of the layer moduli. Yet, this procedure was only limited for a two-layered flexible pavement structure.

To better understand the behavior of pavement structures and their design, computer simulation techniques with the aid of 3D finite element models have been emerging. Thus, offering pavement engineers a prevailing capability to recognize and identify the weakness points present in the pavement structure even prior construction. Bazi and Assi (2020) developed a Finite Element application “*PULSE* 2019” and was further upgraded to “*PULSE* 2020” by improving the estimation of the Jacobian-Matrix, (Bazi et. al, 2021). This application is used in this study to determine the deflection time histories for various flexible and rigid pavement structures.

Chapter Two

Finite Element Method

2.1 FEM Definition

Normally, it is impossible to find analytical/mathematical solutions for problems including intricate geometries, properties and loadings. Such solutions are obtained using a mathematical expression that produce the intended quantities at different locations in the structure under study. Therefore, being only valid and effective for an infinite count of certain locations in the structure. Henceforth, for robust and adequate solutions, one must consider the finite element method (FEM). The latter is a numerical method that produces a system of concurrent algebraical equations and provides approximate solutions for the unidentified at distinct points found in the continuum. This method enables users to acquire the evolution in time and space for one or more variables that represent the physical system's behavior (Oñate 2009). Consequently, the finite element method is considered a powerful and an effective method for the stresses, strains and displacements computations that develop in a structure subjected to a set of loadings.

The main idea of the Finite Element (FE) method is to divide a certain continuum into a correspondent system consisting of a finite number of smaller units, referred to as the finite elements, that should remain interconnected at common points between the elements. These points are termed by nodes and they do control the element's behavior. Each element within the continuum have much simpler and uncomplicated geometries, boundary limitations/conditions, material properties and loading conditions, etc. when compared to the continuum as a whole. This corroborates the monotonic fluctuations in the stresses and the deformations in each individual element. Therefore, the displacements in each element may be approached by certain displacement functions. When allowing the stresses or the deformations present at a definite point within the element to depend on the ones at the nodes, one can write an attainable number of the nodes' differential equations of motion (Logan 2017). Thus, the discretization of any structure will allow the user to formulate equations for the individual finite elements, which will be later on combined for developing a solution of the entire structure. In other words, a problem consisting of infinite numbers of degrees of freedom may be simplified and converted to a problem having a finite amount (Qu 2004).

2.2 Structural Mechanics

Solid or structural mechanics is a branch of applied or continuum mechanics that studies the motion and the displacements of solid structures under the forces' actions. Any structure subjected to various types of either external or internal forces will develop stresses that are generally considered as nonuniform (Kazimi 2001). Such stresses will cause the structure to depart away from its original rest shape and thus generating strains. The latter may be detected as deformations or may be measured through strain gauges. According to Liu and Quek (2013), it is vital to comprehend the mechanics of a certain material and the relationships present among the applied forces, resulting stresses, strains and displacements for a well-designed structural system.

The applied forces may be distinguished as being either static or dynamic. Static forces are the forces that remain constant over time and, generally, will not generate structural vibrations. A static problem mainly has one response, the displacement, that can be determined using the principles of static equilibrium. On the other hand, dynamic forces are considered time-dependent and will result in structural vibrations once the structure is exposed to such forces. In other words, a dynamic problem will have three responses including the displacement, the velocity and the acceleration. The dynamic forces are not only considered a function of time, but it also enthuses the system's mass, thus producing inertial effects. Note that the static equations may be derived from the dynamic equations by simply eliminating the terms related to the dynamic responses (Liu and Quek 2013).

2.3 Axisymmetry

An axisymmetric element, a triangular torus, is a special 2D-element that is rather convenient when a symmetry exists with respect to the loading and to the geometry about a certain axis of the structure under study as shown in Figures 3 and 4.

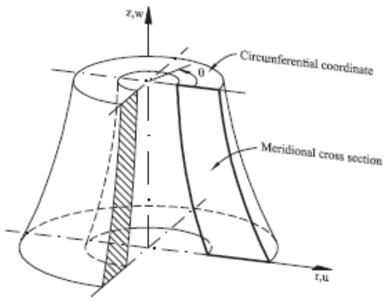

Figure 4: Axisymmetric Solid (Oñate 2009)

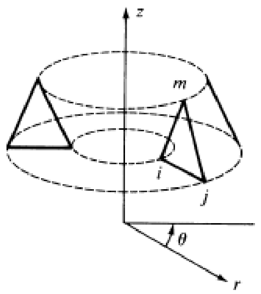

Figure 3: Axisymmetric Element "ijm" (Logan 2017)

In the axisymmetric problems, radial displacements generate circumferential strains which in return induce the stresses σ_θ , σ_z σ_r, and τ_{rz} defined in the cylindrical coordinates (r, θ, z). Note that θ , z and r refer to the circumferential, longitudinal and radial directions, respectively (Hutton 2004, Logan 2017). The symmetry existing about a z-axis causes the stresses to not depend on the θ coordinate. This means that all the derivatives corresponding to the θ disappear; the displacement element tangent to the circumferential direction (θ) , the shear stresses $\tau_{\theta z}$, $\tau_{r\theta}$ and the shear strains $\gamma_{\theta z}$, $\gamma_{r\theta}$ are zero. Therefore, structures having material and geometrical properties independent of the θ coordinate enables the structure's intrinsic 3D behavior to be demonstrated with a simpler 2D -model.

A considerable percentage of engineering problems and structures can be represented by axisymmetric models. Pavements, for example, that are subject to FWD loading can be analyzed using such simple and time efficient 2D-models.

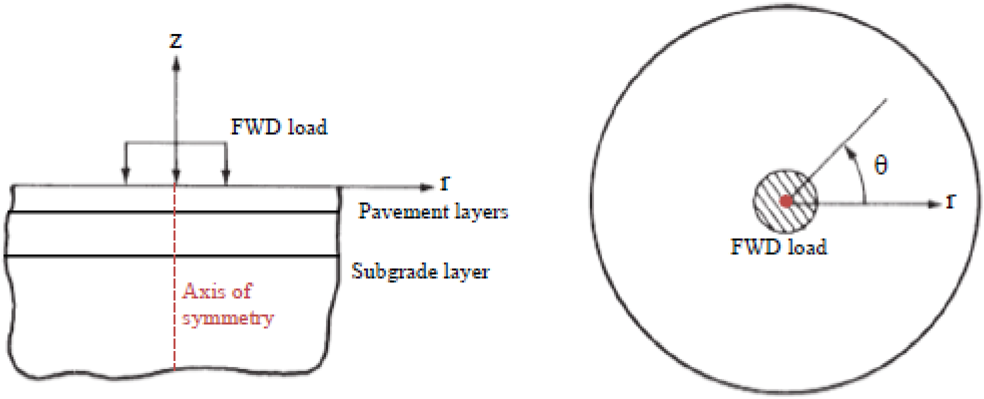

(a) Section View (b) Plan View

Figure 5: Axisymmetric Engineering Problem (Bazi et al. 2020)

2.3.1 Displacement Field

When considering an axisymmetric solid subject to an axisymmetric load as shown in Figure 3, the displacement vector will consist of two components including (u) and (w), the radial and the axial displacements, respectively. However, the circumferential displacement component (v) is equal to zero because of the axial symmetry. Thus, the displacement vector “U” is given by equation (1): (Oñate 2009)

$$\mathrm{U} = \begin{bmatrix} u\ (r,z) \\ w\ (r,z) \end{bmatrix} \tag{1}$$

2.3.2 Strain Field

As previously mentioned, the displacement components are independent of the (θ) coordinate causing the tangential strains to be zero.

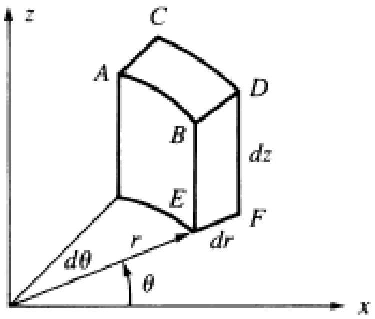

Figure 7: Plane Cross Section (Logan 2017)

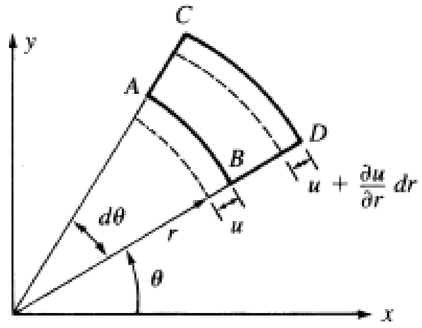

Figure 6 : Axisymmetric Element (Logan 2017)

For the axisymmetric element ABCD expressed in a plane cross section (Figure 6), the sides AB and CD displace in the radial direction an amount of u and $u + \frac{\partial u}{\partial r} dr$ respectively. Whereby, in the radial direction, the normal strain (ε_r) is represented by equation 2 (Logan 2017).

$$\varepsilon_r = \frac{\partial u}{\partial r} \tag{2}$$

Generally, the strain developed in the tangential path is dependent on the radial (u) and the tangential (v) displacements. Yet, evoke that tangential displacement (v) is zero for an axisymmetric deformations (Logan 2017). Therefore, by only having the radial displacement (u), the length of arc AB becomes $(u + r)\ d\theta$ and the tangential strain (ε_θ) is represented by equation 3:

$$\varepsilon_\theta = \frac{(u+r)d\theta - rd\theta}{rd\theta} = \frac{u}{r} \tag{3}$$

For determining the longitudinal and the shear strains, element BDEF is considered by which it is shown to displace a certain amount in the longitudinal and radial directions at each point as depicted in Figure 8 below.

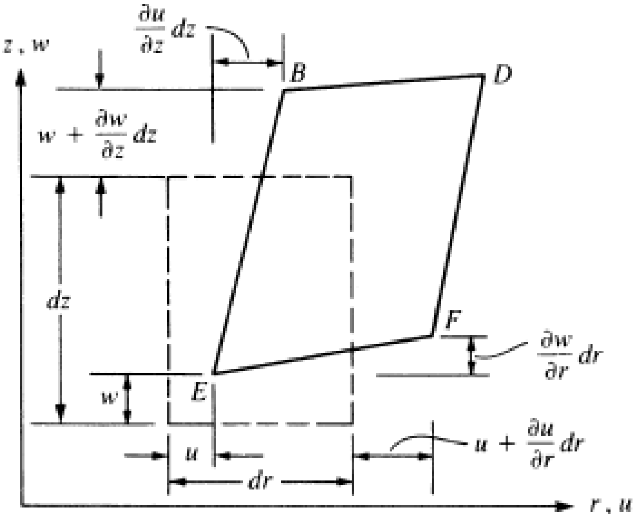

Figure 8: Element Displacement in the r-z Plane (Logan 2017)

Therefore, using the aforementioned displacements' derivatives, the longitudinal (ε_z), and the shear strains (γ_{rz}) are given by equations (4) and (5) respectively.

$$\varepsilon_z = \frac{\partial w}{\partial z} \tag{4}$$

$$\gamma_{rz} = \frac{\partial u}{\partial z} + \frac{\partial w}{\partial r} \tag{5}$$

In summary, the strain vector (ε) at a certain point is represented by the four components:

$$\varepsilon = [\, \varepsilon_r \, , \, \varepsilon_z \, , \, \varepsilon_\theta \, , \gamma_{rz} \,]^T = \left[\frac{\partial u}{\partial r} \, , \frac{\partial w}{\partial z} \, , \frac{u}{r} \, , \frac{\partial u}{\partial z} + \frac{\partial w}{\partial r} \right]^T \tag{6}$$

2.3.3 Stress Field

The stresses related to the strain vector of Eq. (6) may be also expressed in a vector format by:

$$\sigma = [\, \sigma_r \, , \, \sigma_z \, , \, \sigma_\theta \, , \tau_{rz} \,]^T \tag{7}$$

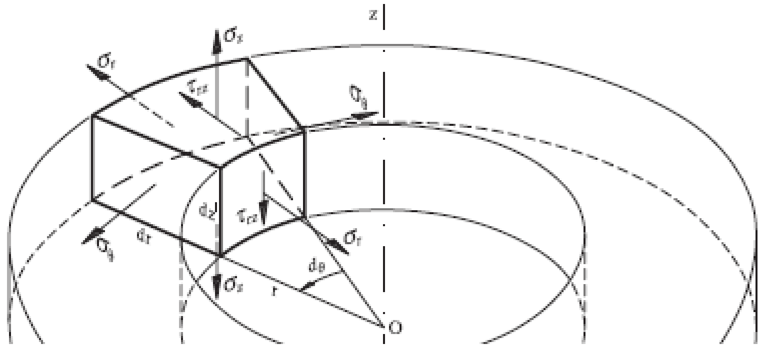

Figure 9: Element Displacement in the r-z Plane, (Logan 2017)

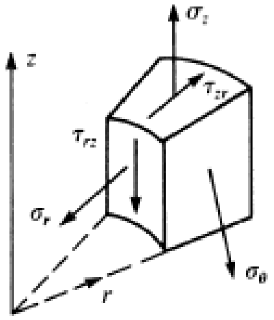

Figure 10: Stresses in an Axisymmetric Structure, (Logan 2017)

Where,

σ_r is the radial stress, σ_z is the longitudinal stress, σ_θ is the circumferential stress and lastly τ_{rz} is the tangential stress illustrated in Figures 9 and 10. Note that the remaining stresses are equal to zero.

2.3.4 Relationship between the Strains and the Stresses

The relationship is mainly deduced from the 3D-elasticity theory in a similar way as that for the plane elasticity (Oñate 2009).

For 2D-axisymmetric problems, the elasticity matrix (D) may be determined using that of a 3D structure by considering that the shear stress (γ_{rz}) is not joined with the circumferential stress (σ_θ) as well as forcing $\gamma_{z\theta} = \gamma_{r\theta} = 0$. Therefore, the elasticity matrix (D) for isotropic materials is expressed by:

$$D = \frac{E}{(1+\nu)(1-2\nu)} \begin{bmatrix} 1-\nu & \nu & \nu & 0 \\ & 1-\nu & \nu & 0 \\ & & 1-\nu & 0 \\ sy. & & & \frac{1-2\nu}{2} \end{bmatrix} \tag{8}$$

Hence, the relationship between the stresses and the strains for isotropic materials is given by:

$$\begin{Bmatrix} \sigma_r \\ \sigma_z \\ \sigma_\theta \\ \tau_{rz} \end{Bmatrix} = \frac{E}{(1+\nu)(1-2\nu)} \begin{bmatrix} 1-\nu & \nu & \nu & 0 \\ & 1-\nu & \nu & 0 \\ & & 1-\nu & 0 \\ sy. & & & \frac{1-2\nu}{2} \end{bmatrix} \begin{Bmatrix} \partial u / \partial r \\ \partial w / \partial z \\ u / r \\ \frac{\partial u}{\partial z} + \frac{\partial w}{\partial r} \end{Bmatrix} \tag{9}$$

2.4 Formulating the Finite Elements

2.4.1 Structure Discretization and Element Types

The structure under study is discretized into a set of elements in which the latter can consist of either a single element type or several element types combined together. This discretization is also referred to as the Finite Element (FE) mesh.

A mesh whereby the inner nodes are surrounded by the same elements' number is known as the structured mesh. The latter follows a certain topological pattern which is repeated in all the space directions (Berzins 1998). Else, the mesh is considered as an unstructured mesh.

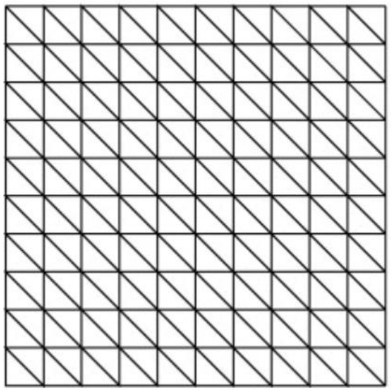

Figure 12: Structured Mesh

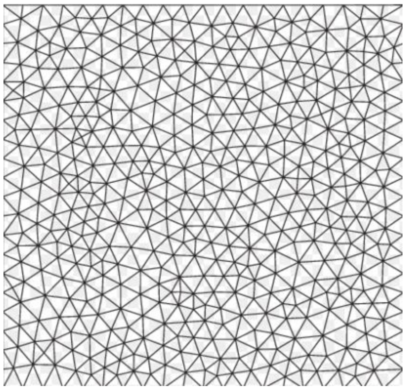

Figure 11:Unstructured Mesh

The selection of elements used in the FE analysis largely depends on the physical constituent of the structure under actual-real loadings and on the result's accuracy level that the analyst seeks for especially when compared to real-life behaviors. Engineering judgement regarding the suitability of which dimension to adopt is essential. Furthermore, the selection of the utmost convenient element for an FE problem is considered one of the main and critical tasks performed by the analyst/engineer. Note that such decisions are also affected by the availability of the element types in the computer program used and on the analyst's experience in solving similar problems using the FEM. The selected element types should be robust whereby the mesh must account for any possible stress gradients that might be present in the solution (Oñate 2009).

Several elements are available for solving FE problems including the plane (2D) elements portrayed in Figure (13). These elements are referred to as triangular and quadrilaterals. Note that linear elements - having nodes placed only at the corners and have straight boundaries - are considered the simplest 2D elements.

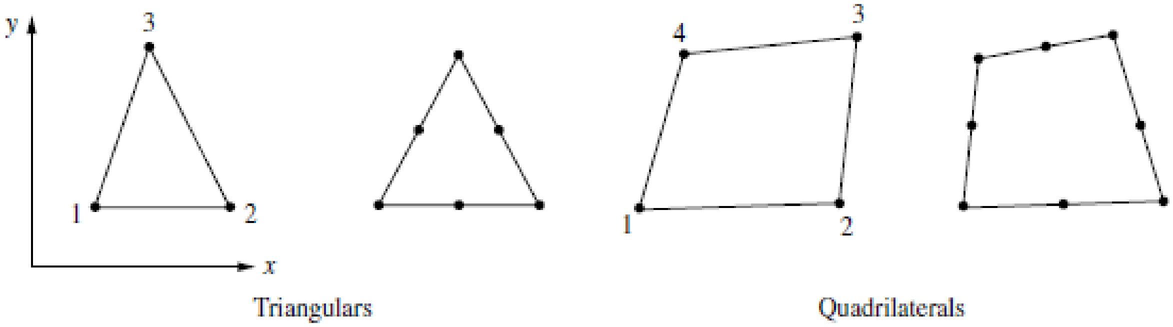

Figure 13: Linear, Quadratic Triangular and Quadrilateral Elements, (Logan 2017)

2.4.1.1 Discretization Accuracy

The structure's geometry is discretized and divided into a mesh of finite elements with allied nodes and modeled with a specific accuracy. Evidently, this discretization presents an additional approximation. Therefore, when compared to the real-life (actual) behavior, two errors arouse from the outset including (1) the discretization error and (2) the modelling error. The latter may be minimized by enhancing the structural and the conceptual models that define the structure's real behavior (Oñate 2009). On the other hand, the discretization error may be minimized by using more elements within the continuum i.e., a finer mesh. The elements should be modeled small in a way to generate robust and reliable results but large in a way to lessen the computational exertion (Logan 2017). Smaller elements are commonly more recommended when the obtained results vary rapidly while larger elements are more desired when the results are moderately constant (Logan 2017). Another way to minimize the error is by increasing the finite elements' accuracy selected through considering a higher order-polynomial expansions for the displacement field approximation in every element (Oñate 2009).

2.4.1.2 Infinite Media

Generally, for the generation of the finite elements, three methods are employed to replicate the infinite media including:

- Far boundary method
- Infinite element boundary method
- Viscous damping method

In this project, the main focus is mainly on the far boundary method. Specifically, the boundary is moved a large interval/distance from the structure's center so that the boundary's influence becomes insignificant.

2.4.2 Axisymmetric Triangle with Three Nodes

The FE analysis for an axisymmetric element is further demonstrated using a linear "triangular" element with three nodes.

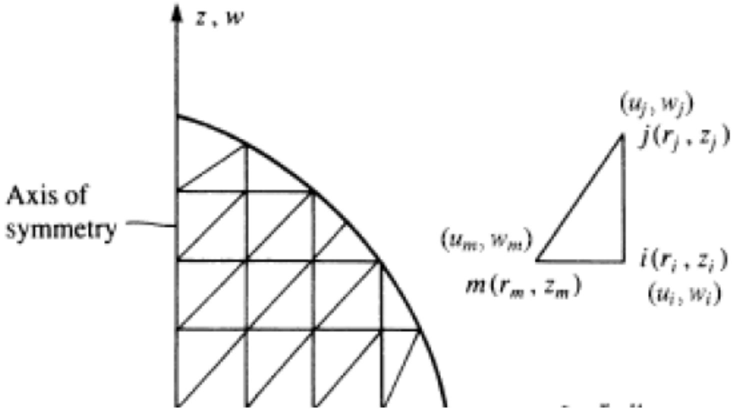

Figure 14: Axisymmetric Structure discretized into Triangular Elements (Logan 2017)

The axisymmetric structure shown in Figure (14) is discretized into interconnected "triangular" elements. The individual elements include 3-nodes whereby each node has 2-degrees of freedom denoted by, for example, u_m and w_m at node m. Each interconnected triangular element is connected, explicitly or implicitly, to other elements through mutual interfaces such as nodes, surfaces and boundary lines. By employing the identified stress and strain properties of the material constituting the structure under study, the behavior of a certain node may be determined in terms of the other element properties found in this structure (Logan 2017). Therefore, the overall union of equations delineating every node's behavior produce a set of algebraic equations represented in a matrix format.

The linear displacement function associated with each triangular element are given by (Logan 2017):

$$\begin{aligned} u(r,z) &= a_1 + a_2 r + a_3 z \\ w(r,z) &= a_4 + a_5 r + a_6 z \end{aligned} \tag{10}$$

Note that the overall number of the a_i's coordinates presented in the displacement function equals the overall count of the degrees of freedom for each element. Thus, the displacement at each node is (Logan 2017):

$$\{d\} = \begin{Bmatrix} d_i \\ d_j \\ d_m \end{Bmatrix} = \begin{Bmatrix} u_i \\ w_i \\ u_j \\ w_j \\ u_m \\ w_m \end{Bmatrix} \tag{11}$$

Whereby, the degrees of freedom u and w will be evaluated at each node within an element. For example, at node m:

$$u\,(r_m, z_m) = u_m = a_1 + a_2 r_m + a_3 z_m$$
$$w(r_m, z_m) = w_m = a_4 + a_5 r_m + a_6 z_m$$

Hence, the displacement function is given by:

$$\{\psi\} = \begin{Bmatrix} u \\ w \end{Bmatrix} = \begin{Bmatrix} a_1 + a_2 r + a_3 z \\ a_4 + a_5 r + a_6 z \end{Bmatrix} = \begin{bmatrix} 1 & r & z & 0 & 0 & 0 \\ 0 & 0 & 0 & 1 & r & z \end{bmatrix} \begin{Bmatrix} a_1 \\ a_2 \\ a_3 \\ a_4 \\ a_5 \\ a_6 \end{Bmatrix} \tag{12}$$

Through the substitution of the nodal points' coordinates in Eq. (12) along with some inversions, the a_i's may be determined while having the following expression:

$$\begin{Bmatrix} a_1 \\ a_2 \\ a_3 \end{Bmatrix} = \frac{1}{2A} \begin{bmatrix} \alpha_i & \alpha_j & \alpha_m \\ \beta_i & \beta_j & \beta_m \\ \gamma_i & \gamma_j & \gamma_m \end{bmatrix} \begin{Bmatrix} u_i \\ u_j \\ u_m \end{Bmatrix}$$

$$\begin{Bmatrix} a_4 \\ a_5 \\ a_6 \end{Bmatrix} = \frac{1}{2A} \begin{bmatrix} \alpha_i & \alpha_j & \alpha_m \\ \beta_i & \beta_j & \beta_m \\ \gamma_i & \gamma_j & \gamma_m \end{bmatrix} \begin{Bmatrix} w_i \\ w_j \\ w_m \end{Bmatrix} \tag{13}$$

Whereby,

$$\alpha_i = r_j z_m - z_j r_m \qquad \alpha_j = r_m z_i - z_m r_i \qquad \alpha_m = r_i z_j - z_i r_j$$
$$\beta_i = z_j - z_m \qquad \beta_j = z_m - z_i \qquad \beta_m = z_i - z_j$$
$$\gamma_i = r_m - r_j \qquad \gamma_j = r_i - r_m \qquad \gamma_m = r_j - r_i \tag{14}$$

A = Triangular Element Area = $\frac{1}{2}\begin{bmatrix}1 & r_i & z_i\\ 1 & r_j & z_j\\ 1 & r_m & z_m\end{bmatrix}$

As for the shape functions (N_i , N_j and N_m) , they characterize the displacement shape $\{\psi\}$ when plotted over a certain element's surface (Logan 2017), and are defined by Eq. (15).

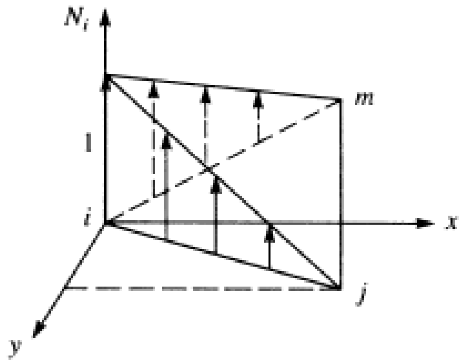

Figure 15: Ni Variation over the X-Y surface for a certain Element (Logan 2017)

$$\begin{aligned} N_i &= \frac{1}{2A}\left[\propto_i + (r\beta_i) + (z\gamma_i)\right]\\ N_j &= \frac{1}{2A}\left[\propto_j + (r\beta_j) + (z\gamma_j)\right]\\ N_m &= \frac{1}{2A}\left[\propto_m + (r\beta_m) + (z\gamma_m)\right]\end{aligned} \tag{15}$$

Hence, by substituting Eq. (13) into equations (12) by taking into account the shape function equations (15), the general function is found to be (Oñate 2009, Logan 2017):

$$\{\psi\} = \begin{Bmatrix} u(r,z)\\ w(r,z)\end{Bmatrix} = \begin{bmatrix} N_i & 0 & N_j & 0 & N_m & 0\\ 0 & N_i & 0 & N_j & 0 & N_m\end{bmatrix}\begin{Bmatrix} u_i\\ w_i\\ u_j\\ w_j\\ u_m\\ w_m\end{Bmatrix} \tag{16}$$

2.4.3 Stress-Strain and Strain-Displacement Relationships

The "strain" vector may be written in this format:

$$\varepsilon = \begin{Bmatrix}\epsilon_r\\ \epsilon_z\\ \epsilon_\theta\\ \gamma_{rz}\end{Bmatrix} = \begin{Bmatrix} a_2\\ a_6\\ \frac{a_1}{r} + a_2 + \frac{a_3 z}{r}\\ a_3 + a_5\end{Bmatrix} = \begin{bmatrix} 0 & 1 & 0 & 0 & 0 & 0\\ 0 & 0 & 0 & 0 & 0 & 1\\ \frac{1}{r} & 1 & \frac{z}{r} & 0 & 0 & 0\\ 0 & 0 & 1 & 0 & 1 & 0\end{bmatrix}\begin{Bmatrix} a_1\\ a_2\\ a_3\\ a_4\\ a_5\\ a_6\end{Bmatrix} \tag{17}$$

The gradient matrix [B] is defined by:

$$[B] = [B_i \;\; B_j \;\; B_m] \tag{18}$$

Whereby,

$$B_i = \frac{1}{2A}\begin{bmatrix} \beta_i & 0 \\ 0 & \gamma_i \\ \frac{\propto_i}{r} + \beta_i + \frac{z\,\gamma_i}{r} & 0 \\ \gamma_i & \beta_i \end{bmatrix}, \quad B_j = \frac{1}{2A}\begin{bmatrix} \beta_j & 0 \\ 0 & \gamma_j \\ \frac{\propto_j}{r} + \beta_j + \frac{z\,\gamma_j}{r} & 0 \\ \gamma_j & \beta_j \end{bmatrix}, \quad B_m = \frac{1}{2A}\begin{bmatrix} \beta_m & 0 \\ 0 & \gamma_m \\ \frac{\propto_m}{r} + \beta_m + \frac{z\,\gamma_m}{r} & 0 \\ \gamma_m & \beta_m \end{bmatrix} \tag{19}$$

Note that [B] is clearly a function of both r and the z-coordinates which means that the circumferential strain (ε_θ) is mainly not constant.

By substituting Eq. (13) into Eq. (17) and linking it by the [B] matrix, the strain vector will be expressed by:

$$\{\varepsilon\} = \frac{1}{2A}\begin{bmatrix} \beta_i & 0 & \beta_j & 0 & \beta_m & 0 \\ 0 & \gamma_i & 0 & \gamma_j & 0 & \gamma_m \\ \frac{\alpha_i}{r} + \beta_i + \frac{\gamma_i z}{r} & 0 & \frac{\alpha_j}{r} + \beta_j + \frac{\gamma_j z}{r} & 0 & \frac{\alpha_m}{r} + \beta_m + \frac{\gamma_m z}{r} & 0 \\ \gamma_i & \beta_i & \gamma_j & \beta_j & \gamma_m & \beta_m \end{bmatrix} \begin{Bmatrix} u_i \\ w_i \\ u_j \\ w_j \\ u_m \\ w_m \end{Bmatrix} \tag{20}$$

Lastly, the stress is therefore expressed by:

$$\{\,\sigma\,\} = [D][B]\{d\} \tag{21}$$

2.5 Linear Viscoelasticity

Many structures are exposed to a certain loading behavior by which the inertial effects are considered one of the main pillars of an efficient dynamic analysis. Normally, for almost any material type, a considered amount of energy absorption and dissipation may be experimentally observed. Whereby the majority of the dissipative materials are mostly defined using time and/or frequency-domains through viscoelastic models.

2.5.1 Viscoelastic Properties

The material's viscoelastic property enables the analyst to determine the amount of energy being dissipated, or even returned to the actual surroundings, once an impact is applied. Such materials are remarked from other material types that are regarded as purely elastic. Viscoelastic materials manifest properties including the relaxation modulus, the creep compliance, the dynamic modulus (complex modulus) and dissipative qualities (Tapia-Romero, M. A., et.al 2020). These properties describing the material's capacity to dissipate energy are referred to as the dynamic properties. Note that the complex modulus (E^*) is mainly composed of a real and imaginary parts, referred to as the storage modulus (E') and the loss modulus (E'') respectively. This relationship is given by Eq. (22):

$$E^* = E' + i\,E'' \tag{22}$$

Whereby, the storage modulus (E') is best defined as the material's capacity of storing energy and returning it to the surrounding. While the loss modulus (E'') is defined as the material's capability to dissipate energy to its own interior structure. For a better understanding of this concept, a graphical representation is shown in Figure (16).

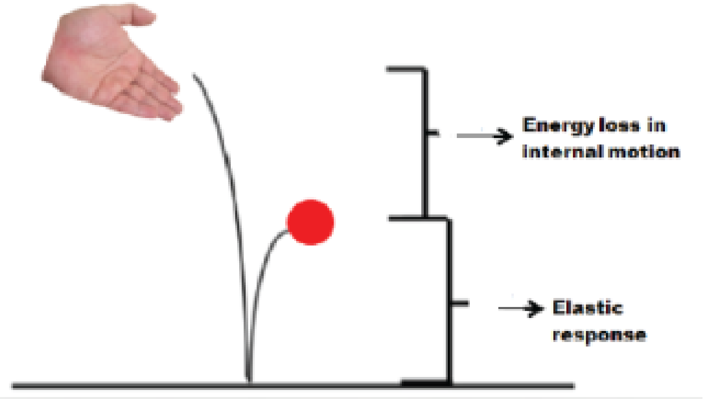

Figure 16: Storage and Loss Moduli Concept (Saba et al., 2016)

2.5.1.1 Viscoelastic Response Discerption

The stress/strain relations and the time-related properties are determined by modeling the viscoelastic materials. Consequently, their responses are controlled by the deformation and its rate when subject to loading. Due to the viscous property, the material will surely experience either relaxation or creep. The relaxation modulus defines the phenomenon by which the stress tends to decrease with time while the strain remains constant. It is mainly necessary to determine in the design procedure and within the finite element analysis the thermal stress that is present in the asphalt pavement structure On contrary, the creep compliance defines the phenomenon by which the strain tends to decrease with time under the effect of constant stresses.

Associated to pavement engineering, the asphalt mixtures' viscoelastic responses can be modeled and expressed by a linear combination of dashpots and springs (Zhao, Y et al. 2014). The aforementioned dashpots and springs are referred to as the Newton and Hooke elements respectively (Figures 17 and 18). Once combined in series, a Maxwell element will be formed, otherwise a Kelvin-Voight element is yielded (Figures 19 and 20).

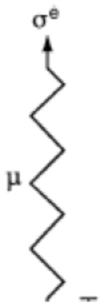

Figure 17: Hooke Element (Elastic Component)

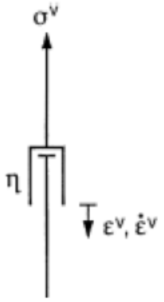

Figure 18: Newton Element (Viscous Component)

Figure 19: Maxwell Element in Series

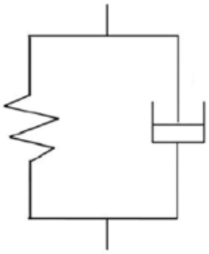

Figure 20: Kelvin-Voight Element

The elastic material (E) constant defines the linear relationship present between (ε^e), the elastic strain, and (σ^e), the elastic stress (Kaliske & Rothert 1997).

$$\sigma^e = E\varepsilon^e \tag{23}$$

For the Newton element, (σ^v), the viscous stress relies on the rate of the strain $(\frac{d\epsilon^v}{dt} = \acute{\varepsilon})$. Such quantities are linearly related by the viscosity coefficient (η).

$$\sigma^v = \eta\,\dot{\varepsilon}^v \tag{24}$$

Note that the viscosity coefficient (η) may be also related to the elastic (E)constant and the relaxation time (τ). The latter is defined as the time required to retain the stress to e^{-1} from its original value right after the strain imposition.

$$\tau = \frac{\eta}{E} \tag{25}$$

An efficient and compact 3D-viscoelastic formulation is essential for FE computations having a large scale. The latter is mainly achieved by modeling the Generalized Maxwell Model (GMM) / element.

2.5.1.2 Generalized Maxwell Model

The generalized Maxwell model/element is mainly comprised of a number of independent Maxwell elements suited in parallel. This implies that this model is applicable for finite small strains. The overall strain for the Maxwell elements is the sum of the both, the elastic (ε^e) and the viscous strains (ε^v), whereas the stress is considered equal in both elements that are said to be rheological (Kaliske & Rothert 1997).

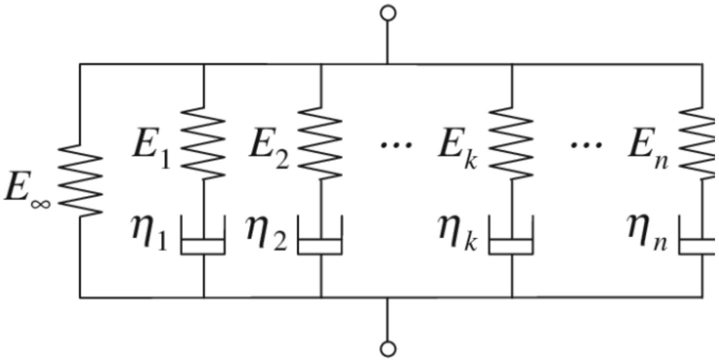

Figure 21: Generalized Maxwell Element

$$\varepsilon_{total} = \varepsilon = \varepsilon^{e} + \varepsilon^{v} \tag{26}$$

$$\sigma = \sigma^{e} = \sigma^{v} \tag{27}$$

At equilibrium state, $\acute{\varepsilon}^{\,v} = 0$, the Maxwell element's viscous strain becomes equal to the total strain ($\varepsilon^{v} = \varepsilon$) whereas the elastic strain (ε^{e}) becomes zero. On the other hand, and through Eq. (26), the Maxwell model's differential equation is given by:

$$\acute{\varepsilon} = \frac{1}{E}\frac{d\sigma}{dt} + \frac{1}{\eta}\sigma \tag{28}$$

By conducting a relaxation test, the solution for the differential Eq. (28) is expressed by:

$$\frac{\sigma(t)}{\varepsilon_o} = Ee^{\frac{-t}{\tau}} = R(t) \tag{29}$$

Where $R(t)$ is known as the relaxation-function which states the explicit material's viscoelastic features and characteristics. Note that at t_∞, the stress becomes zero.

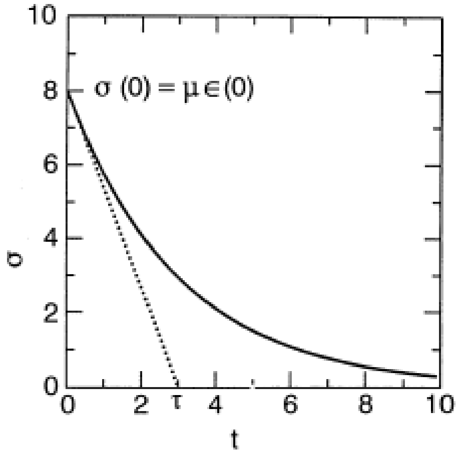

Figure 22: Maxwell Element Relaxation Experiment (Kaliske & Rothert 1997)

The previously mentioned relaxation experiment performed on one Maxwell element is applicable on a generalized maxwell model (GMM). Therefore, using the GMM and its Prony series delineation, the relaxation function is expressed by (Kaliske & Rothert 1997):

$$R(t)_{GMM} = E_{\infty} + \sum_{j=1}^{N} E_j e^{\frac{-t}{\tau_j}} \tag{30}$$

Whereby, (E_{∞}) refers to equilibrium-modulus at t_{∞} (long-term) represented by:

$$E_{\infty} = E_o \sum_{j=1}^{N} \alpha_j = E_o \sum_{j=1}^{N} \frac{E_j}{E_o} \tag{31}$$

τ_j and E_j refer to the time for the viscous relaxation and the elastic stiffness, respectively, that correspond to each element constituting the GMM. As for N, it corresponds to the total number of individual Maxwell elements (j), while α_j is known as the relative modulus for each element (j). At time t_o, (E_o) can be determined where it refers to the deformation's time-independent elastic element i.e., it remains constant over time. The latter is known as the instantaneous modulus represented by:

$$E_o = E_{\infty} + \sum_{j=1}^{N} E_j \tag{32}$$

2.5.1.3 Prony Series

The material's viscoelastic characteristics may be represented through the Prony series. The latter is mainly a mathematical process used to fit a union of equidistant values contingent on a set of damped exponentials (Zhang et al. 2018). It can remarkably enhance the computational efficacy accredited to its relative physical origin corresponding to the mechanical model theory that deals with linear dashpots and springs (Zhang et al. 2018). Consequently, Prony series is generally employed in linear viscoelastic functions.

As previously mentioned, the generalized Maxwell model (GMM) can be utilized to describe the asphalt mixtures' total stress. By distinguishing its corresponding strain by taking into account the elastic theory (Park & Schapery 1999), the complex modulus E^* representation through the Prony Series can be expressed by the following:

$$E^* = E_{\infty} + \sum_{j=1}^{N} \frac{i\omega\tau_j E_j}{i\omega\tau_j + 1} \tag{33}$$

Whereby, i is equal to $\sqrt{-1}$ (complex number) and ω is referred to as an angular frequency in $\frac{rad}{sec}$.

The relaxation modulus's Prony series coefficients may be directly obtained through the fitting of the dynamic modulus's master curve. The latter is explained by the fact that the relaxation and the dynamic moduli share same Prony coefficients (Zhang et al. 2018). It is considerably very difficult to attain the dynamic modulus's exact fitting as, in reference to Eq. (22), the dynamic modulus is equal to the sum of both storage and loss moduli which thus cannot be immediately expressed. In other words, fitting the dynamic modulus must account for the fittings of its two components; the storage and the loss moduli. Hence, the Prony series, by the fitting of either the storage or the loss modulus, may be considered as the dynamic modulus's Prony series (Zhang et al. 2018). This is further explained by the sharing of the same Prony series by the dynamic, storage and loss moduli as expressed in Eqs. (33), (34) and (35). Yet, as presented in Eqs. (34) and (35), the storage modulus's fitting process can produce the long-term equilibrium modulus (E_{∞}), an essential parameter required for the relaxation modulus calculation in Eq. (30). On the contrary, the loss modulus fitting process cannot. Therefore, the dynamic modulus's Prony series is obtained by applying the storage modulus fitting. Consequently, based on the complex modulus representation in Eq. (22), the storage (E') and loss moduli (E'') are expressed respectively by:

$$E'(\omega) = E_{\infty} + \sum_{j=1}^{N} \frac{\omega^2 {\tau_j}^2 E_j}{\omega^2 {\tau_j}^2 + 1} \tag{34}$$

$$E''(\omega) = \sum_{j=1}^{N} \frac{\omega \tau_j E_j}{\omega^2 {\tau_j}^2 + 1} \tag{35}$$

This indicates the availability of an interconversion procedure from the dynamic to the relaxation modulus which mainly includes the following steps (Park & Schapery 1999):

I. The pre-smoothing and the fitting of the dynamic modulus and the phase angle experimental values;

II. Storage modulus $(E'_{experimental})$ calculation using the experimental values;

III. Setting the storage modulus $(E'_{calculated})$ value - obtained using Eq. (34) - equal to the previously determined $(E'_{experimental})$;

IV. Obtaining the Prony series coefficients (E_{∞}) and (E_j) ;

V. Substitution of the (E_{∞}) and (E_j) values into the relaxation function for plotting its corresponding master curve over a broad time domain.

2.5.1.4 Numerical Model Development

The numerical model development originates from the typical integral idealization of the linear viscoelasticity (Kaliske & Rothert 1997):

$$\sigma(t) = E\int_0^t e^{-\frac{t-s}{\tau}}\,\dot{\varepsilon}ds = \int_0^t R(t-s)\dot{\varepsilon}\,ds \tag{36}$$

Whereby $R(t-s) = E_o + \sum_{j=1}^{N} E_j\ \exp(-\frac{t-s}{\tau_j})$

By dividing the integral into the two contributions, the elastic and the viscoelastic, the component of the elastic stress ${\sigma_o}^e(t)$ as well as the internally stressed equivalent variables $X_j(t)$ can be determined (Kaliske & Rothert 1997) as the following:

$$\sigma(t) = E_\infty\acute{\varepsilon} + \sum_{j=1}^{N}\int_o^t E_j\exp\left(-\frac{t-s}{\tau_j}\right)\acute{\varepsilon}ds\ =\ {\sigma_o}^e(t) + \sum_{j=1}^{N} X_j(t) \tag{37}$$

Note that at time (t_∞) in a relaxation experiment, the contribution due to $X_j(t)$ tends to reach zero, thus obtaining the following equation for each individual $X_j(t)$:

$$X_j(t) = \int_o^t E_j\exp\left(-\frac{t-s}{\tau_j}\right)\acute{\varepsilon}ds \tag{38}$$

By performing several substitutions and integrations while taking into account a time interval of t_m , t_{m+1} with a $\Delta t = t_{m+1} - t_m$, the following equation is obtained:

$$X_j^{\ m+1} = \exp\left(-\frac{\Delta t}{\tau_j}\right)X_j^{\ m} + \gamma_j\ \frac{1-\exp(-\frac{\Delta t}{\tau_j})}{\frac{\Delta t}{\tau_j}}\ [\,{\sigma_o}^{m+1} - {\sigma_o}^{m}\,] \tag{39}$$

Where (γ_j) is a factor of the relaxation function that is normalized = $\frac{E_j}{E_\infty}$

A vital characteristic of implementing integration algorithms is their reliable and steady linearization. Using the derivative of the current stress state Eq. (40), the viscoelastic tangent modulus can be determined Eq. (41) (Kaliske & Rothert 1997).

$$\sigma^{t+\Delta t} = {\sigma_\infty}^{t+\Delta t} + \sum_{j=1}^{N} X_j^{\ t+\Delta t} \tag{40}$$

$$V^{m+1} = \frac{d\sigma^{m+1}}{d\varepsilon^{m+1}} = \left[1 + \sum_{j=1}^{N}\gamma_j\ \frac{1-\exp(-\frac{\Delta t}{\tau_j})}{\frac{\Delta t}{\tau_j}}\right]E_\infty \tag{41}$$

2.6 FE Equations

2.6.1 Development of Governing Equations

Generally, the engineer pursues to determine the stresses and the displacements for a structure in equilibrium and exposed to different types of loads. For several structures, it is quite difficult to ascertain the deformational distribution through conventional techniques. Hence, it is essential to use the Finite Element Method.

Several approaches are available for the determination of the governing finite element equations. These approaches include first the direct equilibrium method (direct method) that could be divided into two separate methods known as the displacement/stiffness method, which assumes the nodal displacements to be the unknowns, and the force/flexibility method that considers unknowns to be the internal forces (Logan 2017). Yet, for the computational goals, it was noticed that the stiffness (displacement) method is recommended as it has a much simpler formulation for structural problems. Based on the direct equilibrium method, the stiffness matrices as well as the element equations that relate the forces and the displacements at each node are determined by considering equilibrium force settings in addition to displacement/force relations for a certain element (Logan 2017). Another approach for determining the equations is the variational methods that consist of different principles including the potential energy theorem and the principle of virtual work. The former principle applies on materials that have a linear elastic behavior while the latter applies on materials that have either a linear or a nonlinear behavior. Lastly, the weighted residual methods can be employed.

2.6.2 Dynamic Response Equilibrium Equations

Associated to pavement engineering, an FWD testing applies on the pavement's surface an impulse load of a certain duration. Therefore, ideally, dynamic backcalculation should be considered to determine the individual layer's modulus within the pavement structure along with the damping coefficients (Matsui, K. et al. 2006). Consequently, for this FWD load, the equation of motion can be determined whereby one must account for the inertial and damping forces that depend on the acceleration and on the velocity respectively. Additionally, for a system of finite elements, the equilibrium equations controlling the dynamic responses is given by (Bathe 2014):

$$M\acute{\acute{\upsilon}} + C\acute{\upsilon} + K\upsilon = R \qquad (42)$$

Whereby $[M]$ is the mass matrix, $[C]$ is the damping matrix, $[K]$ is the stiffness matrix, $\{R\}$ is the vector that includes the external loadings applied, $\{\upsilon\}$, $\{\acute{\upsilon}\}$, and $\{\acute{\acute{\upsilon}}\}$ represent the displacement, velocity and acceleration vectors, respectively.

When a time dependent load R(t) is applied to the scheme presented in Figure (21), the problem under study is detailed with the particle's mass (m), the parameters representing the Maxwell Chain Model including the spring's elastic stiffness (E_∞), the stiffness of the spring (E_n), and lastly the damping viscosity coefficient (η_n). Consequently, Eq. (42) can be expressed in another format representing the inertial, damping ad elastic forces as function of time. In other words, ($M\ddot{v}$) represents the forces related to inertia $f_I(t)$, ($C\dot{v}$) represents the forces related to damping $f_D(t)$, and (Kv) represents the forces related to elasticity $f_E(t)$. The equation is therefore given by:

$$f_I(t) + f_D(t) + f_E(t) = R(t) \tag{43}$$

2.6.3 Element Stiffness Matrix Development

The stiffness matrix for a certain element is determined by Eq. (44) (Logan 2017):

$$[k] = \iiint_V [B]^T[D][B]dV = 2\pi \iint_A [B]^T[D][B]rdrdz \tag{44}$$

Whereby, [B] is the gradient matrix defined in section 3.4.c, $[B]^T$ is the gradient matrix transpose, [D] is the elasticity matrix.

The element stiffness matrix $[k]$ can be evaluated by evaluating the gradient matrix $[B]$ for an element's centroidal point ($\hat{r}, \hat{z}$), and thus represented by Eq. (46):

$$\hat{r} = \frac{r_i + r_j + r_m}{3} \quad , \; \hat{z} = \frac{z_i + z_j + z_m}{3} \tag{45}$$

$$[k] = 2\pi\hat{r}A[B]^T[D][B] \tag{46}$$

2.6.4 Element Mass Matrix Development

The domain under study is meshed through the displacement based finite element method. Consequently, the structure's total volume (V) is discretized itself into a count of (N) elements by which each individual element has its own relative elementary volume. Generally, the mass matrix $[M]$ defines the system's global mass and inertia. Accordingly, the mass matrix for each element is determined as shown below (Bazi et al. 2020):

$$[m] = \iiint_V \rho \, [N]^T[N]dV \; = 2\pi \iint_A \rho \, [N]^T[N]rdrdz \tag{47}$$

When deriving each element's mass matrix by the relationship expressed in Eq. (47), the $[N]$ matrix should correspond to all the nodal displacements even the ones in the local coordinate system.

For a linear-triangular element, the 6x6 mass matrix is expressed as follows:

$$[m] = \frac{\pi\rho A}{10}\begin{bmatrix} 2\hat{r}+\frac{4}{3}r_1 & & & & & sym. \\ 0 & 2\hat{r}+\frac{4}{3}r_1 & & & & \\ \frac{-r_3}{3}+2\hat{r} & 0 & 2\hat{r}+\frac{4}{3}r_2 & & & \\ 0 & \frac{-r_3}{3}+2\hat{r} & 0 & 2\hat{r}+\frac{4}{3}r_2 & & \\ \frac{-r_2}{3}+2\hat{r} & 0 & \frac{-r_1}{3}+2\hat{r} & 0 & 2\hat{r}+\frac{4}{3}r_3 & \\ 0 & \frac{-r_2}{3}+2\hat{r} & 0 & \frac{-r_1}{3}+2\hat{r} & 0 & 2\hat{r}+\frac{4}{3}r_3 \end{bmatrix} \qquad (48)$$

Whereby the ρ is the density expressed in lbf.s^2/in^4 .

For the analysis, the lumped mass matrix is taken into account to produce more reliable and robust results when calculating the model's natural frequency in the numerical experiments (Bazi et al. 2020) . The lumped mass matrix formulation results in a fully diagonal system matrix, it is determined by summing the values in each row in the previously determined consistent mass matrix.

2.6.5 Element Damping Matrix Development

The damping capacity is mainly explicated as the dissipated energy in one oscillation cycle over the maximum accumulated energy within the structure (Alipour & Zareian 2008). Several mechanisms exist for the structure's damping including the interfacial damping on one hand and the material damping on the other. The latter's contribution originates from the interaction of a complex molecules constituting the material. This indicates that the damping depends on the material, its manufacturing and finishing methods (Kareem and Gurley 1996).

Rayleigh damping, a classical/proportional damping model, is considered to model the structure's characteristics of energy depletion (Rayleigh 1954) i.e., calculating the damping ratio. This model describes the damping as a linear combination of both, the mass matrix and the stiffness matrix, thus, given by:

$$[c] = \alpha_R\,[m] + \beta_R\,[k] \qquad (49)$$

Whereby (α_R) and (β_R) are real scalars, known as the Rayleigh damping coefficients and expressed in $\left(\frac{1}{second}\right)$ and $(second)$ respectively.

2.6.6 Global Matrix Development

To develop the global stiffness $[K]$, mass $[M]$ and damping $[C]$ matrices, it is essential to first identify each element's corresponding nodes and degrees of freedom (DOF). The selection of the DOF and abiding with the chosen distribution is crucial for the formulating the global matrices. Note that deformations at DOF where there is support or symmetry should be zero.

This is illustrated in Figures (23) and (24) whereby the structure was discretized using four triangular elements in which each has its own degrees of freedom that must be attained during the calculation process.

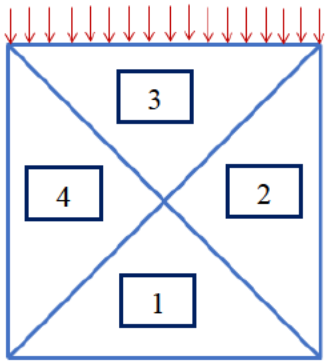

Figure 23: Discretization by Four Triangular Elements

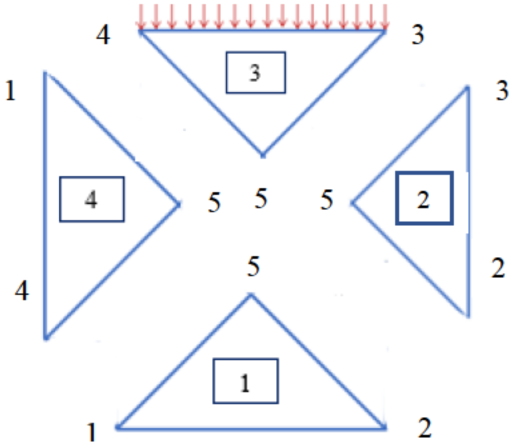

Figure 24: Degrees of Freedom Distribution

By assembling the individual element stiffness $[k]_{element}$ matrices, the global stiffness matrix will be formulated. The same procedure is followed for developing the mass and damping matrices. Note that a special case applies for global damping matrix whereby it can be can be calculated from assembled $[M]$ and $[K]$ matrices, on condition that all elements should have the same properties.

2.6.7 Applied Surface Forces

According to (Logan 2017), the surface forces are given by:

$$\{f_s\} = \iint_s [N_s]^T \{T\} ds \tag{50}$$

Where $[N_s]^T$ refers to the shape function matrix studied on the surface by which the traction surface acts on. The aforementioned surface forces representation is employed to simulate the FWD loading.

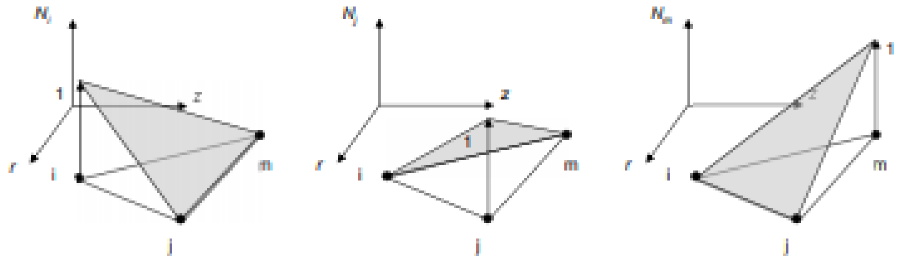

Figure 25: Linear Triangular Element Shape Functions

For a triangular element, the forces at each node are portrayed in Figure (26) and are determined as follows in Eq. (51) and (52) for a unit pressure (Bazi et al. 2020):

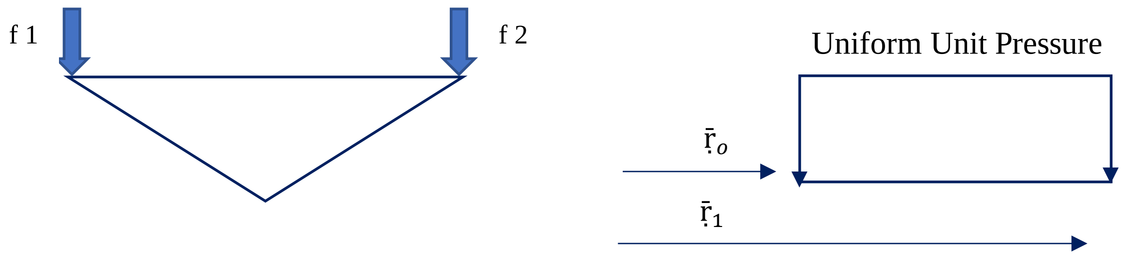

Figure 26: Nodal Forces Surface Traction

$$f_1 = \frac{2\pi}{6}(\bar{r}_1^2 + \bar{r}_1\bar{r}_o - 2\bar{r}_o^2) \quad (51)$$

$$f_2 = \frac{2\pi}{6}(\bar{r}_1^2 - \bar{r}_1\bar{r}_o - 2\bar{r}_o^2) \quad (52)$$

2.7 Dynamic Analysis

For a certain numerical system, the equation of motion's analytical solution is typically impossible if the system under study is not linear or whether the applied forces arbitrarily vary with time. These problems, that especially arise in a wide subject domain of applied mechanics, can be unraveled through the use of time stepping approaches for the differential equation integrations. Such approaches are developed through examining their corresponding convergence, computer implementation, stability and their accuracy.

The dynamics of viscoelastic structures defined by the generalized Maxwell model results in a set of initial value problems linking the variables and the equation of motion. As the full system's numerical integration is considered costly, an alternate method, which was initially established for quasistatic problems (Zienkiewicz et al. 1968), was followed which solves the equation of motion approximately, while solves the evolutionary constitutive equations and results in an update equation for the internal variables that enter the equation of motion (Schmidt et al. 2019). Though, (Hatada et al., 2000) considered this approach in dynamics whereby the authors established a Newmark type algorithm for a Maxwell model with three parameters.

2.7.1 Newmark's Method

In structural mechanics, the Newmark's method (Newmark 1959) is considered one of the utmost essential methods that are based on time steps. This method is clearly an implicit method that considers the inversion of matrices. It requires solving a series of linear algebraical equations in order to determine the solution at each step. This implies that implicit algorithms are not time efficient approaches as the system of matrices should be solved at every step. Nevertheless, the Newmark's method is considered a stable method whereby the time step's size (Δt) will not have an effect on the solution's stability, yet it is relatively governed through accuracy aspects.

The Newmark's method is mainly based on the recursion given by:

$$\upsilon^{t+\Delta t} = \upsilon^{t} + (\Delta t)\dot{\upsilon}^{t} + \left[\left(\frac{1}{2} - \beta\right)(\Delta t)^{2}\right]\ddot{\upsilon}^{t} + [\beta(\Delta t)^{2}]\,\ddot{\upsilon}^{t+1} \tag{53}$$

$$\dot{\upsilon}^{t+1} = \dot{\upsilon}^{t} + [(1-\gamma)\,\Delta t\,]\ddot{\upsilon}^{t} + (\gamma\Delta t)\ddot{\upsilon}^{t+1} \tag{54}$$

Note that β and γ are integration parameters that specify the system's accuracy, stability and dissipative characteristics.

2.7.1.1 Newmark $\beta -$ Method Special Cases

The Newmark's method is known by the Newmark $\beta -$ method once $(\gamma) = \frac{1}{2}$ (Wood 1984).

I. For $\gamma = \frac{1}{2}$ and $\beta = \frac{1}{4}$, the previously written Eqs. (53) and (54) refer to the "average" acceleration method as illustrated in Figure (25) and the equations below:

$$\ddot{\upsilon}\,(\Delta t) = \frac{1}{2}\,(\ddot{\upsilon}^{t+1} + \ddot{\upsilon}^{t}) \tag{55}$$

$$\dot{\upsilon}^{t+1} = \dot{\upsilon}^{t} + \frac{\Delta t}{2}\,(\ddot{\upsilon}^{t+1} + \ddot{\upsilon}^{t}) \tag{56}$$

$$\upsilon^{t+1} = \upsilon^{t} + \dot{\upsilon}^{t}\Delta t + \frac{\Delta t^{4}}{4}\,(\ddot{\upsilon}^{t+1} + \ddot{\upsilon}^{t}) \tag{57}$$

The assumptions that consider the acceleration's variation over a certain time-step constant and equals the average acceleration is described by Eq. (55). As for Eq. (56), it corresponds to integrating the acceleration in Eq. (55) over (Δt) to determine the velocity. In a similar fashion, the displacement is obtained in Eq. (57) by integrating the previously determined velocity over (Δt).

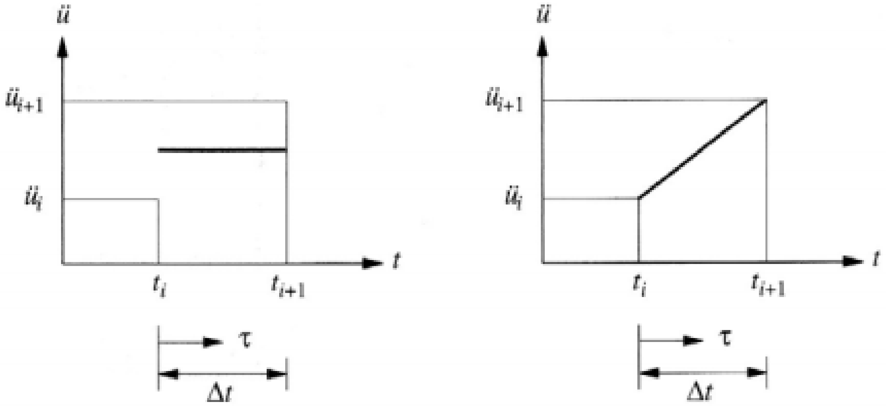

Figure 27: Average Acceleration Method (Left), Linear Acceleration Method (Right)

II. For $\gamma = \frac{1}{2}$ and $\beta = \frac{1}{6}$, the previously written Eqs. (53) and (54) refer to the "average" acceleration method as illustrated in Figure (27) and the equations below:

$$\ddot{v}\,(\tau) = \ddot{v}^{\,t} + \frac{\tau}{\Delta t}\,(\ddot{v}^{\,t+1} - \ddot{v}^{\,t}) \tag{58}$$

$$\dot{v}^{t+1} = \dot{v}^{t} + \frac{\Delta t}{2}\,(\ddot{v}^{\,t+1} + \ddot{v}^{\,t}) \tag{59}$$

$$v^{t+1} = v^{t} + \dot{v}^{t}\Delta t + \Delta t^{2}\,(\frac{\ddot{v}^{\,t+1}}{6} + \frac{\ddot{v}^{\,t}}{3}) \tag{60}$$

Note that the same explanation for Eqs. (56 – 57) applies here, whereby, $\tau = \Delta t$.

For the sake of the project, the integration parameters γ and β are determined by Hilber-Hughes-Taylor-α (HHT-α) method which becomes equal to the Newmark's method for an $\alpha = 0$.

$$\gamma = \frac{1}{2} - \alpha \tag{61}$$

$$\beta = \frac{(1-\alpha)^{2}}{4} \tag{62}$$

After several rearrangements for the Newmark Eqs. (53-54), the velocity and the acceleration equations can be written with respect to the integration-constants p_o till p_7 , and then replaced in the equation of motion to obtain Eq. (63) (Bazi et al. 2020):

$$p_o = \frac{1}{\Delta t^{2}\beta} \ , \quad p_1 = \frac{\gamma}{\Delta t\beta} \ , \quad p_2 = \frac{1}{\Delta t\beta} \ , \quad p_3 = \frac{1}{2\beta} - 1 \, , \quad p_4 = \frac{\gamma}{\beta} - 1$$

$$p_5 = \frac{\Delta t}{2}\left(\frac{\gamma}{\beta} - 2\right) \ , \quad p_6 = (1-\gamma)\Delta t \ , \quad p_7 = \gamma\Delta t$$

$$[\boldsymbol{M}]\,[\,(p_o\,v^{t+1}) - (p_o v^{t}) - (p_2\dot{v}^{t}) - (p_3\ddot{v}^{\,t})\,] + [\boldsymbol{C}]\,[\,(p_1 v^{t+1}) - (p_1\,v^{t}) - (p_4\dot{v}^{t}) - (p_5\ddot{v}^{\,t})] + [\boldsymbol{K}]v^{t+1} = \boldsymbol{R}^{\,t+\Delta t} \tag{63}$$

This equation can be represented by Eq. (66) as function of the “effective” load ($\widehat{\mathrm{R}}^{t\,+\,\Delta t}$)and effective(tangential) stiffness matrix ($\hat{\mathrm{k}}$):

$$\hat{\mathrm{k}} \;=\; p_o[M] + \;p_1[C] + [K] \tag{64}$$

$$\widehat{\mathrm{R}}^{t\,+\,\Delta t} = \big[p_o[M] + \;p_1[C]\big]\upsilon^t + \big[p_2[M] + \;p_4[C]\big]\dot{\upsilon}^t + \;\big[p_3[M] + \;p_5[C]\big]\ddot{\upsilon}^{\,t} \;+\; R^{\,t\,+\,\Delta t} \tag{65}$$

$$\hat{\mathrm{k}}\,\upsilon^{t+1} = \;\widehat{\mathrm{R}}^{t\,+\,\Delta t} \tag{66}$$

Initially, the displacement υ^{t+1} is determined and the value shall be used in Eqs (53 and 54) to determine the velocity and acceleration. This process is further repeated for each time interval until the desired time is reached. At each time interval, a set of algebraical equations is solved for the unknown (υ^{t+1}). Note that if the time interval (Δt) varies, the $[\hat{\mathrm{k}}]$ matrix should be computed for each (Δt) value, otherwise it can be determined once. In addition, the “effective” load $\widehat{\mathrm{R}}^{t\,+\,\Delta t}$ should be updated after each time interval. After computing the velocity ($\dot{\upsilon}^{t\,+\,\Delta t}$) and acceleration ($\ddot{\upsilon}^{\,t\,+\,\Delta t}$), these values are then considered (υ^t) , ($\dot{\upsilon}^t$) and ($\ddot{\upsilon}^{\,t}$) for the next time interval.

Chapter Three

LOESS Regression Analysis

The regression analysis aims to portray the relationship present between variables depending on a certain experiential data and to anticipate the dependent variable value contingent on the independent variable value.

3.1 Locally Weighted Regression

For several decades, polynomial local fitting has been considered for a certain scatterplot of (x_i, y_i) data, as a mean to smoothen the time series plots; whereby the (x_i) values for the successive points have equal intervals (Macauley 1931). Similarly, the locally weighted regression method is mainly considered an extension of the aforementioned technique to a broader (x_i) configuration. Local Regression, LOESS, is initially presented by Cleveland (1979) and was further advanced by Cleveland and Devlin (1988) which explicitly represents a method known by the locally weighted polynomial regression.

LOESS is considered one of the several contemporary modeling approaches which is built on classical approaches including the nonlinear and the linear least squares regression. Contemporary regression approaches are designed in a way to report certain situations whereby classical approaches do not have an efficient performance or cannot be applicable without excessive labor. The local regression LOESS merges the nonlinear regression’s flexibility along with the linear least squares regression’s simplicity. This is mainly accomplished through fitting certain models to localized data subsets for developing a function which defines the deterministic section of the variability in data.

3.1.1 LOESS Model Description

For every point provided in the (**m**) dataset, a polynomial with a degree (**d**) is fit to a subset of this data, having the variable values close to the point under study i.e., the response of this point is under evaluation. The latter point is referred to as the estimation point (x_p). By considering the weighted least squares approach, the polynomial will be fit by which the points that are closer to the estimation point (x_p) are given more weight, while the farther points are given less weight. The regression function is therefore determined by assessing the local polynomial estimates using the point's explanatory variable values after obtaining the values of the regression function for all the (**m**) points.

3.1.2 Data's Localized Subsets and Smoothing Parameter

The data subsets employed for the individual LOESS weighted least squares fit are computed through the closest neighbor's algorithm. The smoothing parameter (**f**) is a user-dependent input that specifies the number of data points considered to fit every local polynomial. The aforementioned parameter controls the model's flexibility. In other words, it manages how firmly the function will be smoothening and fitting the data. Increasing the value of the smoothing parameter (**f**) tends to increase the influential points' neighborhood and thus increasing the smoothness of the already smoothed points (Cleveland 1979). It is important to note that when selecting a certain value for this parameter, one must carefully choose the largest value possible in order to lessen the variation in the smoothened points without altering the data's original pattern. Selecting a very small value is not quite desirable as the function will start ultimately to recognize the data's random error. Cleveland (1979) presented several guidelines for the selection of the smoothing parameter (**f**) that is essential to proceed with the LOESS procedure. It is mainly found within the following range $\frac{d+1}{m} < f < 1$.

3.1.3 Local Polynomials Degree

Every subset of the data will be fitted using local polynomials with either a zero-, first- or a second-order degree. When considering a zero-degree polynomial, the LOESS becomes a weighted moving average. Computationally-wise, a zero- degree is considered the simplest case. However, assuming local linearity appears to assist better than assuming constancy which may not be efficiently approximating the fundamental function. This is explained by the fact that one's propensity is to plot different variables that are related to each other (Cleveland 1979). As for polynomials with a higher degree, they are more likely to be numerically unstable and cause overfitting in every subset, thus allowing for more difficult computations. When having a second-order degree polynomial, the computational means start to override the necessity of having the flexibility. While taking a first-order degree polynomial must provide computational proficiency and ease as well as obtaining acceptable smoothed points (Cleveland 1979).

3.1.4 Weight Function

As previously mentioned, the weight function provides the least weight for the points that are far away from the estimation point (x_p) while it provides the highest for the closest points. The weights increase as the distance between a point (**x**) and the estimation point (x_p) decreases. Taking each point's weight into account is mainly based on the idea which states that points that are close to each other tend to be related to one another more than the ones that are farther away. This implies that points with abscissas closer to (x_p) play an important role in determining the new fitted ordinates, while the ones that are farther tend to have a much lesser role (Cleveland 1979). The weight function is mainly defined by the following requirements whereby (Cleveland 1979):

I. $w(x) > 0 \ \ for \ |x| < 1$

This property is essential as the weight function should be, logically, a positive value.

II. $w(x) = \ w(-x)$

The latter dictates that the points to the right of the x_i should be treated in a similar manner as those to the left.

III. $w(x)$ is defined as a function that does not increase for $x \ \geq 0$

This ensures having the appropriate weight distribution among the x_i values.

IV. $w(x) = 0 \, for \ \ |x| \geq 1$

The weight function, $W(x)$, followed in the LOESS is referred to as the tricube weight function and given by the following representation (Cleveland 1979):

$$w(x) = \begin{cases} (\,1 - |x|^3)^3 & for\ |x| < 1 \\ 0 & for\ |x| \geq 1 \end{cases} \tag{67}$$

3.2 LOESS Procedure

The information visualized on a certain scatterplot may be largely enhanced through some additional computations and plotting of the smoothed points. A scatterplot consisting of (x_i, y_i) with $i = 1,2, \dots, m$, is represented by Figure (28). The exact identical scatterplot data is summarized and represented by a new set of coordinates $(x_i, \tilde{y}_i)$ shown in Figure (29), whereby the successive points are joined through straight lines. For a given variable plotted on the X-axis, any point $(x_i, \tilde{y}_i)$ depicts the location and the position of the variable distribution on the Y-axis (Cleveland 1979). The newly formed points will be mainly referred to the scatterplot smoothed points. In other words, a point $(x_i, \tilde{y}_i)$ is a smoothened point at the x_i whereby $\tilde{y}_i$ is referred to the fitted value at the abscissa x_i.

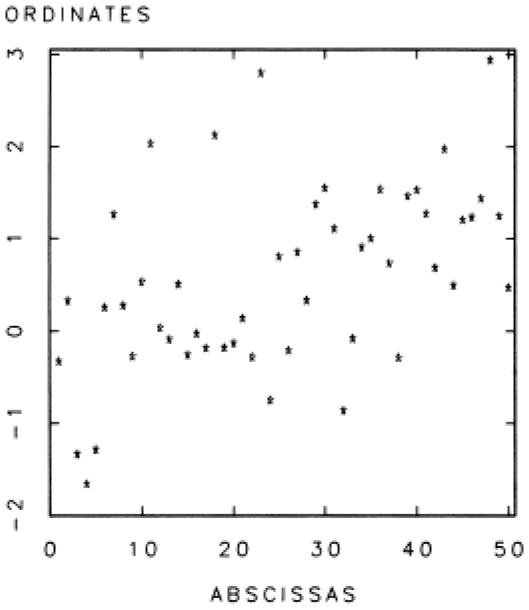

Figure 28: Artificial Data Scatterplot (Cleveland 1979)

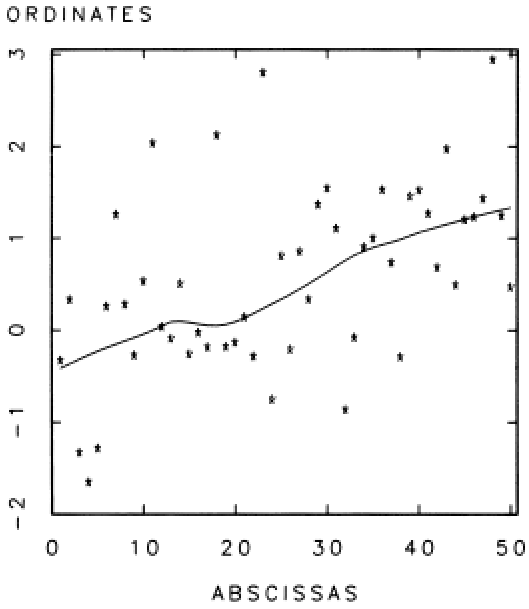

Figure 29: Artificial Data Scatterplot with Smoothed Points (Cleveland 1979)

To initiate with the LOESS computations, the data is divided into several subsets (**r**) by multiplying the smoothing parameter with the data size (**m**), whereby the resulting value shall be rounded to the closest integer (Cleveland 1979). For each subset, an estimation point (x_p) shall be defined. It is important to appropriately select the data subsets in a way that the values are relatively close to the (x_p). Moreover, for every (x_i), a weight $[w_p(x_i)]$ is assigned for the different (x_p) defined within each subset data through a weight function (W). The latter is mainly obtained by the following steps:

I. Computing the distance between every point (x_i) and (x_p) in absolute values.

$$|x_i - x_p| \tag{68}$$

II. Scaling the distances by considering the maximum distance obtained from all (x_i) points within the subset data in the previous step.

III. Computing the individual weights $[w_p(x_i)]$ for every point using the tricube weight function given in Eq (67) where "x" represents the scaled distance.

Locally weighted linear regression typically models first- and second- degree polynomials whereby the following regression equations apply respectively:

$$\tilde{y}_i = \rho_o + \rho_1 x \tag{69}$$

$$\tilde{y}_i = \rho_o + \rho_1 x + \rho_2 x^2 \tag{70}$$

The objective in the weighted least squares is to determine the coefficients ρ_o, ρ_1 and ρ_2, therefore,

$$\sum_{i=1}^{m} w_i[y_i - \tilde{y}_i]^2 \tag{71}$$

And the weighted equation is given by:

$$\rho = [X^T W X]^{-1}[X^T W Y] \tag{72}$$

Whereby W represents the diagonal weight matrix given by Eq. (73) for $i = 1,2, \dots, m$.

$$W = \begin{bmatrix} w_m(x_1) & 0 & 0 & 0 \\ 0 & w_m(x_i) & 0 & 0 \\ 0 & 0 & w_m(x_i) & 0 \\ 0 & 0 & 0 & w_m(x_m) \end{bmatrix} \tag{73}$$

Y represents the ordinates (y_i ... y_m) vector:

$$Y = \begin{Bmatrix} y_1 \\ y_2 \\ y_3 \\ \vdots \\ y_m \end{Bmatrix} \tag{74}$$

X represents a matrix defining the abscissas (x_i ... x_m) values for a 1st – and 2nd order polynomials as shown in Eqs. (75 and 76) respectively:

$$X = \begin{bmatrix} 1 & x_1 \\ 1 & x_2 \\ 1 & x_3 \\ \vdots & \vdots \\ 1 & x_m \end{bmatrix} \tag{75}$$

$$X = \begin{bmatrix} 1 & x_1 & {x_1}^2 \\ 1 & x_2 & {x_2}^2 \\ 1 & x_3 & {x_3}^2 \\ \vdots & \vdots & \vdots \\ 1 & x_m & {x_m}^2 \end{bmatrix} \tag{76}$$

Hence, the solution for $[\rho]$ represents the local parameter approximations - the slope and the intercepts - for the new 1st – or 2nd degree polynomial equation. Lastly, the regression function value is computed through evaluating the local polynomial at the (x_p). Thus, the newly fitted ($\tilde{y}_i$) value at every (x_i) corresponds to the value fitted for a $\boldsymbol{d^{th}}$-degree polynomial fitting to the data by the weighted least squares (Cleveland 1979). A new weight set (φ_i) will be defined for the coordinates (x_i, y_i) depending on the residual size ($y_i - \tilde{y}_i$). This implies that the new fitted values will be computed with $\varphi_i w_p(x_i)$. The same procedure is repeated for a new model with a new estimation point that corresponds to the new subset data. The whole procedure including both the preliminary computations and the iterations is known by the robust locally weighted regression (Cleveland 1979), whereby a value (t) which represents the robust fitting process iterations number shall be selected. The robust fitting process will therefore detect any outliers that distort the smoothened points (Cleveland 1979).

3.2.1 LOESS Advantages and Disadvantages

Unlike other classical methods, the LOESS approach does not mandate specifying a function that fits the model to the sample data under study. In lieu, the analyst shall only provide and specify a value for the smoothing parameter (**f**) as well as the polynomial degree (**d**). Moreover, the LOESS is considered to be flexible, therefore allowing it to be an ideal approach for the modeling of complicated processes whereby a theoretical model does not exist. Such advantages, along with its simplicity, makes it one of the efficient contemporary regression approaches for numerous applications that comply with the least squares regression's broad framework. Even though it is inconspicuous when compared to other approaches that are related to the least squares regression, LOESS ensues the majority of the benefits usually shared and used by these methods. The paramount importance of these is the theorem of computing and determining the quandaries and the perplexities for calibration and prediction. It is important to note that several procedures and methods used for the least squares' models validation may be also extended and broadened to the LOESS models.

Though the LOESS shares a lot of the finest aspects of the further least squares approaches, yet it does not utilize the data efficiently. This approach necessitates a dense, large sampled datasets to build effective and reliable models. This is explained by the fact that the LOESS requires suitable empirical data for the local fitting process. Furthermore, the LOESS results in a regression function that cannot be easily characterized and represented by mathematical equations. This will therefore increase the difficulty when it comes to transferring the obtained analysis results to the concerned persons who in return require the software and the dataset for the LOESS computations. On the other hand, writing functional forms is the only requirement to approximate the uncertainty and estimate the unknown parameters in the nonlinear regression. Hence, reliant on the application, this might either be a significant or an insignificant drawback for the LOESS. In addition, the LOESS method is also disposed to the consequence of the outliers present in the data provided. Cleveland (1979) proposed an upgraded version based on an iterative process that tends to reduce the sensitivity of the LOESS to the outliers.

Chapter Four

FWD Indices and FWD Parameters

Once subjected to various traffic loads, the response mechanism comprises the initiation of three-dimensional strains, stresses, displacements and deformation within the pavement structure. Of main significance are the surface vertical displacements in the vicinity of the load application point.

The FWD equipment measures the responses at critical nodes throughout the deflection region's surface (deflection basin) by simulating the moving wheel loads. Various Deflection Bowl Parameters (DBPs) have been developed by researchers from the obtained deflection basin/bowl to verify the existing pavements' structural integrity, to correlate to the critical responses and to approximate the moduli of the in-situ pavement layers through backcalculation methods (Fuentes et. al 2020). However, prior to the FWD development, several deflection indicators were established from data obtained using Road Rater device, Benkelman beam or Dynaflect. Though, such devices were only capable of measuring the deflection at only one point (Hossain and Zaniewski 1991). The most common deflection bowl parameters suggested in the literature will be presented in the upcoming subsections. Generally, the DBP are explicated as indicators that utilize the FWD deflection curves as a mean to identify and evaluate obstacles within the pavement structures. When being compared with the backcalculation process, the use of the DBPs will not produce thorough results, but rather provide only an indication of the pavement's structural condition. As subsequently discussed, some of the deflection bowl parameters have been outlined to offer acceptable correlative outcomes with the pavement's performance and structural condition, while some have intrinsic limitations and challenges.

4.1 Maximum Deflection (D_o)

The maximum deflection (D_o) refers to the deflection that is measured under the applied load. It describes the pavement's behavior as a whole/complete structure, yet does not provide any indication related to the mechanical characteristics of each individual layer and their performance against permanent deformation or fatigue (Shahin 2005). Past studies verified that the D_o must not be considered alone as a sufficient parameter to determine the pavement's structural condition, rather to conduct backcalculation to characterize the existing layers' moduli (Whitcomb 1982, Stubstad and Connor 1983). Furthermore, studies performed by Horak (1987b) and Joubert (1992) stated that for pavement structures with diverse deflection basins or/and various material properties, similar D_o values can be obtained. It is vital to mention that, originally, the D_o was measured by the Benkelman beam, yet the FWD equipment can be also used.

4.2 Radius of Curvature (RoC)

A simplified empirical approach was proposed by Dehlen (1961) to evaluate the performance of the pavement structure using the Benkelman beam. To be able to plot the entire section of the deflection basin, Dehlen (1961) advised taking deflection measurements using intervals of 75mm. As a result, the Radius of Curvature (RoC) was thus proposed as an indicator parameter. The Radius of Curvature (RoC) at the point of peak deflection - spotted in the deflection basin - is determined by establishing the best fit curve/circle over the 250mm central radius. Moreover, Dehlen (1961) explained that the RoC can be considered as an adequate flexural stresses indicator. Therefore, it can be used when designing against the flexural cracking. Based on Dehlen's outcomes, the RoC was found to be sensitive to the Hot Mix Asphalt surfacing only for thick layers that exceed 50 or 75mm. Primarily, the RoC depended on the base and subbase moduli and was impartially not sensitive to the subgrade layer.

For different sensors, the radius of curvature (RoC) can be represented by the following equations, (Dehlen,1962):

$$RoC = \frac{L^2}{2D_o(\frac{D_o}{D_{20o}} - 1\ )} \tag{77}$$

With L being the radial distance from the load's center = 8 inches (200mm).

Whereby,

- D_o is the surface deflection at the center of the test load
- D_8 $(D_{200}\ )$is the surface deflection at an offset of 8 inches (200 mm) from the test load
- D_{12} $(D_{300}\ )$is the surface deflection at an offset of 12 inches (300 mm) from the test load

Though, with the evolution of technology, FWD devices were introduced in order to overcome few of the Benkelman beam challenges including the efficiency and the intensiveness of labor. As the FWD devices are capable of capturing the entire response in the load application area, several researchers, Rohde and Van Wijk (1996) and Horak et al. (2015), suggested some alterative deflection basin parameters for evaluating the structural capacity of the pavement instead of the radius of curvature parameter. Such parameters include, for example, the Surface Curvature Index which manifested an acceptable correlation with the radius of curvature. Horak (1987a, 1987b) evaluated various FWD deflection bowl parameters and performance indicators under "heavy" vehicle simulators. Horak concluded that the most significant indicators that resulted with a good correlation with the pavement's structural capacities and the behavioral condition are: (1) Maximum Deflection D_o , (2) Radius of Curvature, (3) Surface Curvature Index (BLI), (4) Base Damage Index (MLI), (5) Base Curvature Index (LLI).

It is important to note that a simplified method was proposed by Horak and Emery (2006) and Horak (2008) by using 3-zones demonstrated in Figure 31 to analyze the deflection basin. The three zones are discovered by the initial parameters suggested by Anderson (1977) and Kilareski and Anani (1982) and were renamed to the Base Layer Index (BLI), the Middle Layer Index (MDI) and lastly the Lower Layer Index (LLI), respectively. Zone 1 usually falls within a radius of 12 inches (300mm) from the point of load application. The deflection basin within that zone has a positive (+ve) curvature. Horak (2008) stated that this Zone is typically associated to the RoC or BLI. As for Zone 2, the deflection basin switches to a negative (-ve) curvature (reverse curvature) and is frequently known by the inflection zone. It falls within an offset of approximately 12 inches (300mm) to an offset of about 24 inches (600mm) from the point of load application. This zone is largely affected by the base and the subbase mechanical properties and is mainly associated to MLI (Horak 2008). Lastly, Zone 3 stretches from an offset of 24 inches (600mm)

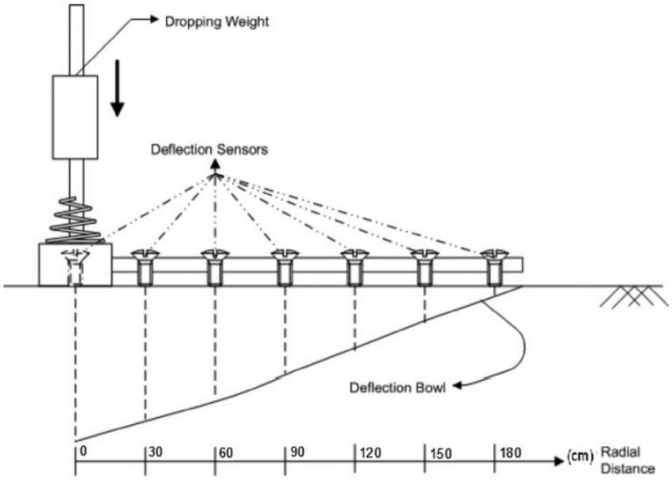

Figure 30: Deflection Basin

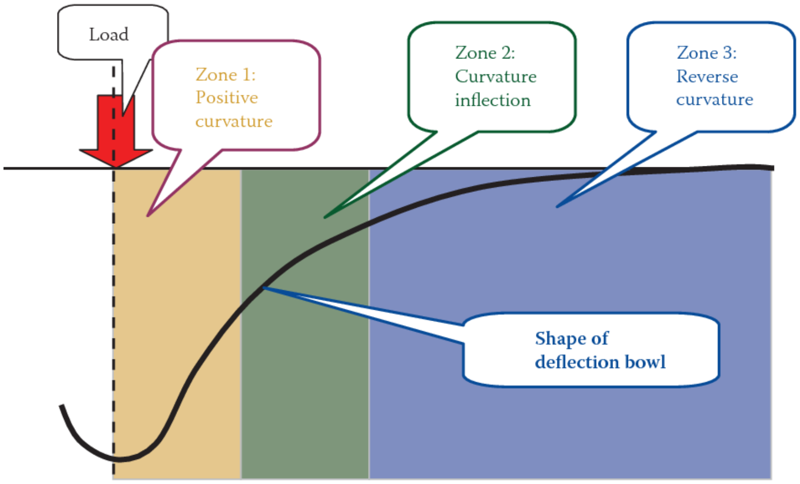

Figure 31: Curvature Zones of the Deflection Basin

and its extent typically depends on the pavement's real depth and the subgrade's structural responses. According to Horak (2008), it is associated to LLI.

4.3 Surface Curvature Index (SCI)

The Surface Curvature Index (SCI), also referred to as the Base Layer Index (BLI), was considered one of the initially used Deflection Bowl Parameters. As previously mentioned, it is mainly obtained by calculating the difference between the maximum (peak) deflection D_o and the deflection measured at the sensor located at an offset of 12 inches (300 mm) from the point of load application (Eq. (78)). It indicates the surface layer's structural strength and the bound layer's relative stiffness (Anderson, 1977). According to Horak (1987a, 1987b), the surface curvature index was assumed to be one of the relevant parameters associated to the peak horizontal strain measured at the bottom of the Hot Mix Asphalt layer. However, due to its poor association with the coefficient of determination ($R^2 < 38\%$), the SCI should not be considered to obtain the subgrade strains (FHWA 2016). The relationship between the deflection bowl parameters and the conditions of the layers was validated by Xu et al. (2002) while perceiving that this parameter was the utmost sensitive one to the Hot Mix Asphalt layer properties.

$$SCI = D_o - D_{12}\ ,\ SCI = D_o - D_{300} \tag{78}$$

Kilareski and Anani (1982) conducted a study using the deflection measured by a Road Rater equipment to determine the in-situ layer properties and evaluate the remaining life of a certain pavement structure. Two parameters/indicators were proposed; the Base Damage Index and the Base Curvature Index.

4.4 Base Damage Index (BDI)

The Base Damage Index (BDI), also referred to as the Middle Layer Index (MLI), indicates the damage and the structural condition of the base layer (Kilareski and Anani 1982). It is mainly calculated by the difference between the deflections measured at an offset of 12 inches (300mm) and 24 inches (600mm) from the center of the testing load (Eq. (79)).

$$BDI = D_{12} - D_{24}\ ,\ BDI = D_{300} - D_{600} \tag{79}$$

This parameter is significant for characterizing and determining the stiffness of the pavement's intermediate layers (Horak 1987b, Xu et al. 2002).

4.5 Base Curvature Index (BCI)

The Base Curvature Index (BCI), also referred to as the Lower Layer Index (LLI), indicates the structural strength, condition and the curvature of the subgrade and the subbase (Kilareski and Anani 1982). It is determined by difference between the deflections measured at an offset of 24 inches (600mm) and 36 inches (900mm) from the center of the testing load (Eq. (80)).

$$BCI = D_{24} - D_{36}\ ,\ BCI = D_{600} - D_{900} \tag{80}$$

- D_o, D_{12} (D_{300}) previously defined
- D_{24} $(D_{600})$is the surface deflection at an offset of 24 inches (600 mm) from center
- D_{36} $(D_{900})$is the surface deflection at an offset of 36 inches (900 mm) from center

A benchmarking classification was developed by Horak (2007) for several pavement types. The structural condition for each pavement was rated between sever, warning and sound conditions. The contribution of each layer's structural strength, depending on which zone they fall into, can be correlated to the rating criteria shown in Tables 1 and 4. Therefore, the relative structural deficiencies of the pavement layers can be recognized along the road's length. In other words, the causes of any possible structural deficiencies can be presumed from the previously rated conditions.

Table 1: Structural Condition Rating for DBPs (Horak 2007)

Pavement Type	Rating of Structural Condition	Deflection Bowl Parameters (DBPs)				
		D_o (µm)	RoC (m)	SCI (BLI) (µm)	BDI (MLI) (µm)	BCI (LLI) (µm)
Granular Base	Sound	< 500	> 100	< 200	< 100	< 50
	Warning	500 – 750	50 – 100	200 – 400	100 – 200	50 – 100
	Severe	> 750	< 50	> 400	> 200	> 100
Cementitious Base	Sound	< 200	> 150	< 100	< 50	< 40
	Warning	200 – 400	80 – 150	100 – 300	50 – 100	40 - 80
	Severe	> 400	< 80	> 300	> 100	> 80
Bituminous Base	Sound	< 400	> 250	< 150	< 100	< 50
	Warning	400 – 600	100 -250	150 -300	100 -150	50 – 80
	Severe	> 600	< 100	> 300	> 150	> 80

4.6 The AREA Parameter

The AREA method was introduced by Hoffman and Thompson (1981) to represent the deflection basins of a two parameter backcalculation process for the flexible pavement structures. Yet, its usage has been extended to the rigid pavement structures as well. This method was a continuation/ mirror of earlier research performed by Vaswani (1971) who suggested a parameter known by the spreadability factor (S) by combining the readings from five sensors of the Dynaflect. The normalized area of a certain slice/piece cut through the deflection basin between the test load's center and at diversifying radial distances from that test load is mainly represented by the AREA method. The area "normalized" denotes that the area of the deflection basin slice/piece is typically divided by the maximum (peak) deflection that is measured at the test load's center. In this method, the deflections measured in the deflection basin curve are mainly combined into one indicator, thus minimizing the effects of any possible malfunctions in the sensors. According to Hoffman and Thompson (1981), the AREA of the deflection basin is considered an appropriate parameter to characterize the whole pavement structure. On the other hand, Saleh (2015) specified that the AREA parameter showed an adequate relationship with the elastic modulus (stiffness of the pavement). Yet, it has not been broadly used for evaluating the pavement structure since there was not any rating standards/scales developed for raking the pavement structure between two extreme cases i.e., pavement structures of poor and high quality.

The spreadability (S) is given by the following equation:

$$S = \frac{D_o + D_{12} + D_{24}}{3D_o} x\ 100 \tag{81}$$

While the AREA equation for a configuration of four sensors is represented by:

$$AREA = 6\left[1 + \frac{2D_{12}}{D_o} + \frac{2D_{24}}{D_o} + \frac{2D_{36}}{D_o}\right] \tag{82}$$

Or, in metric, the equivalent equation is shown by:

$$AREA_{Metric} = 150\left[1 + \frac{2D_{300}}{D_o} + \frac{2D_{600}}{D_o} + \frac{2D_{900}}{D_o}\right] \tag{83}$$

Whereby,

- AREA is the area determined under the deflection basin
- D_o, D_{12} (D_{300}), D_{24} (D_{600}), D_{36} (D_{900}) previously defined
- D_{48} $(D_{1200})$is the surface deflection at an offset of 48 inches (1200 mm) from center

It is important to note that the AREA's unit of measure is in inches (mm) since it is normalized by the maximum (peak) surface deflection (D_o).

Determining the AREA for a single-layer system is equivalent to deflecting the upper part of the subgrade layer. This testing will result in the minimum value that the AREA can attain which is equal to 11.1 inches. The latter value is obtained by replacing the ratios shown in Eqs. (86) in the AREA Eq. (82),

$$\frac{D_{12}}{Do} = 0.26\,,\ \frac{D_{24}}{Do} = 0.125\,,\ \frac{D_{24}}{Do} = 0.083 \qquad (84)$$

The minimum AREA value proposes that the elastic moduli that corresponds to the pavement structures will be equal. Yet, this is vastly not probable to occur for the existing pavement structures. Low values indicate that the pavement structure tend to be more likely similar to the underlying subgrade structure. On the other hand, the maximum AREA value is obtained when the surface deflection measurements ($D_o = D_{12} = D_{24} = D_{36}$) are equal, though it is unlikely to happen. Thus, by replacing the aforementioned deflection measurements' values in the AREA Eq. (82), the maximum AREA value will be obtained and is equal to 36 inches. Having the surface deflections D_o , D_{12} , D_{24} , D_{36} equal (or approximately equal) indicates that the pavement structure tends to be very stiff.

For a configuration of four sensors, typical values for the AREA and the surface deflection at the testing load's center are presented in Table (2) (Pierce et. al 2017). Table (3) presents general guides and typical insights for using the AREA values from the FWD surface deflections.

Table 2: Typical Area and Do values for a 4-Sensor Configuration, Pierce et. al (2017)

Pavement Structure Type *Inches (mm)	AREA Inches (mm)	D_o mil (μm)
Thin HMA ≤ 4 (200)	16 - 21 (410 -530)	30 - 50 (760 - 1,200)
Thick HMA ≥ 4 (200)	21 -30 (530 -760)	20 - 40 (500.- 1,000)
Portland Cement Concrete	29.-32 (740 -810)	10 -20 (250 - 500)

Table 3: General Trends and Guides of AREA and Do Values, Pierce et. al (2017)

AREA	**Maximum Surface Deflection (D_o)**	**Insights***	
		Structure	**Subgrade**
Low	Low	Weak	Strong
Low	High	Weak	Weak
High	Low	Strong	Strong
High	High	Strong	Weak

** 1 Exceptions might take place*

In summary, the AREA method aids in characterizing the deflection basin's shape that is close to the applied load by the means of the normalized area on top of the deflection basin (Kim et al. 2000, Talvik 2007)

Moreover, another parameter related to the deflection basin is the Area Under Pavement Profile (AUPP) which will be discussed subsequently.

4.7 Area Under Pavement Profile (AUPP)

Based on the study performed by Garg and Thompson (1997) using the MnRoad testing sections, an acceptable correlation was observed between the HMA mechanical responses and the AUPP. This parameter helps in characterizing the pavement's upper layers' condition. It can be also used to estimate the tensile strain at the bottom of the hot mix asphalt layers with a high statistical precision; $R^2 \geq 90\%$, (Kim and Park 2002, FHWA 2016). AUPP is represented by the following equation:

$$AUPP = \frac{5Do - 2D_{12} - 2D_{24} - D_{36}}{2} \tag{85}$$

4.8 Area Indices

Horak (2015) proposed several area indices including AL_1, AL_2, AL_3 and AL_4 as indicators of the pavement's layer structural condition. The AL_1 parameter is significant for determining the structural condition of the upper layer of the pavement structure. On the other hand, AL_2 and AL_3 parameters are significant for the middle layer structural condition while AL_4 is for the lower layer structural condition. The area indices presented by Horak (2015) were suggested as alternatives, yet commendatory parameters to BLI, MLI and the LLI parameters. The area indices are mainly given by the following equations:

$$AL_1 = \frac{D_o + D_{300}}{2D_o} \tag{86}$$

$$AL_2 = \frac{D_{300} + D_{600}}{2D_o} \tag{87}$$

$$AL_3 = \frac{D_{600} + D_{900}}{2D_o} \tag{88}$$

$$AL_4 = \frac{D_{900} + D_{1200}}{2D_o} \tag{89}$$

Table 4 : Structural Condition Rating for DBPs (Hoffman and Thompson 1981, Horak 2015)

Pavement Type	Structural Condition's Rating	Deflection Bowl Parameters (DBPs)				
		AUPP (inches)	AL_1	AL_2	AL_3	AL_4
Granular Base	Sound	> 7.4	> 0.84	> 0.54	> 0.31	> 0.18
	Warning	6.6 – 7.4	0.75 –0.84	0.36 –0.54	0.19 –0.31	0.14 –0.18
	Severe	< 6.6	< 0.75	< 0.36	< 0.19	< 0.14

4.9 Shape Factors

The shape factors correspond to the amount - or the proportion - of the deflection bowl curvature. They are inversely proportional to the stiffness of the pavement over the stiffness of the subgrade. In other words, the shape factors tend to reflect the bound or the upper parts of the pavement structure's relative stiffness and tend to determine the layer's condition at an equivalent depth (Kim et al 2000, Talvik 2007).

The shape factors F_1 and F_2 are expressed by Eq. (90) and Eq. (91), respectively:

$$F_1 = \frac{D_O - D_{24}}{D_{12}} \tag{90}$$

$$F_2 = \frac{D_{12} - D_{36}}{D_{24}} \tag{91}$$

4.10 Deflection Ratio (Q_R)

According to Claessen et al. (1976), the deflection ratio (Q_R) is useful for determining the layer's condition at a certain equivalent depth and evaluating the pavement's structural integrity. It is mainly defined as the ratio between the measured deflection at an offset of 24 inches (600mm) from the load application to the maximum (peak) deflection as indicated in Eq. (94). A sensitivity analysis was conducted by University of Dundee (1980) on a 3-layer pavement structure to study the deflection bowl parameters. The deflection ratio Q_R showed some sensitivity when varying the other parameters. Contrarily, Koole (1979) stated that the Q_R can be considered reliable. The inconsistency in the results was due to the lack of coherence to the precondition assumed by Koole (1979) which considers $D_r = \frac{D_O}{2}$ while determining the deflection ratio. University of Dundee, however, considered $D_r = D_{600}$ in the analysis which explained the Q_R's insensitivity to the changes in the other parameters. It is important to note that the input required to determine the deflection ratio may vary based on the location of the sensor needed for evaluation. For example, D_r may be taken as D_{250} i.e., to evaluate the deflection measured at an offset of 10 inches (250mm) from the load applied. Yet, the latter is not considered in this research as D_{250} does not fall within the scope of the project. In this research, however, Eq. (94) is used.

$$Q_R = \frac{D_r}{Do} = \frac{D_{24}}{Do}, or\ \frac{D_{600}}{Do} \tag{92}$$

$$Q_R = \frac{D_r}{Do} = \frac{D_{10}}{Do}, or\ \frac{D_{250}}{Do} \tag{93}$$

$$Q_R = \frac{D_r}{Do} = \frac{D_{48}}{Do}, or\ \frac{D_{1200}}{Do} \tag{94}$$

The pavement structure is said to be stronger and stiffer for higher deflections ratio. Based on the deflectograph, FWD load of 40 KN or Benkelman Beam, Table 5 represent the recommended deflection ratio (Q_R) values with their corresponding indications.

Table 5: Deflection Ratio (Q_R) Values and Indications (Saleh 2016)

Deflection Ratio (Q_R)	**Indication**
< 0.6	Likely a weak unbound pavement structure with a thin asphalt layer
$0.6 \leq Q_R \leq 0.7$	Unbound pavement structure with good quality
≥ 0.8	Bound pavement structure

4.11 Bending Index (BI)

Hveem (1955) conducted a study on the response of pavement structures under repeated loadings and evaluated the fatigue failures. Reasonable approximate values for the maximum (peak) permissible deflections were reported for different pavement types and base constructions. However, a relationship proposed by A.C. Benkelman and W.N. Carey proved to be better and consistently substantial than only measuring the deflections (Hveem 1955). The aforementioned relationship is known by the bending index. The latter is generally difficult to determine, yet it can be obtained by the following equation:

$$\mathrm{BI} = \frac{D_o}{a} \tag{95}$$

Whereby,

- a is the length of the deflection basin

4.12 Radius of Influence (RI)

Ford and Bissett (1962) studied the pavement structures to evaluate the pavement's performance with its corresponding deflection and the physical properties of the base and the subgrade. From the deflection curves obtained, the wheel's radius of influence (RI) was assumed to be measured from the point of the peak deflection extended to the location whereby the curve starts becoming tangent to the plane surface/horizontal. The Helmer recorder was used to generate the RI measurements on certain "high-type" pavement stations. Ford and Bissett (1962) further determined the ratio of the RI to the measured pavement deflections (Eq. (96)). A high ratio value indicated a larger influence zone or smaller deflections. The results showed that the outer wheel-path ratio was more indicative of the pavement's structural condition. A ratio of 800 appeared as a benchmark to differentiate poor from good pavements whereby a value greater than 800 indicated a good structural condition (Ford and Bissett 1962). In other words, the ratio of RI to deflection is a relevant criterion to evaluate the overall performance of the pavement structure.

$$\mathrm{RI} = \frac{R^1}{D_o} \tag{96}$$

Whereby,

- R^1 is the distance measured from the peak deflection to the point where the curve starts becoming tangent to the plane surface.

4.13 Slope of Deflection

The slope of deflection is an important parameter that helps in reflecting the stiffness of different layers of the pavement structure. The relative stiffness of the upper parts of the pavement section and the bound layers are reflected when measuring the slope in the section of the deflection bowl that is close to the applied load. As for the relative stiffness of the lower parts and the base layer, they are reflected by measuring the slope in the middle section of the deflection basin.

The slope of deflection is given by the following equation, Kung (1967).

$$SD = \tan^{-1} \frac{D_o - D_{24}}{L} \tag{97}$$

Where L is the radial distance from the load's center.

4.14 Normalized Area Ratio (A_r')

After using a deflectograph device for evaluating the pavement's structural condition, Saleh (2015) argued that the Normalized Area Ratio (A_r') provides valuable information concerning the structural capacity of the pavement above the soil; subgrade layer. It is mainly significant in characterizing the subgrade structural condition. Saleh (2016) defined the area ratio parameter (A_r) as a ratio between the area parameter (AREA) of a certain pavement to that of the stiffest pavement structure. The value of the area ratio is expected to be large for strong pavement sections over strong subgrades. However, the value will be very low for weak pavement sections over weak subgrades. For other combinations of subgrade conditions and pavement structures, the area ratio will fall within the two extremes aforementioned. Different pavements will have different responses depending on the load applied, therefore the normalized area ratio will vary from one pavement structure to another. For this reason, it is essential to take into account the composition of each pavement structure to have a better classification of the structural capacities. Saleh (2016) proved that the A_r is subtle to the condition of the subgrade and well associated to the compressive strain found on top of the subgrade ($R^2 = 90.5\%$). For a deflection basin of 36 inches (900mm) length, the area ratio is expressed by the following equation.

$$A_r = \frac{50}{900 D_o} x \left(\frac{D_o + D_{900}}{2} + \sum_{i=50}^{850} D_i \right) \tag{98}$$

Whereby,

- A_r is the area ratio parameter
- D_{50} , D_{100} ... D_{900} are the surface deflections at offsets of 50 mm, 100mm …900mm from the test load's center

Moreover, the area ratio parameter was found to be strongly correlated with the deflection ratio (Saleh 2016). However, the area ratio parameter is more desirable as it addresses a longer deflection basin extending from 0 to 36 inches (900mm), thus accounting the entire pavement layers situated above the soil; subgrade layer. Additionally, the deflection ratio is more prone to measurement errors as it is based only on two deflection measurements unlike the area ratio parameter. Combining the maximum deflection D_o with the area ratio (A_r) to form a single indicator will provide even more valuable information regarding the pavement structure condition. Dividing the area ratio by the maximum deflection D_o will produce the normalized area ratio (A_r') represented in the equation below:

$$A_r = \frac{50}{900 {D_o}^2} x \left(\frac{D_o + D_{900}}{2} + \sum_{i=50}^{850} D_i \right) \quad (99)$$

The structural capacity for several pavement types were classified by Saleh (2016) based on the normalized area ratio (Table 6).

Table 6: Structural Capacity Classification based on the Normalized Area Ratio (Saleh 2016)

Pavement Type	Structural Capacity Classification based on Ar’			
	Weak	Fair	Good	Strong
Unbound Granular + Surface Treatment	< 0.1	0.1 – 0.25	0.25 – 0.45	> 0.45
Unbound Granular + Thin Asphalt	< 0.25	0.25 – 0.4	0.4 – 0.7	> 0.7
Structural Asphalts	< 0.6	0.6 – 1	1 – 1.5	> 1.5
Cement Stabilized Base	< 1	1 – 2	2 – 3	>3

Saleh’s (2016) results verified the correlation between the normalized area ratio (A_r’) and the maximum deflection (D_o). For small D_o values, the A_r’ was found to be very high signifying, thus, a strong subgrade and pavement structure. Contrarily, high D_o values were associated with small A_r’ values reflecting a very weak subgrade and pavement structure.

The normalized area ratio, however, cannot be used in this study as it requires input values that are not taken into account within the scope of project.

4.15 Surface Modulus

Plotting the surface modulus is very useful as it provides an indication of the stiffnesses of the layers at various corresponding depths. For a certain depth (z_e), the surface modulus approximates a certain combined modulus of the layers situated under each other. The surface modulus is found to be nearly equivalent to that of the subgrade when the equivalent depth (z_e) is larger than the total thickness of the pavement. Hence, the surface modulus equations at the loading plate’s center(E_o) and at a certain distance z (E_z) are given by Eq. (100) and Eq. (101) respectively.

$$E_o = \frac{2\ x\ \sigma_o\ x\ r_p\ x\ (1 - v^2)}{d_z} \quad (100)$$

$$E_z = \frac{\sigma_o\ x\ {r_p}^2\ x\ (1 - v^2)}{d_z\ x\ z} \quad (101)$$

As for the equivalent depth, the equation is given by:

$$h_{e,m} = \left[h_1 \sqrt[3]{\frac{E_1}{E_2}} + h_2 \sqrt[3]{\frac{E_2}{E_3} + \cdots h_{m-1} \sqrt[3]{\frac{E_{m-1}}{E_m}}} \right] x\, f_m \tag{102}$$

Whereby,

- E_o is the surface modulus at the loading plate's center, lbf/inch^2 (MPa)
- E_z is the surface modulus at a certain distance z, lbf/inch^2 (MPa)
- σ_o is the contact pressure beneath the loading plate, lbf/inch^2 (MPa)
- υ is the Poisson's ratio
- z is the distance from the sensor to the loading center, inches (mm)
- d_z is the deflection measured at the distance z, inches (mm)
- r_p is the loading plate radius, inches (mm)
- $h_{e,m}$ is the equivalent depth, inches (mm)
- f_m is a factor ranging from 0.8 -1, dependent on the thickness, the number of layers and modular ratio
- h_m is the thickness of the layer m, lbf/inch^2 (MPa)
- E_m is the stiffness modulus of the layer m, lbf/inch^2 (MPa)

In order to calculate the aforementioned FWD Indices, the FWD parameters shall be initially determined. These parameters are subsequently discussed in the upcoming section.

4.16 FWD Parameters

An ample amount of information can be extracted from the FWD deflection time histories that are distinctive to the individual pavement structures, whereby, several FWD parameters can be examined to efficiently determine the variables within each layer. The backcalculation procedure considers a forward model to calculate the theoretical surface deflections; the aforementioned model is based on either static or dynamic analysis. Yet, the static analysis makes use of only the peak deflections, unlike the dynamic analysis that uses the FWD peak deflections along with the time lag between the latter and the peak loading.

Bazi and Assi (2020) used the FWD parameters in the PULSE 2019 to comprehend the magnitude and the shape of the time histories for each sensor. The FWD parameters mainly included **"D_{Peak}"** (FWD peak deflection) that takes place at **"T_{DPeak}"** time, **"T_{50R}"** and **"T_{50L}"**

which are the times to the right and left of the FWD peak, respectively; and represent 50% of the FWD peak deflection. Lastly, “**Dur$_{50}$**” is the pulse duration at the 50% of the FWD peak defections; it is obtained by the difference between the **“T$_{50R}$”** and **“T$_{50L}$”**

Besides the above-mentioned parameters, the authors further explored, in their PULSE 2020 application, 17 more parameters that are essential for the backcalculation procedure. Thus, resulting with a total of 22 FWD parameters illustrated in Figures 32 and 33. For each sensor, the 22 FWD parameters are mainly extracted using the “PULSE Analyzer” module. The latter uses polynomial fittings to precisely quantify the parameters (Bazi et al. 2021). For an accurate determination of the FWD Parameters, it is essential to allow for the data fitting as the measured and calculated FWD values are not continuous, but rather discrete. As for the FWD surface velocity plot (Figure 33), it is determined through the central difference method, while the parameters are obtained through fitting the deflection time-histories data.

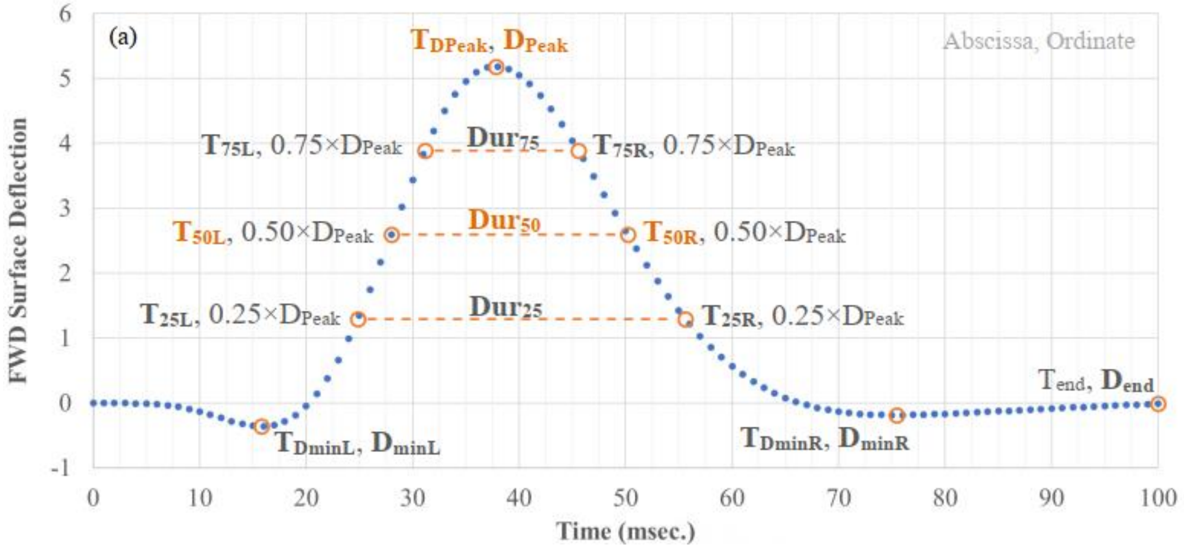

Figure 32: A Typical FWD Deflection Time History, Bazi, Brynick, Bou Assi, and Gagnon (2021)

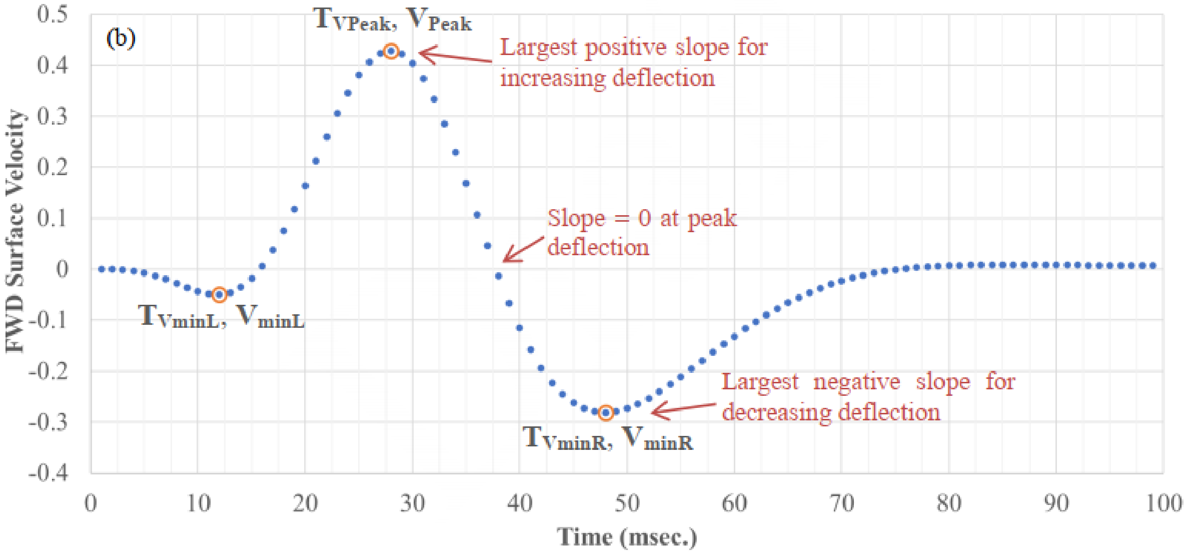

Figure 33: A Typical FWD Velocity Time History, Bazi, Brynick, Bou Assi, and Gagnon (2021)

After quantifying the contribution of the layer moduli, layer thicknesses and Rayleigh damping coefficients, etc. on the 22 parameters, (Bazi et al. 2021) found that the subgrade modulus (E$_3$) predominantly controlled the 22 parameters, then the damping coefficient (β_R), AC thickness and lastly the depth to the rigid/stiff layer when available. As for the FWD parameters that showed significant contributions for usage in the dynamic backcalculation included **“T_{Peak}”, “D_{Peak}”, “D_{minL}”, “D_{minR}”, “T_{VPeak}”, “V_{Peak}”, “V_{minL}”, “V_{minR}”, “T_{50R}”, “T_{50L}”, “T_{75R}”** and **“T_{75L}”**, (Bazi et al. 2021).

It is important to note that some FWD parameters, including the **“D_{minL}”, “T_{DminL}”, “D_{minR}”, “T_{DminR}”, “V_{minL}”, “T_{VminL}”** will not exist for all pavement structures and sensors at all offsets. However, these parameters provide relevant information about the pavements that must be considered during the dynamic backcalculation procedure. For this reason, they ought to be evaluated when available. **“D_{minR}”** and **“T_{DminR}”**, for example, designate the existence of a stiff shallow layer (Bazi, Brynick, Bou Assi, and Gagnon, 2021). Hence, if this layer was not accounted in the model, substantial errors are then expected.

4.17 Difference Variables

Using the aforementioned FWD parameters, additional variables are determined and referred to as the “Difference Variables”. The latter are defined by the difference between individual FWD parameters at subsequent offsets. The denotations and the equations of such variables are found below:

$$\mathrm{Dp08} = \mathrm{DPeak\_D.0} - \mathrm{DPeak\_D.8} \tag{103}$$

$$\mathrm{Dp812} = \mathrm{DPeak\_D.8} - \mathrm{DPeak\_D.12} \tag{104}$$

$$\mathrm{Dp1218} = \mathrm{DPeak\_D.12} - \mathrm{DPeak\_D.18} \tag{105}$$

The logic behind the denotation is followed for "Dp1824", "Dp2436", "Dp3648","Dp3648", "Dp4860", Dp6072", "Dp7284", "Dp8496", "Dp96108", "Dp108120".

$$\mathrm{Tp08} = \mathrm{TPeak\_D.0} - \mathrm{TPeak\_D.8} \tag{108}$$

$$\mathrm{Tp812} = \mathrm{TPeak\_D.8} - \mathrm{TPeak\_D.12} \tag{109}$$

The logic behind the denotation is followed for "Tp1218","Tp1824","Tp2436","Tp3648", "Tp4860","Tp6072","Tp7284","Tp8496","Tp96108","Tp108120"

$$\mathrm{Dml08} = \mathrm{DminL\_D.0} - \mathrm{DminL\_D.8} \tag{110}$$

The same logic for "Dml812", " Dml1218", " Dml1824", " Dml2436", " Dml3648", "Dml4860", "Dml6072", "Dml7284", "Dml8496","Dml96108","Dml108120"

$$\mathrm{Tml08} = \mathrm{TDminL\_D.0} - \mathrm{TDminL\_D.8} \tag{111}$$

The same logic for "Tml812", " Tml1218", " Tml1824", " Tml2436", " Tml3648", "Tml4860", "Tml6072", "Tml7284", "Tml8496","Tml96108","Tml108120"

$$\mathrm{Dmr08} = \mathrm{DminR\_D.0} - \mathrm{DminR\_D.8} \tag{112}$$

The same logic for "Dmr812", "Dmr1218", "Dmr1824", "Dmr2436", "Dmr3648", "Dmr4860", "Dmr6072", "Dmr7284", "Dmr8496","Dmr96108","Dmr108120"

$$\mathrm{Tr08} = \mathrm{DminR\_D.0} - \mathrm{DminR\_D.8} \tag{113}$$

The same logic applies to "Tr812","Tr1218", "Tr1824", "Tr2436", "Tr3648", "Tr4860", "Tr6072", "Tr7284", "Tr8496","Tr96108","Tr108120"

$$\mathrm{TVPD08} = \mathrm{TVPeak\_D.0} - \mathrm{TVPeak\_D.8} \tag{114}$$

The same logic applies to "TVPD812", "TVPD1218", "TVPD1824", "TVPD2436", "TVPD3648", "TVPD4860","TVPD6072","TVPD7284","TVPD8496","TVPD96108","TVPD108120"

$$\mathrm{TVP08} = \mathrm{TVPeak.0} - \mathrm{TVPeak.8} \tag{115}$$

The same logic applies to "TVP812", "TVP1218", "TVP1824", "TVP2436", "TVP3648", "TVP4860","TVP6072","TVP7284","TVP8496","TVP96108","TVP108120"

$$\mathrm{VPD08} = \mathrm{VPeak\_D.0} - \mathrm{VPeak\_D.8} \tag{116}$$

The same logic applies to "VPD812", "VPD1218", "VPD1824", "VPD2436", "VPD3648", "VPD4860","VPD6072","VPD7284","VPD8496","VPD96108","VPD108120"

$$\mathrm{VP08} = \mathrm{VPeak.0} - \mathrm{VPeak.8} \tag{117}$$

The same logic applies to "VP812", "VP1218", "VP1824", "VP2436", "VP3648", "VP4860","VP6072","VP7284","VP8496","VP96108","VP108120"

$$\mathrm{TVMD08} = \mathrm{TVminR\_D.0} - \mathrm{TVminR\_D.8} \tag{118}$$

The same logic applies to "TVMD812", "TVMD1218", "TVMD1824", "TVMD2436", "TVMD3648","TVMD4860","TVMD6072","TVMD7284","TVMD8496","TVMD96108", "TVMD108120"

$$\mathrm{TVM08} = \mathrm{TVminR.0} - \mathrm{TVminR.8} \tag{119}$$

The same logic applies to "TVM812", "TVM1218", "TVM1824", "TVM2436", "TVM3648","TVM4860","TVM6072","TVM7284", "TVM8496", "TVM96108", "TVM108120"

$$\mathrm{VMD08} = \mathrm{VminR\_D.0} - \mathrm{VminR\_D.8} \tag{120}$$

The same logic applies to "VMD812", "VMD1218", "VMD1824", "VMD2436", "VMD3648", "VMD4860","VMD6072","VMD7284","VMD8496","VMD96108", "VMD108120"

$$\mathrm{VM08} = \mathrm{VminR}_0 - \mathrm{VminR.8} \tag{121}$$

The same logic applies to "VM812", "VM1218", "VM1824", "VM2436", "VM3648", "VM4860","VM6072","VM7284","VM8496","VM96108", "VM108120

$$\mathrm{T25L08} = \mathrm{T25L\_D.0} - \mathrm{T25L\_D.8} \tag{122}$$

$$\mathrm{T25R08} = \mathrm{T25R\_D.0} - \mathrm{T25R\_D.8} \tag{123}$$

$$\mathrm{T50L08} = \mathrm{T50L\_D.0} - \mathrm{T50L\_D.8} \tag{124}$$

$$\mathrm{T50RL08} = \mathrm{T50R\_D.0} - \mathrm{T50R\_D.8} \tag{125}$$

$$\mathrm{T75L08} = \mathrm{T75L\_D.0} - \mathrm{T75L\_D.8} \tag*{(124)}$$

$$\mathrm{T75RL08} = \mathrm{T75R\_D.0} - \mathrm{T75R\_D.8} \tag*{(125)}$$

The same logic applies for "T25L_D.", "T50L_D.", "T75L_D.", "T25R_D.", "T50R_D.", "T75R_D." at subsequent offsets.

$$\mathrm{D25\_08} = 0.25 \text{ x } (\mathrm{Dp08}) \tag{126}$$

The same logic applies to "D25_812","D25_1218", "D25_1824", "D25_2436", "D25_3648","D25_4860","D25_6072","D25_7284","D25_8496","D25_96108","D25_108120"

$$\mathrm{D0\_2550} = 0.5 \text{ x } (\mathrm{DPeak\_D.0}) \tag{127}$$

$$\mathrm{D8\_2550} = 0.5 \text{ x } (\mathrm{DPeak\_D.8}) \tag{128}$$

The same logic applies to "D12_2550", "D18_2550", "D24_2550", "D36_2550", "D48_2550", "D60_2550","D72_2550","D84_2550","D96_2550","D108_2550","D120_2550"

Chapter Five

Machine Learning Algorithms and Variable Selection

5.1 Neural Networks

A Neural Network (NN), also known by the Multi-Layer Perception (MLP), is an algorithm based on data-processing and can be regarded as analogous to the human's nervous system. The latter consist of neurons that are mainly interconnected. In a similar manner, the Neural Network consist of interconnected data-processing units. Neural Networks are widespread calculating engines capable of identifying different patterns within the data under study (Sarle,1994). The main objective is to associate simple data-processing units (neurons) to resolve complex and intricate problems. The units are mainly organized into multiple layers whereby each has a definite role. Such units do not function in a linear fashion. In fact, the strength of Neural Networks comes from the simultaneous processing of data, which makes it possible to handle the nonlinearity. The interconnected data-processing units use an activation function that characterizes Neural Networks to convert the input data into output data (Sarle,1994). The input data is received by the first layer in the Neural Network to proceed with the analysis and pass the processed data to the hidden layers. The hidden layer will in return pass the data to the final layer to generate the requested outcome. It is important to mention that the connections between the data-processing units (neurons) are referred to as weights. One of the main advantages of the Neural Networks is that they are

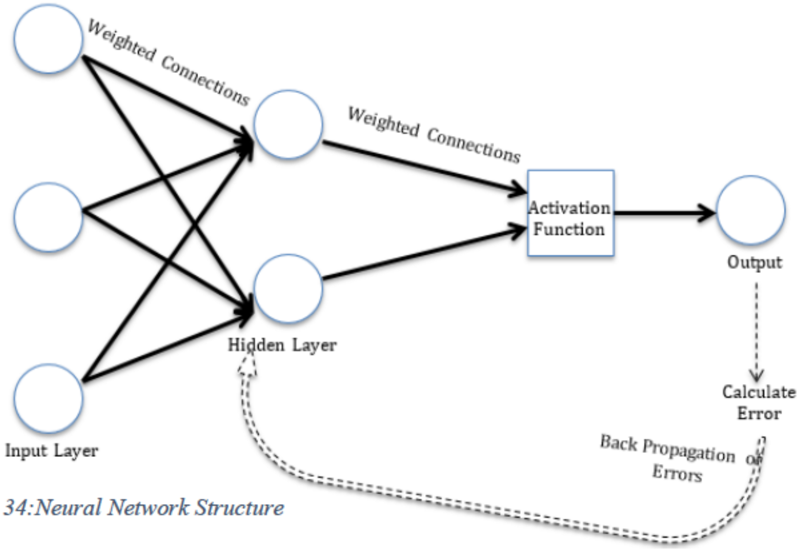

Figure 34:Neural Network Structure

considered naturally adaptive. They learn and train themselves from a data that has an identified outcome, and manage to optimize their weights to provide more accurate predictions in circumstances with obscure outcome.

A zoomed view to an output or a hidden node is presented in Figure 35. The node accepts the output (x_i) of the preceding nodes to which it is linked to. These are further multiplied by the weights (w_i) and then summed. Then, the sum is transformed using the function $f(\,)$ and transmitted to the next layer's nodes or to an output as an outcome.

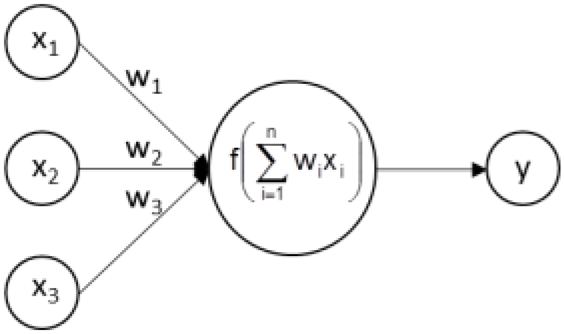

Figure 35: Functioning of a Data-Processing-Unit (Neuron)

Following the setup of the Neural Network architecture (i.e., number of hidden layers, number of units per layer and the function $f(\,)$ per unit), the network is then trained by determining the weights that generate the desired outcome.

The learning algorithms used to calculate the error include: (1) Least Mean Square, (2) Gradient Descent, (3) Newton's Rule, (4) Conjugate Gradient. The error calculated is backpropagated to the whole data-processing units (neurons) in a way that the error at every neuron is proportional to the neuron's contribution towards the total error determined at the output neuron. The weights at the connections between the units (neurons) are accordingly adjusted by the learning algorithms to minimize the squared difference between the target variables' actual value and the ones determined by the Neural Network. Therefore, the Neural Network can be defined as a series of trained, numerical conversions applied to an input data and generate an outcome, (Sarle,1994). Increasing the count of the hidden layers will deepen the Neural Network. Deep Neural Networks, however, will have thousands to million units and connections.

5.2 Decision Trees

Trees have several correspondences in real life, they have also influenced a broad extent of Machine Learning (ML), comprising both regression and classification. Fundamentally, regression refers to predicting a certain quantity while classification refers to predicting a class or a label. In the Decision Analysis, Decision trees are used to explicitly and visually represent the decision makings and decisions. As the name indicates, it typically considers a tree like structure of conclusions and decisions.

A Decision Tree is mainly a supervised, nonparametric algorithm considered in Machine Learning (ML), it can be used to either develop prediction models/algorithms for a specific target variable or to establish a classification system that depends on multiple covariates. The method used in Decision Trees classifies the population under study into sections – looking like branches - that would construct inverted trees having root, internal and leaf nodes. (1) The root node i.e., the decision node, mainly represents a specific choice that leads to the subdivision of the entire record into several mutually-special subsets. (2) The internal nodes i.e., the chance nodes that represent one of the available probable choices at that specific point in the Decision Tree model; the node's top edge is linked to its parent node while the bottom edge is linked to its leaf nodes. (3) The end nodes i.e., the leaf nodes that represent the end result of the decision combinations. Decision Trees can competently handle complicated and large datasets without the imposition of intricate parametric structures. The data is generally divided into a training dataset to build the Decision Tree model, and a testing dataset to determine the adequate size of a tree structure required to attain the optimal model. The target variables are generally presented in the leaves. It is worth mentioning that the branches represent the occurrences or the outcomes that originate from the decision and internal nodes. The Decision Tree model is thus formed by the hierarchy of the branches. Therefore, a "classification" decision rule is signified by every path from the decision node, to the internal nodes and lastly to the end nodes. Initiating at the root node, the sample is allowed to propagate throughout the nodes in order to reach the tree leaf. A decision, related to which successor node the information should proceed to, is made at each node. This decision depends on the selected feature of the sample. In other words, the growth of the tree is based on deciding what features must be chosen, which conditions must be used for the data splitting and lastly to be aware of stopping (Song & Ying, 2015). Generally, the tree model arbitrarily grows, thus it needs to be trimmed for it to be more efficient.

When building the tree model, the required input variables must be initially identified. Then, the records are split at the decision and the subsequent choice nodes into several categories depending on the status of the aforementioned variables (Song & Ying, 2015). To select among the various probable input variables, the features associated to the purity degree of the ensuing child-nodes are used. The features include the classification error, entropy, information gain, etc. (Patel & Upadhyay, 2012). Using the entire training dataset, the critical feature is initially identified through a statistical measure after comparing all the features. Based on the resultant splitting outcome, the training dataset is then subdivided. For each resultant subset, the second critical feature will be identified, thus creating a new split. The splitting process is repeated on every resultant subset up until the end nodes in each branch are determined, or it will proceed until a stopping principle or a predetermined homogeneity are met. Yet, the robustness and the complexity of the model are considered as competing features that must be considered when building statistical models. As the complexity increases, the robustness of the model decreases when considered for predictions. An intricate Decision Tree model, that can extend sufficiently wide to allow for 100% purity in the records at each end note, can be built in extreme cases. This tree model, however, will be overfitted to the extant observations and have scarce records in the leaf nodes, thus generating poor predictions. For this reason, it is vital to implement stopping rules to prevent the tree model from being tremendously complex (Patel & Upadhyay 2012). But, for some cases, the stopping rules are not efficient. Hence, initially growing a large-tree model, then pruning it to an optimal size through the elimination of unnecessary nodes can be considered as an alternative method to build an efficient model (Friedman, 2017).

5.3 Random Forests

As previously mentioned, a Decision Tree is considered an easy model for creation. It has the ability to handle various types of inputs (numerical and categorical) and is explicable because of its form of representation. However, such models are often unreliable when applied to new datasets. This can be explained by their propensity to effortlessly fit the samples found in a training set. Therefore, a weak application performance/quality will be obtained if the dataset contains any outliers. Alternatively, Random Forests models are considered the solution for this issue. Random Forests are actually part of the Decision Tree algorithm family.

A forest is mainly considered as a collection of single trees by definition. Each tree model is unique, but they form a forest when combined together (Breiman,1996). The Random Forest algorithm, in this comparison, creates diverse trees from the same training dataset. In other words, the algorithm adopted depends on combining the predictions performed by several Decision Tree models of changing depths (Breiman,2001). At each node, a distinct, arbitrarily selected subset from the training dataset and an arbitrarily selected subset of the characteristics are mainly used to form the Decision Tree model. Therefore, trees are constantly constructed using only a subset of the dataset. In comparison to the standard Decision Tree previously described, each tree within the Random Forest model represents a weak decision tree model since it does not have permission to access to the entire dataset during the building process. In the case of classification, they comprise an ensemble of "decision makings," and the collective outcome can be determined by either majority voting or by averaging if the regression model was adopted (Bauer & Kohavi,1999). This adjusts for potential single tree errors in the forest, thus making the model less likely to generate results that are too far from the actual values. Random Forests are commonly used in applications with tree sizes ranging from 100 to 500. They have shown to be of high qualities in their practical applications. In addition, in case of any missing information, the Random Forests are still capable of performing in an efficient manner. In fact, this designates one of their main strengths. Based on the principles that these models follow for construction; each tree uses different features than the other. Hence, if missing values for a certain feature were observed during the application, there are usually several trees, that do not consider the aforementioned feature, and are available to generate robust predictions. However, when modeled for regression problems, it is important to note that Random Forests may exhibit limitations related to the range of the target variable values that are used in the training. Hence, having a dataset that does not fall within the original training dataset range might lead to a poor performance by the Random Forest models.

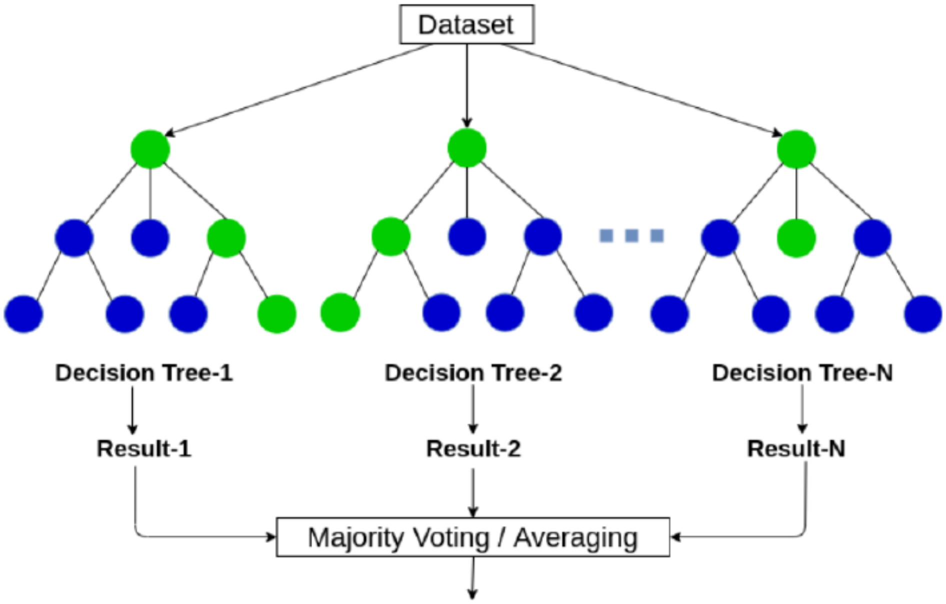

Figure 36: Radom Forest Model

5.4 Reasons Behind Adopting the Random Forest Algorithm

Neural Networks (NN) are known for their efficient performance in several industry fields when compared to other ML algorithms. They remain learning up until the best model, or the finest set of the features, that satisfies the predictive performances are generated. Yet, the Neural Network scales the variables into a set of numbers whereby features tend to become indiscernible to the analyst once the learning phase is complete. Neural Network is a diverse technique that learns in a different manner when compared to the Random Forest (RF) algorithm. Yet, both can be considered in analogous domains. Moreover, Random Forests are preferred over a Decision Tree (DT) model. The ultimate reason behind using an RF model instead of the DT model is the ability to combine the outcome (predictions) of several DTs into single robust model. As a result, RFs are thus less prone to the problem of overfitting. The latter typically takes place while using flexible models such as the DT, whereby the model tends to memorize a training dataset while learning any noise, if present, in the dataset. This will therefore hinder the model from making predictions. Briefly, random forests have the ability to lessen the large variance resulting from decision trees through combining several trees into a single model. Random Forests provide different interpretations than a Decision Tree, yet with an improved performance. On the other hand, an effective Neural Network performance requires more datasets than an average analyst may have. Neural Networks decimate the variables' interpretability to a point whereby they tend to be meaningless for performing.

From an economical perspective, the costs and the time allocated for building a model, whether Neural Network, Random Forest or a Decision Tree, play a significant role. The training of the Neural Network is computationally very intensive and time consuming. A great amount of preparation effort is required, in addition to the learning mechanism itself, to have the inputs in their appropriate format. They should, for example, be in the "number" form and also be normalized. Several versions must be calculated and evaluated in order to find the optimal model. The various parameters, also known by the hyperparameters, such as the layers number or the neurons per each layer, as well as the learning rates, can be changed. A comprehensive model must be calculated, tested and evaluated for each combination. The greater the number of hyperparameters, the more combinations must be examined. When combined with the time required to train a certain model, this therefore results in a significant time and expense investment. Random Forests, on the other hand, necessitate far less data preparations for the inputs. They are able to handle categorical, binary, and numerical variables, and they don't require variable normalization. Random Forests are easy to learn and tune based on their hyperparameters (Ahmad et al. 2017). As a result, the computational time and cost required to train a Random Forest are quite minimal. Moreover, a Random Forest may be trained with relatively little data. To reach the same degree of accuracy, Neural Networks typically require more data. Random Forests frequently gain little performance once a specific quantity of data is achieved, but Neural Networks benefit from enormous volumes of data and continuously improve accuracy. For such reasons, and knowing that this research project includes enormous amount of data, the Random Forest algorithm is adopted to perform the predictions for the necessary variables.

5.5 Random Forests Variable Importance Measures (VIMs)

5.5.1 Random Forest Model

As previously explained in section (5.3), each Random Forest is mainly an ensemble/collection of several Decision Trees. According to Breiman (1996), each tree within the Random Forest is expanded and grown using a data subset made of random variables subsets and bootstrap. The bagging method generally describes the bootstrap sampling process from the original dataset to determine the training set for every tree. As for the randomization method, it typically describes the variable subset selection process from the original variable set for the tree node split. For the new instance classification, the Random Forest places that new instance in each of the forest's trees. Each tree delivers a certain predicted label as a prediction vote. Hence, the classification with the most votes is chosen by the RF. The so-called “Out-Of-Bag (OOB) dataset” is made up of all the excluded samples. In other words, it is a set of the data (observations) that are not utilized to build the current or a specific tree. It is mainly used to approximate the error of the prediction made and to also evaluate the importance of each variable considered. The accuracy determined through the OOB dataset is always produces and applied when evaluating the performance of the Random Forest model. For each tree within the Random Forest model, the prediction error obtained on the OOB data sample is recorded and presented as an “error percentage” or as a “Mean Square Error” for the classification and the regression analysis, respectively. The same process is performed following the permutation of every predictor variable.

5.5.2 Variable Selection

5.5.2.1 Importance of Variable Selection and Strategies Used

In a variety of applications, variable selection is extensively used to select the discriminating traits from a large number of variable datasets. Prediction models are useful for determining the relationship between specific variables utilized in a model and a certain outcome obtained, as well as for forecasting the future of the projected outcome. The prediction model offers information concerning the variables that influence the outcome, as well as their strength of correlation with that outcome, and forecast the future of a particular outcome based on their specific values. Several methods are present for developing prediction models, yet, an adequate strategy for variable section should be followed and adopted each time. The selection of the most promising variables for incorporation in the model is frequently considered as the most difficult and significant part when building the model. Large datasets often include thousands of features/variables which makes it arduous to efficiently handle using the conventional approaches. Subsequently, choosing the proper variables must be taken prudently to evade counting any noise in the final/optimal model. The main objective of such selections is to discover variables that will offer the better fit to the model on hand, thus generating accurate and robust predictions. In other words, variable selection provides several benefits such as enhancing the model's performance in terms of the predictions, conveying variables more rapidly, simplifying the visualizations of data, reducing the utilization and the training time and lastly presenting an improved understanding of the basic process that produced the data (Guyon & Elisseeff, 2003).

Several reasons that explain the importance of selecting variables do exist in the literature, including the practicality problems. Using large variable sets in a certain model is not practical. Several variables might negligibly influence an outcome, and thus can be eliminated. Moreover, having less variables in the model will definitely reduce the complexity and the computational time required (Kuhn & Johnson, 2013). Based on the parsimony principle, the simplest models with less variables are generally preferred and desired over complex and intricate models having several variables. As more variables exist in a certain model, the latter's dependency in the observed datasets increase. Contrarily, simpler models are much easier to analyze, interpret, generalize, i.e., to be used in practice. Yet, it is essential to assure that the most significant variables are not eliminated from that simple model.

Initially selecting the most promising variables, known as the candidate variables, can be considered as a strategy to restrict the count of the probable variables. By definition, the candidate variables are the ones that have established previous extrapolative performance with a certain outcome. Moreover, grouping similar and associated variables based on statistical methods and knowledge may also assist in restricting the variables count. Combining the variables into a single variable, especially if they exhibit a strong correlation, has been proved to be prudent. Additionally, the variable distribution can as well offer a particular indication of the ones to be restricted. The variables that exhibit a large count of missing values may be eliminated as imputing such variables tend to be doubtful because of the poor estimations. Following the identification of the number of the possible "candidate" variables from the list of all accessible variables in the dataset, an additional variable selection for inclusion is made in the final/optimal model. For the latter, there are several methods for choosing variables. The entire model approach is considered when including all the possible "candidate" variables in the model. Moreover, there are several suggestions to initiate the variable selection process through "univariate" analysis for every variable. Thus, variables with a predefined significance shall be used in the "multivariate" analysis. However, such method is not practical for use in this research due to the large number of variables. Generally, formal variable selection methods should be used when there are several candidate variables offered and there is doubt or confusion about which variables to use in developing the final model. Forward selection, backward elimination, all possible subset selection and stepwise selection are the four significant variable selection strategies that are frequently used.

For the Random Forest models, on the other hand, several Variable Importance Measures (VIMs) are available for selecting the most promising variables and will be subsequently discussed in the upcoming section. It is important to note that Random Forests, just like Neural Networks and Decision Trees, are not linear and the underlying algorithm used to build the models will exclude or minimize the impact of any variable that is not useful in yielding a "pure" prediction. Therefore, there is no need to worry about the multicollinearity among the predictor variables.

5.5.2.2 Variable Selection using Mean Decrease Accuracy (MDA) and Mean Decrease Gini (MDG) Measures

Variable selection is becoming very vital and essential in the statistical learning, and has been given great attention as the variables are showing a remarkable increase to thousands and more. Hence, new methods are being proposed to address such demanding tasks that involve several redundant and irrelevant variables. The Variable Importance Measures (VIMs) stability, that is based on the Random Forest model, has been lately given greater focus and attention (Wang et.al, 2016). Random Forests offer two VIMs including the Mean Decrease Accuracy (MDA) and Mean Decrease Gini (MDG). The variable rankings provided by either the MDA or the MDG, serve as a filter-like tool that eliminates any redundant or irrelevant variables of lower importance. The MDA and MDG values are considered as the Random Forest’s vital outcomes/measures that can be plotted to illustrate the importance of each variable in classifying the dataset. The Mean Decrease Accuracy (MDA) plot shows the amount of accuracy lost when each variable is excluded from the model. As the accuracy declines, the more critical the variable becomes for a successful and effective classification. The variables shown in the plot are generally listed in order of decreasing relevance. The MDA index/measure exploits the permuting Out-Of-Bag (OOB) samples to determine the variable’s importance. The Mean Decrease in Gini coefficient (MDG), however, is a measure of the degree of each variable’s contribution to the homogeneity of the leaves and the nodes in the resultant random forest. It is defined as the overall decrease in the impurities of each node after splitting on a certain variable. For the classification analysis, the node impurities are measured using the Gini index. As for the regression analysis, it is mainly measured through the residual sum of squares. The greater the MDA or MDG value, the more significant and the purer the variable is in the model.

The advantage of using the Random Forest VIMs measures, especially when compared to the univariate screening techniques, is their capability of covering the influence of each of the predictor variables “individually", in addition to the multivariate interactions and connections with the remaining predictor variables (Strobl et.al, 2008). According to Lunetta et.al (2004), the correlations among the variables may be efficiently detected through Random Forest models than by considering other techniques and approaches. Moreover, the main reasons to select the MDA and MDG as measures used to evaluate the importance of each variable mainly falls within the following aspects: (1) Even though the OOB error is considered slightly more optimistic, it generates fair estimations when compared to the typical alternative testing, (2) The Gini Index is suitable for both regression and classification, (3) MDA and MDG measures are considered as the Random Forest model default outputs which makes them convenient for usage, (4) Considering both measures together is considered to be more robust and reliable than using only one measure.

Hence, the most promising variables, that serve as appropriate predictor variables, are selected in this research using the MDA and MDG measures.

Chapter Six

Methodology

6.1 Research Program

The pavement structure is composed of multiple layers – mainly two or three layers - resting on top of the natural soil; known as the subgrade layer. For both flexible and rigid pavements, each layer, including the subgrade layer, can have one or more properties, referred to as variables. The aforementioned properties mainly include the modulus of elasticity and the Rayleigh damping coefficients for all layers, except for the asphalt concrete layer that typically include four variables representing the master curve sigmoidal function coefficients. For further elaborations, the seed variables and the predictor variables considered in this research paper are listed below:

The seed variables (response variables) under study are the following:

1. For the Asphalt Concrete (AC) layer in flexible pavements:
    - AC master curve sigmoidal function coefficient “alpha (α)”
    - AC master curve sigmoidal function coefficient “Beta_prime (β')”
    - AC master curve sigmoidal function coefficient “Delta (δ)”
    - AC master curve sigmoidal function coefficient “Gamma (γ)”
2. For the Portland Cement Concrete (PCC) layer in rigid pavements:
    - Modulus of elasticity (E_1)
    - Rayleigh Damping Parameters (α_{RPCC}) and (β_{RPCC})
3. For the unbound layers within both flexible and rigid pavements,
    - Modulus of elasticity of the base layer (E_2)
    - Modulus of elasticity of the subgrade layer (E_3)
    - Modulus of elasticity of the stiff layer (E_4)
    - Rayleigh Damping Parameters (α_R) and (β_R)
    - Stiff layer thickness measured from the surface (h_3)

The predictor variables used to build the models for the aforementioned seed variables include:

1. Surface layer thickness (h_1)

2. Base layer thickness (h_2)
3. FWD Pulse Duration
4. FWD Indices (Discussed in Chapter 4)
5. FWD Parameters at offsets 0,8”,12” 18”,24”,36”,48”,60”,72”,84”,96”,108”, 120” from the center of the applied load (Discussed in Chapter 4)
6. The difference between individual FWD parameters at subsequent offsets referred to as the “difference variables” (Discussed in Chapter 4)

Generally, the FWD deflection parameters are obtained from the FWD time histories that are based on field testing. The models - that shall be built- are expected to predict the initial set of layer variables for use in dynamic backcalculation. Those models will be developed based on simulated (synthetic) data from the thousands of thousands of combinations that will be subsequently discussed.

In other word, using machine learning and classification analysis, models will be developed for predicting each seed layer variable for the use in the dynamic backcalculation. As previously mentioned, pavement structures with three and four layers will be considered. For flexible pavements, the Asphalt Concrete (AC) Layer is modeled as linear viscoelastic material. As for the Portland Cement Concrete layer for the rigid pavements along with all other unbound layers, are modeled as linear elastic materials including damping. The flowchart in Figure 39 illustrates the steps performed in order to develop the predictive Random Forest (RF) models for the individual seed (response/target) variables

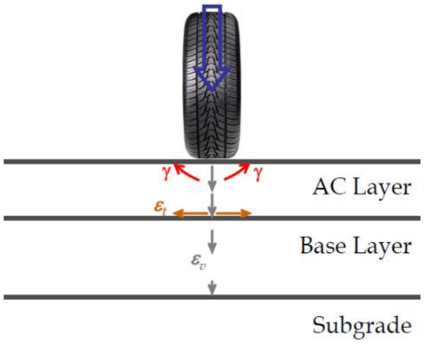

Figure 37: Multi-Layer Flexible Pavement

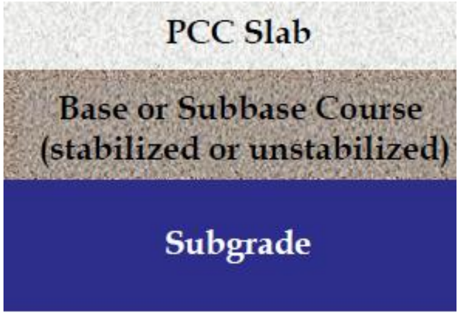

Figure 38: Multi-Layer Rigid Pavement

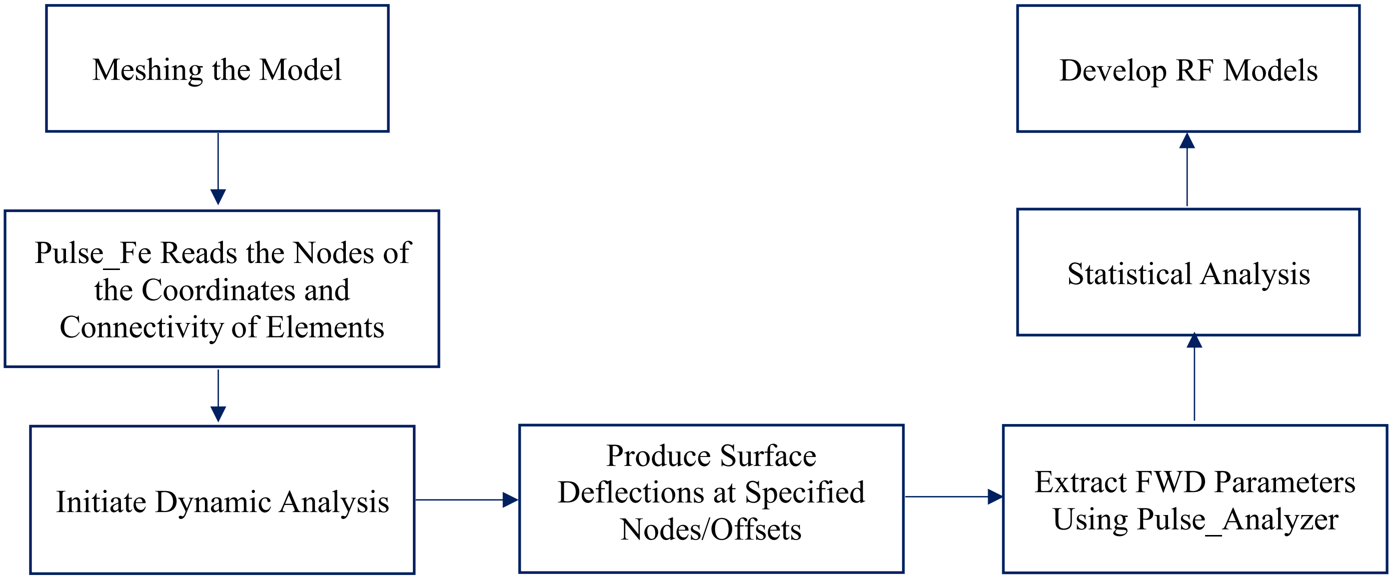

Figure 39: Steps for Developing RF Models

6.1.1 Software Used

6.1.1.1 Gmsh Software

Gmsh is a software that generates 2D and 3D finite element meshes. It has a CAD engine and a post processor that are built in (Geuzaine and Remacle 2009). Consequently, this software is used to yield the discretization of the flexible and rigid pavements models.

6.1.1.2 PULSE 2020 Application

"PULSE 2020" is used in this research project for the determination of the flexible and rigid pavement layer variables. The latter is an application that consist of several modules, including PULSE_Analyzer, PULSE_FE and optimizer module. It considers the finite element modelling to allow the forward calculation, (Bazi and Assi (2020), Bazi et. al, 2021).

6.1.1.3 R-Studio and R

R-Studio is used to build the optimal model for each seed variable while providing an elaborate statistical analysis. This software is mainly an IDE – Integrated Development Environment – for the "R". Several R-Packages are used in this research project including: "dplyr", "caret", "randomForest" and "neuralnet".

6.1.2 Combinations

The combinations that are used in the study were developed for both the flexible and the rigid pavements (Table 7).

Table 7:Combinations for the Flexible and Rigid Pavement Structures

Pavement Type		Flexible	Rigid
Surface Layer	Thickness	*3 levels:* h_1 (inch) = 3, 6 & 12	*3 levels:* h_1 (inch) = 9, 15 & 21
	Property [Flexible: Linear Viscoelastic & Rigid: Linear Elastic]	*2 levels:* $\delta = 0.5$ & 1	*3 levels:* E_1 (ksi) = 2000, 4000 & 6000
		3 levels: $\delta + \alpha = 3.5$, 3.6 & 3.7	
		3 levels: β' (0, 20 and 40°C) $= \beta + \gamma * \log[a(T)]$ $\log[a(T)] = 3.066$, 0 & -2.674 at 0, 20 and 40°C, respectively	
		2 levels: $\gamma = -0.46$ & -0.51	
	Rayleigh Damping Parameters (PCC Layer)	--	*3 levels:* α_{RPCC} (1/sec.) = 0, 10 & 20
		--	*3 levels:* β_{RPCC} (sec.) = 0.002, 0.004 & 0.006
Base Layer	Thickness	*3 levels:* h_2 (inch) = 6, 12 & 36	
	Property [Linear Elastic]	*3 levels:* E_2 (ksi) = 20, 50 & 200	
Subgrade Layer	Property [Linear Elastic]	*3 levels:* E_3 (ksi) = 5, 15 & 30	
Stiff Layer	Thickness [1) and Property	*7 levels:* None, 10-ft with E_4 = 100 ksi, 10-ft with E_4 = 250 ksi, 20-ft with E_4 = 100 ksi, 20-ft with E_4 = 250 ksi, 50-ft with E_4 = 100 ksi & 50-ft with E_4 = 250 ksi	
Rayleigh Damping Parameters (Base, Subgrade & Stiff Layers)		*3 levels:* α_R (1/sec.) = 0, 10 & 20	
		3 levels: β_R (sec.) = 0.002, 0.004 & 0.006	
FWD Load		*3 levels:* 20, 30 & 40 msec. haversine pulse with the radius of the loaded area = 5.906-inch, and Load level = 27 kips	

1) Stiff layer thickness determined from surface.

In other words, 551,124 combinations are selected for flexible pavements while 413,343 combinations for the rigid pavements for a total of 964,467 combinations.

For each response variable, the most relevant values were selected based on the maximum and minimum values that each variable can take. However, a different strategy was followed to choose the levels needed for the AC master curve sigmoidal coefficients.

6.1.2.1 AC master curve sigmoidal coefficients

The asphalt concrete master curves are mainly constructed through the use of frequency- (or time-) temperature superpositions signified by the shift factors. A master curve connecting the temperature and the load rate can be used to depict their combined effects. This is achieved by relating the dynamic modulus (E*) to the reduced frequency through a sigmoidal function. The latter is expressed by Eq. (129). On the other hand, the most used equations for expressing the temperature shift factor include the WilliamsLandel-Ferry, Arrhenius and the 2nd order polynomial equations (Pellinen et al. 2004, Kutay et al. 2011). It is important to note that the shift factor equation utilized by the LTPP is the polynomial equation Eq. (131) while the one used in this research is the Arrhenius equation Eq. (132).

The E* values provided in the TST_ESTAR_MODULUS LTPP table were estimated using Artificial Neural Network models at several temperatures (14°- 40°- 143°- 70°- 100°- 130°F) and frequencies (0.1- 0.5- 1- 5- 10- 25Hz). The details on the aforementioned estimates are presented in the LTPP Computed Parameter: Dynamic Modulus (Kim, et al. 2011) report. The E* estimates were used by the LTPP teams to compute the master curve sigmoidal function coefficients and the time-temperature shift factors and were stored in the TST_ESTAR_MODULUS_COEFF table.

$$\log(E) = \delta + \frac{\alpha}{1+e^{\beta+\gamma\log(fr)}} \tag{129}$$

$$\log(fr) = \log(f) + \log(a_T) \tag{130}$$

$$\log(a_T) = \alpha_1 T^2 + \alpha_2 T + \alpha_3 \tag{131}$$

$$\log(a_T) = \frac{\Delta E_a}{2.303R}\left(\frac{1}{T} - \frac{1}{To}\right) \tag{132}$$

Whereby,

- δ, α ,β and γ are the coefficients,
- 10^{δ} is the minimum modulus,
- $10^{\delta+\alpha}$ is the maximum modulus,
- fr is the inverse of the loading's reduced angular frequency, f is the frequency,
- α_1, α_2 and α_3 are the shift factor coefficients
- T is the temperature of interest, To is the reference temperature in Kelvin (294.261K in this case)
- ΔE_a is the activation energy, R is the universal gas constant (8.314 J/°K-mol),

The exponent $\beta + \gamma\log(fr)$ in the sigmoidal function presented in Eq. (129) can be also re-written as $\beta' + \gamma\log(f)$ whereby $\beta' = \beta + \gamma\log(a_T)$. This replacement permits the determination of the four sigmoidal function coefficients for any temperature and without considering the time-temperatures superposition models.

In this study and for the flexible pavement modelling, the limits of the master curve sigmoidal function δ, α ,β and γ are determined using tables stored in the LTPP database. The master curve construction and the coefficient computations were performed using the Sum of Squared Error (SSE) method along with solver functions and optimization techniques in the Microsoft Excel software. The main objective in the Sum of Squared Error (SSE) method is to minimize the SSE between the dynamic modulus (E*) and the fitted dynamic modulus. This is achieved by iteratively varying the δ, α ,β,γ, ΔEa, α_1, α_2 and α_3 using the Excel's solver until the SSE between the measured and fitted dynamic modulus becomes closer to zero.

Initially, 40 random sets of coefficients and their corresponding E* estimate values were extracted from the TST_ESTAR_MODULUS_COEFF and TST_ESTAR_MODULUS LTPP tables, respectively, to regenerate those coefficients and check how do they compare. In other words, the sigmoidal function variables (δ, α ,β and γ) and the shift factor coefficients (α_1, α_2 and α_3) were simultaneously computed using the LTPP shift factor Eq (131) on one hand and the Arrhenius shift factor Eq. (132) on the other hand. This was performed in order to determine the shift factor equation that generates the best fit to the measured dynamic modulus master curve. After calculating the coefficients, the percentage error was determined between the computed and the ones stored in the LTPP database for each of the 40 sets. Examples shown below for sets 25 and 37 in Tables 8 and 9, respectively.

Table 8:Sigmoidal Function and Shift Factor Coefficients Comparison (Mix25)

Mix 25							
	δ	α	β	γ	α_1	α_2	α_3
Arrhenius Eq	1.262	2.7894	-0.600	-0.488			
Shift factor Eq	0.886	2.7940	-3.054	-0.470	0.00110	-0.1628	-0.3654
TST_ESTAR_MODULUS_COEFF	4.439	2.241	-1.138	0.484	0.001	-0.1650	3.161
% Error Arrhenius vs. TST Table	-0.47	24.473	-47.24	-200.9			
% Error Shift factors vs. TST Table	-12.4	24.67667	168.3703	-197.1	10.7957	-1.2885	-111.56

Table 9: Sigmoidal Function and Shift Factor Coefficients Comparison (Mix37)

Mix 37							
	δ	α	β	γ	α_1	α_2	α_3
Arrhenius Eq	0.829	2.7286	-0.363	-0.493			
LTPP Shift factor Eq	0.838	2.719	-0.492	-0.494	0.0021	-0.15688	2.9
TST_ESTAR_MODULUS_COEFF	3.97	2.586	-0.32	0.502	0.001	-0.1650	3.161
% Error Arrhenius vs. TST Table	-0.478	5.5179	13.729	-198.32			
% Error Shift factors vs. TST Table	-3.31	5.1653	53.97	-198.459	114.0668	-4.9192	-8.2548

Based on the percentage error outcomes and the fact that the TST_ESTAR_MODULUS_COEFF coefficients were determined from moduli that were in return obtained using ANN methods, the moduli estimates from the TST_ESTAR_MODULUS are considered the most reliable. For this reason, the master curve sigmoidal function coefficients are recalculated by the Arrhenius equation using the moduli stored in the LTPP database for all the mixes. 1,331 unique datasets were identified in the TST_ESTAR_MODULUS, each containing 30 records, for a total of 39,930 data points. This was verified by calculating the count, average, minimum, maximum, difference between the average and the minimum, difference between the maximum and the average for every combination of ESTAR_LINK, temperature and frequency. The average, minimum and maximum turned out to be the same for every combination, verifying, thus, the 1,331 unique datasets. A sample from the 39,930 data points is shown in Table (10) for ESTAR_LINK 1. Note that the ESTAR_LINK variable serves as an associative link between the tables stored in the LTPP database. Each set was further linked to the layer type corresponding to it. The layer types encountered were as follows: (1) Original Surface Layer, (2) AC Layer Below Surface (Binder Course), (3) Overlay, (4) Friction-Course, (5) Seal-Coat, (6) Base Layer. However, the sets corresponding to the base layer type are removed as only asphalt concrete mixes shall be considered for evaluation.

Table 10: ESTAR_LINK 1 Sample Data

Temperature °F	Frequency Hz	Count	Average	Minimum	Maximum	Ave - Min	Max - Ave
14	0.100000001	15	3,060,654	3,060,654	3,060,654	0	0
14	0.5	15	3,399,437	3,399,437	3,399,437	0	0
14	1	15	3,525,000	3,525,000	3,525,000	0	0
14	5	15	3,771,795	3,771,795	3,771,795	0	0
14	10	15	3,860,307	3,860,307	3,860,307	0	0
14	25	15	3,962,665	3,962,665	3,962,665	0	0
40	0.100000001	15	1,503,553	1,503,553	1,503,553	0	0
40	0.5	15	1,976,677	1,976,677	1,976,677	0	0
40	1	15	2,181,177	2,181,177	2,181,177	0	0
40	5	15	2,636,015	2,636,015	2,636,015	0	0
40	10	15	2,817,848	2,817,848	2,817,848	0	0
40	25	15	3,041,535	3,041,535	3,041,535	0	0
70	0.100000001	15	333,509	333,509	333,509	0	0
70	0.5	15	557,515	557,515	557,515	0	0
70	1	15	682,813	682,813	682,813	0	0
70	5	15	1,039,894	1,039,894	1,039,894	0	0
70	10	15	1,218,727	1,218,727	1,218,727	0	0
70	25	15	1,472,424	1,472,424	1,472,424	0	0
100	0.100000001	15	63,670	63,670	63,670	0	0
100	0.5	15	111,374	111,374	111,374	0	0
100	1	15	142,552	142,552	142,552	0	0
100	5	15	251,806	251,806	251,806	0	0
100	10	15	319,282	319,282	319,282	0	0
100	25	15	431,672	431,672	431,672	0	0
130	0.100000001	15	20,565	20,565	20,565	0	0
130	0.5	15	31,576	31,576	31,576	0	0
130	1	15	38,797	38,797	38,797	0	0
130	5	15	65,252	65,252	65,252	0	0
130	10	15	82,779	82,779	82,779	0	0
130	25	15	114,285	114,285	114,285	0	0

Following the master curve sigmoidal coefficients computations, it is essential to identify whether any outlier exist within each set. The datasets were graphically depicted using boxplots based on their individual quartiles. Q_1 and Q_3 represents the 25th and the 75th percentiles, respectively. The interquartile range (IQR) was calculated as the difference between the 75th and 25th percentiles. Lastly, the upper and lower outlier limits were calculated using the following equations:

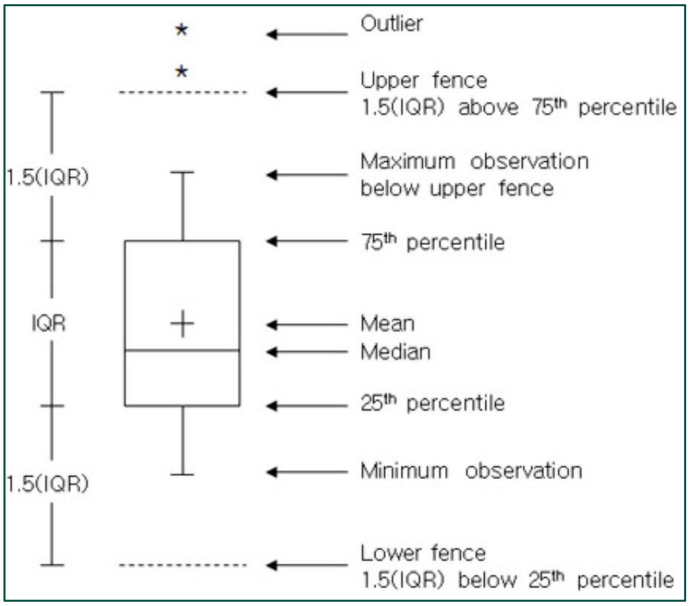

Figure 40: Boxplot Explanation

$$Lower\ Outlier\ Limit = Q_1 - (IQR\ x\ 1.5) \tag{133}$$

$$Upper\ Outlier\ Limit = Q_3 + (IQR\ x\ 1.5) \tag{134}$$

Any data point that fell above or below the upper and lower outlier limit was considered as an outlier. After the first trial, the results (Table 11) with their corresponding boxplots (Figure 41) showed a number of outliers for each coefficient. Hence, sets that contained an outlier were removed. The same process was repeated for several trials until no more outliers were encountered anymore (Table 12, Figure 42).

Table 11: Lower and Upper Outlier Limit- First Trial

	δ	α	β	γ	ΔEa
Mean	1.54597	2.11312	-0.5258	-0.6327	1015116.577
Q1	0.84427	1.30682	-0.9988	-0.6316	131269.968
Q3	2.3317	2.79153	-0.1491	-0.4756	247089.5317
Interquartile Range (IQR)	1.48743	1.48472	0.84966	0.15606	115819.5636
Lower Outlier Limit	-1.3869	-0.9203	-2.2733	-0.8657	-42459.37737
Upper Outlier Limit	4.56285	5.01861	1.12539	-0.2415	420818.8771

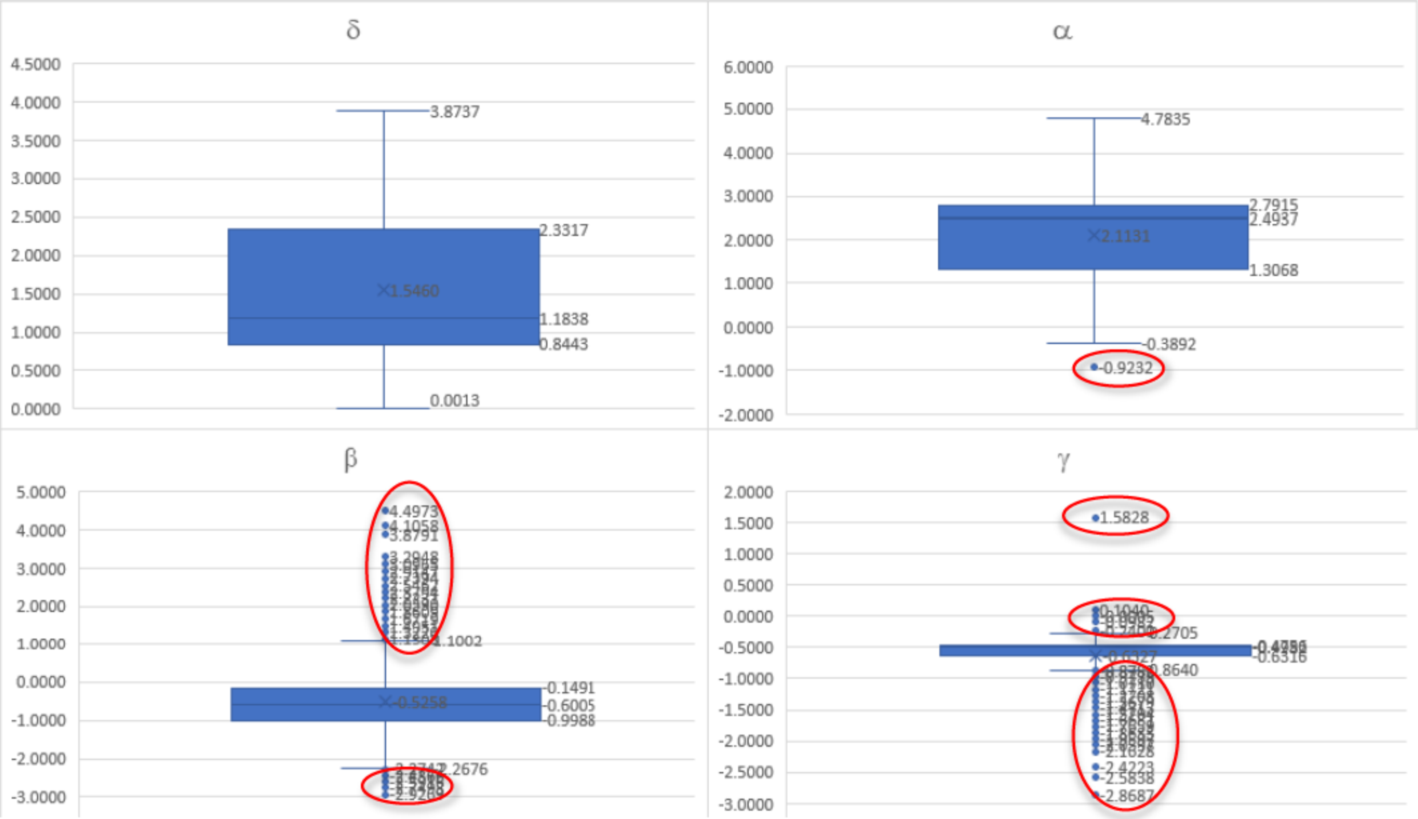

Figure 41: Box Plots for (δ, α ,β and γ) after First Trial

Table 12:Lower and Upper Outlier Limit- Last Trial

	δ	α	β	γ	ΔEa
Mean	0.876692	2.75266	-0.7148	-0.4876	235508.1958
Q1	0.790203	2.65232	-0.8742	-0.4935	235299.7096
Q3	0.957258	2.838	-0.5285	-0.4817	235661.9849
Interquartile Range (IQR)	0.167054	0.18568	0.34564	0.01179	362.2752942
Lower Outlier Limit	0.539622	2.3738	-1.3926	-0.5112	234756.2966
Upper Outlier Limit	1.207839	3.11653	-0.0101	-0.464	236205.3978

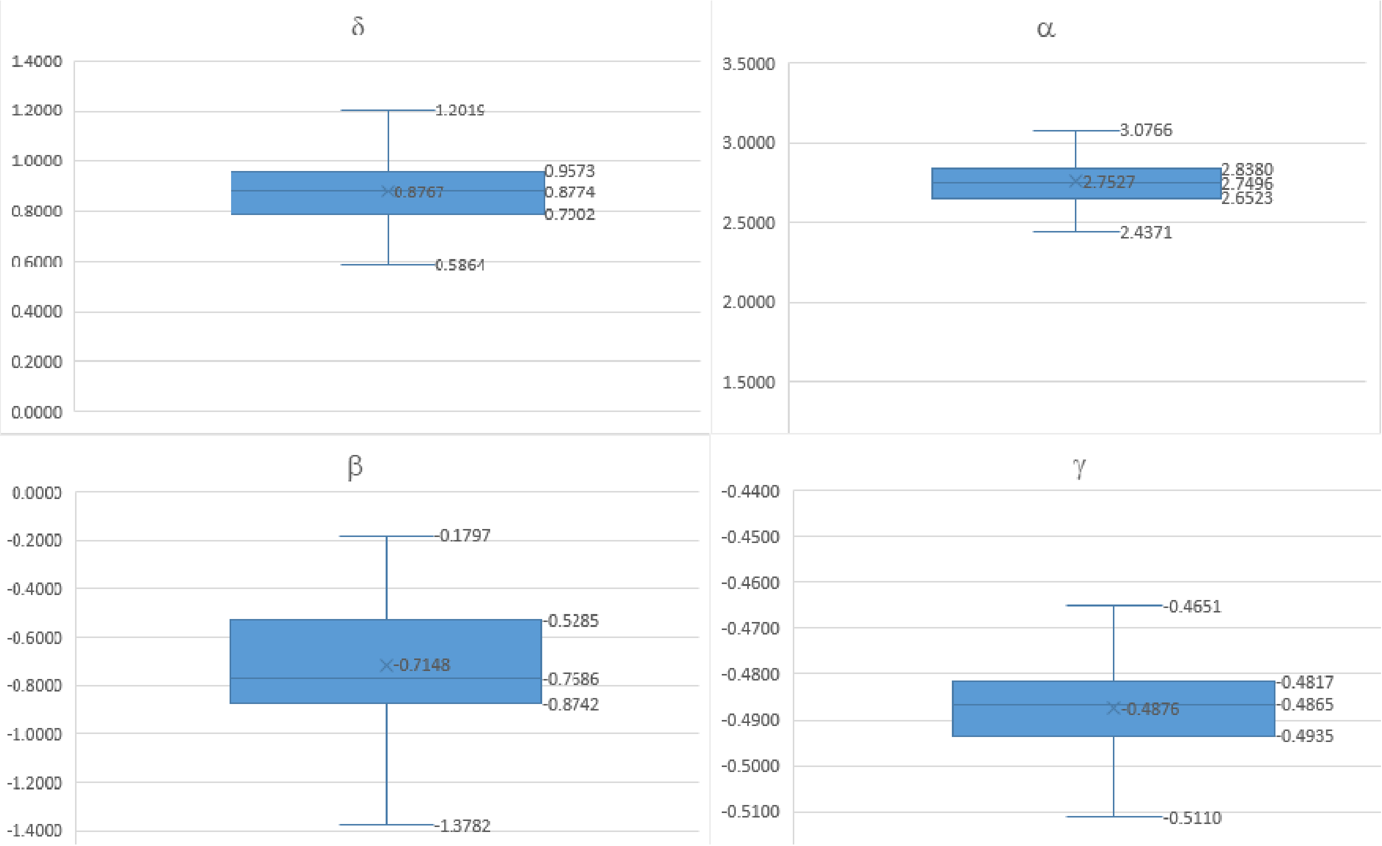

Figure 42: Box Plots for after (δ, α ,β and γ) Last Trial

The number of sets has significantly dropped from 1,331 sets to 344 sets. The standard deviation, maximum, minimum, mean, 16th and 84th percentiles were reported for the 344 sets (Table 13). The sigmoidal coefficients showed minimal variability when compared to the activation energy Ea. It is important to mention that the maximum values of each of the sigmoidal coefficients cannot be selected for the finite element modeling. If the maximum values for Delta and Alpha are taken from the 344 sets to compute the maximum modulus, a modulus value of $10^{1.2019+3.0766}$ = 18,990ksi is obtained which is not realistic as the modulus of steel is 29,000 ksi.

Table 13: Statistics Values for the Sigmoidal Coefficients from the 344 Sets

Statistic	δ	α	β	γ	Ea	$\delta + \alpha$
Mean	0.876692	2.75266	-0.7148	-0.4876	235508	3.6294
Minimum	0.5864	2.4371	-1.3782	-0.5110	234796	3.5375
Maximum	1.2019	3.0766	-0.1797	-0.4651	236205	3.7204
Standard Deviation	0.1289	0.1335	0.2373	0.0091	271.25	0.0417
16th Percentile	0.7478	2.6191	-0.9521	-0.4966	235237	3.5876
84th Percentile	1.0056	2.8862	-0.4775	-0.4785	235779	3.6711

However, calculating the maximum modulus for each of the 344 combinations, the following values (Table 14) are obtained where the average modulus is 4,279 ksi and the maximum is 5,253 ksi (as high as the PCC). For this reason, delta and alpha were combined into one variable for the finite element modeling selection process.

Table 14: Maximum Modulus Values

Statistic	Maximum Modulus (ksi)
Average	4279
Minimum	3448
Maximum	5253

As a result, the sigmoidal coefficients selected for the finite element modeling of the flexible pavement structure are shown in Table 15. This selection generates 12 sets whereby each set was evaluated at 3 temperatures (0, 20 and 40°C), hence, ending with a total of 36 combinations (Table16).

Table 15:Sigmoidal Coefficients Selected for FE Modeling

2 levels: δ =	0.5 & 1.0
3 levels: $\delta + \alpha$ =	3.5, 3.6 & 3.7
3 levels: α =	$(\delta + \alpha) - \alpha$
	Beta = -0.70
3 levels: β' (0, 20 and 40°C) =	Beta + Gamma*log[a(T)] log[a(T)] = 3.066, 0 & -2.674 at 0, 20 and 40°C, respectively
2 levels: γ =	-0.46 &-0.51

The 12 sets (36 combinations) were plotted as illustrated in Figure 43.

Table 16: The 12 Sets Resulting after the Sigmoidal Coefficients' Selection

Set	δ	δ + α	(δ + α) - α	Beta	γ
1	0.5	3.6	3.1	-0.7	-0.51
2	0.5	3.5	3	-0.7	-0.46
3	0.5	3.6	3.1	-0.7	-0.46
4	0.5	3.7	3.2	-0.7	-0.46
5	0.5	3.5	3	-0.7	-0.51
6	0.5	3.7	3.2	-0.7	-0.51
7	1	3.5	2.5	-0.7	-0.46
8	1	3.6	2.6	-0.7	-0.46
9	1	3.7	2.7	-0.7	-0.46
10	1	3.5	2.5	-0.7	-0.51
11	1	3.6	2.6	-0.7	-0.51
12	1	3.7	2.7	-0.7	-0.51

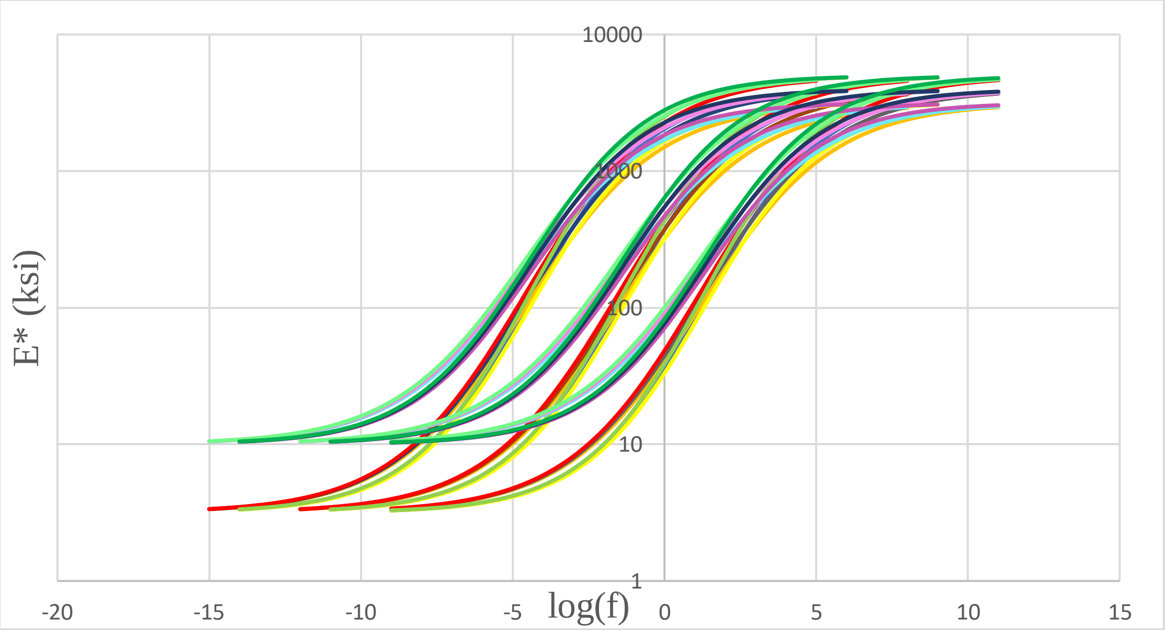

Figure 43: Master Curve showing the 12 Sets, each at 3 Temperatures

Consequently, the levels (classes) of the AC master curve sigmoidal coefficients used in this research project are shown in Table 17.

Table 17: AC Master Curve Sigmoidal Coefficients Classes

Seed Variable	Class 1	Class 2	Class 3	Class 4	Class 5	Class 6
Alpha (α)	2.5	2.6	2.7	3	3.1	3.2
Beta_prime (β')	-2.263	-2.1101	-0.7	0.53001	0.6637	-
Delta (δ)	0.5	1	-	-	-	-
Gamma (γ)	-0.51	-0.46	-	-	-	-

6.2 Model Development and Optimal Mesh Selection

The initial step in the finite element computations is to discretize the domain of the problem into a set of elements that could either be of the same or different types. In this study, only linear triangular elements are used. Analyzing the mesh density (size of the finite element) is considered as a critical task in the finite element computations as it leads to the selection of the optimal model. In other words, the accuracy, the precision as well as the complexity level of the finite element model are directly related to the mesh density (Liu, Y., & Glass, G. 2013). The finite element models having a small sized elements (fine mesh) will generate vastly accurate output yet it will have a longer computational time and will increase the complexity of the model. Hence, it is preferably to be used only when high precision and accuracy are needed. On the other hand, models having a large sized elements (coarse mesh) may end up with less likely accurate results but it will surely save much more computational time and will reduce the size of the model under study. Hence, it is rather substantially used in more simplified FE models to provide a rough and a fast design estimation (Liu, Y., & Glass, G. 2013). For this reason, it is essential to select the most optimal model with the element sizes that are capable of providing accurate results while at the same time saving computational time as much as possible.

The mesh of the flexible and rigid pavement models is generated using a Gmsh software. In order to simulate the infinite media in this research, the far boundary was chosen.

The main objective is to obtain one mesh that is applicable for all the combinations previously discussed. As the thicknesses of the combinations are in order of 3-inches, the model was developed on Gmsh by having the first 57-inch in increments of 3-inch followed by the 10/20-ft rigid layer as shown in Figure 44. As a result, a total of 23 surfaces were drawn in Gmsh to model the pavement structure along with the subgrade layer and a stiff layer if any. Hence, once the model is discretized into an infinite number of elements, the element limits separating one surface from another can be determined to be used later on when generating the vertical deflection for each combination.

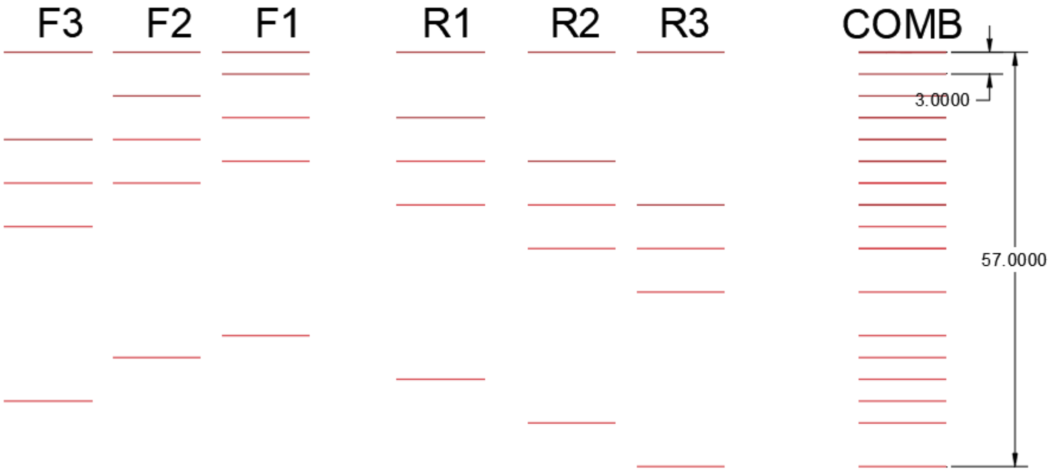

Figure 44: Model Development Initial Steps on AUTOCAD

Figure 45 represents a flexible pavement structure that consist of an asphalt concrete (AC) surface layer of 3-inch thickness, an aggregate base of 6-inch thickness and lastly a subgrade layer that expands to 3000-inch (250- ft) for the infinite media simulation employing the far boundary method. The optimal model, in terms of the accuracy and the mesh density, was generated by performing a sensitivity analysis by testing the pavement model without and with a rigid layer (Testing No.1 and testing No.2 respectively) while checking the validity of the optimal mesh.

Table 18: Combinations used for Sensitivity Analysis

	Surface Layer		**Base Layer**		**Subgrade Layer**		**Rigid Layer**	
Testing No.	Thickness (in)	Modulus (ksi)	Thickness (in)	Modulus (ksi)	Thickness (in)	Modulus (ksi)	Thickness from Surface (ft)	Modulus (ksi)
1	3	500	6	50	-	5	None	
2	3	500	6	50	111	5	10	100

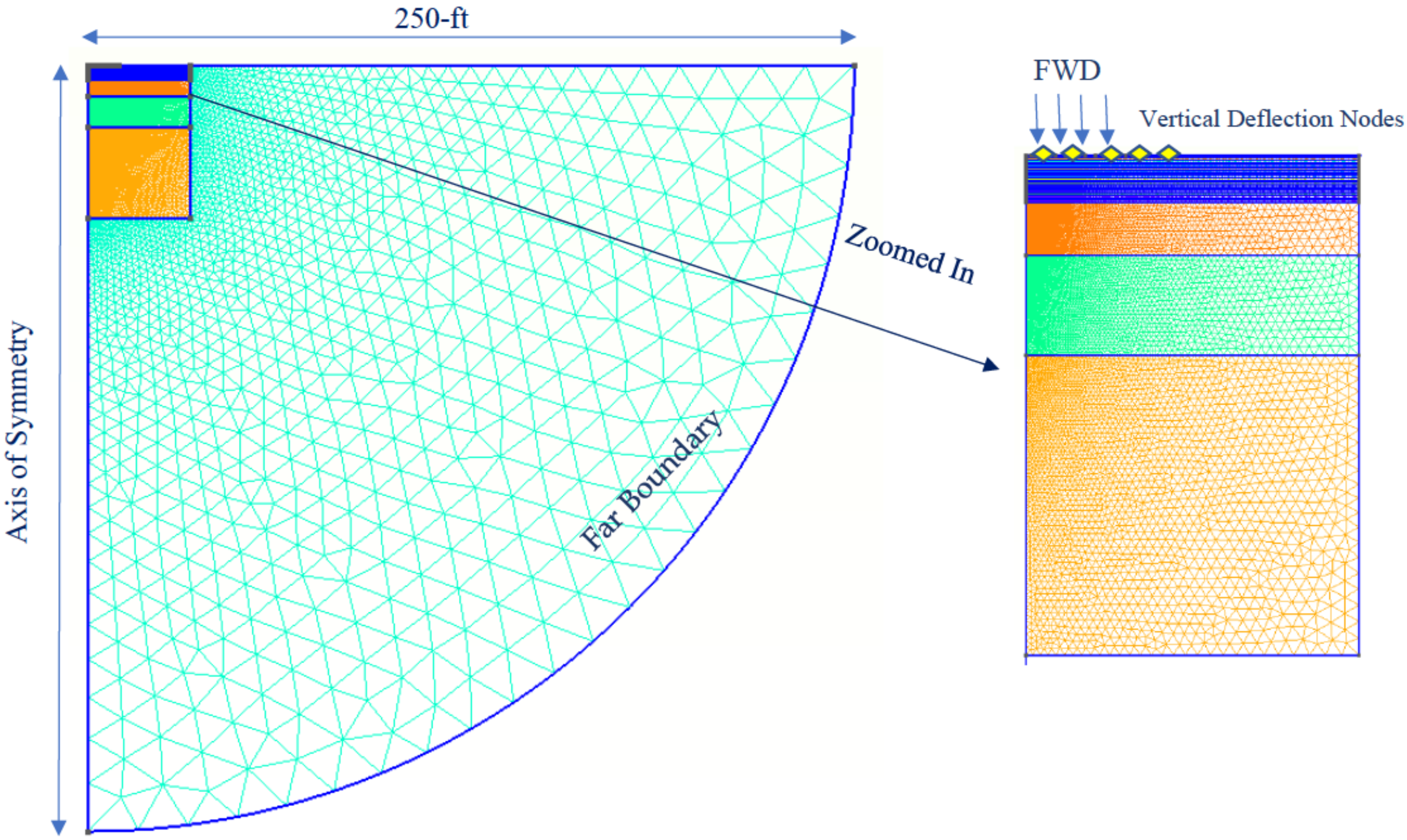

Figure 45 : Optimal Model Generation by Gmsh

The scale of the mesh was determined by Eq. (135). It was varied after each iteration by varying the values of “a”, “b” and “c” and was tested for a pavement width of 200- and 400-inches.

$$Scale = aR^{b} + cZ^{b} + 0.5 \tag{135}$$

Whereby, R and Z correspond to the radial and the vertical distances, respectively, for each point/ coordinate used while drawing the model, “a” and “c” correspond to the R- and Z-coefficients respectively, “b” is the power.

Following the meshing of the model under study, an input file is produced and is manually adjusted into the correct format prior to its utilization by PULSE_FE. The latter is a finite element module programmed using the (C#) language (Bazi and Bou Assi 2020a). PULSE_FE reads, from the input file, the coordinates of every node and the connectivity of each element to (1) initiate the dynamic process and (2) produce the vertical deflections on the specified nodes that are located at a certain offset from the center. A series of finite element models (different mesh sizes) were generated to the previously mentioned model.

The parameters for the various meshes are plotted versus the mesh density to visualize the variations. To determine the optimal mesh, the coarsest mesh must be chosen whereby the FWD parameters would not change if a finer mesh is selected. In other words, the minimum deflection and the time that corresponds to that minimum were extracted from the time histories and compared separately for offsets 0, 24-inches, 48-inches, and 72-inches from the center (Figures 46,48,50,52). Moreover, the percentage difference in deflection relative to the densest mesh (143,947 elements) was determined (Figures 47,49,51,53). It is observed in latter that the finite element model with a mesh of 15,233 elements to have the least percentage error when compared to the densest mesh (between ~0.0003 and 0.0007% difference i.e., 0.0186% ~ 0.074% error). For this reason, this finite element mesh was tested versus the denser (finer) meshes for the same structure but with a 10-ft rigid layer measured from the surface (Testing No.2 -Table 18) to check the validity of the 15,233 elements. According to Liu, Y., & Glass, G. (2013), an acceptable error can range between 0.5% and 1%. It was noticed that the percentage error relative to the densest mesh started to increase as the offset from the center increases to reach 27.64% at offset 120-inch. As a result, the model with 15,233 elements was eliminated and replaced by a mesh with 25,383 elements which resulted in an acceptable percentage error (Table 19).

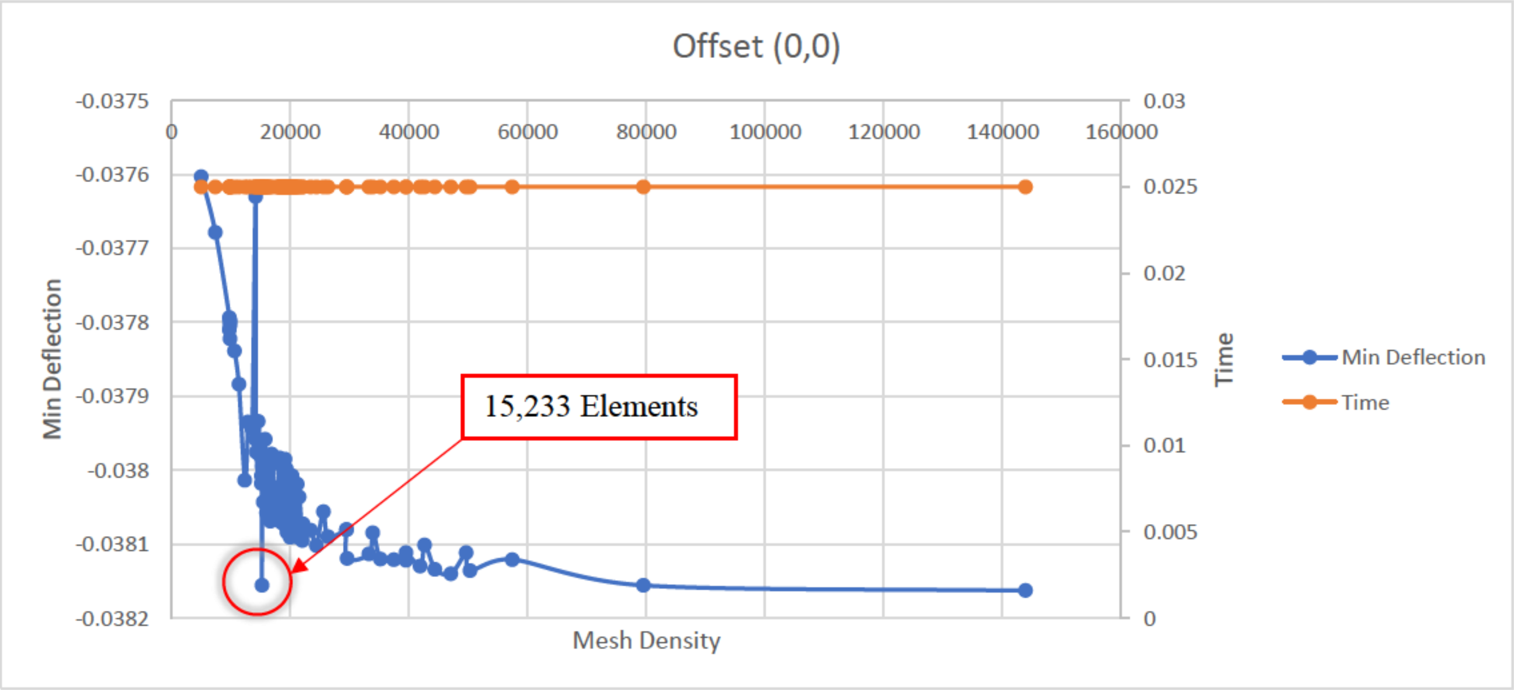

Figure 46: Finite Element Sensitivity Analysis at Offset (0,0)

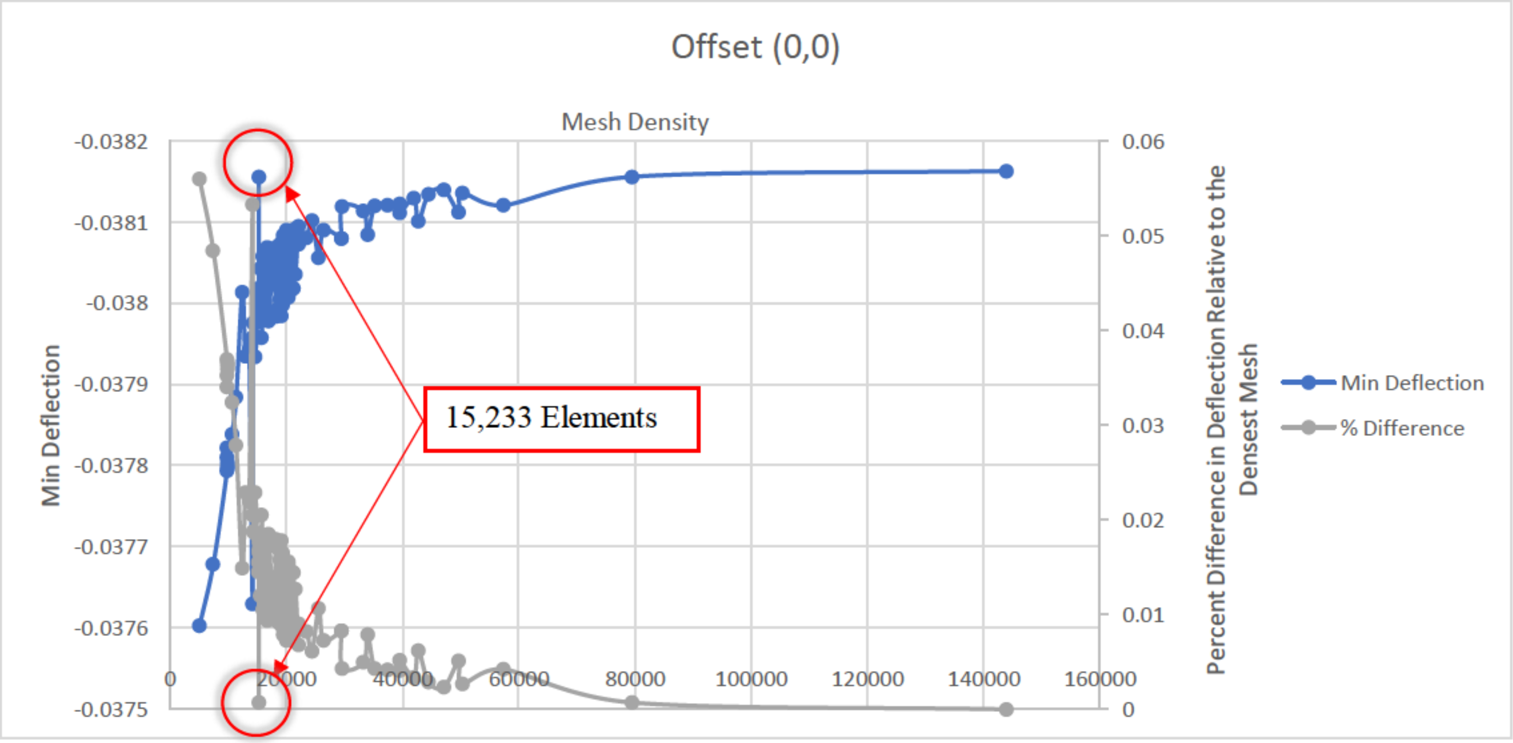

Figure 47: Percent Difference in Deflection Relative to the Densest Mesh at Offset (0,0)

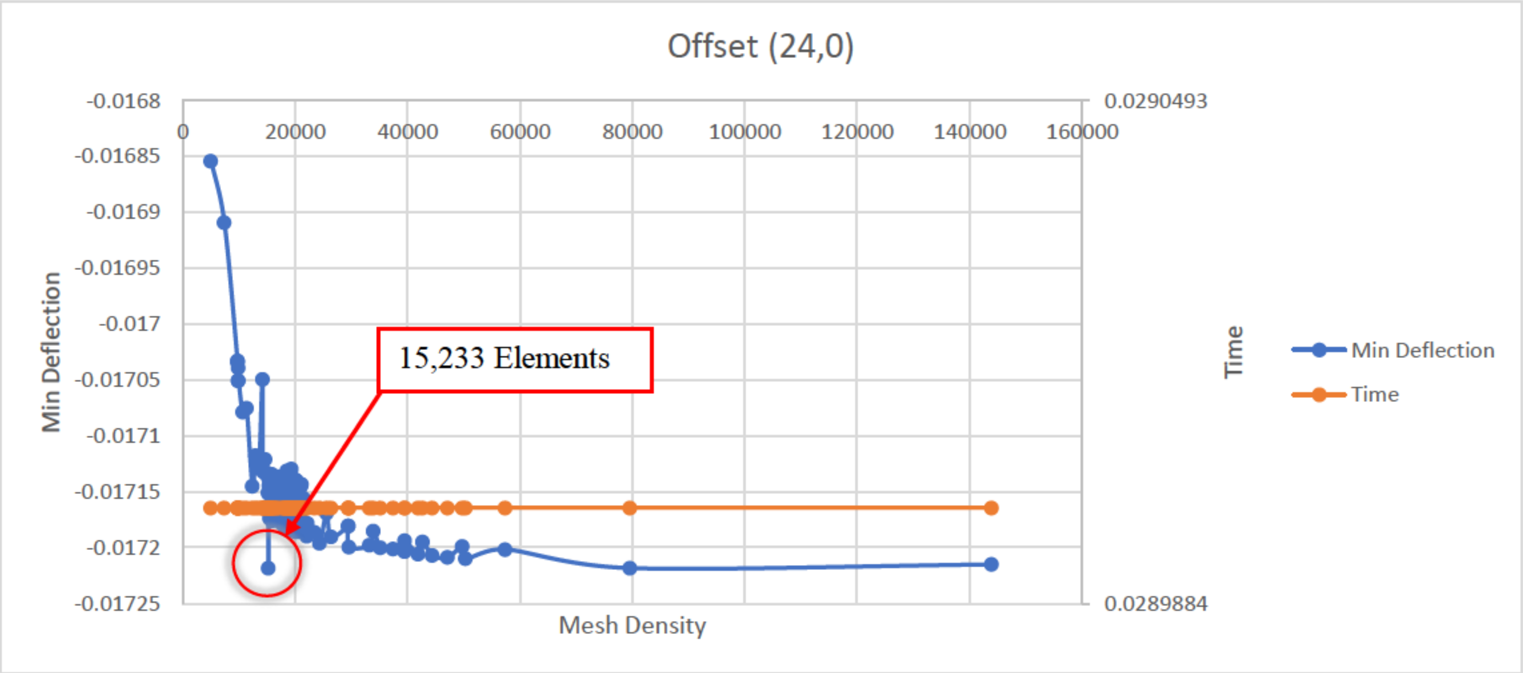

Figure 48: Finite Element Sensitivity Analysis at Offset (24,0)

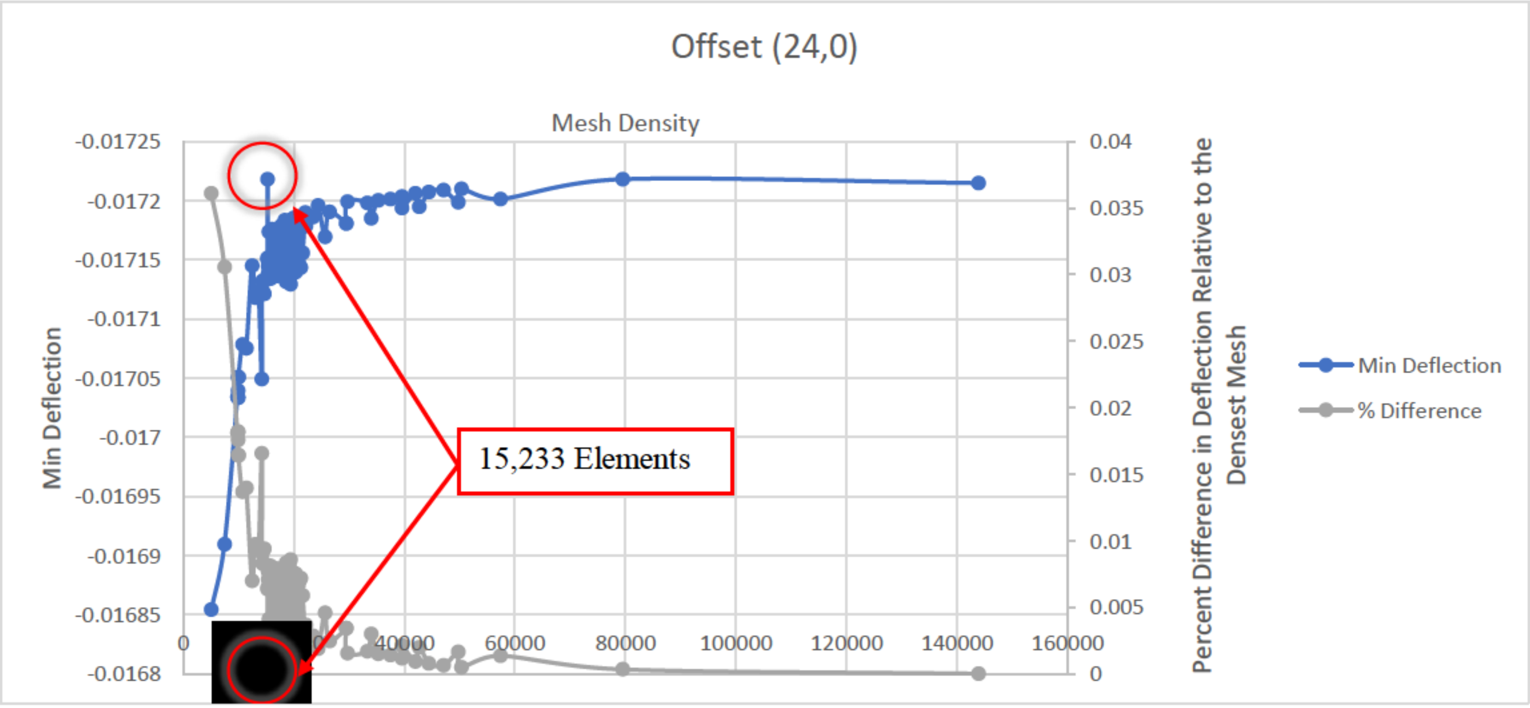

Figure 49 : Percent Difference in Deflection Relative to the Densest Mesh at Offset (24,0)

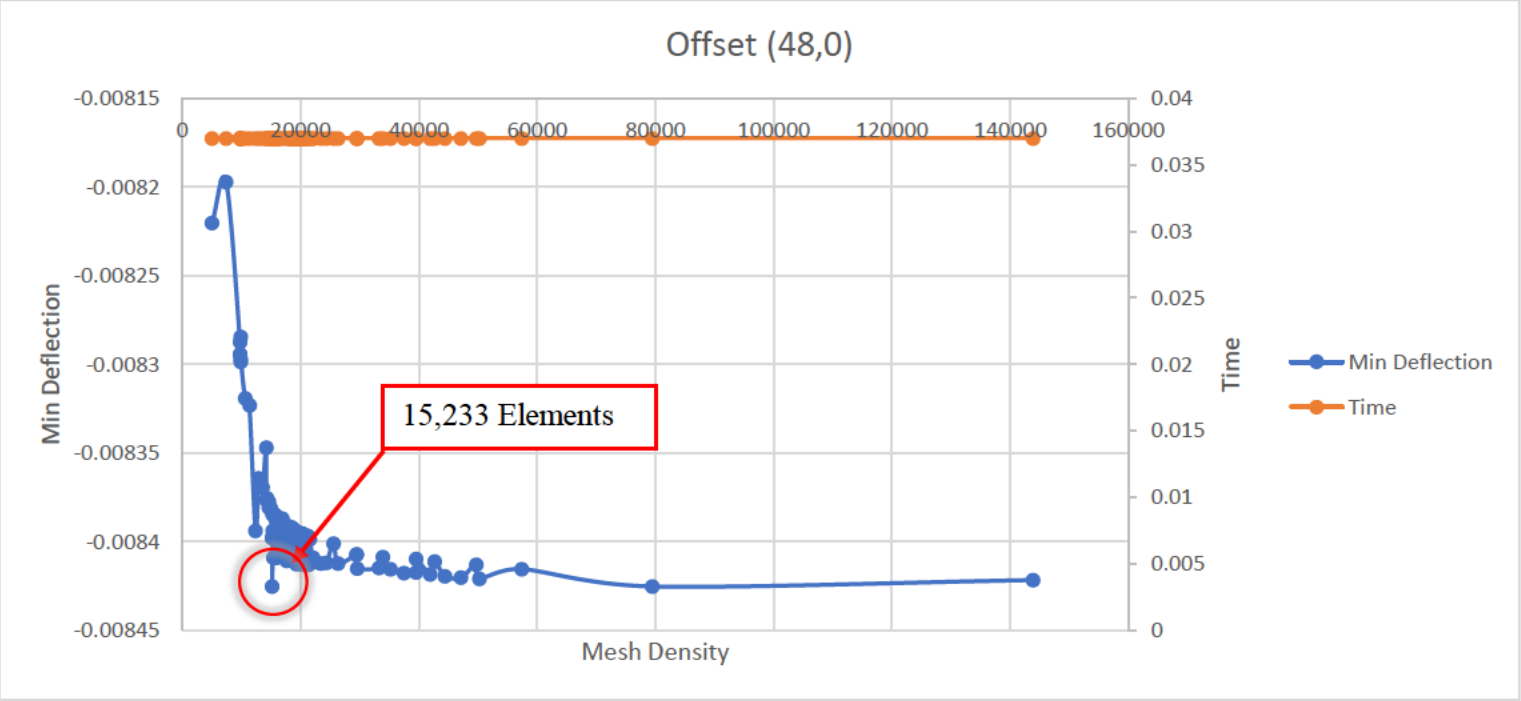

Figure 50 : Finite Element Sensitivity Analysis at Offset (48,0)

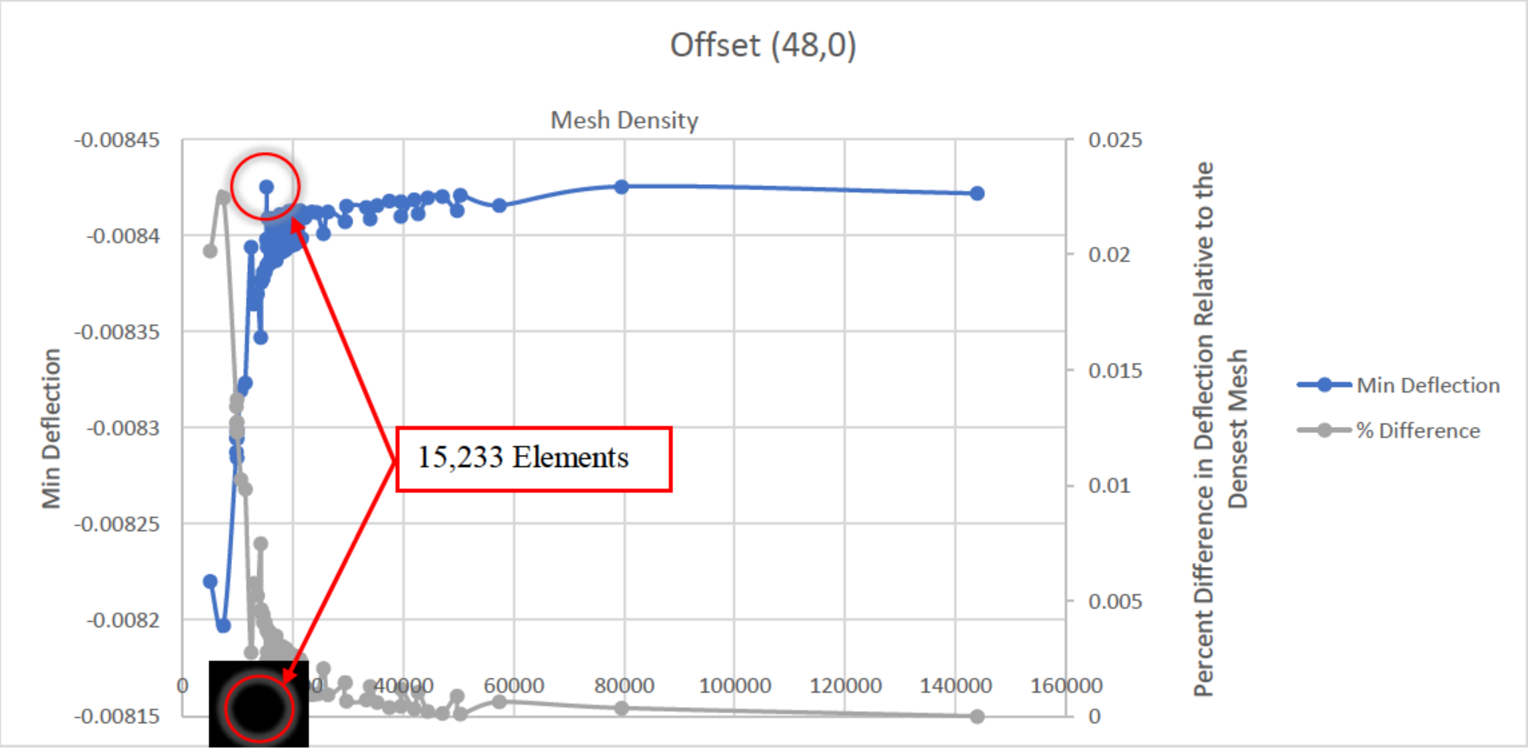

Figure 51: Percent Difference in Deflection Relative to the Densest Mesh at Offset (48,0)

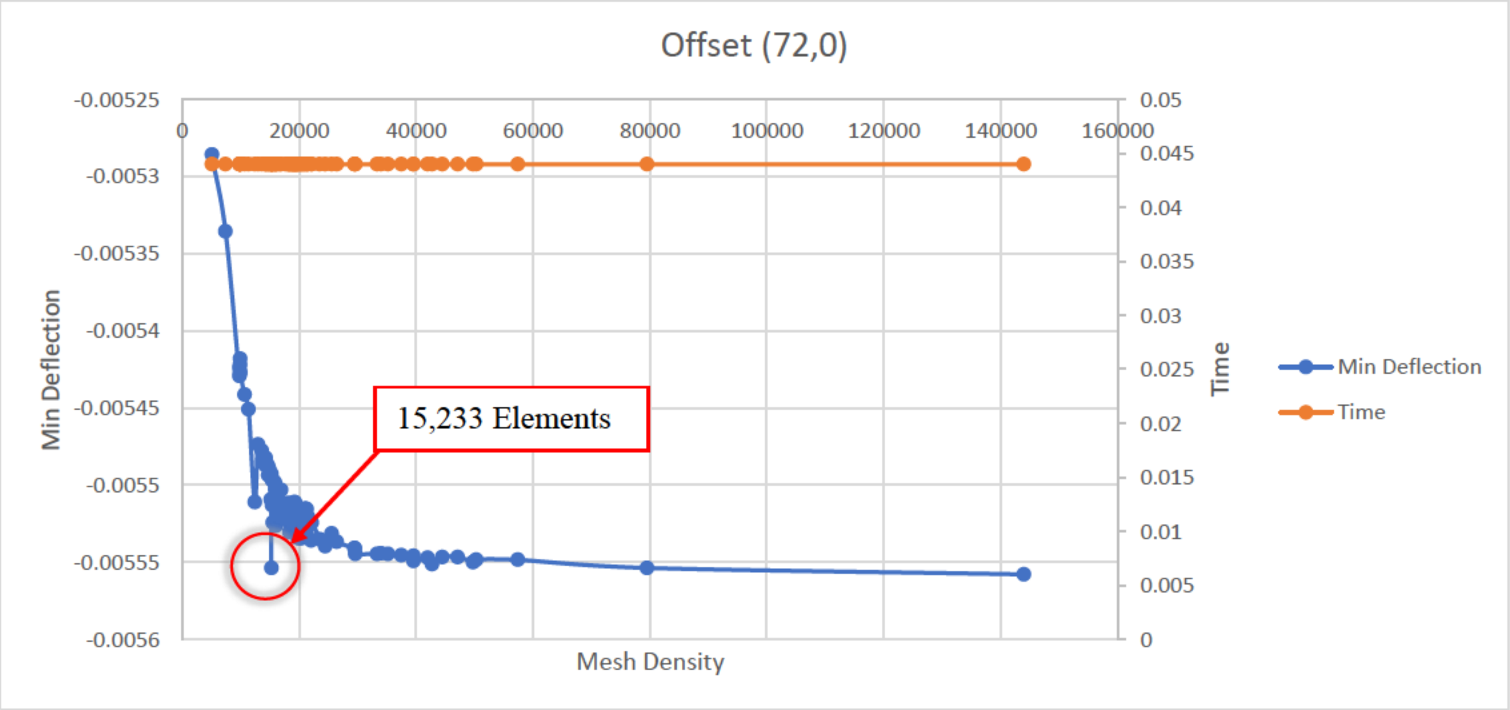
Offset (72,0)

15,233 Elements

Figure 52: Finite Element Sensitivity Analysis at Offset (72,0)

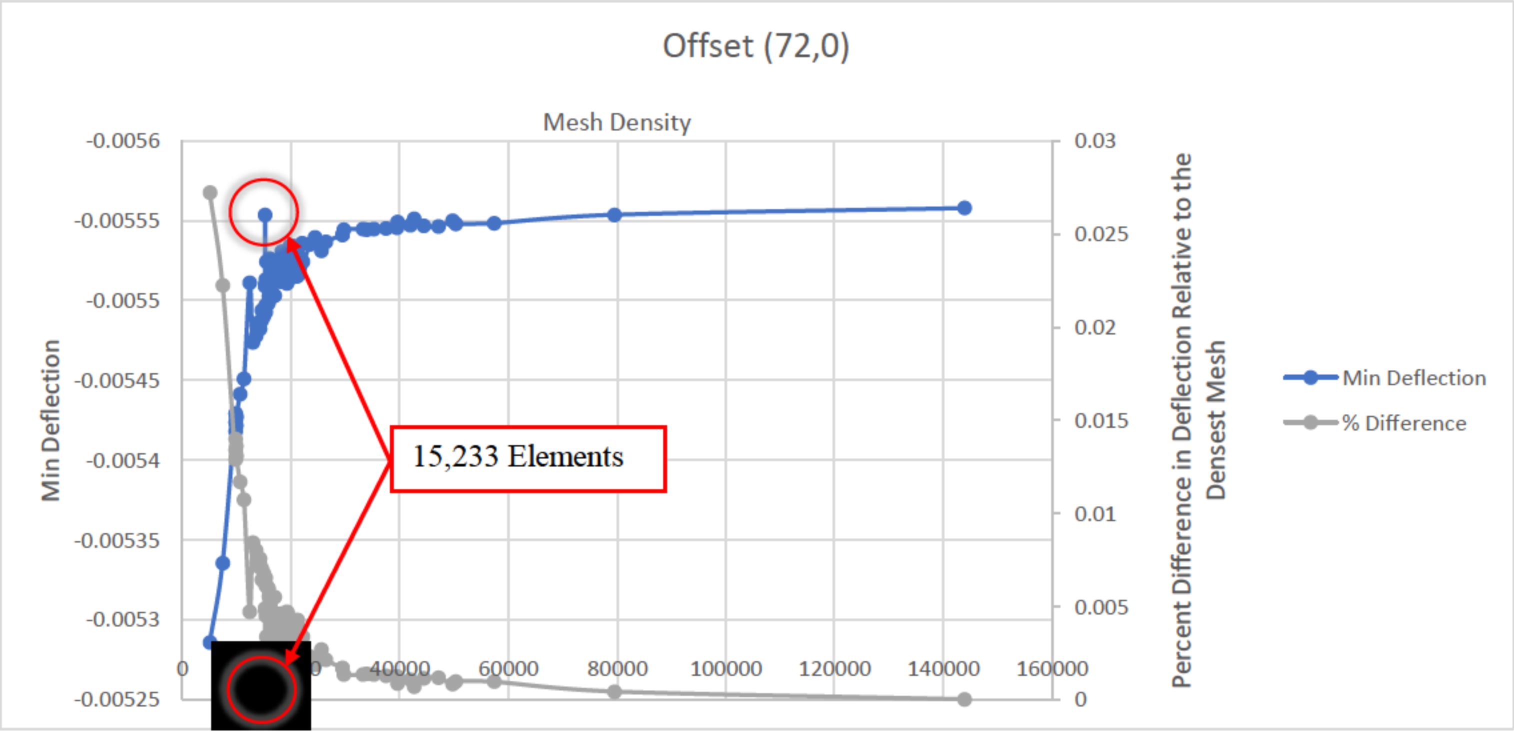
Offset (72,0)

15,233 Elements

Figure 53: Percent Difference in Deflection Relative to the Densest Mesh at Offset (72,0)

Table 19:Percentage Error in Minimum Deflection Relative to Densest Mesh

	Min Deflection at Offsets (inch)					
Mesh Density	**0**	**24**	**48**	**72**	**96**	**120**
25,383	-0.1085	-0.04619	-0.02103	-0.0119	-0.00756	-0.005412
143,947	-0.1088	-0.04635	-0.0211	-0.012	-0.00766	-0.005500
	Absolute Percentage Error (%)					
	0.2875	0.335	0.3690	0.6659	1.2433	1.6032

The finite element model with a mesh of 25,383 elements was tested using different combinations along with the finest mesh (143,947 elements):

- Thick flexible pavement with and without rigid layer
- Thin rigid pavement with and without rigid layer
- Thick rigid pavement with and without rigid layer’

Whereby the thickness of the rigid layer is measured from the surface in ft.

The average error from offsets 0 till 72-inches was calculated for the different combinations tested. It was observed that the last combination in Table 20 is the critical one as the error exceeded 1%; thus, the model is optimized to a mesh of 29,462 elements that was optimal to all combinations with an error less than 1% (Table 21).

Table 20: Testing 25,383 Elements using Different Combinations

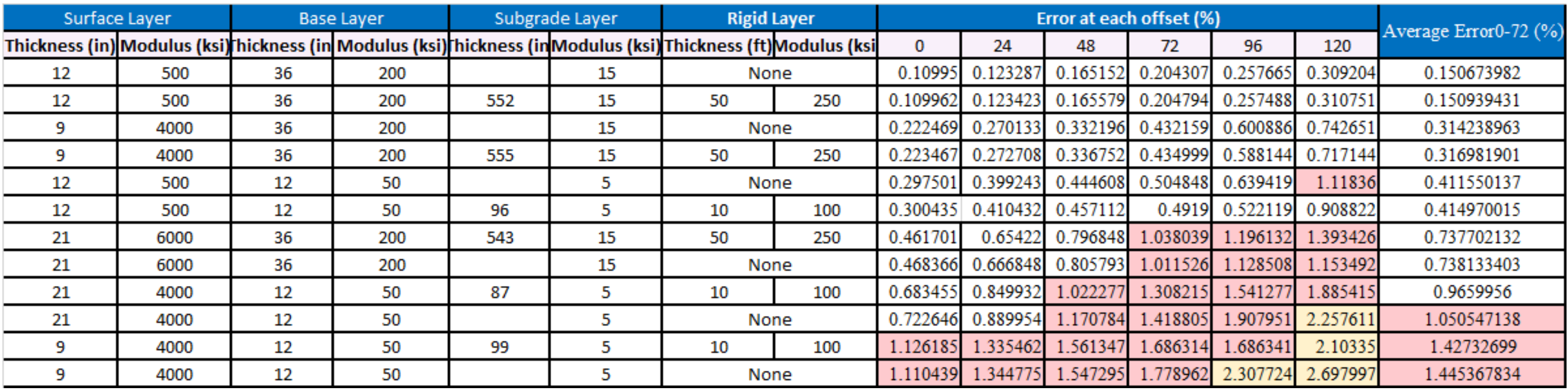

Surface Layer		Base Layer		Subgrade Layer		Rigid Layer		Error at each offset (%)						Average Error0-72 (%)
Thickness (in)	Modulus (ksi)	Thickness (in	Modulus (ksi)	Thickness (in	Modulus (ksi)	Thickness (ft)	Modulus (ksi	0	24	48	72	96	120	
12	500	36	200		15	None		0.10995	0.123287	0.165152	0.204307	0.257665	0.309204	0.150673982
12	500	36	200	552	15	50	250	0.109962	0.123423	0.165579	0.204794	0.257488	0.310751	0.150939431
9	4000	36	200		15	None		0.222469	0.270133	0.332196	0.432159	0.600886	0.742651	0.314238963
9	4000	36	200	555	15	50	250	0.223467	0.272708	0.336752	0.434999	0.588144	0.717144	0.316981901
12	500	12	50		5	None		0.297501	0.399243	0.444608	0.504848	0.639419	1.11836	0.411550137
12	500	12	50	96	5	10	100	0.300435	0.410432	0.457112	0.4919	0.522119	0.908822	0.414970015
21	6000	36	200	543	15	50	250	0.461701	0.65422	0.796848	1.038039	1.196132	1.393426	0.737702132
21	6000	36	200		15	None		0.468366	0.666848	0.805793	1.011526	1.128508	1.153492	0.738133403
21	4000	12	50	87	5	10	100	0.683455	0.849932	1.022277	1.308215	1.541277	1.885415	0.9659956
21	4000	12	50		5	None		0.722646	0.889954	1.170784	1.418805	1.907951	2.257611	1.050547138
9	4000	12	50	99	5	10	100	1.126185	1.335462	1.561347	1.686314	1.686341	2.10335	1.42732699
9	4000	12	50		5	None		1.110439	1.344775	1.547295	1.778962	2.307724	2.697997	1.445367834

Table 21: Testing the Optimal Mesh with 29,462 Elements

Surface Layer		Base Layer		Subgrade Layer		Rigid Layer		Error at each offset (%)					
Thickness (in)	Modulus (ksi)	Thickness (in)	Modulus (ksi)	Thickness (in)	Modulus (ksi)	Thickness (ft)	Modulus (ksi)	0	24	48	72	96	120
3	500	6	50	111	5	10	100	0.232828	0.23754	0.266557	0.463243	0.881187	1.151795
6	500	12	50	102	5	10	100	0.208468	0.276338	0.28891	0.316028	0.644906	0.886876
12	500	12	50		5	None		0.241698	0.341305	0.38667	0.425092	0.535299	0.683646
12	500	12	50	96	5	10	100	0.244104	0.350745	0.398426	0.409597	0.465223	0.568922
9	4000	12	50		5	None		0.569306	0.709681	0.884319	1.080694	1.257068	1.455507
9	4000	12	50	99	5	10	100	0.578638	0.702285	0.881535	1.01754	0.958107	1.057919
21	4000	12	50		5	None		0.501349	0.609475	0.79317	0.957519	1.34499	1.652822
21	4000	12	50	87	5	10	100	0.483856	0.593377	0.702627	0.89899	1.045011	1.319433
12	500	36	200		15	None		0.082476	0.098137	0.124135	0.145719	0.182654	0.227707
12	500	36	200	552	15	50	250	0.082493	0.098259	0.124383	0.14578	0.18194	0.229507
9	4000	36	200		15	None		0.139708	0.160556	0.194124	0.263004	0.386288	0.517898
9	4000	36	200	555	15	50	250	0.140417	0.162389	0.197454	0.265489	0.378578	0.501085
21	6000	36	200		15	None		0.322365	0.456508	0.554254	0.706467	0.811063	0.861707
21	6000	36	200	543	15	50	250	0.31821	0.448421	0.548811	0.725954	0.851998	1.022198

6.3 Output Generation for Rigid and Flexible Pavement Structures

Following the optimal mesh selection, the input file generated by Gmsh, which contains the nodes and the 29,462 elements, is read by Pulse_FE.

For the rigid pavement structure, several inputs are required to initiate the run including the Layer properties (Modulus, Rayleigh Damping Parameters), elements for each layer from the FE model as well as the nodes sets for the far boundary, axis of symmetry and the surface loading. The same applies for the flexible pavement structure, however, the AC master curve sigmoidal coefficient “Delta (δ)”, “Gamma (γ)”, $\delta + \alpha$ and the temperature are inputs instead of the surface layer modulus of elasticity.

The code generates a CSV file that contains the vertical deflections at specified offsets for each combination. For one combination, the surface deflections obtained were further tested to ensure correct values. After verification, the surface deflections are generated for the rigid and the flexible pavement structures, i.e., surface deflections for the 413,343 rigid pavement combinations and 551,124 flexible combinations.

For a mesh of 29,462 elements, the time taken to run each combination on Visual Studio was ranging between 7 to 9 seconds including the build time. Therefore, to speed up the process, the code for the rigid combinations was run on four different computers while that for the flexible combinations was run on five different computers simultaneously (Tables 22 and 23). For example, and for the rigid pavement, computer 1 was responsible for the all the combinations excluding the ones with a stiff layer (59,049 combinations). On the other hand, each of computers 2, 3 and 4 were responsible for running the combinations with a stiff layer and layer 1 thickness of 9-inches, 15-inches and 21-inches respectively (118,098 combination each). The same logic applies to the distribution of the combinations for the flexible pavement.

Table 22: Distribution of the Rigid Pavement Combinations

Computer	From	To	Count
1	1	59,049	59,049
2	59,050	177,147	118,098
3	177,148	295,245	118,098
4	295,246	413,343	118,098
Sum			**413,343**

Table 23: Distribution of the Flexible Pavement Combinations

Computer	From	To	Count
1	1	78,732	78,732
2	78,733	183,708	104,976
3	183,709	288,684	104,976
4	288,685	393,660	104,976
5	393,661	551,124	157,464
Sum			**551,124**

6.4 Extracting FWD Parameters

The PULSE_Analyzer module is used to determine the FWD parameters for use in the statistical and classification analysis. The PULSE_Analyzer module has two components that smoothens the data through Local regression and extracts the FWD parameters. In other words, it considers polynomial fittings to smoothen the deflections.

After running the PULSE_Analyzer, the following FWD parameters are obtained whereby an **"_D"** denotes a discrete value. If a value is not available, a double.NaN is reported.

TPeak_D, DPeak_D, TDminL_D, DminL_D, TDminR_D, DminR_D, T25L_D, T50L_D, T75L_D, T25R_D, T50R_D, T75R_D, Dur25_D, Dur50_D, Dur75_D, TVPeak_D, VPeak_D, TVPeak, VPeak, TVminR_D, VminR_D, TVminR, VminR.

The FWD surface deflection time histories for combination R036109 under the FWD load and at an offset of 8-inches far from the load are illustrated respectively in Figures 54 and 55. The properties of each layer within the pavement structure for combination R036109 is shown in Table 24.

Table 24: Layer Properties for Combination R036109

h_1 (in)	h_2 (in)	E_1 (ksi)	E_2 (ksi)	E_3 (ksi)	α_{RPCC}	β_{RPCC}	α_R	β_R	FWD Pulse Duration (msec)
15	36	4000	50	15	10	0.006	10	0.002	20

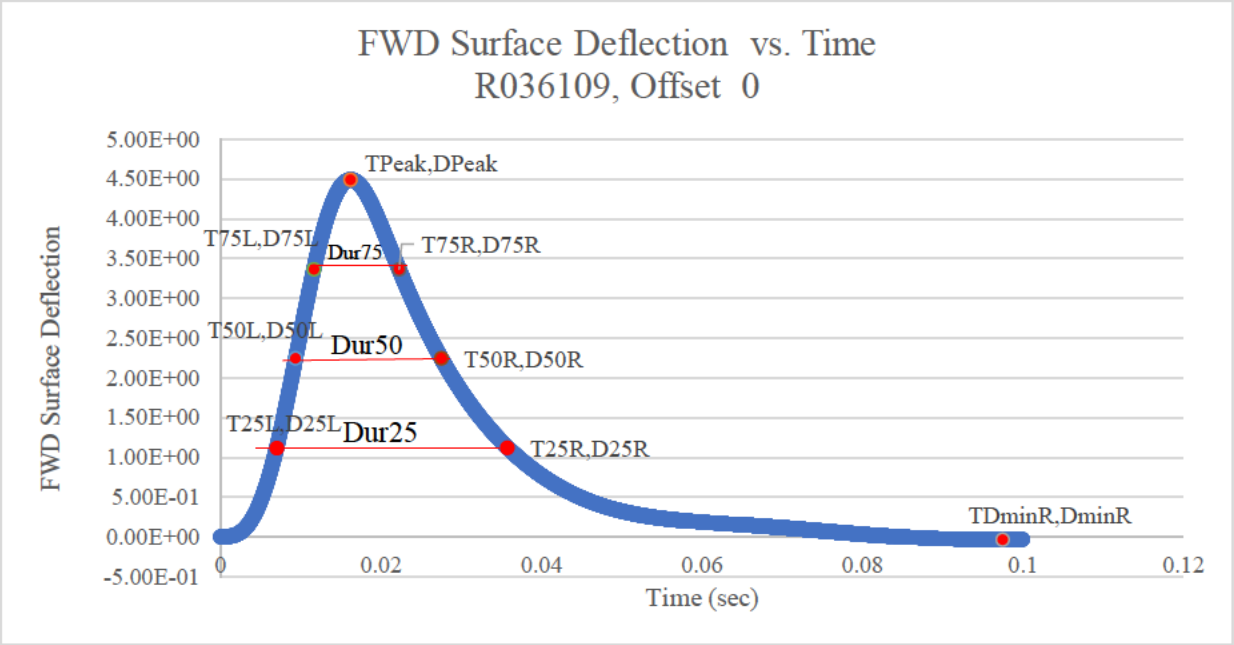

Figure 54: FWD Surface Deflection Time Histories for Combination R036109 under the FWD Load

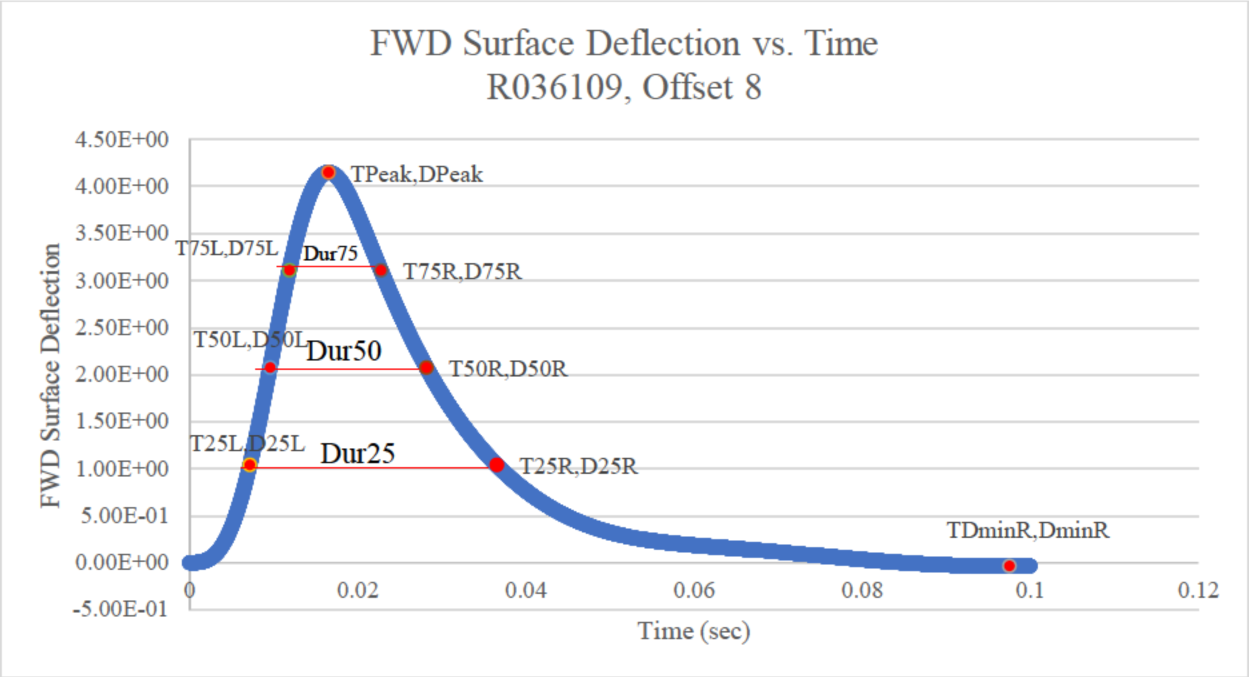

Figure 55: FWD Surface Deflection Time Histories for Combination R036109 at Offset 8-inches

After extracting the FWD parameters, the FWD Indices and the Difference Variables discussed in Chapter 4 are calculated in Microsoft Excel.

6.5 Initial Steps: Building Neural Networks and Decision Trees through Regression Analysis

After extracting the FWD parameters using Pulse_Analyzer, calculating the FWD indices and the difference parameters to serve as predictor variables, the data was combined in a CSV file and brought into R as a structured data frame. The data was then divided into training and testing sets which constitute a randomly selected 60% and 40% of the whole data, respectively. The input was received by the neural network's first layer to process it and pass the information to the hidden layers and the final layers to generate the output. It is important to mention that the neural network was fit to the data using the "neuralnet" package in R-studio. The testing set is further run through the block box (the neural network previously generated) to predict values for each of the response variables. A vector of predictions was then generated. In order to assess the predictions, the RSME values are then calculated to compare the actual vs. predicted values. The same process is repeated by building a new NN model through tuning the hidden layers and the nodes in those layers, and/or selecting better predictor variables. Following the same strategy, and using the “evtree” package in R, Decision Trees were modeled for each response variable.

The outcomes from both models were not promising, thus a classification model was considered instead of a regression model.

6.6 Building Random Forests through Classification Analysis

Since the Radom Forests are mainly considered to be more powerful and effective in the classification when compared to the regression, the RF algorithm is adopted in this research project. To achieve the goal of this research, the R-package “randomForest” was used. After bringing the data into R, the seed (response) variables, including (h_3), (E_1), (E_2), (E_3), (E_4), the Rayleigh Damping Parameters (α_{RPCC}) and (β_{RPCC}) of the PCC layer, the Rayleigh Damping Parameters (α_R) and (β_R) of the unbound layers and lastly the sigmoidal coefficients: alpha (α), Beta_prime (β'), Delta (δ), Gamma (γ) were converted to factors. For each response variable, the candidate predictor variables were selected to create a vector with the names of the variables desired for the model. Then, the reference vector with the predictor and the response variables was setup to pull a subset of the data for use in the model. The data, in this case, was then divided into training and testing sets which constitute a randomly selected 65% and 35% of the whole data, respectively. A Random Forest model is built for each response variables using the optimal number of trees and the default splitting value. The variable importance is then examined and stored as data frame, while being ordered based on the MDA accuracy. The variable importance is further plotted for visual representation of the response variables. The quality of the model was assessed using the testing dataset by evaluating the MDA and MDG measures for each variable. In other words, variables with higher importance were selected for building a new Random Forest model. The variable selection process consisted of the following steps:

1. Run the RF algorithm and record the MDA and MDG values for each predictor variable.
2. Rank the predictor variables based on the MDA accuracy.
3. Assign a score for each predictor variable depending on the MDA and MDG values. For efficient scoring, the MDA and MDG values were scaled and rounded up. Thus, each predictor variable will have two individual scores, one for each measure.
4. The total score is computed for each predictor variable and sorted in descending order.
5. The first fifty percent of the variables with the highest scores are selected for building a new model. If a decimal value was obtained, then the number is rounded up.

6. The RF algorithm is run again using the newly selected variables, and the error rate for the new model is then recorded.

Note that step 5 may be adjusted depending on the accuracy and the error rate obtained. For example, if an accuracy of 100% was obtained for a certain model, and for the variables that have the same total score, the variable that has a lower importance based on the MDA score is excluded. The aforementioned procedure is iteratively implemented until achieving an acceptable accuracy and error rate. In other words, the same process was repeated for several iteration, and for each response variable, until the best model is obtained.

Chapter Seven

Results

The results for the response variables (seed variables) under study are presented in the upcoming section. For each seed variable within the flexible and rigid pavement layers, the optimal model that generates the highest prediction accuracy was found.

The seed variables for the AC layer in the flexible pavement structure are the AC master curve sigmoidal function coefficients: alpha (α), Beta_prime (β'), Delta (δ), Gamma (γ). The seed variables for the PCC layer in the rigid pavement structure are the modulus of elasticity (E_1) and the Rayleigh Damping Parameters (α_{RPCC}) and (β_{RPCC}). For the base, subgrade and the stiff layers underlying both flexible and rigid pavements, the seed variables are the moduli of elasticity (E_2), (E_3) and (E_4) respectively, as well as the Rayleigh Damping Parameters (α_R) and (β_R). Lastly, the stiff layer thickness measured from the surface (h_3). Hence, a total of 13 seed variables.

Several models with various combinations of predictor variables were tested for each seed variable. The model's accuracy along with other characteristics are shown in Tables 25 and 26.

Table 25: Time taken to Build RF-Model and to Predict the Seed Variables

Seed Variable	Time to Build RF Model	Prediction Time
Alpha (α)	18 min	16 sec.
Beta_prime (β')	39 min, 40 sec	21 sec.
Delta (δ)	42 min	18 sec.
Gamma (γ)	77 min, 53 sec	32 sec.
E_1	3 min, 57 sec.	1 sec.
α_{RPCC}	53 min, 28 sec.	46 sec.
β_{RPCC}	5 min	3 sec.
E_2	84 min, 37 sec.	23 sec.
E_3	24 min, 22sec.	7 sec.
E_4	5 hrs, 24min	38 sec.
α_R	~ 19 hrs	1 min, 26 sec.
β_R	10 hrs, 24 min	59 sec.
h_3	26 min, 19 sec.	6 sec.

Table 26: Optimal Model Characteristics for each Seed Variable

Seed Variable	Number of Trials/Models Tested	Number of Predictor Variables in Optimal Model	Optimal Model Accuracy (%)
Alpha (α)	200	12	97.38
Beta_prime (β')	191	19	98.14
Delta (δ)	167	20	97.86
Gamma (γ)	166	25	97.85
E_1	16	9	100
α_{RPCC}	30	14	58.65
β_{RPCC}	42	11	100
E_2	121	24	99.84
E_3	59	17	100
E_4	80	65	99.67
α_R	33	175	98.48
β_R	83	124	99.82
h_3	80	21	99.99

The detailed results, the Variable Importance Measures (VIM) plots and the statistical analysis generated by R-Studio for each seed variable are presented in the subsequent sections as follows:

- Section 7.1 Seed Variables for the Asphalt Concrete (AC) Layer
- Section 7.2 Seed Variables for the Portland Cement Concrete (PCC) Layer
- Section 7.3 Seed Variables for Unbound Layers

Note that due to the large count of predictor variables needed to build the RF models for (E_4),(α_R) and (β_R), only 30 predictor variables are shown by R-studio in the VIM plots.

7.1 Seed Variables for the Asphalt Concrete (AC) Layer

7.1.1 AC Master Curve Sigmoidal Coefficient "Alpha (α)"

The predictor variables that built up the optimal model for "Alpha (α)" are: "DminL_D.0","DminL_D.60","DminL_D.72", "DminL_D.96","TDminL_D.48", "T75R_D.0", "SCI", "Dp08", "D25_08" ,"T25L08" ,"T50L08","T75L08"

As per the plots displaying the Mean Decrease Accuracy (MDA) and Mean Decrease Gini (MDG) measures (Figure 57), the predictor variable that showed the highest importance for the MDA measure is "T75R_D.0" with a value of 393 while that for the MDG measures is "SCI" with a value of 38,164.

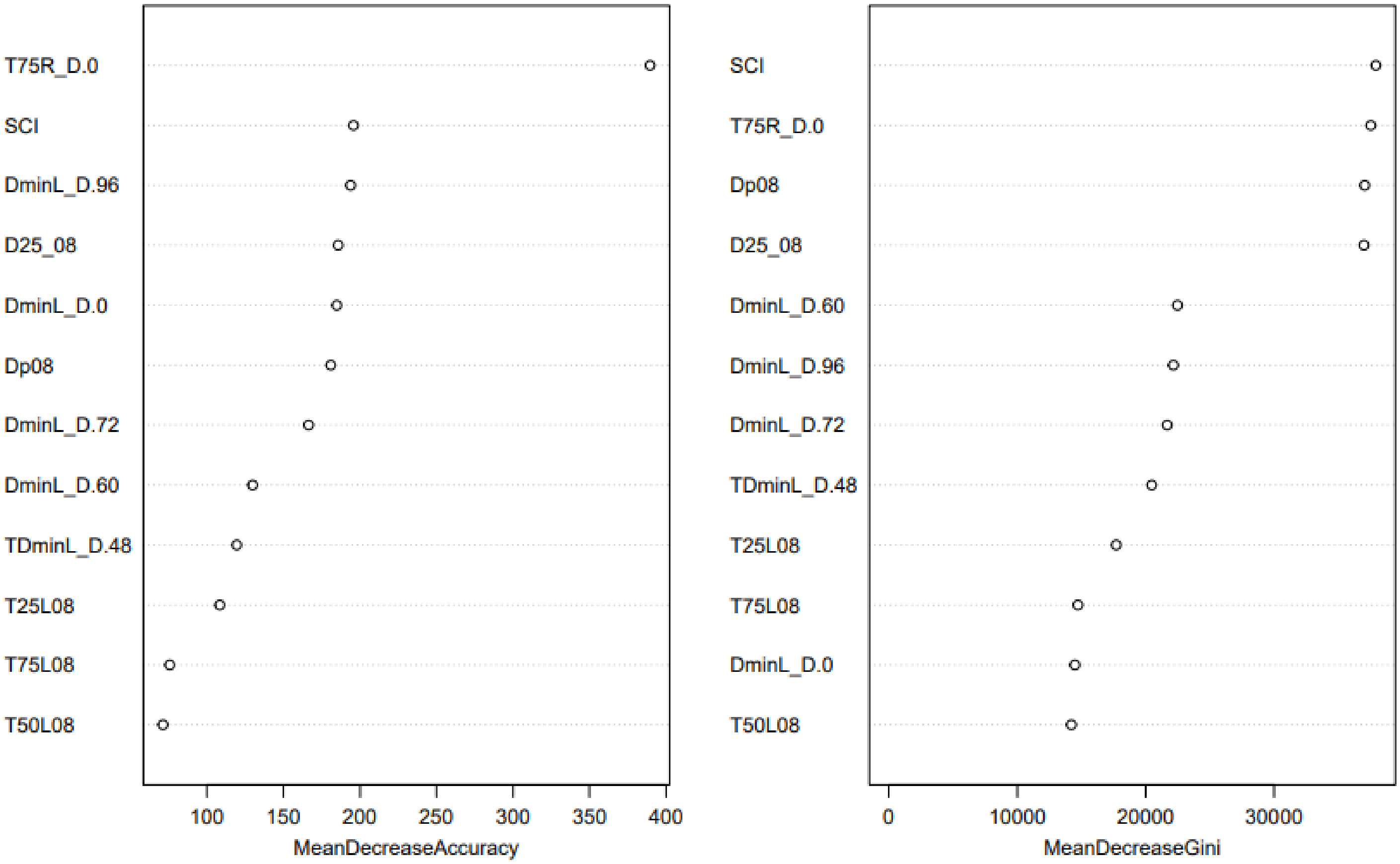

Figure 57: MDA and MDG Plots for "Alpha (α)"

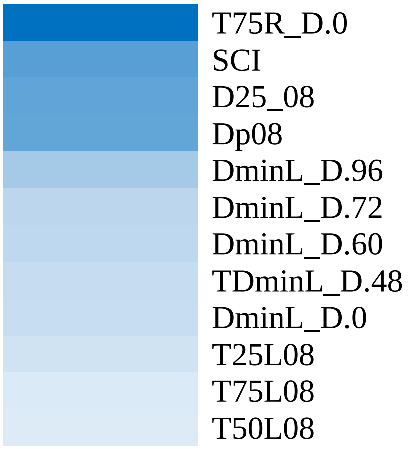

For each predictor variable, a total score was determined by summing the values of the MDA and MDG measures. The variables that are essential to predict the AC Master Curve Sigmoidal Coefficient "Alpha (α)" are arranged in descending order of importance (Figure 58). As the color intensity decreases, the importance of the corresponding predictor variable decreases.

Figure 58: Importance of each Predictor Variable for Predicting “Alpha (α)” based on MDA and MDG Total Score

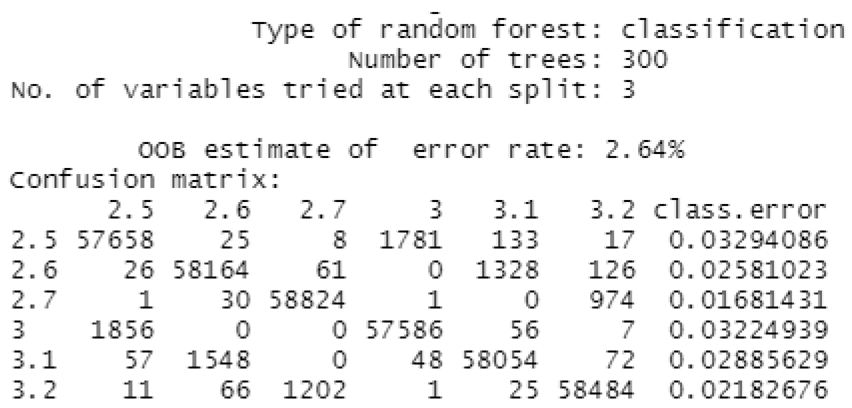

```
                 Type of random forest: classification
                       Number of trees: 300
 No. of variables tried at each split: 3

        OOB estimate of  error rate: 2.64%
 Confusion matrix:
       2.5   2.6   2.7     3   3.1   3.2 class.error
 2.5 57658    25     8  1781   133    17  0.03294086
 2.6    26 58164    61     0  1328   126  0.02581023
 2.7     1    30 58824     1     0   974  0.01681431
 3    1856     0     0 57586    56     7  0.03224939
 3.1    57  1548     0    48 58054    72  0.02885629
 3.2    11    66  1202     1    25 58484  0.02182676
```

Figure 59: Training Data Confusion Matrix and OOB Estimate for “Alpha (α)”

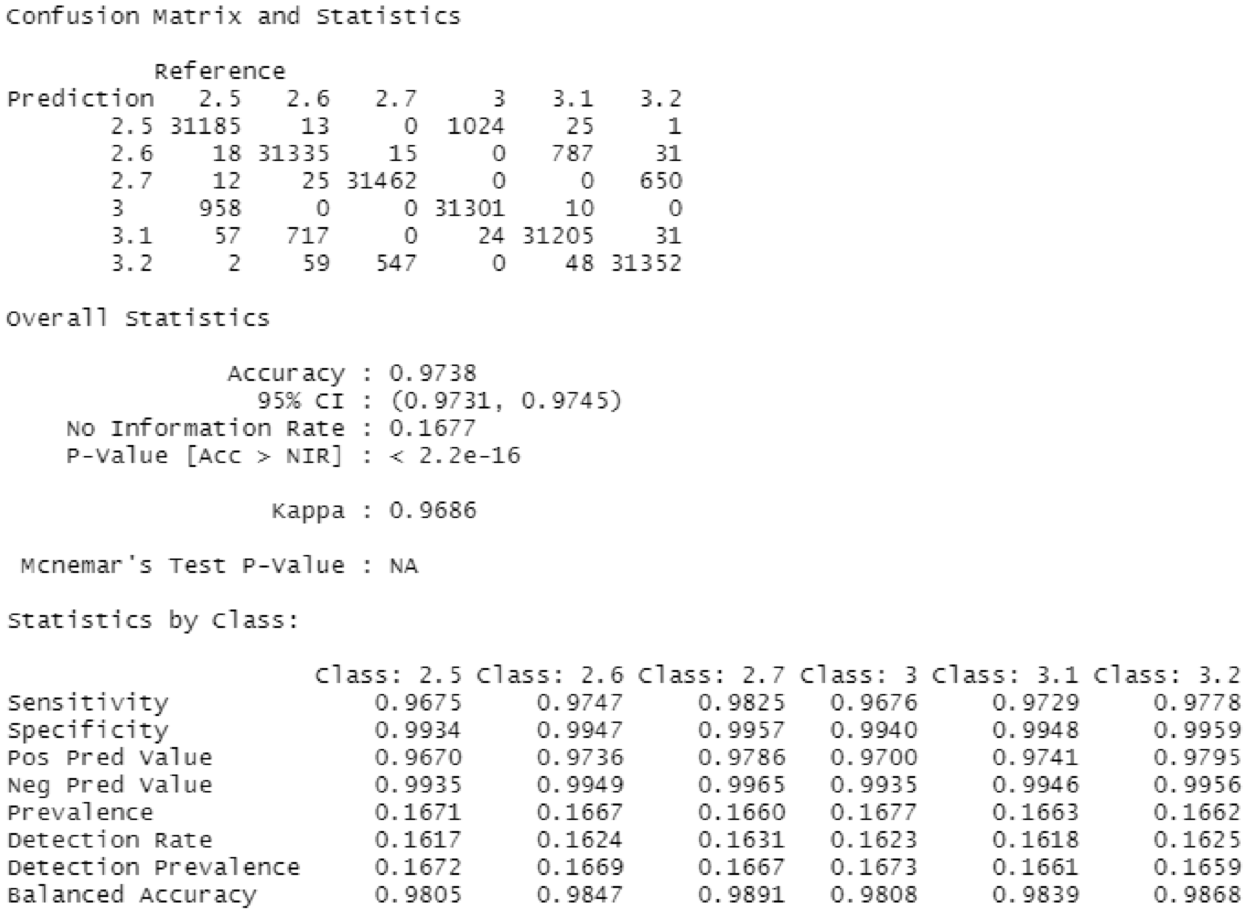

```
Confusion Matrix and Statistics

          Reference
Prediction   2.5   2.6   2.7     3   3.1   3.2
       2.5 31185    13     0  1024    25     1
       2.6    18 31335    15     0   787    31
       2.7    12    25 31462     0     0   650
       3     958     0     0 31301    10     0
       3.1    57   717     0    24 31205    31
       3.2     2    59   547     0    48 31352

Overall Statistics

               Accuracy : 0.9738
                 95% CI : (0.9731, 0.9745)
    No Information Rate : 0.1677
    P-Value [Acc > NIR] : < 2.2e-16

                  Kappa : 0.9686

 Mcnemar's Test P-Value : NA

Statistics by Class:

                     Class: 2.5 Class: 2.6 Class: 2.7 Class: 3 Class: 3.1 Class: 3.2
Sensitivity              0.9675     0.9747     0.9825   0.9676     0.9729     0.9778
Specificity              0.9934     0.9947     0.9957   0.9940     0.9948     0.9959
Pos Pred Value           0.9670     0.9736     0.9786   0.9700     0.9741     0.9795
Neg Pred Value           0.9935     0.9949     0.9965   0.9935     0.9946     0.9956
Prevalence               0.1671     0.1667     0.1660   0.1677     0.1663     0.1662
Detection Rate           0.1617     0.1624     0.1631   0.1623     0.1618     0.1625
Detection Prevalence     0.1672     0.1669     0.1667   0.1673     0.1661     0.1659
Balanced Accuracy        0.9805     0.9847     0.9891   0.9808     0.9839     0.9868
```

Figure 60: Testing Data Confusion Matrix and Statistics for “Alpha (α)”

7.1.2 AC Master Curve Sigmoidal Coefficient “Beta_prime (β')”

The predictor variables that built up the optimal model for “Beta_prime (β')” are: "DminL_D.0","DminL_D.48","DminL_D.60","DminL_D.72","DminL_D.84","DminL_D.96", "DminL_D.108","DminL_D.120","TDminL_D.48","TDminL_D.60","TPeak_D.0","h1","BI", "SCI","Dp08", "VP08", "TVP08", "T50L08","T25L08"

Based on the MDA and MDG plots (Figure 61), the predictor variables that showed the highest importance for the MDA measure is "h_1" with a value of 193 while that for the MDG measures is "Dp08" with a value of 50,384.

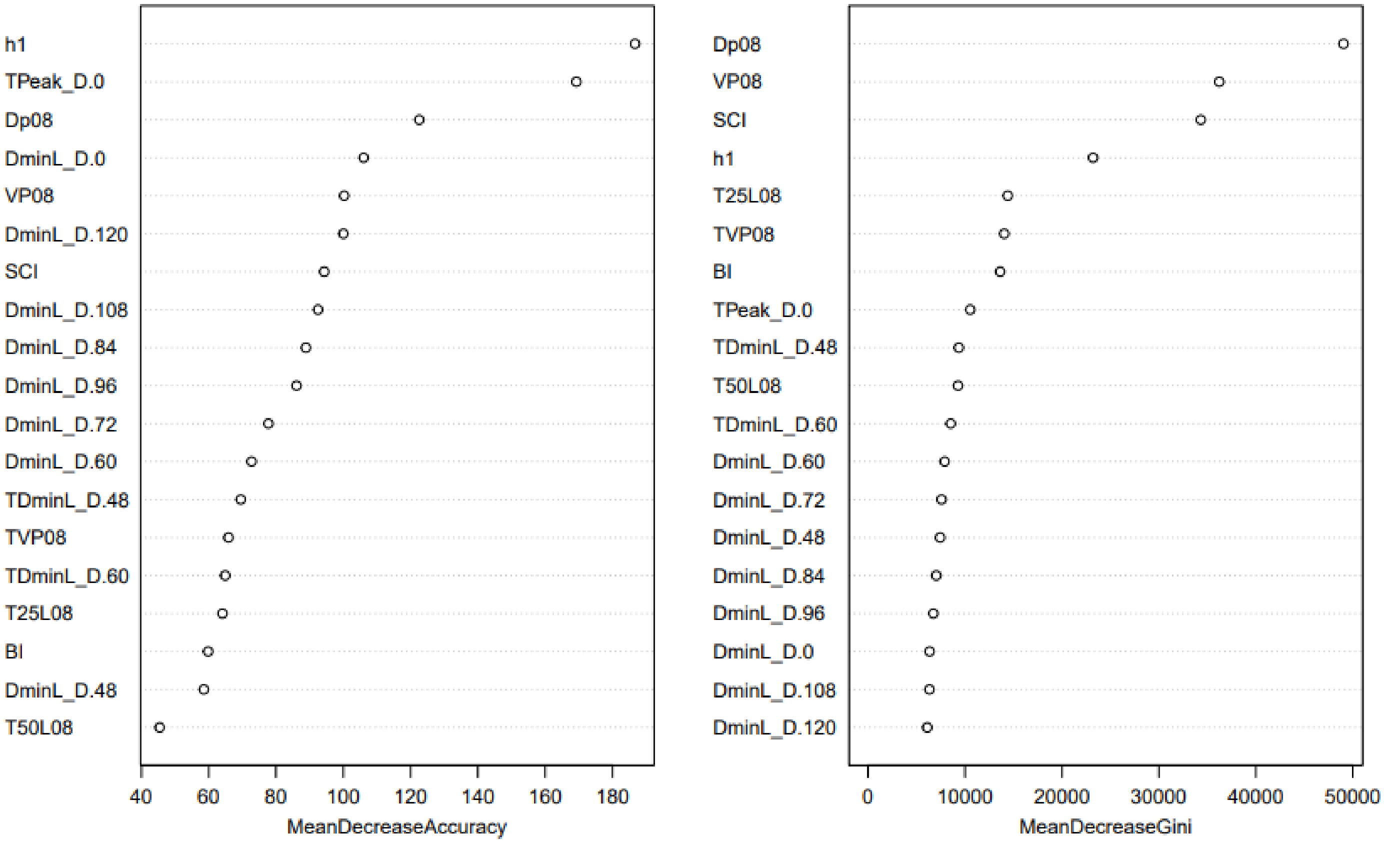

Figure 61:MDA and MDG Plots for “Beta_prime (β')”

Based on the total score calculated for each predictor variable, the color for the predictor variable “Dp08” showed the strongest intensity (Figure 62), indicating that this variable is the most important for predicting the AC Master Curve Sigmoidal Coefficient “Beta_prime (β')”. Moving towards “DminL_D.48”, the color intensity starts fading away, indicating a decrease in the corresponding variable importance.

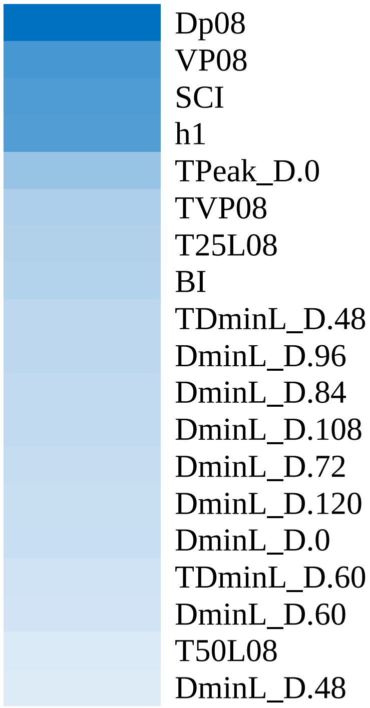
Dp08
VP08
SCI
h1
TPeak_D.0
TVP08
T25L08
BI
TDminL_D.48
DminL_D.96
DminL_D.84
DminL_D.108
DminL_D.72
DminL_D.120
DminL_D.0
TDminL_D.60
DminL_D.60
T50L08
DminL_D.48

Figure 62: Importance of each Predictor Variable for Predicting “Beta_prime (β')” based on MDA and MDG Total Score

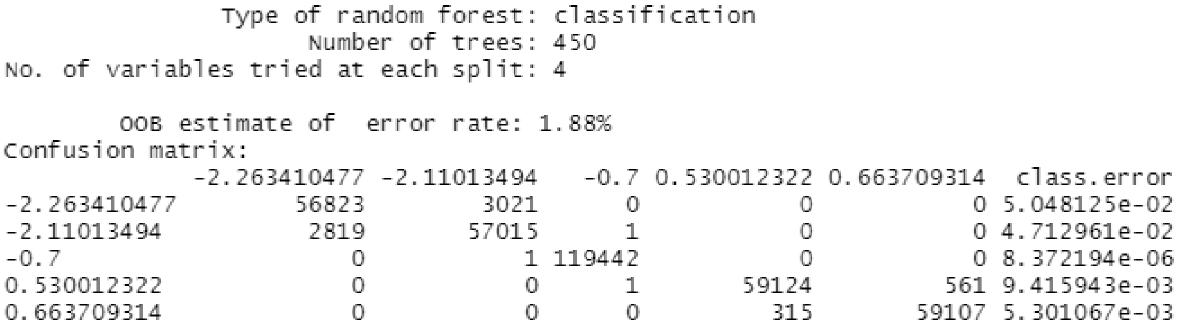
```
               Type of random forest: classification
                     Number of trees: 450
No. of variables tried at each split: 4

        OOB estimate of  error rate: 1.88%
Confusion matrix:
             -2.263410477 -2.11013494   -0.7 0.530012322 0.663709314  class.error
-2.263410477        56823        3021      0           0           0 5.048125e-02
-2.11013494          2819       57015      1           0           0 4.712961e-02
-0.7                    0           1 119442           0           0 8.372194e-06
0.530012322             0           0      1       59124         561 9.415943e-03
0.663709314             0           0      0         315       59107 5.301067e-03
```

Figure 63: Training Data Confusion Matrix and OOB Estimate for “Beta_prime (β')”

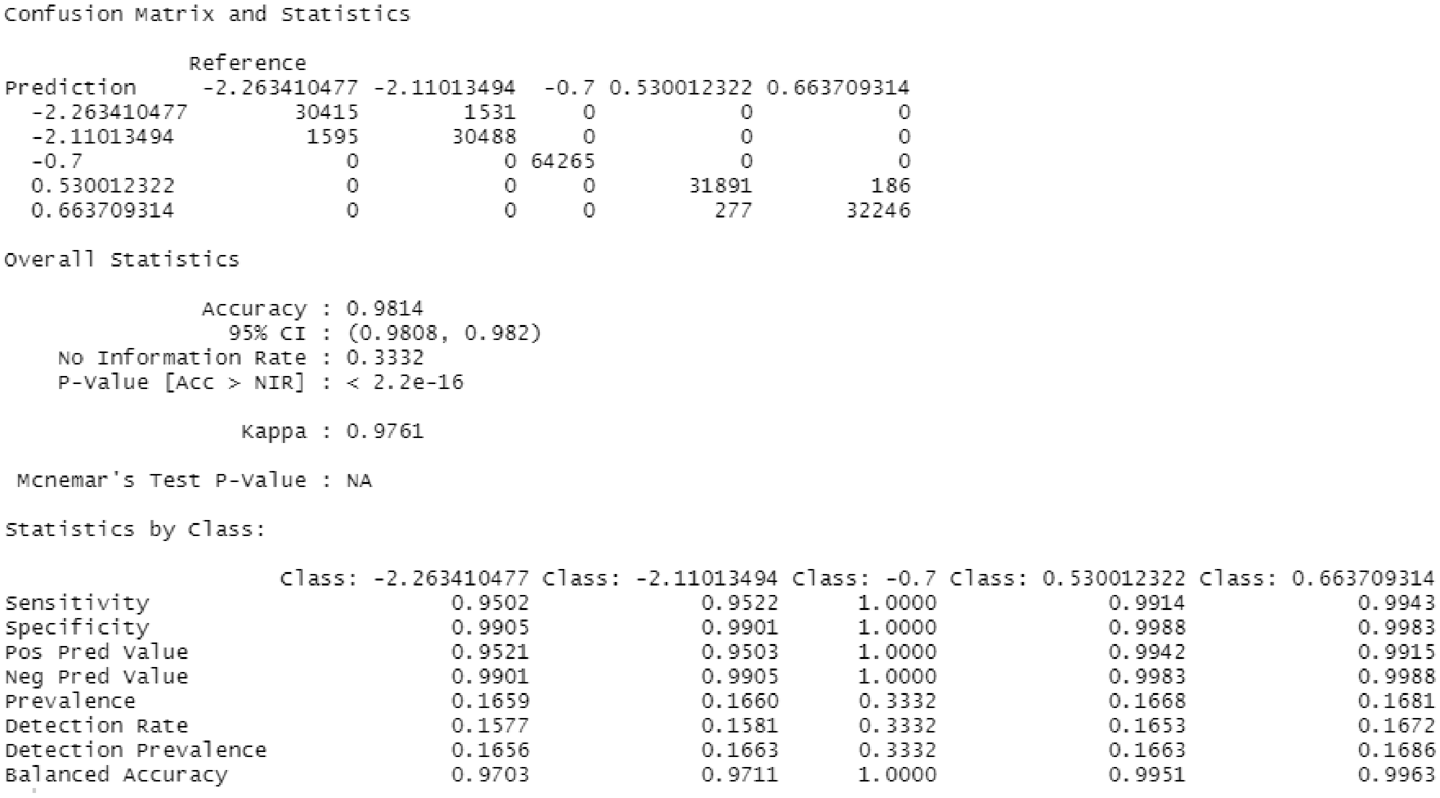

```
Confusion Matrix and Statistics

              Reference
Prediction     -2.263410477 -2.11013494  -0.7 0.530012322 0.663709314
  -2.263410477        30415        1531     0           0           0
  -2.11013494          1595       30488     0           0           0
  -0.7                    0           0 64265           0           0
  0.530012322             0           0     0       31891         186
  0.663709314             0           0     0         277       32246

Overall Statistics

               Accuracy : 0.9814
                 95% CI : (0.9808, 0.982)
    No Information Rate : 0.3332
    P-Value [Acc > NIR] : < 2.2e-16

                  Kappa : 0.9761

 Mcnemar's Test P-Value : NA

Statistics by Class:

                     Class: -2.263410477 Class: -2.11013494 Class: -0.7 Class: 0.530012322 Class: 0.663709314
Sensitivity                       0.9502             0.9522      1.0000             0.9914             0.9943
Specificity                       0.9905             0.9901      1.0000             0.9988             0.9983
Pos Pred Value                    0.9521             0.9503      1.0000             0.9942             0.9915
Neg Pred Value                    0.9901             0.9905      1.0000             0.9983             0.9988
Prevalence                        0.1659             0.1660      0.3332             0.1668             0.1681
Detection Rate                    0.1577             0.1581      0.3332             0.1653             0.1672
Detection Prevalence              0.1656             0.1663      0.3332             0.1663             0.1686
Balanced Accuracy                 0.9703             0.9711      1.0000             0.9951             0.9963
```

Figure 64: Testing Data Confusion Matrix and Statistics for "Beta_prime (β')"

7.1.3 AC Master Curve Sigmoidal Coefficient "Delta (δ)"

The predictor variables that built up the optimal model for "Delta (δ)" are: "DminL_D.60", "DminL_D.72", "TPeak_D.0" ,"TVPeak.0", "T75R_D.0", "h1","SCI","Dp08", "Dmr08","Dmr812", "Dml7284","Tml7284","D25_08", "D25_812","VPD08","VP08","TVP08", "T25R08", "T25R812", "T25L1218"

For the MDA measure, "TVPeak.0" showed the highest importance with a value of 159. As for the MDG measure, "T25R08" showed the highest value of 14,197 (Figure 65).

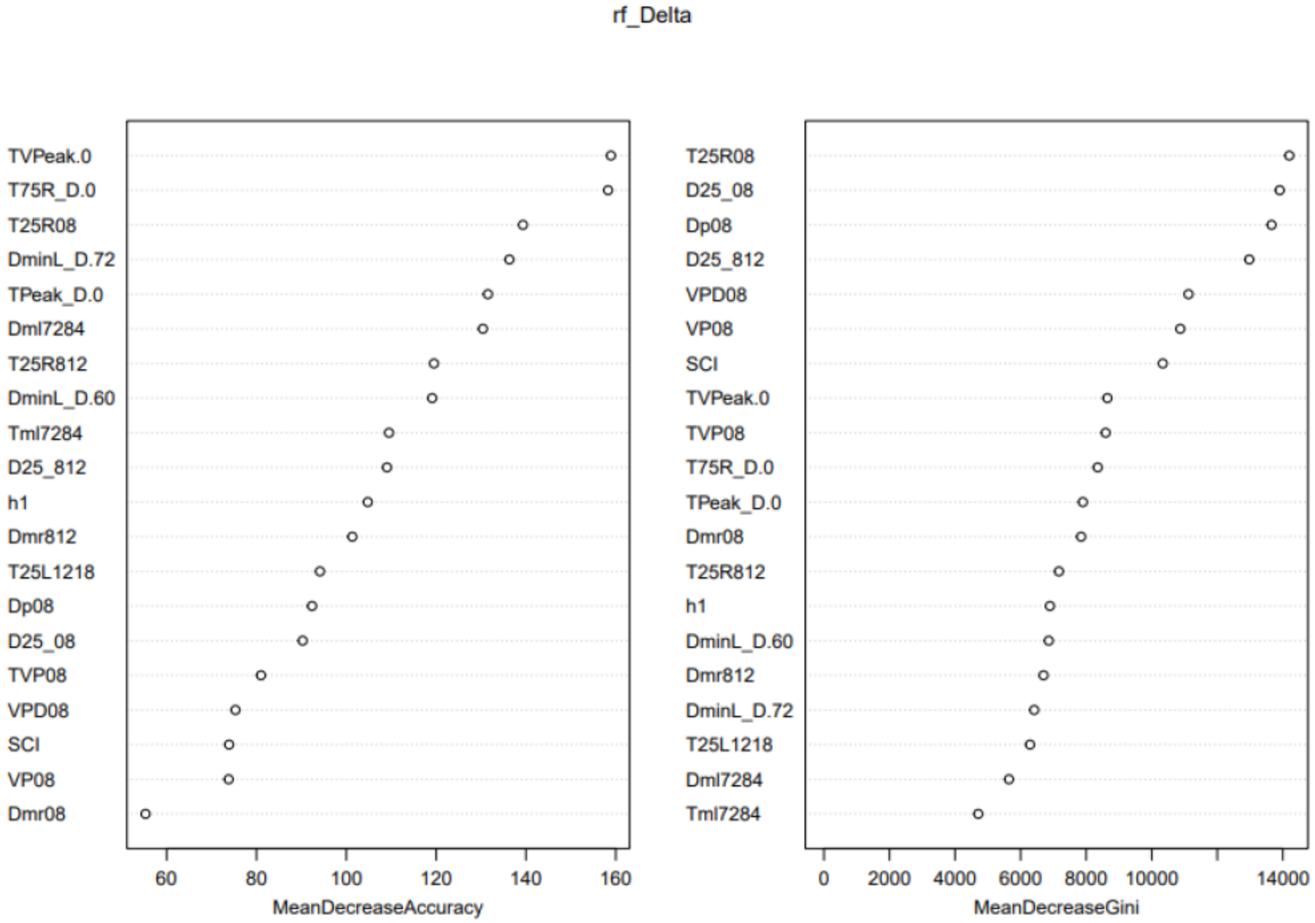

Figure 65: MDA and MDG Plots for "Delta (δ)"

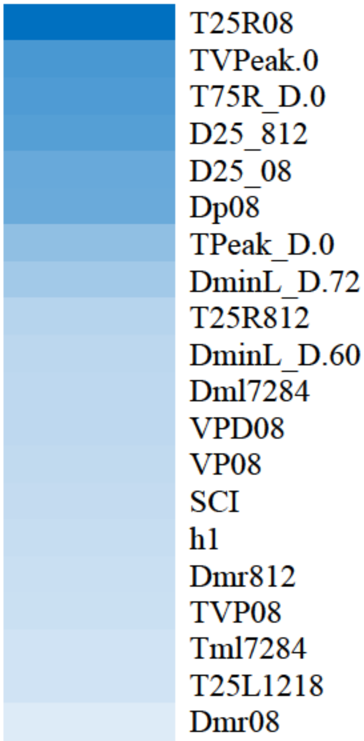
T25R08
TVPeak.0
T75R_D.0
D25_812
D25_08
Dp08
TPeak_D.0
DminL_D.72
T25R812
DminL_D.60
Dml7284
VPD08
VP08
SCI
h1
Dmr812
TVP08
Tml7284
T25L1218
Dmr08

Figure 66: MDA and MDG Total Score for "Delta (δ)"

According to the total score calculated for each predictor variable, the color for the predictor variable "T25R08" showed the strongest intensity, in dicating that this variable is the most important for predicting the AC Master Curve Sigmoidal Coefficient "Delta (δ)". Moving towards "Dmr08", the color intensity starts fading away, indicating a decrease in the corresponding variable importance.

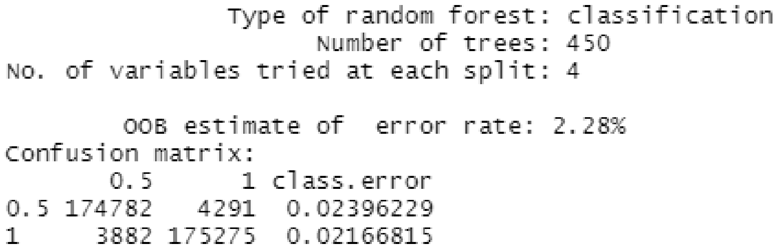

```
               Type of random forest: classification
                     Number of trees: 450
No. of variables tried at each split: 4

        OOB estimate of  error rate: 2.28%
Confusion matrix:
       0.5      1 class.error
0.5 174782   4291  0.02396229
1     3882 175275  0.02166815
```

Figure 67: Training Data Confusion Matrix and OOB Estimate for "Delta (δ)"

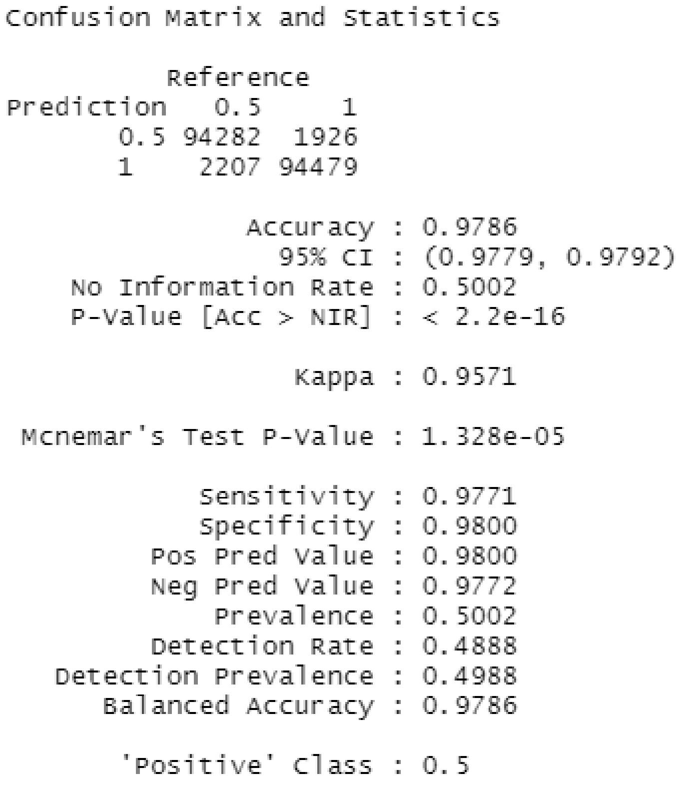

```
Confusion Matrix and Statistics

          Reference
Prediction   0.5     1
       0.5 94282  1926
       1    2207 94479

               Accuracy : 0.9786
                 95% CI : (0.9779, 0.9792)
    No Information Rate : 0.5002
    P-Value [Acc > NIR] : < 2.2e-16

                  Kappa : 0.9571

 Mcnemar's Test P-Value : 1.328e-05

            Sensitivity : 0.9771
            Specificity : 0.9800
         Pos Pred Value : 0.9800
         Neg Pred Value : 0.9772
             Prevalence : 0.5002
         Detection Rate : 0.4888
   Detection Prevalence : 0.4988
      Balanced Accuracy : 0.9786

       'Positive' Class : 0.5
```

Figure 68: Testing Data Confusion Matrix and Statistics for "Delta (δ)"

7.1.4 AC Master Curve Sigmoidal Coefficient "Gamma (γ)"

The predictor variables that built up the optimal model for "Gamma (γ)" are: "DPeak_D.0", "DminL_D.36", "DminL_D.48", "DminL_D.60", "DminL_D.72", "DminL_D.84", "DminL_D.96","DminL_D.120","TDminL_D.48","TDminL_D.60","TDminL_D.72", "TDminL_D.108", "VPeak_D.0", "TVPeak_D.0", "RoC", "SCI", "Dp08","Dp812", "Dp1218", "VMD08", "VPD08", "VP08", "T25L08", "T50L08", "D25_08"

As per the graphs observed in Figure 69, the predictor variables that showed the highest importance based on the MDA and MDG measures are "TVPeak_D.0" and "VPD08" respectively, with values of 182 for MDA and 12,082 for MDG.

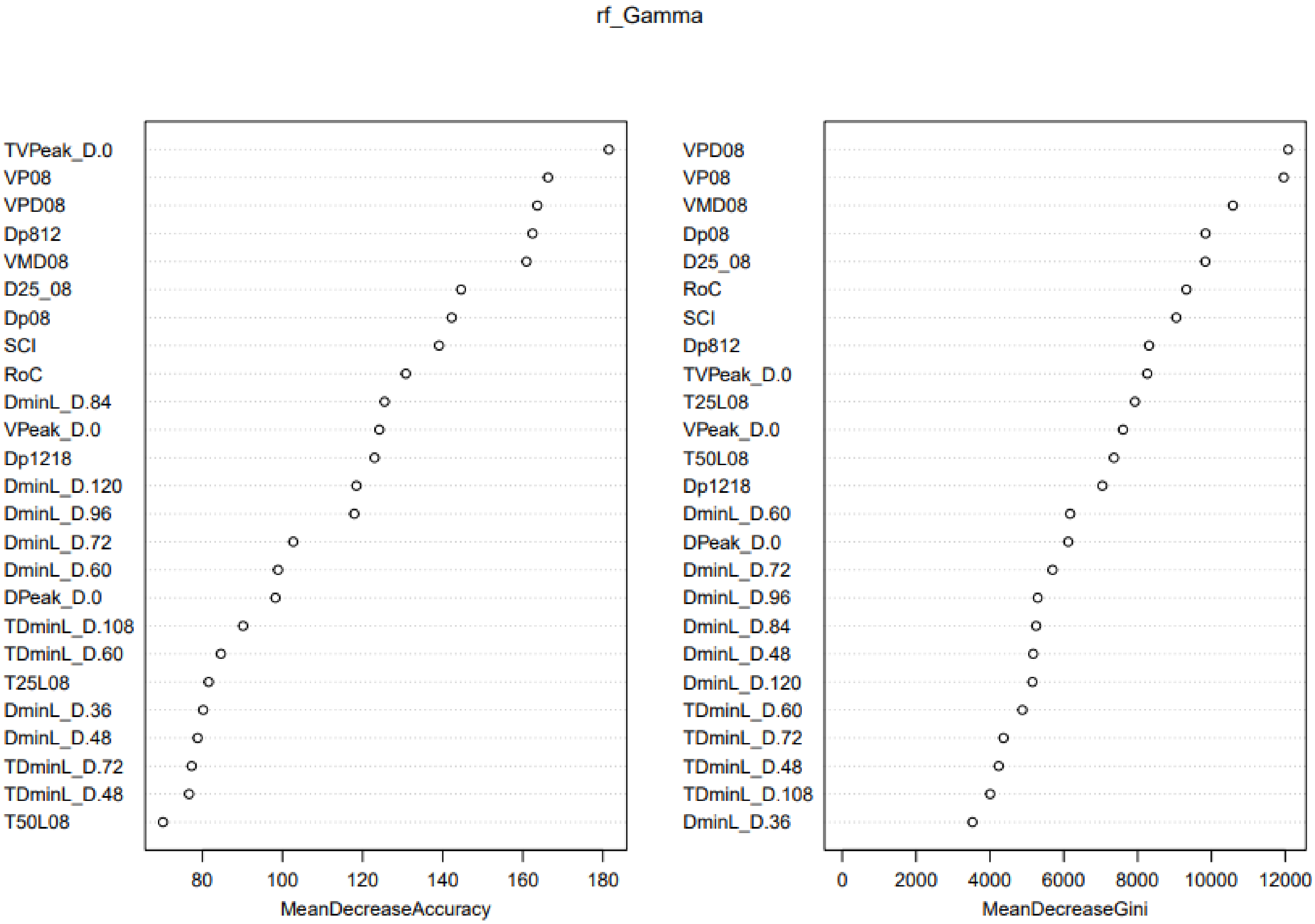

Figure 69: MDA and MDG Plots for "Gamma (γ)"

According to the total score calculated for each predictor variable, the color for the predictor variable “VP08” showed the strongest intensity, indicating that this variable is the most important for predicting the AC Master Curve Sigmoidal Coefficient “Gamma (γ)”. Moving towards “DminL_D.36”, the color intensity starts fading away, indicating a decrease in the corresponding variable importance.

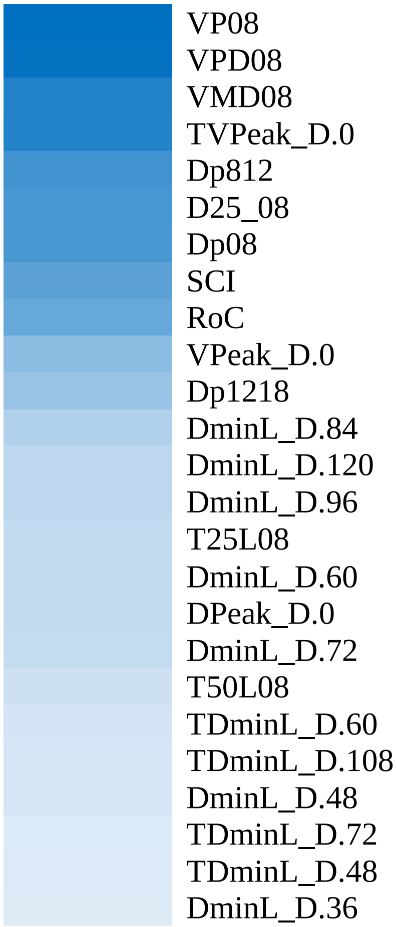

Figure 70: Importance of each Predictor Variable for Predicting “Gamma (γ)” based on MDA and MDG Total Score

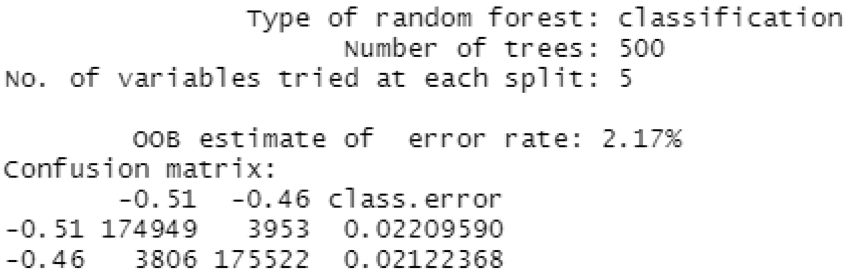

```
               Type of random forest: classification
                     Number of trees: 500
No. of variables tried at each split: 5

        OOB estimate of  error rate: 2.17%
Confusion matrix:
       -0.51  -0.46 class.error
-0.51 174949   3953  0.02209590
-0.46   3806 175522  0.02122368
```

Figure 71: Training Data Confusion Matrix and OOB Estimate for “Gamma (γ)”

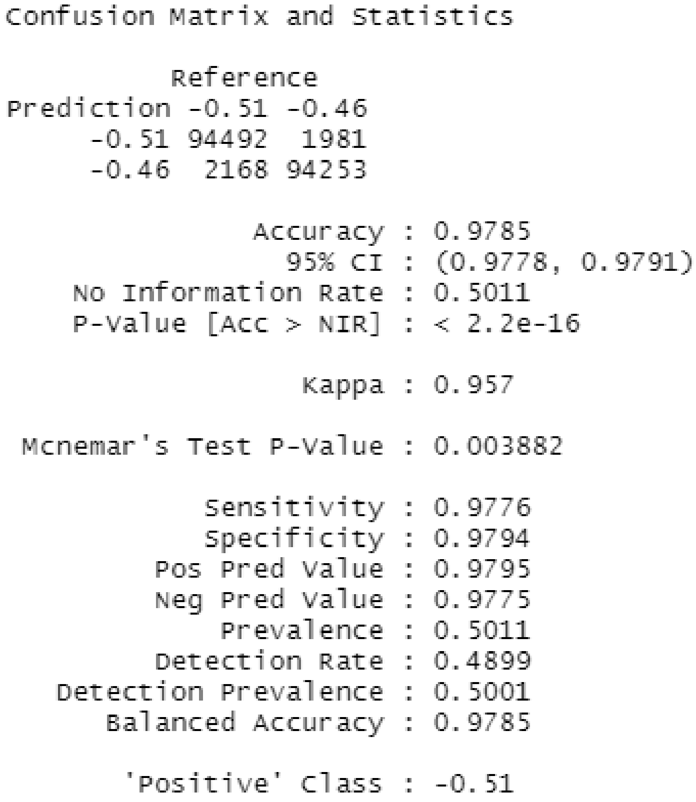

```
Confusion Matrix and Statistics

          Reference
Prediction -0.51 -0.46
     -0.51 94492  1981
     -0.46  2168 94253

               Accuracy : 0.9785
                 95% CI : (0.9778, 0.9791)
    No Information Rate : 0.5011
    P-Value [Acc > NIR] : < 2.2e-16

                  Kappa : 0.957

 Mcnemar's Test P-Value : 0.003882

            Sensitivity : 0.9776
            Specificity : 0.9794
         Pos Pred Value : 0.9795
         Neg Pred Value : 0.9775
             Prevalence : 0.5011
         Detection Rate : 0.4899
   Detection Prevalence : 0.5001
      Balanced Accuracy : 0.9785

       'Positive' Class : -0.51
```

Figure 72: Testing Data Confusion Matrix and Statistics for "Gamma (γ)*"*

7.2 Seed Variables for the Portland Cement Concrete (PCC) Layer

7.2.1 Modulus of Elasticity (E_1)

The predictor variables that built up the optimal model for "E_1" are:

"RoC", "SCI", "BDI", "BCI", "AUPP", "AL1", "SD", "h1", "T75L_D.18"

As per the graphs shown in Figure 73, the predictor variables that showed the highest importance based on the MDA and MDG measures are "T75L_D.18" and "RoC" respectively, with values of 203 for MDA and 66,621 for MDG.

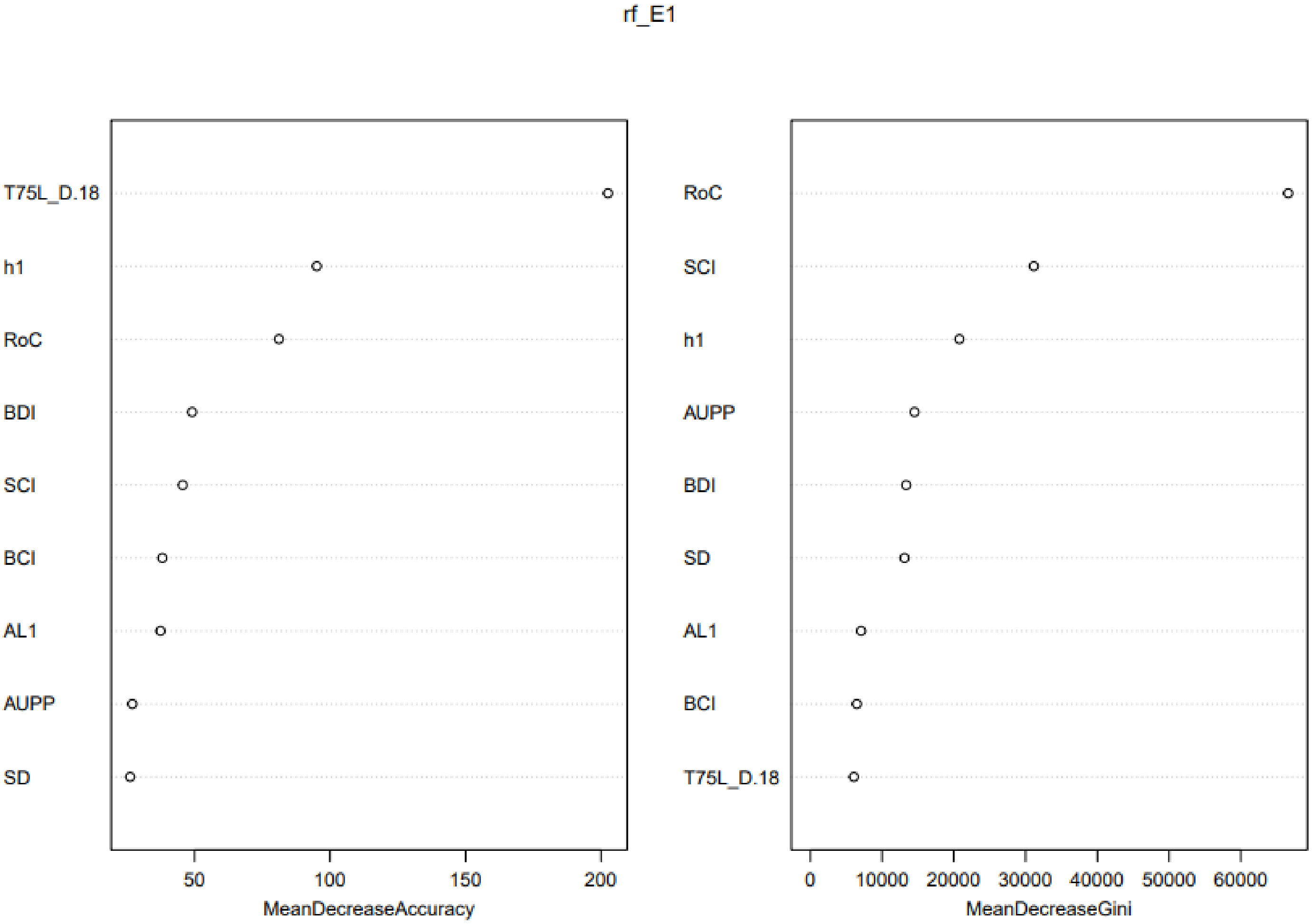

Figure 73: MDA and MDG Plots for "E_1"

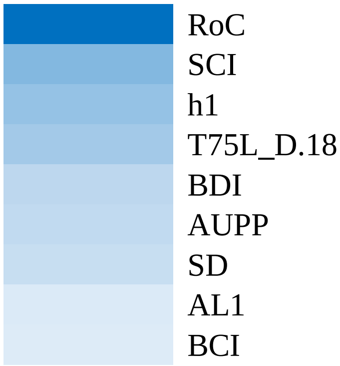

According to the total score calculated for each predictor variable, the color for the predictor variable "RoC" showed the strongest intensity, indicating that this variable is the most important for predicting the modulus of elasticity "E_1" of the PCC layer. Moving towards "BCI", the color intensity starts fading away, indicating a decrease in the corresponding variable importance (Figure 74).

Figure 74: Importance of each Predictor Variable for Predicting "E_1" based on MDA and MDG Total Score

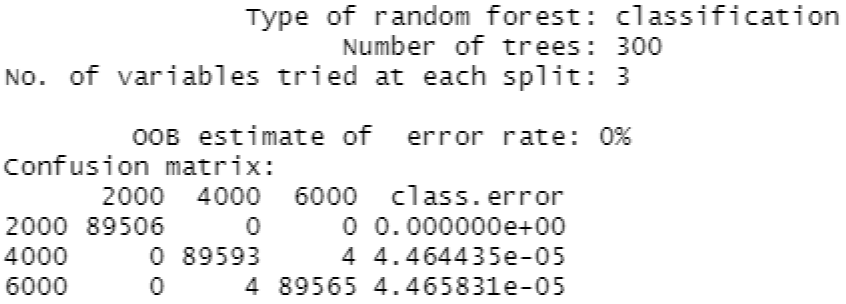

```
                Type of random forest: classification
                      Number of trees: 300
No. of variables tried at each split: 3

        OOB estimate of  error rate: 0%
Confusion matrix:
      2000  4000  6000  class.error
2000 89506     0     0 0.000000e+00
4000     0 89593     4 4.464435e-05
6000     0     4 89565 4.465831e-05
```

Figure 75: Training Data Confusion Matrix and OOB Estimate for “E_1”

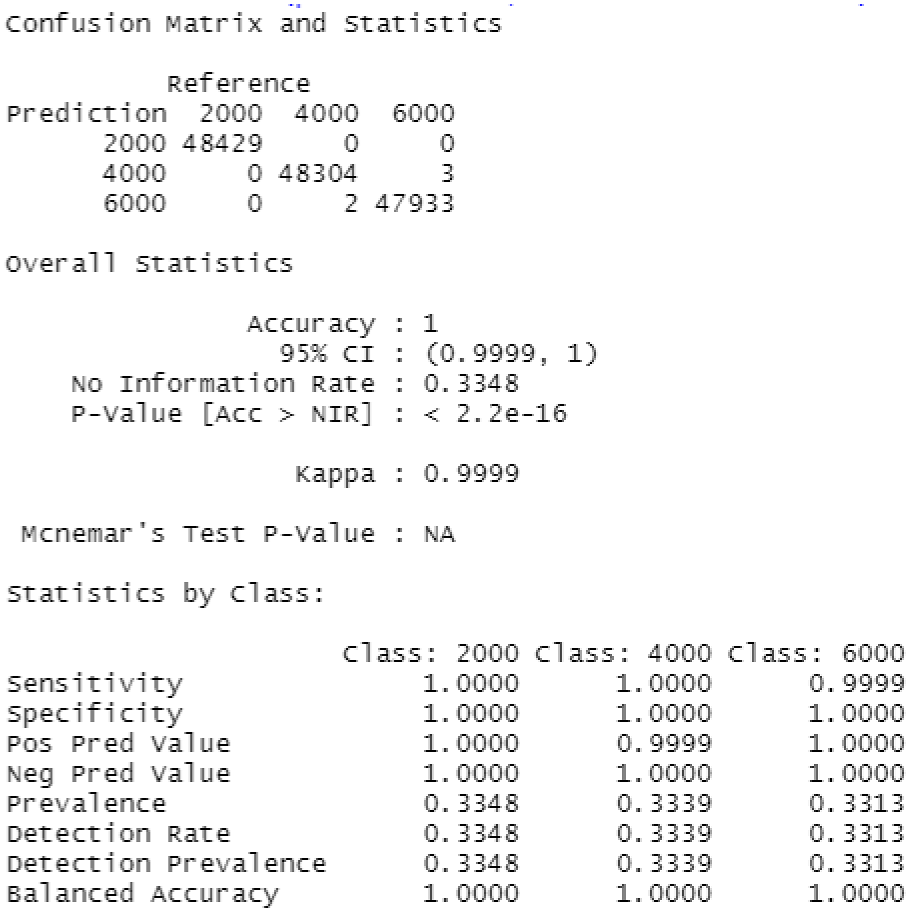

```
Confusion Matrix and Statistics

          Reference
Prediction  2000  4000  6000
      2000 48429     0     0
      4000     0 48304     3
      6000     0     2 47933

Overall Statistics

               Accuracy : 1
                 95% CI : (0.9999, 1)
    No Information Rate : 0.3348
    P-Value [Acc > NIR] : < 2.2e-16

                  Kappa : 0.9999

 Mcnemar's Test P-Value : NA

Statistics by Class:

                     Class: 2000 Class: 4000 Class: 6000
Sensitivity               1.0000      1.0000      0.9999
Specificity               1.0000      1.0000      1.0000
Pos Pred Value            1.0000      0.9999      1.0000
Neg Pred Value            1.0000      1.0000      1.0000
Prevalence                0.3348      0.3339      0.3313
Detection Rate            0.3348      0.3339      0.3313
Detection Prevalence      0.3348      0.3339      0.3313
Balanced Accuracy         1.0000      1.0000      1.0000
```

Figure 76: Testing Data Confusion Matrix and Statistics for “E_1”

7.2.2 Rayleigh Damping Parameters (α_{RPCC})

The predictor variables that built up the optimal model for “α_{RPCC}” are: "DPeak_D.0", "DPeak_D.18", "DPeak_D.36", "RoC", "AL4","Qr", "SCI", "AL1", "f1", "S", "AREA", "D8_2550","D12_2550", "D24_2550"

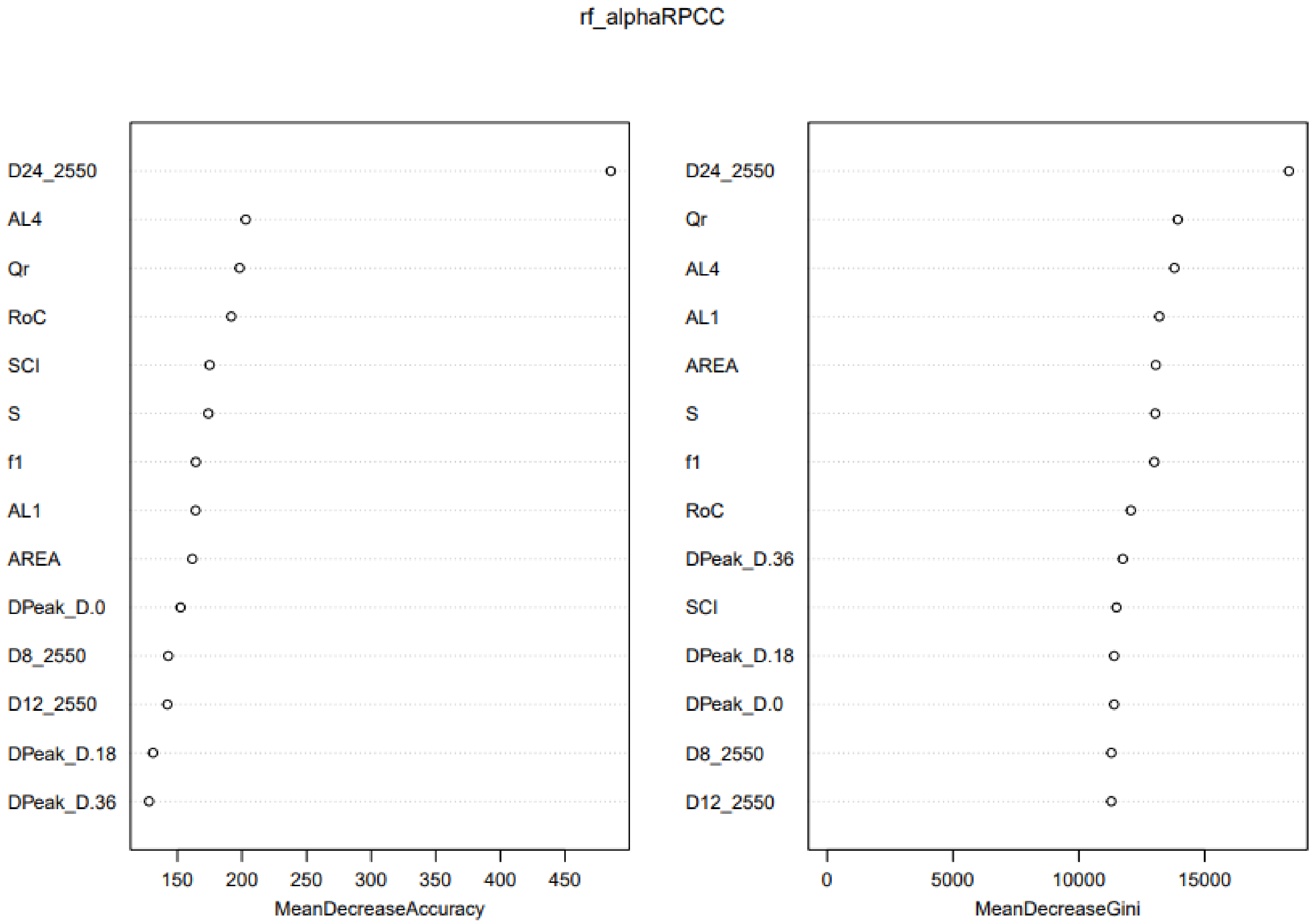

Figure 77: MDA and MDG Plots for "α_{RPCC}"

The predictor variable "D24_2550" showed the highest importance for both, MDA and MDG measures with values of 486 and 18,350, respectively.

Based on the total score calculated for each predictor variable, the color for the predictor variable "D24_2550" showed the strongest intensity, indicating that this variable is the most important for predicting the Rayleigh Damping Parameter (α_{RPCC}) of the PCC layer. Moving towards "DPeak_D.36", the color intensity starts fading away, indicating a decrease in the corresponding variable importance (Figure 78).

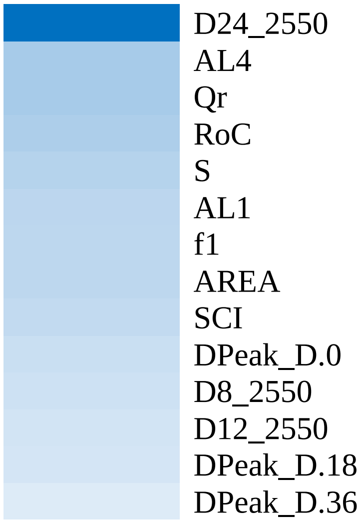

Figure 78: Importance of each Predictor Variable for Predicting "α_{RPCC}" based on MDA and MDG Total Score

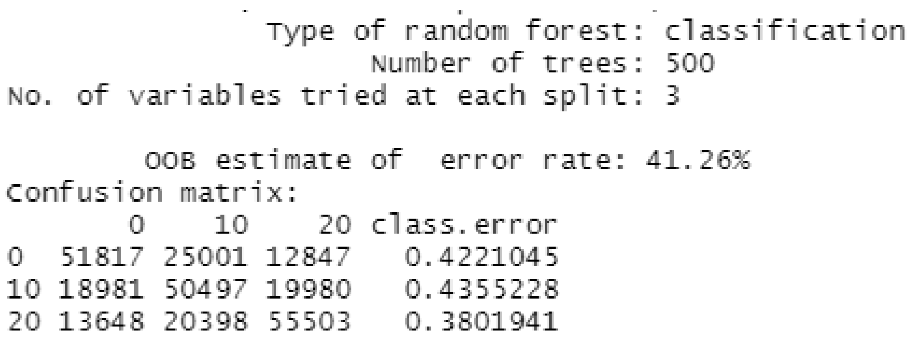

```
               Type of random forest: classification
                     Number of trees: 500
No. of variables tried at each split: 3

        OOB estimate of  error rate: 41.26%
Confusion matrix:
       0    10    20 class.error
0  51817 25001 12847   0.4221045
10 18981 50497 19980   0.4355228
20 13648 20398 55503   0.3801941
```

Figure 79: Training Data Confusion Matrix and OOB Estimate for "α_{RPCC}"

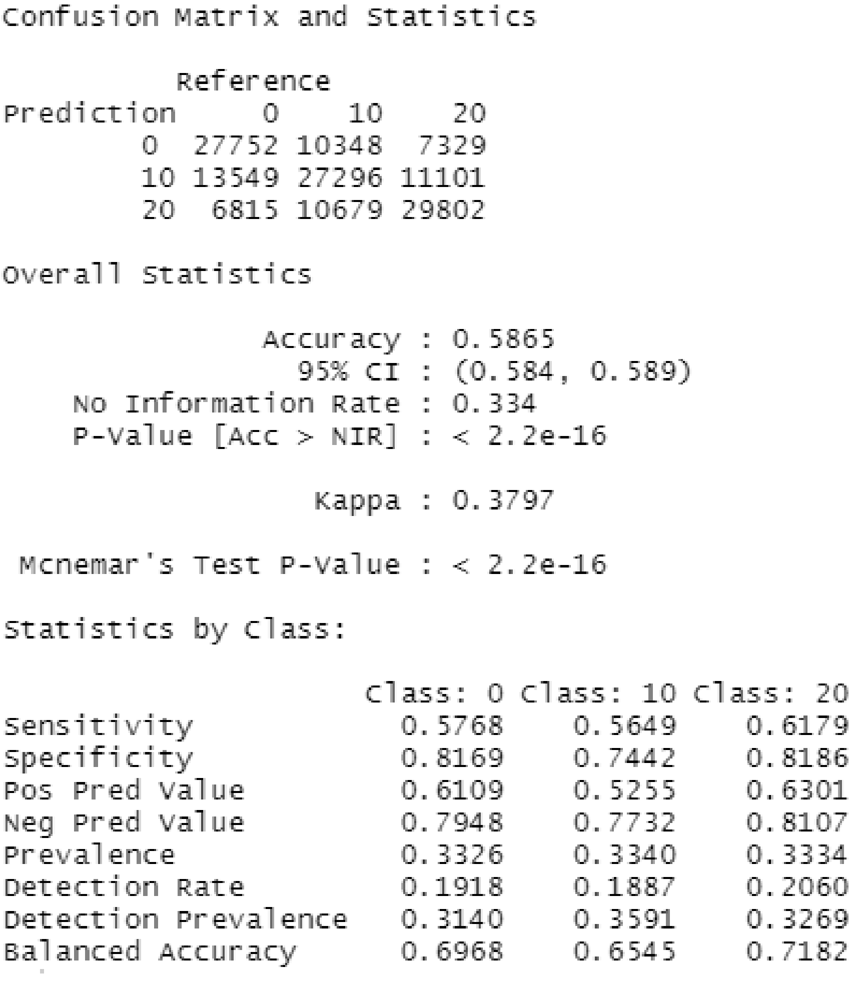

```
Confusion Matrix and Statistics

          Reference
Prediction     0    10    20
        0  27752 10348  7329
        10 13549 27296 11101
        20  6815 10679 29802

Overall Statistics

               Accuracy : 0.5865
                 95% CI : (0.584, 0.589)
    No Information Rate : 0.334
    P-Value [Acc > NIR] : < 2.2e-16

                  Kappa : 0.3797

 Mcnemar's Test P-Value : < 2.2e-16

Statistics by Class:

                     Class: 0 Class: 10 Class: 20
Sensitivity            0.5768    0.5649    0.6179
Specificity            0.8169    0.7442    0.8186
Pos Pred Value         0.6109    0.5255    0.6301
Neg Pred Value         0.7948    0.7732    0.8107
Prevalence             0.3326    0.3340    0.3334
Detection Rate         0.1918    0.1887    0.2060
Detection Prevalence   0.3140    0.3591    0.3269
Balanced Accuracy      0.6968    0.6545    0.7182
```

Figure 80:Testing Data Confusion Matrix and Statistics for "α_{RPCC}"

7.2.3 Rayleigh Damping Parameters (β_{RPCC})

The predictor variables that built up the optimal model for “β_{RPCC}” are: "T25L_D.0", "T25L_D.48", "RoC","Dp08","Dp6072","Dp8496", "Dp96108", "Dp108120", "Tp08","Tp812","Tp1218"

For the MDA and MDG measures, "T25L_D.0" predictor variable showed the highest importance with a value of 199 and 53,747, respectively.

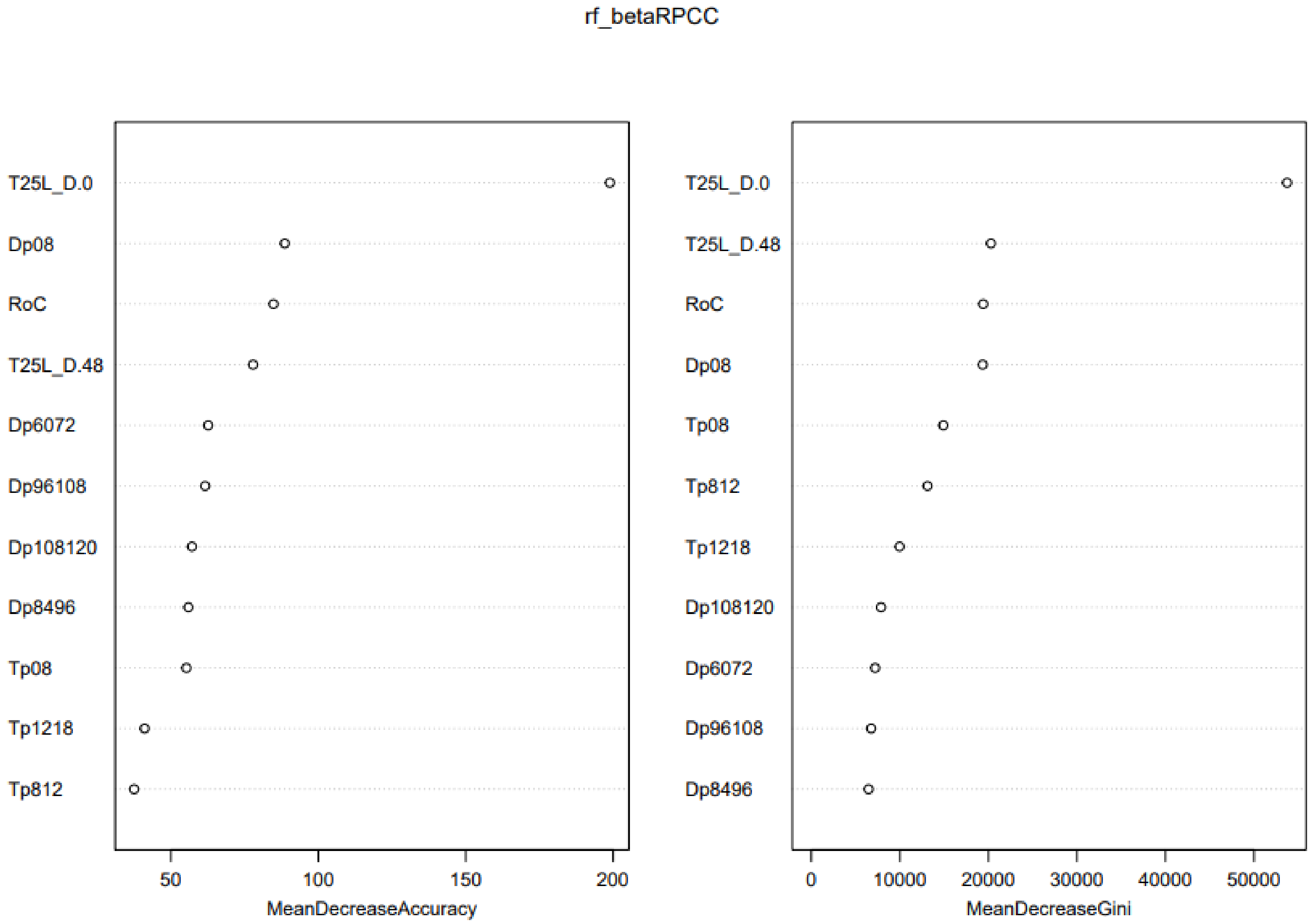

Figure 81: MDA and MDG Plots for “β_{RPCC}”

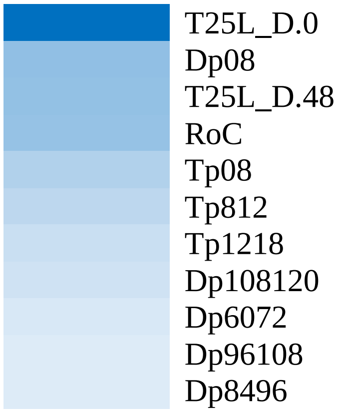

Based on the total score calculated for each predictor variable, the color for the predictor variable “T25L_D.0” showed the strongest intensity. Moving towards “Tp1218”, the color intensity starts fading away, indicating a decrease in the corresponding variable importance (Figure 82).

Figure 82: Importance of each Predictor Variable for Predicting “β_{RPCC}” based on MDA and MDG Total Score

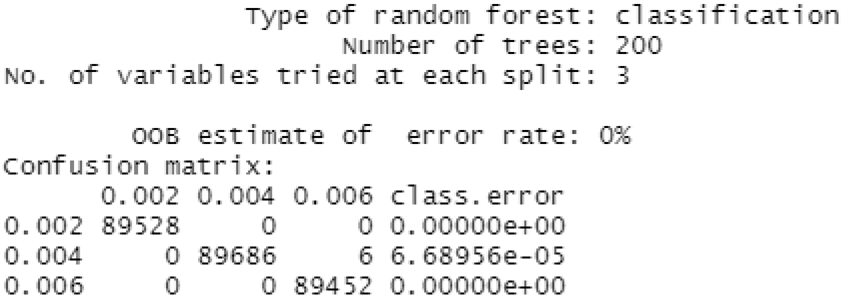

```
               Type of random forest: classification
                     Number of trees: 200
No. of variables tried at each split: 3

        OOB estimate of  error rate: 0%
Confusion matrix:
      0.002 0.004 0.006 class.error
0.002 89528     0     0 0.00000e+00
0.004     0 89686     6 6.68956e-05
0.006     0     0 89452 0.00000e+00
```

Figure 83: Training Data Confusion Matrix and OOB Estimate for “β_{RPCC}”

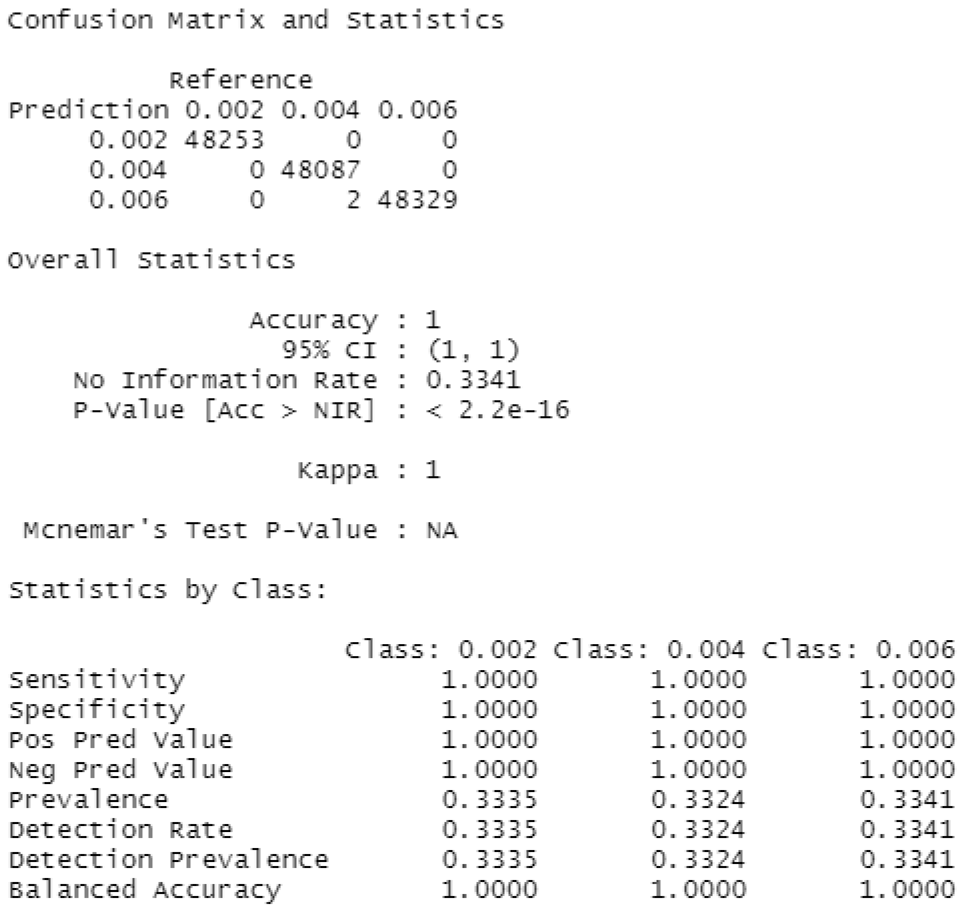

```
Confusion Matrix and Statistics

          Reference
Prediction 0.002 0.004 0.006
     0.002 48253     0     0
     0.004     0 48087     0
     0.006     0     2 48329

Overall Statistics

               Accuracy : 1
                 95% CI : (1, 1)
    No Information Rate : 0.3341
    P-Value [Acc > NIR] : < 2.2e-16

                  Kappa : 1

 Mcnemar's Test P-Value : NA

Statistics by Class:

                     Class: 0.002 Class: 0.004 Class: 0.006
Sensitivity                1.0000       1.0000       1.0000
Specificity                1.0000       1.0000       1.0000
Pos Pred Value             1.0000       1.0000       1.0000
Neg Pred Value             1.0000       1.0000       1.0000
Prevalence                 0.3335       0.3324       0.3341
Detection Rate             0.3335       0.3324       0.3341
Detection Prevalence       0.3335       0.3324       0.3341
Balanced Accuracy          1.0000       1.0000       1.0000
```

Figure 84: Testing Data Confusion Matrix and Statistics for "β_{RPCC}"

7.3 Seed Variables for Unbound Layers

7.3.1 Base Layer Modulus of Elasticity (E_2)

The predictor variables that built up the optimal model for "E_2" are:

"DPeak_D.8", "DminL_D.120", "DminL_D.108", "TPeak_D.8", "TPeak_D.12", "TDminL_D.120", "h2", "BDI", "BCI", "RoC", "SCI", "AL1", "Tp08", "T25R1218" "T25L108120", "T50L08", "T50L1218", "T50L1824", "T50L2436", "T75L08", "Dml7284", "Dml108120", "Tml108120", "D25_1218"

As per the MDA and MDG plots (Figure 85), the predictor variables that showed the highest importance for the MDA measure is "h2" with a value of 169 while that for the MDG measures is "D25_1218" with a value of 30,345.

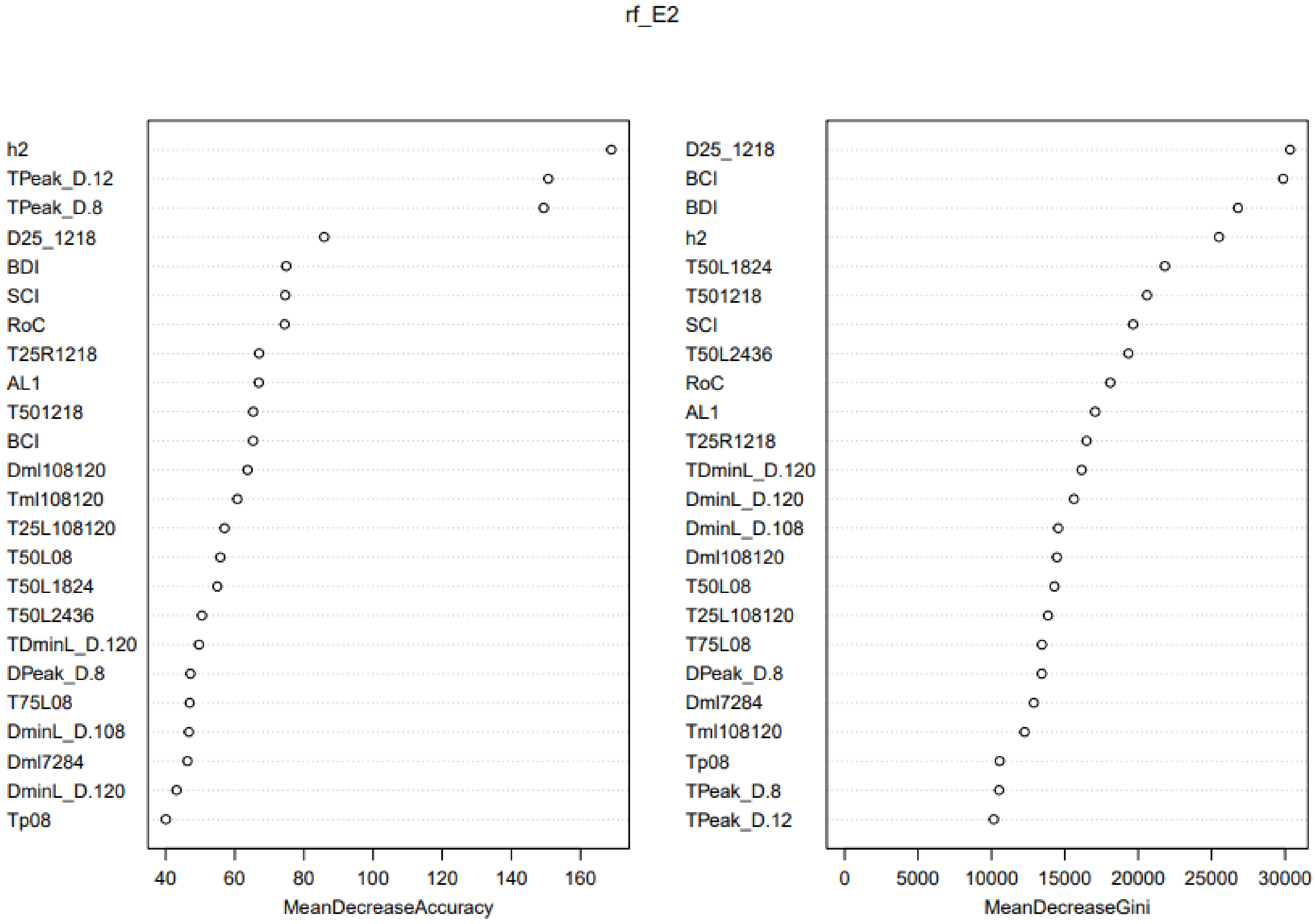

Figure 85: MDA and MDG Plots for “E_2”

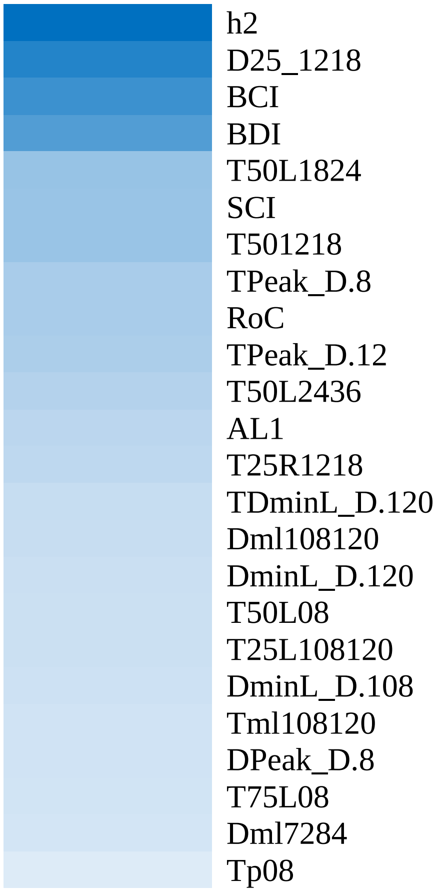

Based the total score calculated for each predictor variable, the color for the predictor variable “h_2” showed the strongest intensity, indicating that this variable is the most important for predicting the modulus of elasticity “E_2” of the base layer. Moving towards “Tp08”, the color intensity starts fading away, indicating a decrease in the corresponding variable importance (Figure 86).

Figure 86: Importance of each Predictor Variable for Predicting “E_2” based on MDA and MDG Total Score

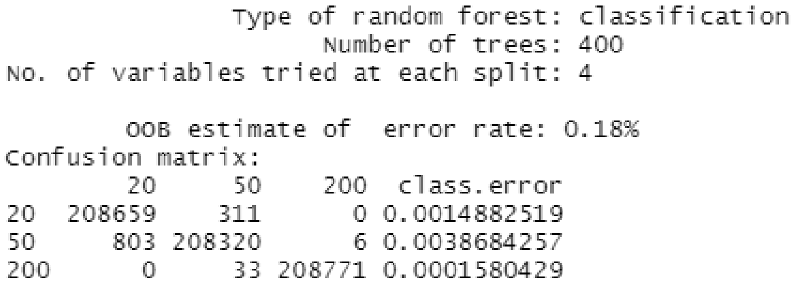

```
               Type of random forest: classification
                     Number of trees: 400
No. of variables tried at each split: 4

        OOB estimate of  error rate: 0.18%
Confusion matrix:
        20     50    200  class.error
20  208659    311      0 0.0014882519
50     803 208320      6 0.0038684257
200      0     33 208771 0.0001580429
```

Figure 87: Training Data Confusion Matrix and OOB Estimate for “E_2”

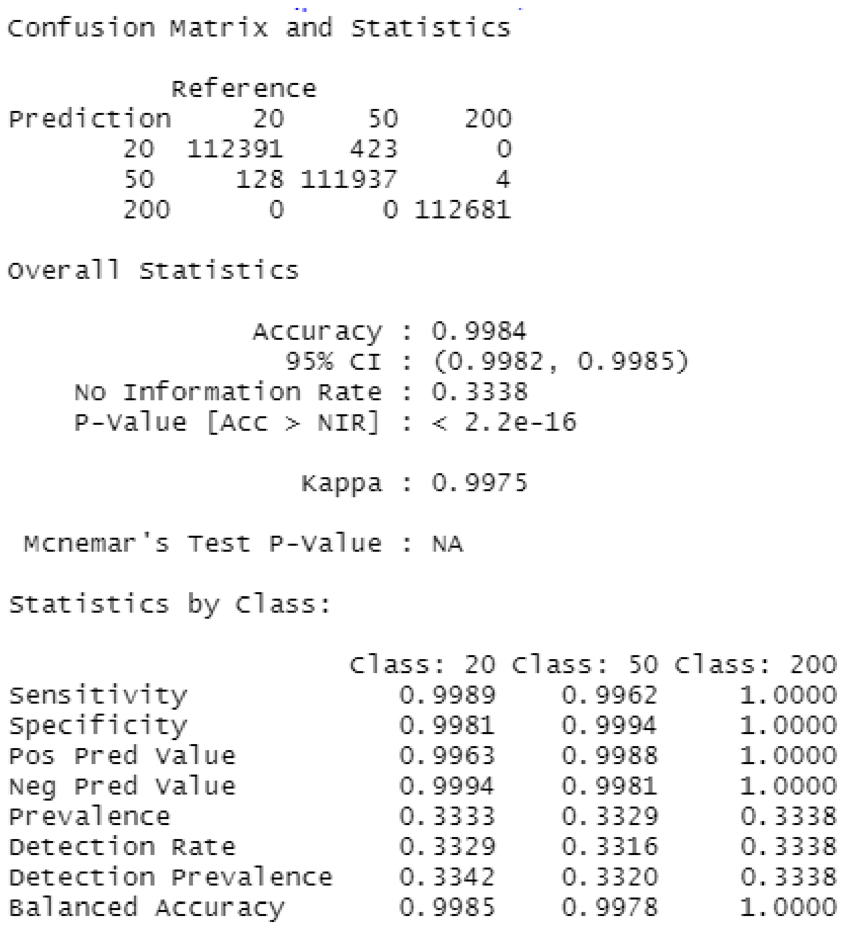

```
Confusion Matrix and Statistics

          Reference
Prediction     20     50    200
       20  112391    423      0
       50     128 111937      4
       200      0      0 112681

Overall Statistics

               Accuracy : 0.9984
                 95% CI : (0.9982, 0.9985)
    No Information Rate : 0.3338
    P-Value [Acc > NIR] : < 2.2e-16

                  Kappa : 0.9975

 Mcnemar's Test P-Value : NA

Statistics by Class:

                     Class: 20 Class: 50 Class: 200
Sensitivity             0.9989    0.9962     1.0000
Specificity             0.9981    0.9994     1.0000
Pos Pred Value          0.9963    0.9988     1.0000
Neg Pred Value          0.9994    0.9981     1.0000
Prevalence              0.3333    0.3329     0.3338
Detection Rate          0.3329    0.3316     0.3338
Detection Prevalence    0.3342    0.3320     0.3338
Balanced Accuracy       0.9985    0.9978     1.0000
```

Figure 88: Testing Data Confusion Matrix and Statistics for "E_2"

7.3.2 Subgrade Layer Modulus of Elasticity (E_3)

The predictor variables that built up the optimal model for "E_3" are: "DPeak_D.48", "DPeak_D.84", "DPeak_D.108", "DPeak_D.120", "T25L_D.120", "T50L_D.24", "T50R_D.48", "T50R_D.108", "T50R_D.120", "T75L_D.24", "T75R_D.60", "Dur50_D.108", "Dur75_D.36", "Dur75_D.120", "AL3", "AL4", "f2".

According to the MDA and MDG plots (Figure 89), the predictor variables that showed the highest importance for the MDA measure is "T75L_D.24" with a value of 61 while that for the MDG measure is "DPeak_D.84" with a value of 64,781.

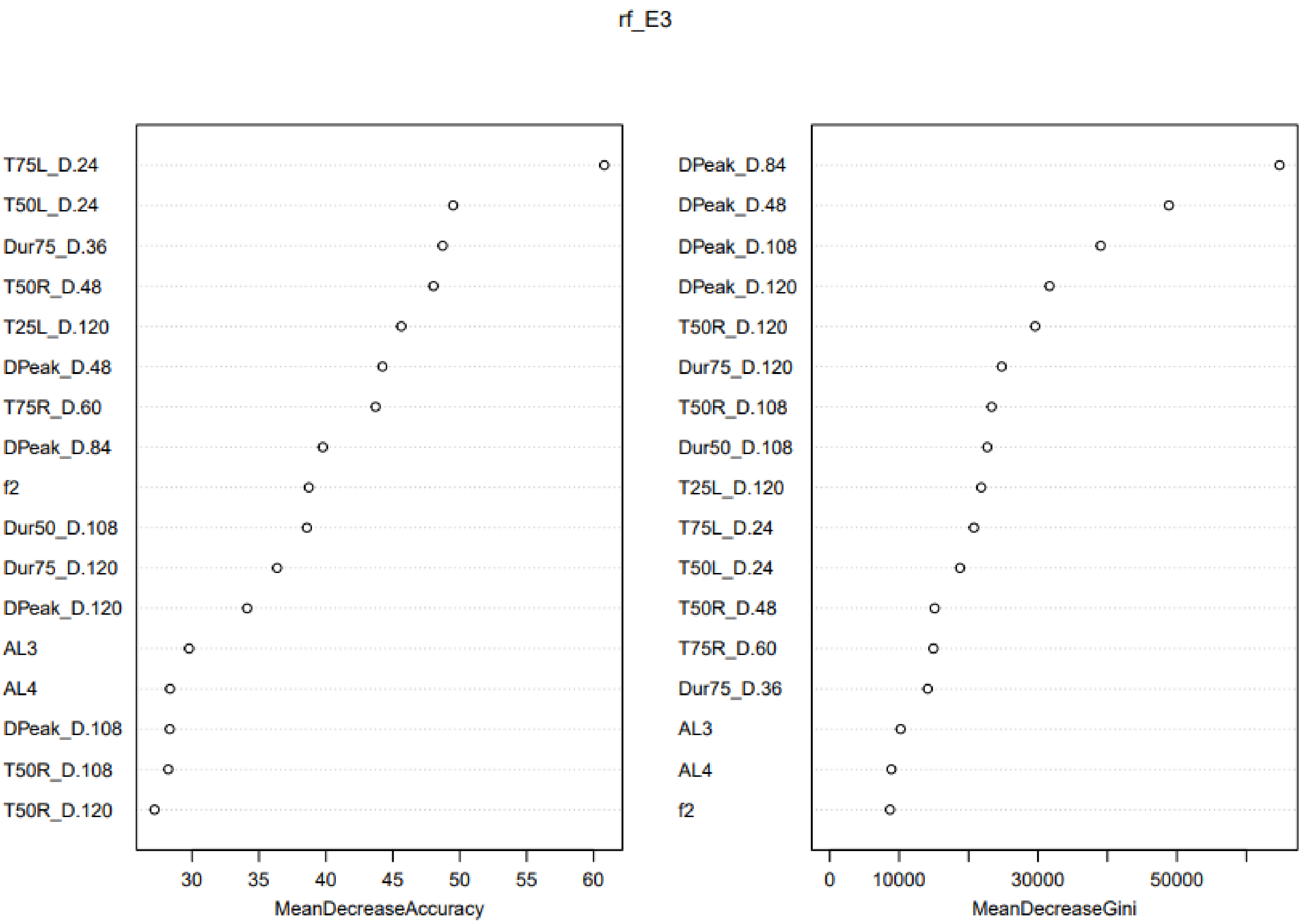

Figure 89: MDA and MDG Plots for "E_3"

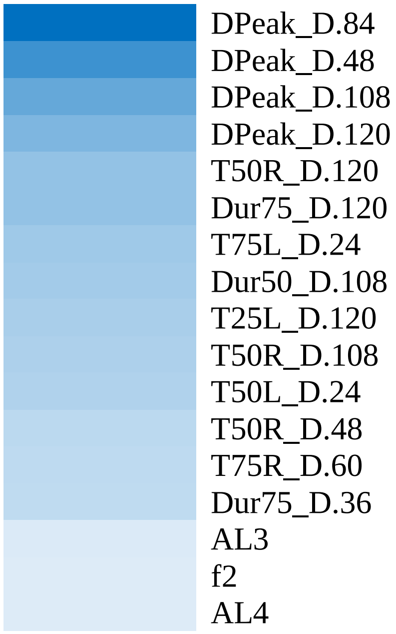

Based the total score calculated for each predictor variable, the color for the predictor variable "DPeak_D.84" showed the strongest intensity, indicating that this variable is the most important for predicting the modulus of elasticity "E_3" of the subgrade layer. Moving towards "AL_4", the color intensity starts fading away, indicating a decrease in the corresponding variable importance (Figure 90).

Figure 90: Importance of each Predictor Variable for Predicting "E_3" based on MDA and MDG Total Score

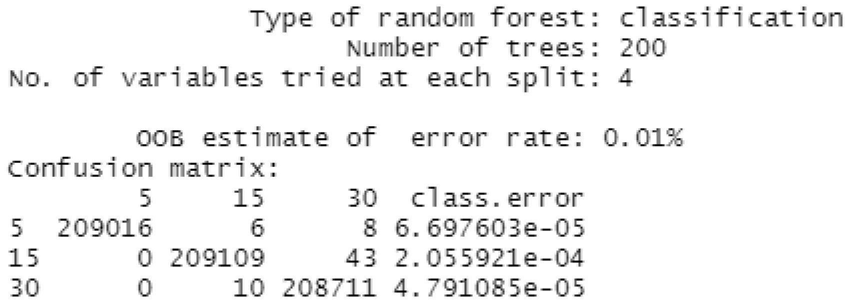

```
               Type of random forest: classification
                     Number of trees: 200
No. of variables tried at each split: 4

        OOB estimate of  error rate: 0.01%
Confusion matrix:
        5     15     30  class.error
5  209016      6      8 6.697603e-05
15      0 209109     43 2.055921e-04
30      0     10 208711 4.791085e-05
```

Figure 91: Training Data Confusion Matrix and OOB Estimate for “E_3”

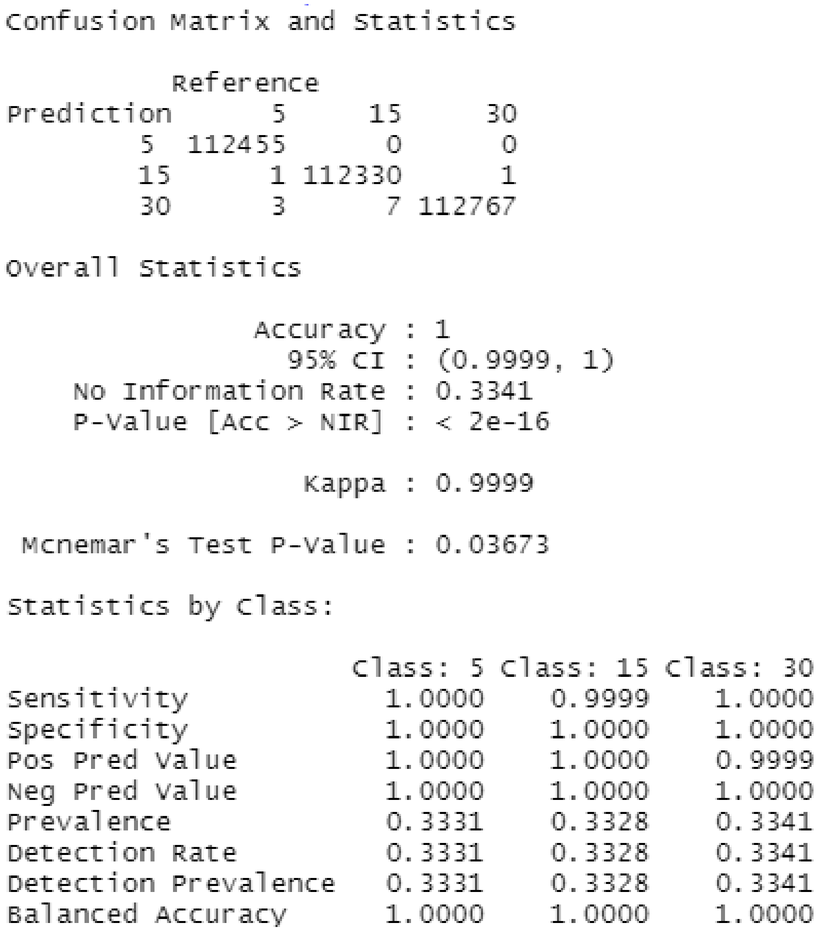

```
Confusion Matrix and Statistics

          Reference
Prediction      5     15     30
        5  112455      0      0
        15      1 112330      1
        30      3      7 112767

Overall Statistics

               Accuracy : 1
                 95% CI : (0.9999, 1)
    No Information Rate : 0.3341
    P-Value [Acc > NIR] : < 2e-16

                  Kappa : 0.9999

 Mcnemar's Test P-Value : 0.03673

Statistics by Class:

                     Class: 5 Class: 15 Class: 30
Sensitivity            1.0000    0.9999    1.0000
Specificity            1.0000    1.0000    1.0000
Pos Pred Value         1.0000    1.0000    0.9999
Neg Pred Value         1.0000    1.0000    1.0000
Prevalence             0.3331    0.3328    0.3341
Detection Rate         0.3331    0.3328    0.3341
Detection Prevalence   0.3331    0.3328    0.3341
Balanced Accuracy      1.0000    1.0000    1.0000
```

Figure 92: Testing Data Confusion Matrix and Statistics “E_3”

7.3.3 Stiff Layer Modulus of Elasticity (E_4)

The predictor variables that built up the optimal model for “E_4” are:

"DPeak_D.0", "DPeak_D.24", "DPeak_D.72", "DPeak_D.96", "DPeak_D.108", "DPeak_D.120", "DminR_D.36","DminR_D.48","DminR_D.60","DminR_D.72","DminR_D.84","DminR_D.96", "DminR_D.108", "DminR_D.120", "TDminR_D.84", "TDminR_D.96", "TDminR_D.108", "TDminR_D.120", "T25R_D.96", "T25R_D.120", "Dur25_D.48", "Dur25_D.60", "Dur25_D.96", "Dur25_D.108", "Dur25_D.120", "Dur75_D.0", "Dur75_D.120","Dur50_D.120", "T25L108120", "T50L812", "T50L108120", "T25L_D.8", "T25L_D.12", "T25L_D.60", "T25L_D.96", "T25L_D.120", "T75L08", "T75L812", "T75L1218", "T75L96108", "T75L108120", "T25R1218", "T25R1824", "T25R6072", "T25R7284", "T25R8496", "T25R96108", "T25R108120", "T50R6072", "T50R7284", "T50R8496", "T50R96108", "T50R108120", "T75R08", "T75R6072", "T75R7284", "T75R108120", "D25_08", "D25_4860", "D25_8496", "D0_2550", "D84_2550", "D96_2550", "D108_2550", "D120_2550"

"T75L08" showed the highest importance for the MDA measure with a value of 104 while is "T25R108120" was the most important predictor variable for the MDG measure with a value of 20,790.

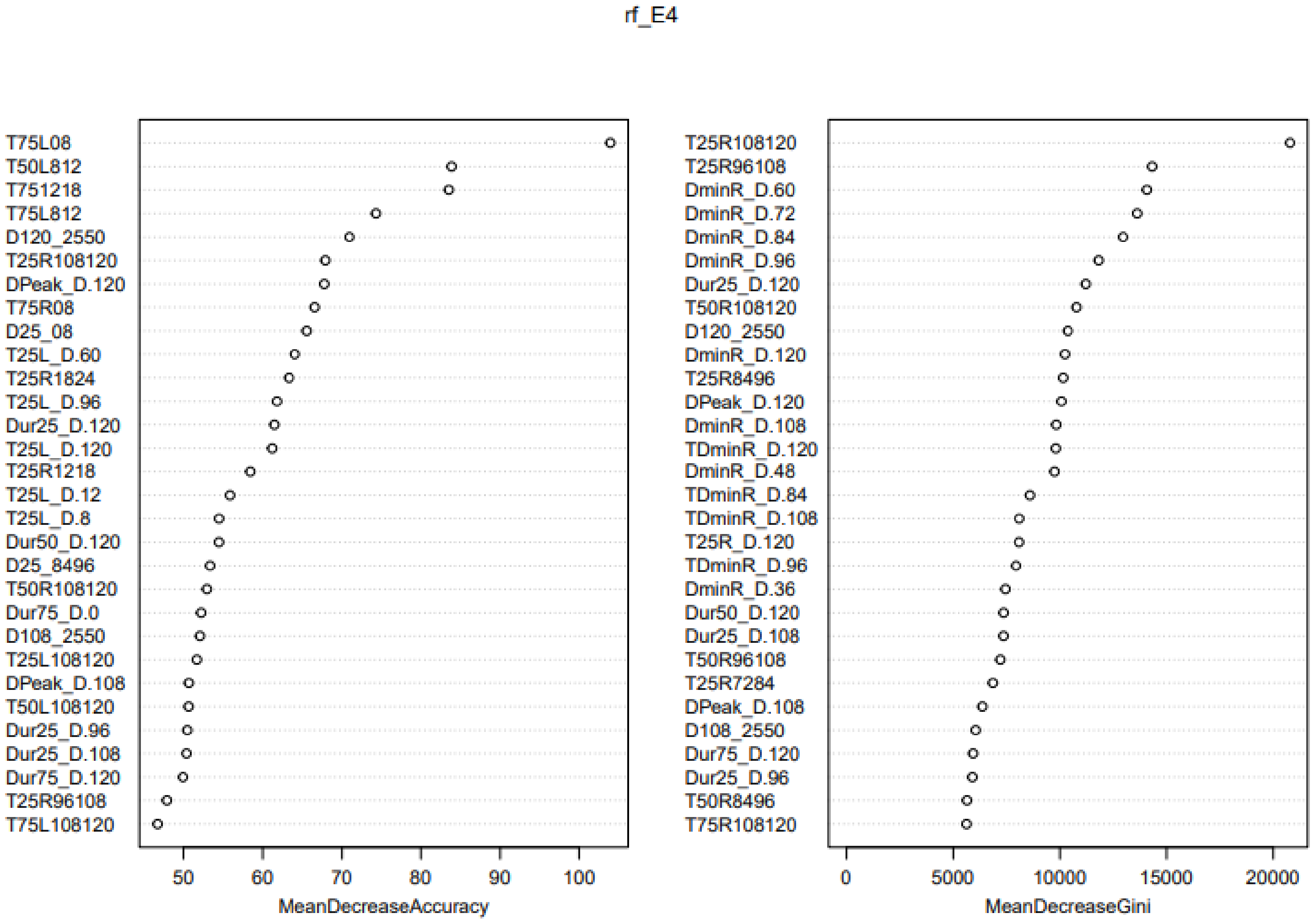

Figure 93: MDA and MDG Plots for "E_4"

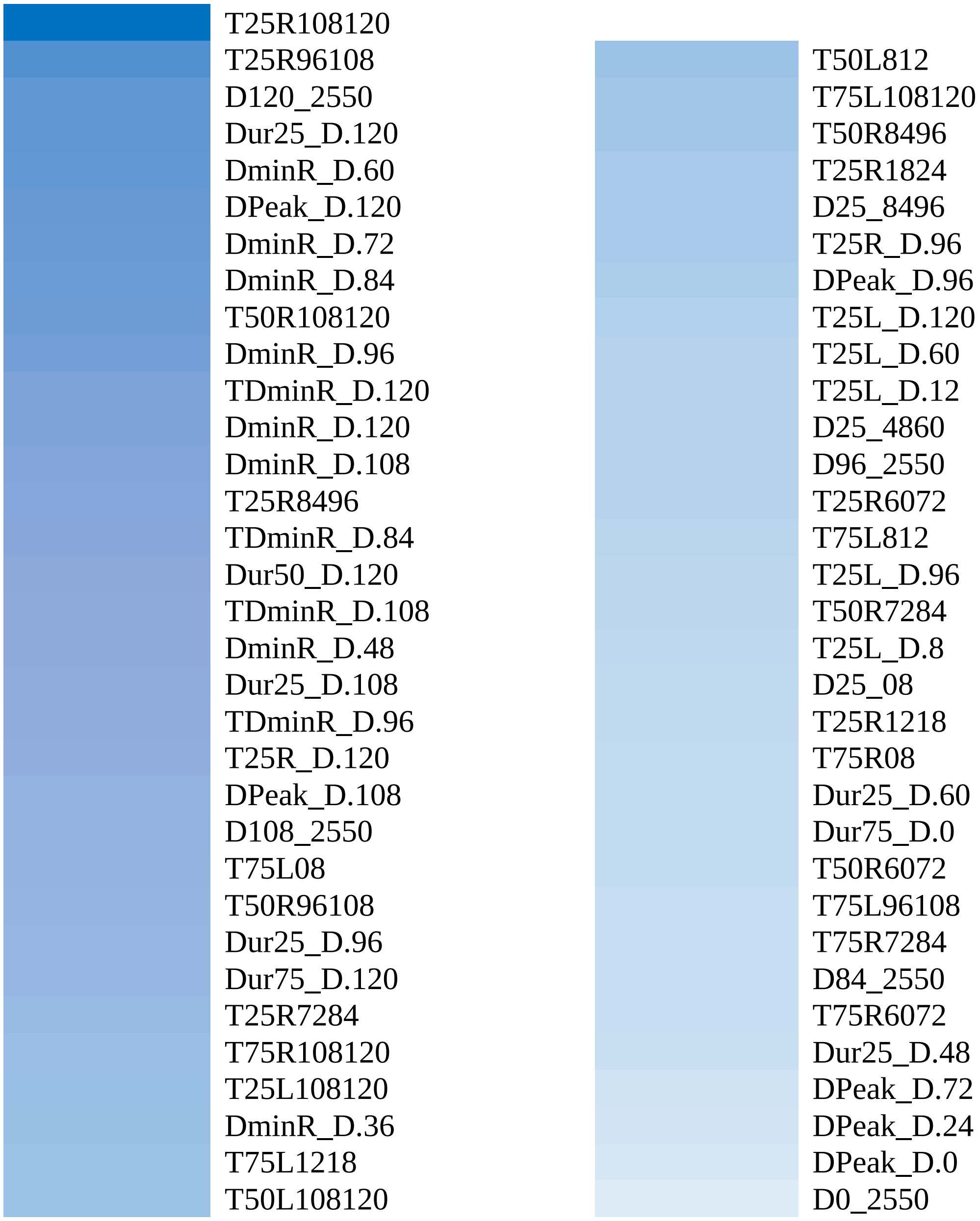

Figure 94: Importance of each Predictor Variable for Predicting "E_4" based on MDA and MDG Total Score (2 Sections)

Based the total score calculated for each predictor variable, the color for the predictor variable "T25R108120" showed the strongest intensity, indicating that this variable is the most important for predicting the modulus of elasticity "E_4" of the stiff layer. Moving towards "D0_2550", the color intensity starts fading away, indicating a decrease in the corresponding variable importance (Figure 94). Note that the variables are divided into 2 sections in descending order of importance from left to right.

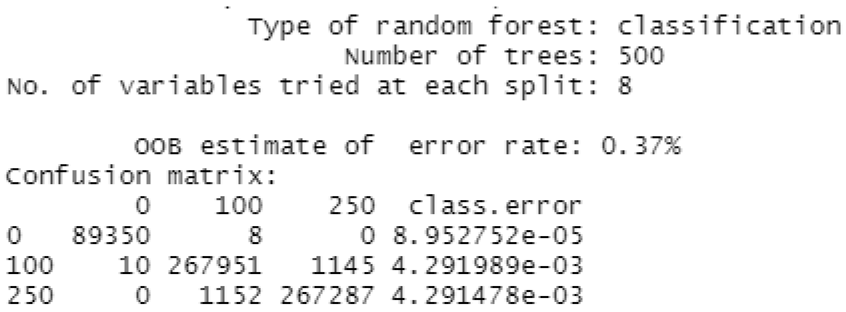

```
               Type of random forest: classification
                     Number of trees: 500
No. of variables tried at each split: 8

        OOB estimate of  error rate: 0.37%
Confusion matrix:
        0    100    250  class.error
0   89350      8      0 8.952752e-05
100    10 267951   1145 4.291989e-03
250     0   1152 267287 4.291478e-03
```

Figure 95: Training Data Confusion Matrix and OOB Estimate for “E_4”

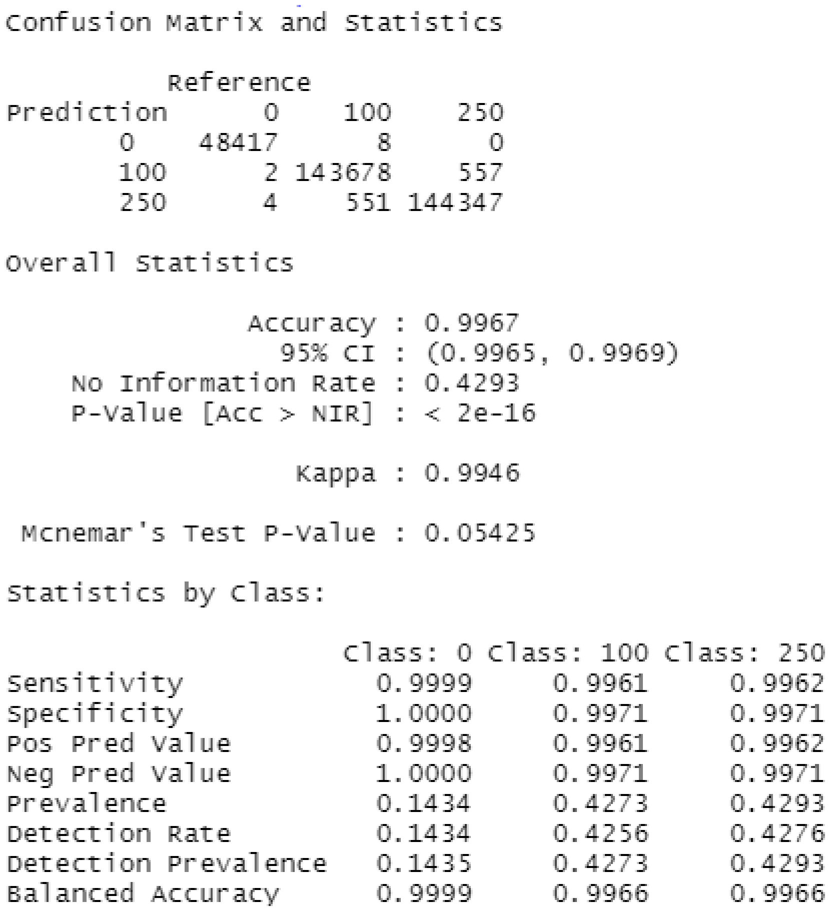

```
Confusion Matrix and Statistics

          Reference
Prediction      0    100    250
       0    48417      8      0
       100      2 143678    557
       250      4    551 144347

Overall Statistics

               Accuracy : 0.9967
                 95% CI : (0.9965, 0.9969)
    No Information Rate : 0.4293
    P-Value [Acc > NIR] : < 2e-16

                  Kappa : 0.9946

 Mcnemar's Test P-Value : 0.05425

Statistics by Class:

                     Class: 0 Class: 100 Class: 250
Sensitivity            0.9999     0.9961     0.9962
Specificity            1.0000     0.9971     0.9971
Pos Pred Value         0.9998     0.9961     0.9962
Neg Pred Value         1.0000     0.9971     0.9971
Prevalence             0.1434     0.4273     0.4293
Detection Rate         0.1434     0.4256     0.4276
Detection Prevalence   0.1435     0.4273     0.4293
Balanced Accuracy      0.9999     0.9966     0.9966
```

Figure 96: Testing Data Confusion Matrix and Statistics “E_4”

7.3.4 Rayleigh Damping Parameters (α_R)

The predictor variables that built up the optimal model for “α_R” are: "DPeak_D.0","DPeak_D.8", "DPeak_D.12", "DPeak_D.18","DPeak_D.24","DPeak_D.36", "DPeak_D.48", "DPeak_D.60", "DPeak_D.72", "DPeak_D.84", "DPeak_D.96", "DPeak_D.108", "DPeak_D.120", "TPeak_D.0", "TPeak_D.8", "TPeak_D.12", "TPeak_D.18", "TPeak_D.24", "TPeak_D.36","TPeak_D.48","TPeak_D.60", "TPeak_D.72", "TPeak_D.84", "TPeak_D.96", "TPeak_D.108", "DminR_D.12", "DminR_D.18", "DminR_D.24", "DminR_D.36", "DminR_D.48","DminR_D.60", "DminR_D.72", "DminR_D.84", "DminR_D.96", "DminR_D.108", "DminR_D.120", "TDminR_D.24", "TDminR_D.36", "TDminR_D.48", "TDminR_D.60", "TDminR_D.84", "TDminR_D.72","TDminR_D.96","TDminR_D.108", "TDminR_D.120", "T25R_D.0", "T25R_D.12", "T25R_D.18", "T25R_D.24", "T25R_D.36", "T25R_D.48", "T25R_D.60", "T25R_D.72", "T25R_D.84", "T25R_D.96", "T25R_D.108", "T25R_D.120", "T50R_D.0","T50R_D.12","T50R_D.18","T50R_D.24", "T50R_D.36", "T50R_D.48", "T50R_D.60", "T50R_D.72","T50R_D.84", "T50R_D.8", "T50R_D.96", "T50R_D.108", "T50R_D.120", "T75R_D.0", "T75R_D.8","T75R_D.12", "T75R_D.18", "T75R_D.24","T75R_D.36", "T75R_D.48", "T75R_D.60", "T75R_D.72", "T75R_D.84", "T75R_D.96", "T75R_D.108", "T75R_D.120","T25L_D.0","T25L_D.8", "T25L_D.12", "T25L_D.18", "T25L_D.24", "T25L_D.36", "T25L_D.48", "T25L_D.60", "T25L_D.72", "T25L_D.84","T25L_D.96","T25L_D.108", "T25L_D.120", "T50L_D.0", "T50L_D.8", "T50L_D.18", "T50L_D.12", "T50L_D.24", "T50L_D.36", "T50L_D.48", "T50L_D.60", "T50L_D.72","T50L_D.84","T50L_D.120", "T75L_D.0", "T75L_D.8", "T75L_D.12", "T75L_D.18", "T75L_D.24", "T75L_D.36", "T75L_D.48", "T75L_D.60", "T75L_D.72", "T75L_D.84", "T75L_D.108", "T75L_D.120", "Dur25_D.60", "Dur25_D.72", "Dur25_D.84", "Dur25_D.96", "Dur25_D.108", "Dur25_D.120","Dur50_D.12","Dur50_D.18","Dur50_D.24", "Dur50_D.36", "Dur50_D.48", "Dur50_D.60", "Dur50_D.72", "Dur50_D.84", "Dur50_D.120", "Dur75_D.0", "Dur75_D.8", "Dur75_D.12", "Dur75_D.18", "Dur75_D.24", "Dur75_D.36", "Dur75_D.48", "Dur75_D.60", "Dur75_D.72", "Dur75_D.84", "Dur75_D.96", "Dur75_D.108", "Dur75_D.120", "AREA", "AL1", "AL2", "AL3", "AL4", "f1", "Qr", "f2", "RoC", "S", "Dp6072", "Dp7284", "Dp8496", "Dp96108", "Dp108120", "Tp3648", "Tp4860", "Tp7284", "Tp108120", "D25_08", "D25_812", "D25_1824","D25_108120", "D24_2550", "D84_2550", "D96_2550", "D108_2550","D120_2550"

"Q_r" showed the highest importance for the MDA measure with a value of 85 while is "DminR_D.120" was the most important predictor variable for the MDG measure with a value of 13,128 (Figure 97).

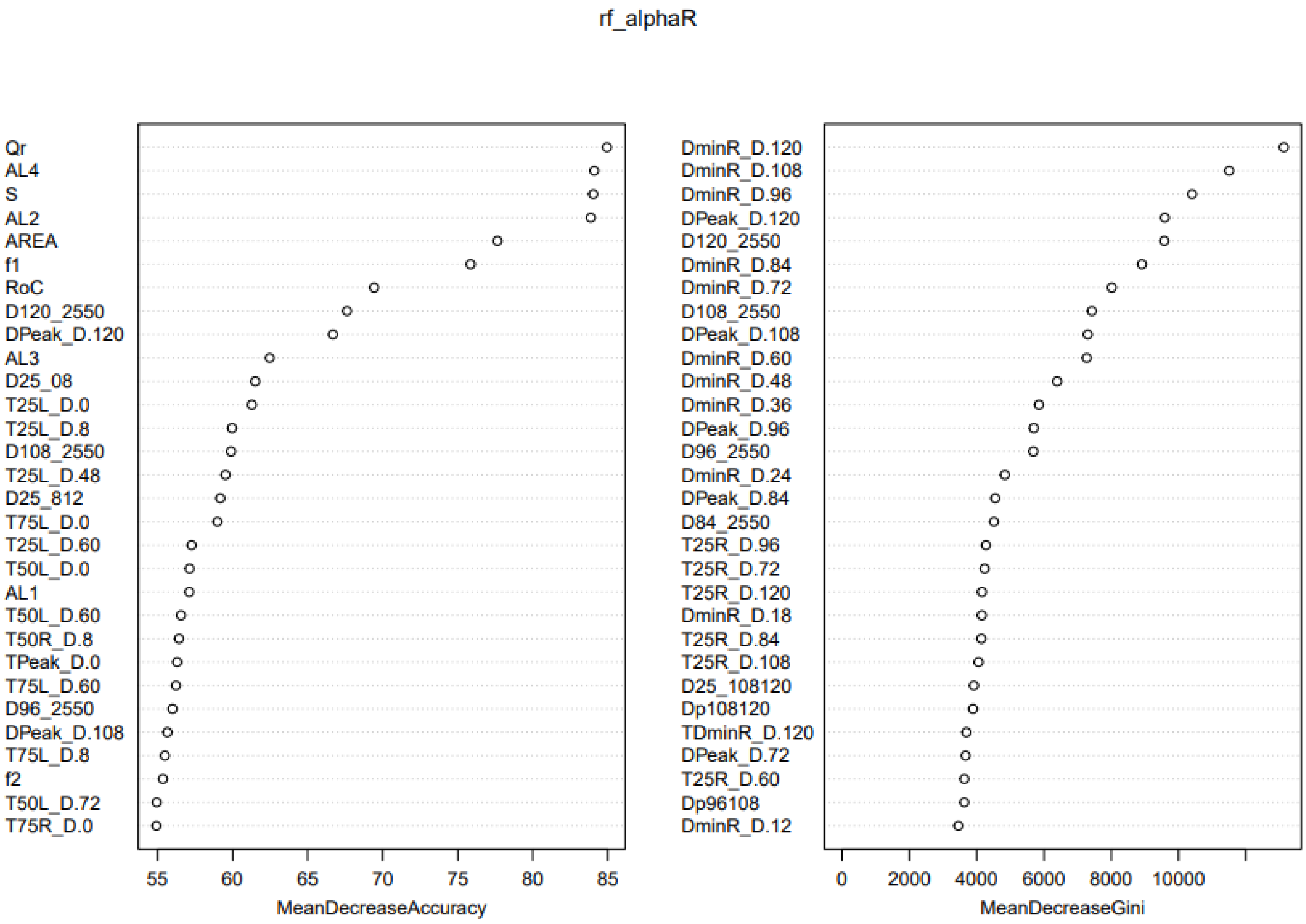

Figure 97: MDA and MDG Plots for “α_R”

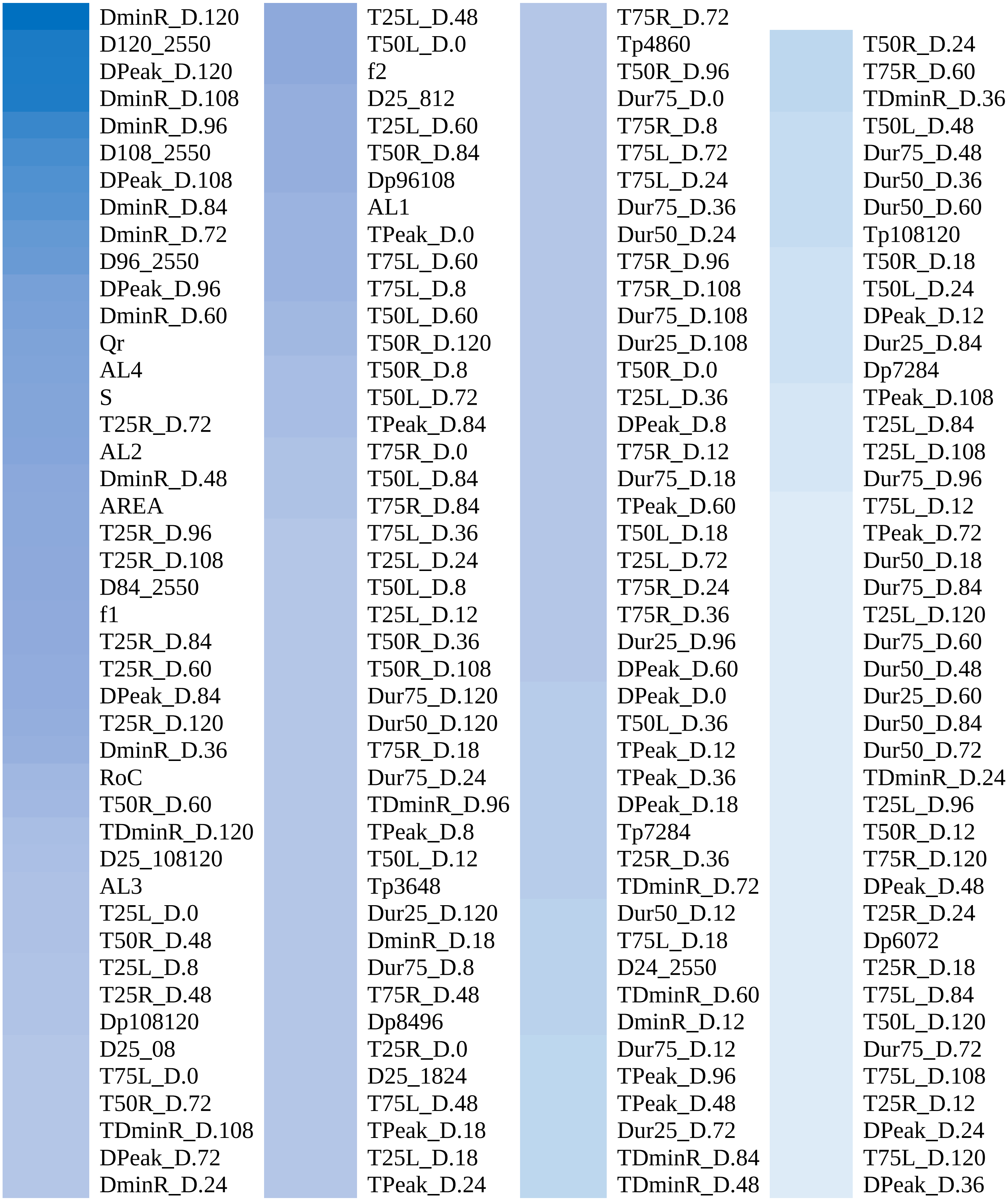

DminR_D.120
D120_2550
DPeak_D.120
DminR_D.108
DminR_D.96
D108_2550
DPeak_D.108
DminR_D.84
DminR_D.72
D96_2550
DPeak_D.96
DminR_D.60
Qr
AL4
S
T25R_D.72
AL2
DminR_D.48
AREA
T25R_D.96
T25R_D.108
D84_2550
f1
T25R_D.84
T25R_D.60
DPeak_D.84
T25R_D.120
DminR_D.36
RoC
T50R_D.60
TDminR_D.120
D25_108120
AL3
T25L_D.0
T50R_D.48
T25L_D.8
T25R_D.48
Dp108120
D25_08
T75L_D.0
T50R_D.72
TDminR_D.108
DPeak_D.72
DminR_D.24
T25L_D.48
T50L_D.0
f2
D25_812
T25L_D.60
T50R_D.84
Dp96108
AL1
TPeak_D.0
T75L_D.60
T75L_D.8
T50L_D.60
T50R_D.120
T50R_D.8
T50L_D.72
TPeak_D.84
T75R_D.0
T50L_D.84
T75R_D.84
T75L_D.36
T25L_D.24
T50L_D.8
T25L_D.12
T50R_D.36
T50R_D.108
Dur75_D.120
Dur50_D.120
T75R_D.18
Dur75_D.24
TDminR_D.96
TPeak_D.8
T50L_D.12
Tp3648
Dur25_D.120
DminR_D.18
Dur75_D.8
T75R_D.48
Dp8496
T25R_D.0
D25_1824
T75L_D.48
TPeak_D.18
T25L_D.18
TPeak_D.24
T75R_D.72
Tp4860
T50R_D.96
Dur75_D.0
T75R_D.8
T75L_D.72
T75L_D.24
Dur75_D.36
Dur50_D.24
T75R_D.96
T75R_D.108
Dur75_D.108
Dur25_D.108
T50R_D.0
T25L_D.36
DPeak_D.8
T75R_D.12
Dur75_D.18
TPeak_D.60
T50L_D.18
T25L_D.72
T75R_D.24
T75R_D.36
Dur25_D.96
DPeak_D.60
DPeak_D.0
T50L_D.36
TPeak_D.12
TPeak_D.36
DPeak_D.18
Tp7284
T25R_D.36
TDminR_D.72
Dur50_D.12
T75L_D.18
D24_2550
TDminR_D.60
DminR_D.12
Dur75_D.12
TPeak_D.96
TPeak_D.48
Dur25_D.72
TDminR_D.84
TDminR_D.48
T50R_D.24
T75R_D.60
TDminR_D.36
T50L_D.48
Dur75_D.48
Dur50_D.36
Dur50_D.60
Tp108120
T50R_D.18
T50L_D.24
DPeak_D.12
Dur25_D.84
Dp7284
TPeak_D.108
T25L_D.84
T25L_D.108
Dur75_D.96
T75L_D.12
TPeak_D.72
Dur50_D.18
Dur75_D.84
T25L_D.120
Dur75_D.60
Dur50_D.48
Dur25_D.60
Dur50_D.84
Dur50_D.72
TDminR_D.24
T25L_D.96
T50R_D.12
T75R_D.120
DPeak_D.48
T25R_D.24
Dp6072
T25R_D.18
T75L_D.84
T50L_D.120
Dur75_D.72
T75L_D.108
T25R_D.12
DPeak_D.24
T75L_D.120
DPeak_D.36

Figure 98: Importance of each Predictor Variable for Predicting "α_R" based on MDA and MDG Total Score (4 Sections)

Based the total score calculated for each predictor variable, the color for the predictor variable “DminR_D.120” showed the strongest intensity, indicating that this variable is the most important for predicting the Rayleigh Damping Parameter “α_R” for the unbound layer. Moving towards “DPeak_D.36”, the color intensity starts fading away, indicating a decrease in the corresponding variable importance (Figure 98). Note that the variables are divided into 4 sections in descending order of importance from left to right.

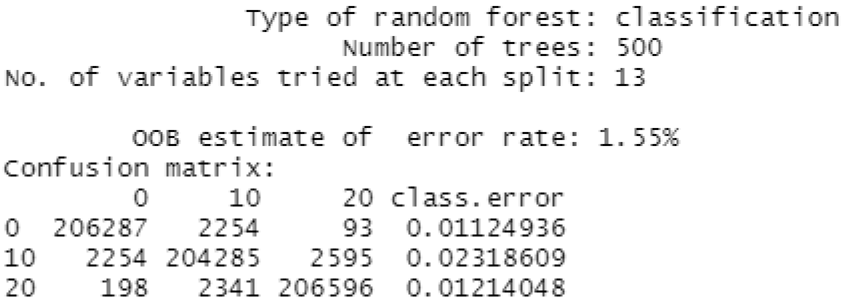

```
               Type of random forest: classification
                     Number of trees: 500
No. of variables tried at each split: 13

        OOB estimate of  error rate: 1.55%
Confusion matrix:
        0     10     20 class.error
0  206287   2254     93  0.01124936
10   2254 204285   2595  0.02318609
20    198   2341 206596  0.01214048
```

Figure 99: Training Data Confusion Matrix and OOB Estimate for “α_R”

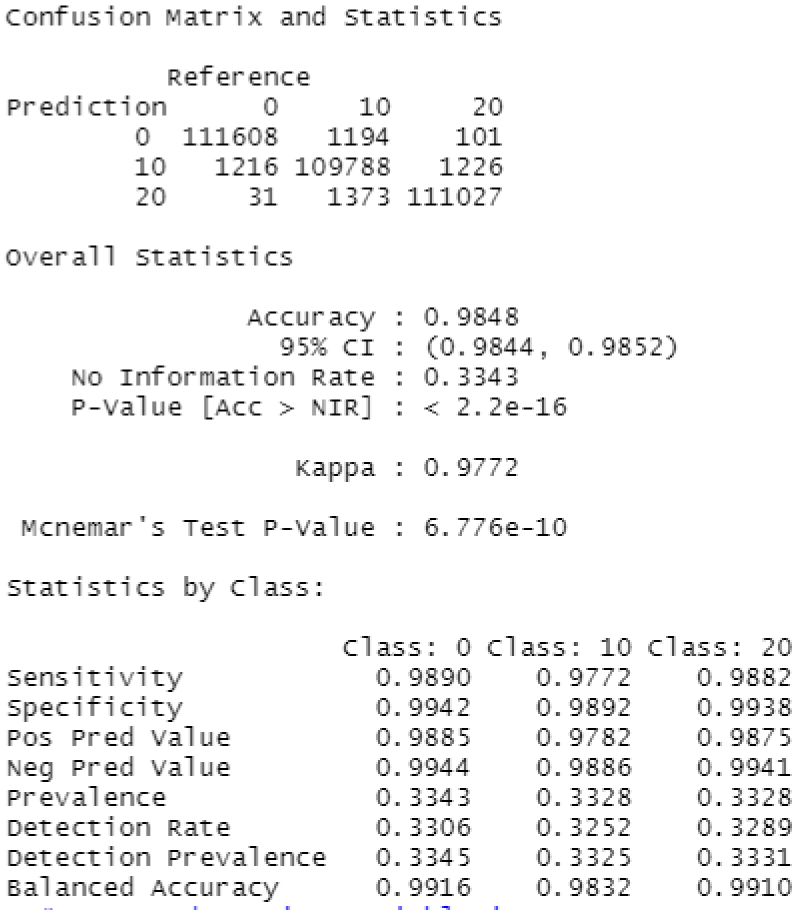

```
Confusion Matrix and Statistics

          Reference
Prediction      0     10     20
        0  111608   1194    101
        10   1216 109788   1226
        20     31   1373 111027

Overall Statistics

               Accuracy : 0.9848
                 95% CI : (0.9844, 0.9852)
    No Information Rate : 0.3343
    P-Value [Acc > NIR] : < 2.2e-16

                  Kappa : 0.9772

 Mcnemar's Test P-Value : 6.776e-10

Statistics by Class:

                     Class: 0 Class: 10 Class: 20
Sensitivity            0.9890    0.9772    0.9882
Specificity            0.9942    0.9892    0.9938
Pos Pred Value         0.9885    0.9782    0.9875
Neg Pred Value         0.9944    0.9886    0.9941
Prevalence             0.3343    0.3328    0.3328
Detection Rate         0.3306    0.3252    0.3289
Detection Prevalence   0.3345    0.3325    0.3331
Balanced Accuracy      0.9916    0.9832    0.9910
```

Figure 100:Testing Data Confusion Matrix and Statistics for “α_R”

7.3.5 Rayleigh Damping Parameters ($\boldsymbol{\beta_R}$)

The predictor variables that built up the optimal model for “β_R” are: "DPeak_D.60","DPeak_D.72", "DPeak_D.84", "DPeak_D.96", "DPeak_D.108", "TPeak_D.0", "TPeak_D.8", "TPeak_D.12", "TPeak_D.18", "TPeak_D.24", "TPeak_D.36", "TPeak_D.48", "TPeak_D.60", "DminR_D.96", "DminR_D.108", "DminR_D.120", "DminL_D.96", "DminL_D.108", "DminL_D.120", "TDminR_D.120", "T25R_D.12", "T25R_D.18", "T25R_D.24", "T25R_D.36", "T25R_D.48", "T25R_D.60", "T25R_D.72", "T25R_D.84", "T25R_D.96", "T25R_D.108", "T25R_D.120", "T25L_D.0", "T25L_D.8", "T25L_D.12", "T25L_D.48", "T25L_D.60", "T25L_D.72", "T25L_D.96", "T25L_D.120","T50L_D.0", "T50L_D.8", "T50L_D.36", "T50L_D.72", "T75L_D.0", "T75L_D.8", "T75L_D.24", "T75L_D.36","T75L_D.48", "Dur25_D.120", "Dur50_D.12", "Dur50_D.18", "Dur75_D.12", "Dur75_D.18", "Dur75_D.24", "Dur75_D.120", ","RoC", "BDI", "AUPP", "AL1", "f2", "Qr", "SD", "BI", "SCI", "BCI", "S", "AREA", "AUPP", "AL2", "AL3","T25L08", "T25L1218", "T25L1824", "T25L2436", "T25L3648", "T25L4860", "T25L7284", "T25L8496", "T25L96108", "T25L108120","T50L08", "T501218", "T50L1824", "T50L2436", "T50L3648", "T50L4860", "T50L6072", "T50L7284", "T50L8496","T50L96108", "T50L108120", "T75L08", "T75L812", "T75L1218", "T75L1824", "T75L2436", "T75L3648", "T75L4860", "T75L6072", "T75L7284", "T75L8496", "T75L96108", "T75L108120", "T25R108120", "T75R08", "T25R96108", "T50R08", "T25R2436", "T50R3648", "T50R2436", "T75R2436", "T25R8496", "T75R8496", "T25R3648", "T75R4860", "T50R1824", "T75R108120", "T75R3648", "Dp96108"," Dp108120", "Dml96108", "Dml108120", "Tr08", "Tml108120"

"T25L108120" showed the highest importance for the MDA measure with a value of 58 while is "DPeak_D.108" was the most important predictor variable for the MDG measure with a value of 14,371 (Figure 101).

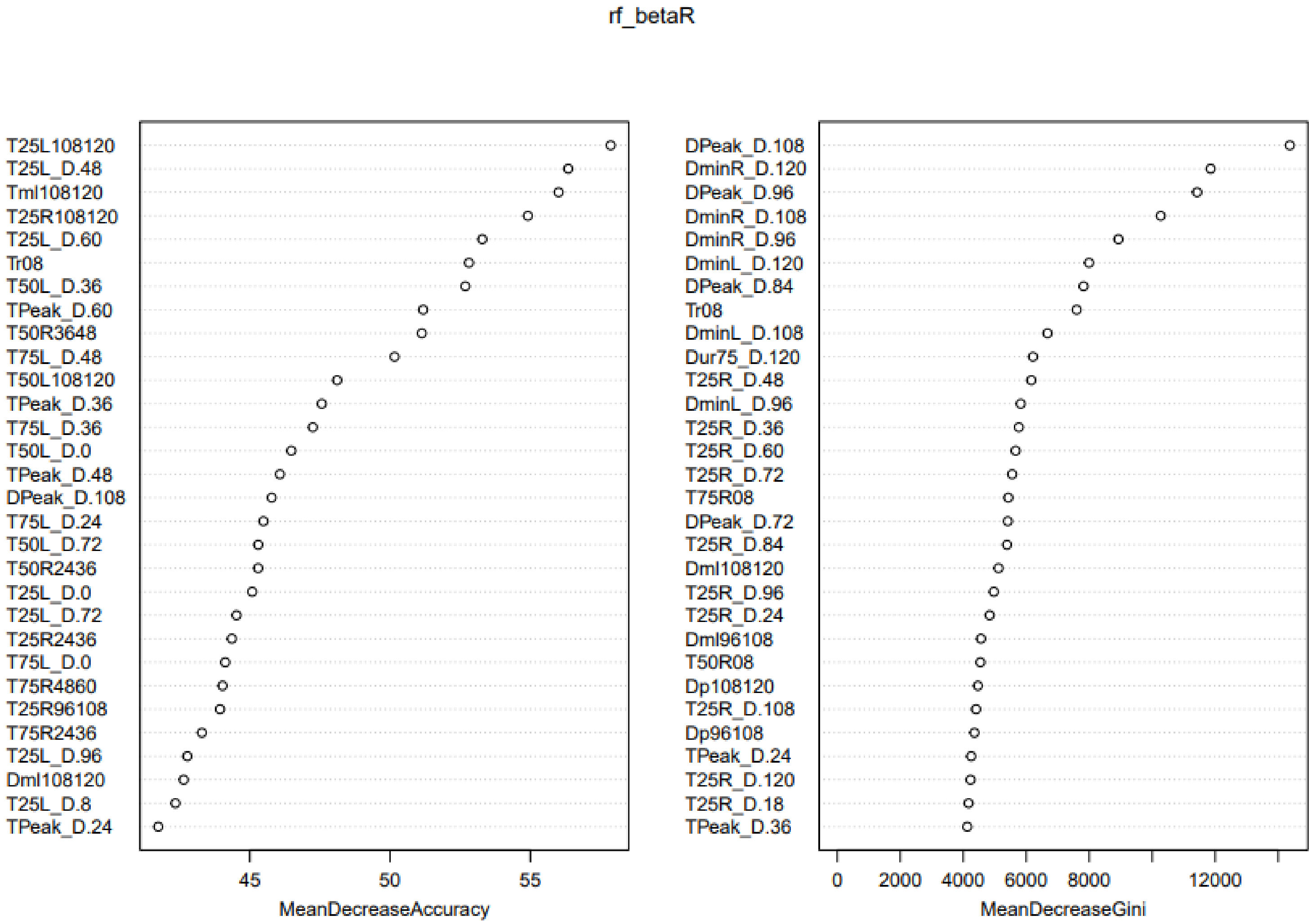

Figure 101:MDA and MDG Plots for “β_R”

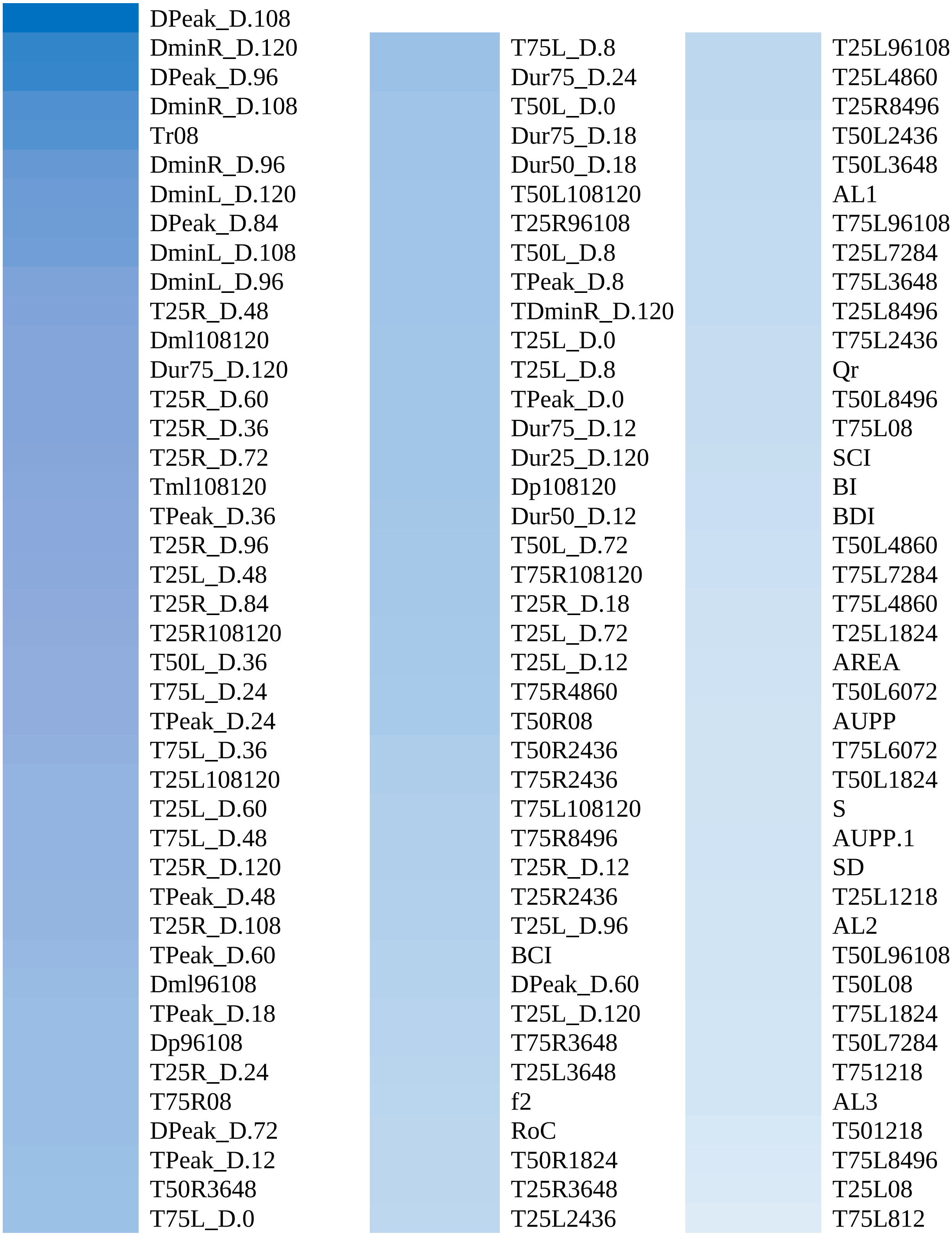

Figure 102:Importance of each Predictor Variable for Predicting "β_R" based on MDA and MDG Total Score (3 Sections)

Based the total score calculated for each predictor variable, the color for the predictor variable "DPeak_D.108" showed the strongest intensity, indicating that this variable is the most important for predicting "β_R". Moving towards "T75L812", the color intensity starts fading away, indicating a decrease in the corresponding variable importance (Figure 102). Note that the variables are divided into 3 sections in descending order of importance from left to right.

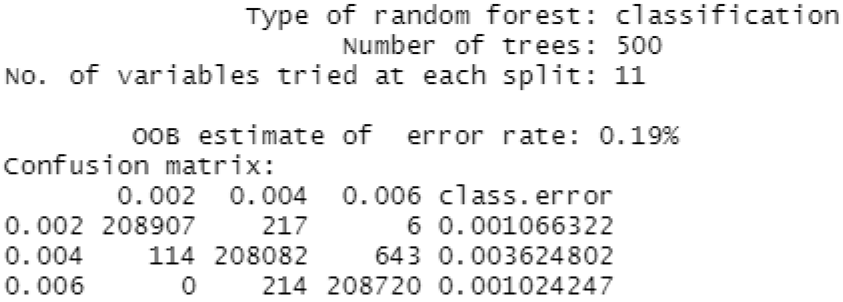

```
               Type of random forest: classification
                     Number of trees: 500
No. of variables tried at each split: 11

        OOB estimate of  error rate: 0.19%
Confusion matrix:
       0.002  0.004  0.006 class.error
0.002 208907    217      6 0.001066322
0.004    114 208082    643 0.003624802
0.006      0    214 208720 0.001024247
```

Figure 103: Training Data Confusion Matrix and OOB Estimate for "β_R"

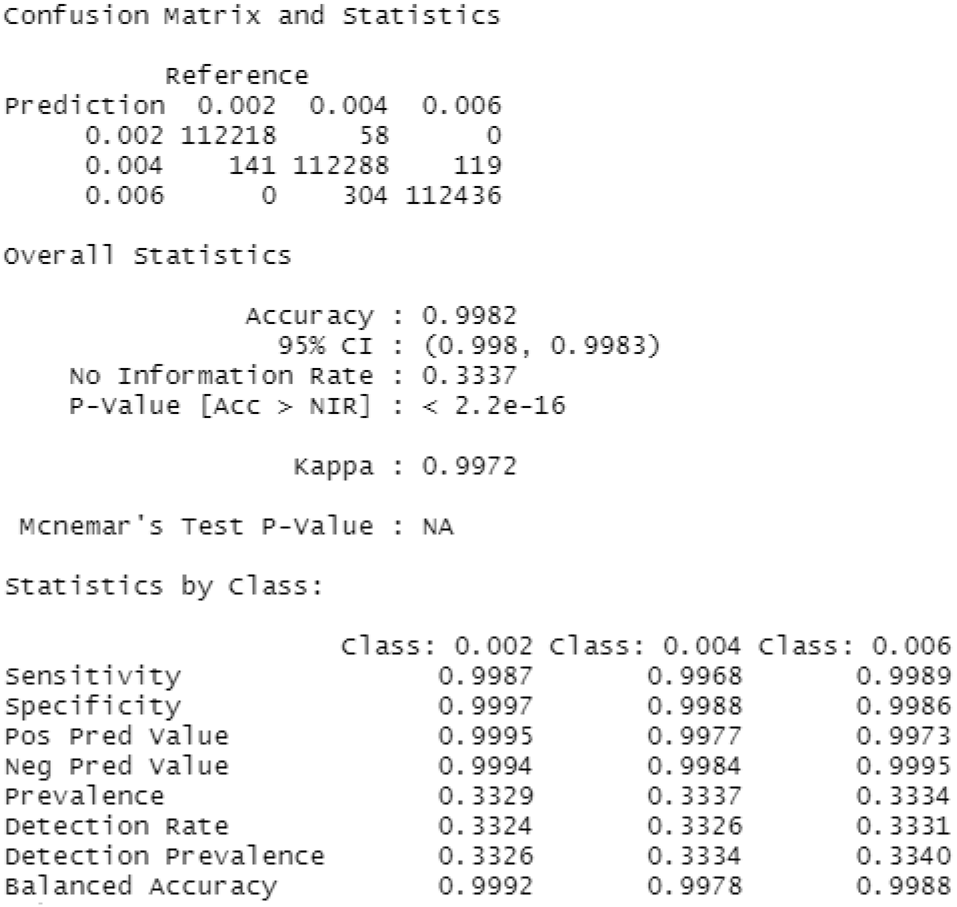

```
Confusion Matrix and Statistics

          Reference
Prediction  0.002  0.004  0.006
     0.002 112218     58      0
     0.004    141 112288    119
     0.006      0    304 112436

Overall Statistics

               Accuracy : 0.9982
                 95% CI : (0.998, 0.9983)
    No Information Rate : 0.3337
    P-Value [Acc > NIR] : < 2.2e-16

                  Kappa : 0.9972

 Mcnemar's Test P-Value : NA

Statistics by Class:

                     Class: 0.002 Class: 0.004 Class: 0.006
Sensitivity                0.9987       0.9968       0.9989
Specificity                0.9997       0.9988       0.9986
Pos Pred Value             0.9995       0.9977       0.9973
Neg Pred Value             0.9994       0.9984       0.9995
Prevalence                 0.3329       0.3337       0.3334
Detection Rate             0.3324       0.3326       0.3331
Detection Prevalence       0.3326       0.3334       0.3340
Balanced Accuracy          0.9992       0.9978       0.9988
```

Figure 104:Testing Data Confusion Matrix and Statistics for "β_R"

7.3.6 Stiff Layer Thickness measured from Surface (h_3)

The predictor variables that built up the optimal model for “h_3” are: "DPeak_D.108","DPeak_D.120","TPeak_D.120","DminR_D.18","DminR_D.48", "DminR_D.60","DminR_D.72","DminR_D.84", "DminR_D.108", "DminR_D.120","Dur25_D.48","Dur25_D.108","Dur25_D.120","Dur50_D.120","Dp108120", "Tp108120", "T25R3648", "T25R8496", "T25R108120", "T50R96108", "T50L108120"

According to the MDA and MDG plots (Figure 105), the predictor variables that showed the highest importance for the MDA measure is "Dp108120" with a value of 70 while that for the MDG measures is "T25R3648" with a value of 28,755.

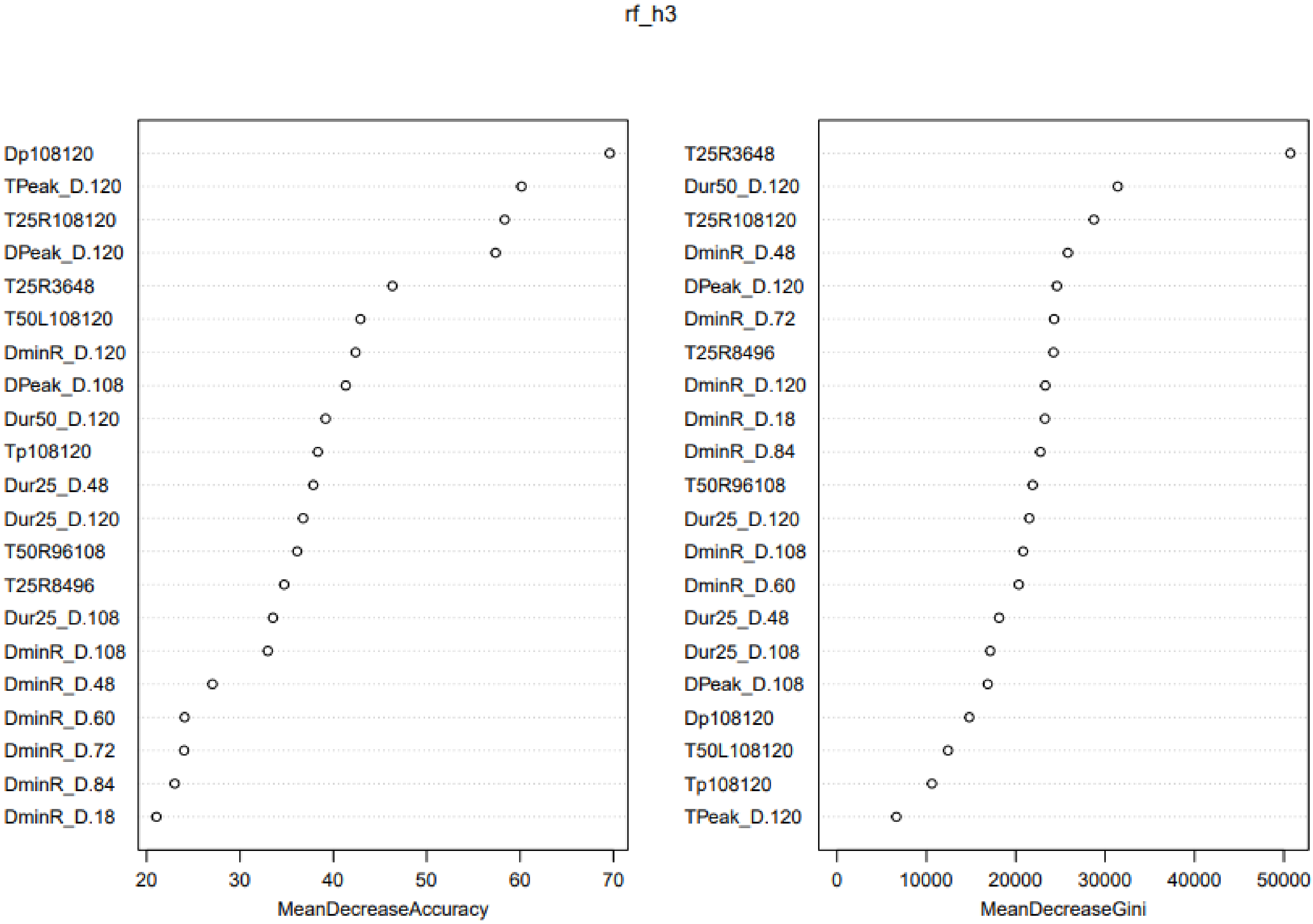

Figure 105: MDA and MDG Plots for “h_3”

Based the total score calculated for each predictor variable, the color for the predictor variable “T25R3648” showed the strongest intensity, indicating that this variable is the most important for predicting the stiff layer thickness measured from the surface “h_3” of the subgrade layer. Moving towards “TPeak_D.120”, the color intensity starts fading away, indicating a decrease in the corresponding variable importance (Figure 106).

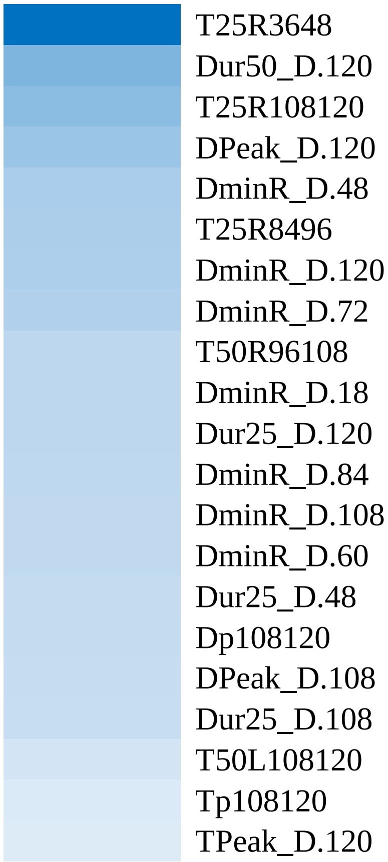

Figure 106: Importance of each Predictor Variable for Predicting “h_3” based on MDA and MDG Total Score

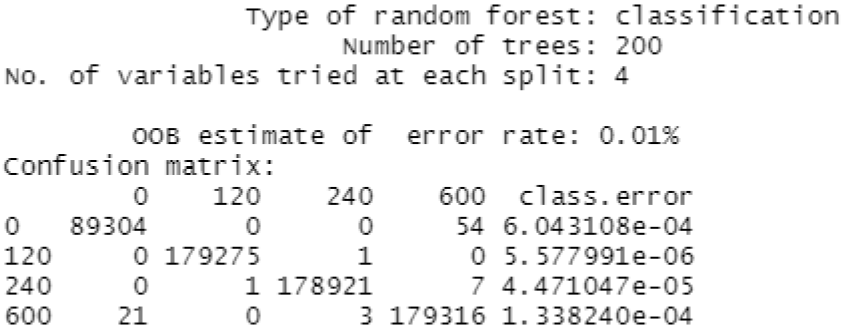

```
                Type of random forest: classification
                      Number of trees: 200
No. of variables tried at each split: 4

        OOB estimate of  error rate: 0.01%
Confusion matrix:
        0    120    240    600  class.error
0   89304      0      0     54 6.043108e-04
120     0 179275      1      0 5.577991e-06
240     0      1 178921      7 4.471047e-05
600    21      0      3 179316 1.338240e-04
```

Figure 107: Training Data Confusion Matrix and OOB Estimate for “h_3”

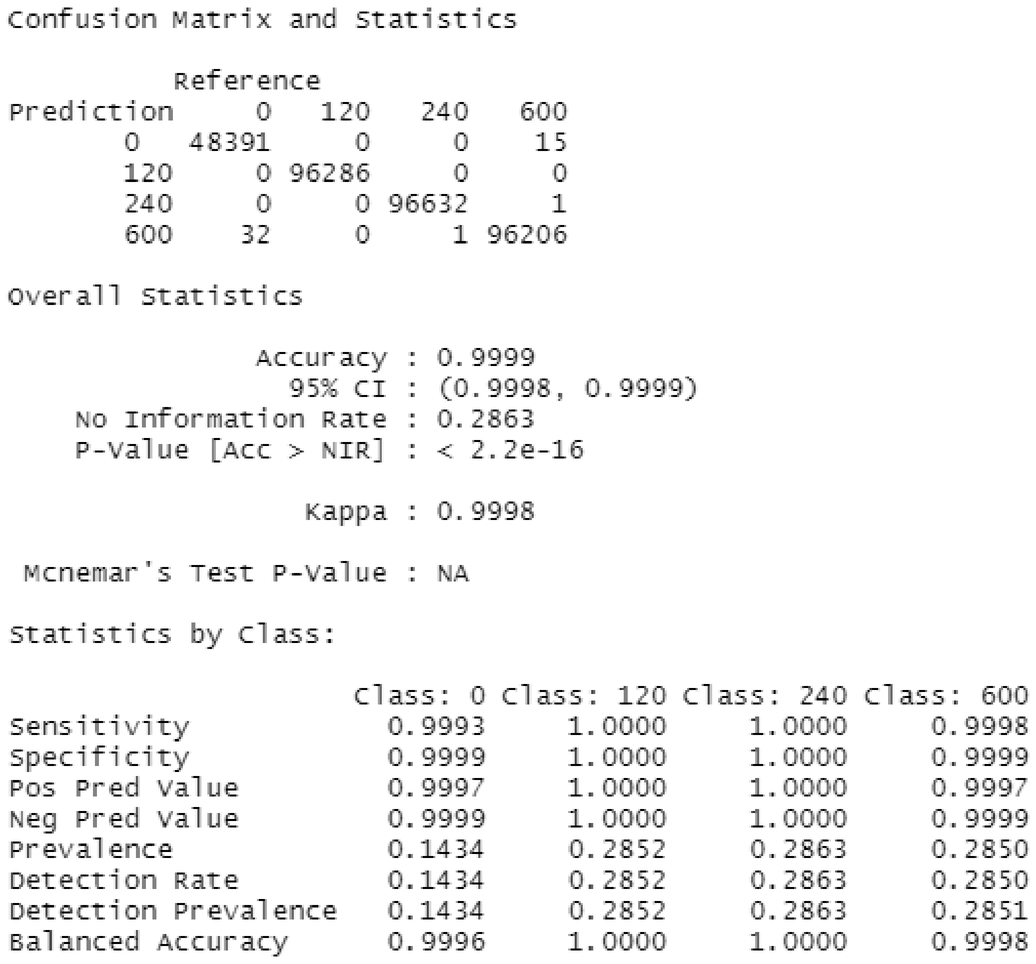

```
Confusion Matrix and Statistics

          Reference
Prediction     0   120   240   600
       0   48391     0     0    15
       120     0 96286     0     0
       240     0     0 96632     1
       600    32     0     1 96206

Overall Statistics
                                          
               Accuracy : 0.9999          
                 95% CI : (0.9998, 0.9999)
    No Information Rate : 0.2863          
    P-Value [Acc > NIR] : < 2.2e-16       
                                          
                  Kappa : 0.9998          
                                          
 Mcnemar's Test P-Value : NA              

Statistics by Class:

                     Class: 0 Class: 120 Class: 240 Class: 600
Sensitivity            0.9993     1.0000     1.0000     0.9998
Specificity            0.9999     1.0000     1.0000     0.9999
Pos Pred Value         0.9997     1.0000     1.0000     0.9997
Neg Pred Value         0.9999     1.0000     1.0000     0.9999
Prevalence             0.1434     0.2852     0.2863     0.2850
Detection Rate         0.1434     0.2852     0.2863     0.2850
Detection Prevalence   0.1434     0.2852     0.2863     0.2851
Balanced Accuracy      0.9996     1.0000     1.0000     0.9998
```

Figure 108: Testing Data Confusion Matrix and Statistics for "h_3"

Chapter Eight

Discussion and Conclusion

8.1 Building Neural Networks (NN) and Decision Trees (DT)

The main objective of this research project was to build a predictive model for the seed (response) variables. Using the training dataset, two strategies were initially tested for regression: (1) Building a Neural network (NN), (2) Building a Decision Tree. Once the model is built, its efficacy can be assessed using the testing dataset. Specifically, the testing data will be run through the model (the built NN or DT) to predict values for each response variable. The Root Mean Square Error (RMSE) is then calculated as a mean to compare the actual versus the predicted values. Note that Neural Networks were built to predict the full vector of response variables while Decision Tree models were built individually for each response variable.

Several hardships were encountered by following these strategies. First, the data itself is large; bringing it into the environment was consuming a lot of time. Second, building the models consistently hits hard memory bounds that regularly crashed R-Studio. Moreover, the algorithm erroneously used the response variables to predict the other response variables, leading therefore to illogical results. Interestingly, even being fed the target variables as part of the predictor set, the algorithm failed to return an RMSE value of zero. This implied that the categorical structure of the target variables, as a result of the simulation design and some of the predictors, is posing problems when they are treated as continuous variable inputs to the machine learning algorithms.

As previously mentioned, the biggest hardship in all of this work is that, building these models required several iterations. Each iteration took more than 24 hours to run and generate an outcome given no access to sufficient computing resources. For this reason, a classification model using Random Forests was adopted instead of a regression model.

8.2 Building Random Forests

The Random Forest (RF) model is considered as a prevalent method in statistics because of its simple applicability to both regression and classification problems. Such models show high applicability and accuracy especially in problems with large dimensions and with correlated predictor variables. Moreover, variable selection is essential for prediction and interpretations, specifically for large sets such as the ones used in this research project. The most promising predictor variables are selected by a method based on RF that uses the (MDA) and the (MDG). When a variable is omitted from a training dataset, the MDA provides an estimation of the loss in the prediction or the model's performance. Note that if two variables are relatively redundant, then eliminating one of these variables may not result in significant improvements in the performance, but it will make the other variable more relevant and important. As for the MDG, the GINI is mainly a measure of the node impurities. In other words, it defines the degree of the nodes' purity if that variable was used to separate the data. The greatest purity indicates that each node includes only components that belong to one class. After omitting a variable, evaluating the decrease in the MDG values helps in realizing how crucial that variable is for accurately splitting the data. Generally, researchers only use the Out-Of-Bag (OOB) impurity or error as a mean to estimate and evaluate the importance of each predictor variable under study, thus considering only one of the MDA or MDG measures. In this research paper, however, both measures are taken into account. The two measures are mainly considered as equally significant, which means that the rule followed when scoring the two measures is identical. A higher score is given for the variable of higher importance. To approach this method from a simpler perspective, the MDA value obtained for each variable is rounded up and considered as the MDA score. As for the MDG, and since the values are generated in thousands, they are scaled by dividing the obtained value by a hundred and rounded up, and then assigned as the MDG score. For example, when predicting the AC Master Curve Sigmoidal Coefficient "Alpha (α)", the MDA and MDG values for the predictor variable "T75R_D.0" were 392.21784 and 37,373.69, respectively. Consequently, "T75R_D.0" was awarded an MDA score of 393 and an MDG score of 374. Then the total score is determined by summing up the aforementioned scores. The predictor variables are therefore sorted in descending order of importance whereby the higher total score matches higher importance. Based on that, the first fifty percent of the variables' count are selected as the new variables to build a new RF model. The process is repeated as the error rate keeps on decreasing. Once the error rate starts increasing, a new set of predictor variables is tested while following the aforementioned process. Consequently, the final set of predictor variables that build the best RF model is determined for each seed variable. Note that the total score value of a predictor variable shall only be compared to the total score value of the other predictor variables that build the model for one seed variable. It is meaningless to compare the total score values between different seed variables. For this reason, the total score values for each seed variable are visualized by color rather by a numeric value (Figures 58, 62, 66, 70, 74, 78, 82, 86, 90, 94, 98, 102, 106). As the color intensity decreases, the total score corresponding to that predictor variable decreases, i.e., the importance of this predictor variable also decreases.

The error rate is mainly computed from the overall accuracy value which is extracted from the confusion matrix. By definition, the latter categorizes the actual values against the predictions made. It mainly includes 2-dimentions, whereby the first dimension represents the predicted values while the other indicates the actual values. The individual rows within the confusion matrix represents the actual values while each column is responsible for the predictor variables. This may also be presented in an opposite manner as it is the case in this research project. Normally in a confusion matrix, the target class is known by the positive class while all the other classes are referred to as the negative classes. The relationship between both, the positive class and the negative classes, is expressed in the confusion matrix through four categories: (1) TP (True Positive) whereby the class is classified correctly as a target class, (2) TN (True Negative) whereby the class is classified correctly as a negative class, (3) FP (False Positive) whereby the class is classified wrongly as a target class, (4) FN (False Negative) whereby the class is classified wrongly as a negative class. The items placed on the diagonal of the confusion matrix designate the correct classifications/predictions i.e., (TP) and (TN), while the off- diagonal items designate the wrong classifications/predictions i.e., (FP) and (FN). However, in this research, the main objective is to have correct classifications whereby the predictions match the actual values irrespective of the class type. For this reason, the true negatives and the true positives are both vital. Though it is important to mention that R-studio sets, by default, the first level as a positive-class for the seed variables (response variables) that only have two levels such as the AC Master Curve Sigmoidal Coefficients “Delta (δ)” (0.5, 1) and “Gamma (γ)” (-0.51, -0.46). The positive class was therefore selected by R-Studio to be class “0.5” for “Delta (δ)” and class “-0.51” for “Gamma (γ)”, (Figures 68 and 72). Additionally, the specificity, sensitivity, Positive Predictive Values (PPV) and Negative Predictive Values (NPV) are statistical measures generated by R-Studio. The proportion of the TNs and the TPs are expressed by the specificity and sensitivity, respectively. The PPV (also known by precision) is the ratio of the TPs over the total predicted results while the NPV is the ratio of the TNs over the total predicted results. The difference between PPV and the sensitivity is that the PPV refers to the certainty degree of the TPs while the sensitivity refers to the certainty degree of not excluding the positives. High values for the aforementioned statistical measures correspond to correct predictions, which is the case for all the seed variables except for the Rayleigh Damping Parameter of the PCC layer "α_{RPCC}". For seed variables with more than 2 classes, the aforementioned statistical measures are determined by comparing each class to the other classes. For each case, the Kappa statistic and the overall accuracy are computed. Note that the latter is mainly calculated while considering a 95% confidence and a 1-sided test to check whether the overall accuracy exceeds the No Information Rate (NIR). By definition, the class with the highest percentage in the testing dataset is deemed to represent the NIR. The significance of the RF models created for each seed variable was confirmed as the overall accuracy was found to be greater than the No Information Rate. This is also validated by the small P-values generated for the models built. Additionally, the Kappa (Cohen's k-coefficient) determines the agreement degree between the variables. The values normally range between -1 ≤ Kappa value ≤ 1 whereby a value of 0 indicates no agreement while a value of 1 indicates a full agreement. However, a negative value indicates an agreement that is deemed worse than the random. The Kappa values generated by the RF models built showed values closer or equal to 1 for all the seed variables except for "α_{RPCC}". Thus, indicating a good agreement between the variables. Lastly, the McNemar's Test P-value is computed to compare the classifiers' performance from the testing dataset. The McNemar test generated NA values for the following seed variables alpha (α), Beta_prime (β'), E_1 , E_2 , β_{RPCC} , , β_R and h_3 .

As previously mentioned, the dataset was divided into testing and training sets. Several practices have been considered for data-preprocessing. Once the data is relatively fully-preprocessed, the analysis can be initiated. Yet, if the entire dataset is used to run the model and is reused to evaluate the results, a rather too optimistic outcome is most likely generated. Therefore, it is essential to divide the dataset into a training set that can be used to build the model and a testing set to test and evaluate the results. The most common division was applied in this research project which considers a training dataset that constitute around two-thirds of the data (~65%) and a testing dataset that contains around one-thirds of the data (~35%). The number of observations differed between the seed variables that belong to the AC layer in the flexible pavements, the PCC layer in the rigid pavements and in the unbound layers underlying both AC and PCC layers.

Table 27: Number of Observations for AC Layer in Flexible Pavements

	Number of observations for AC Layer
Entire Dataset	551,124
Training Dataset	358,230
Testing Dataset	192,894

Table 28: Number of Observations for PCC Layer in Rigid Pavements

	Number of observations for PPC Layer
Entire Dataset	413,343
Training Dataset	268,672
Testing Dataset	114,671

Table 29:Number of Observations for Unbound Layer Underlying AC and PCC Layers

	Number of observations for Unbound Layers
Entire Dataset	964,467
Training Dataset	626,903
Testing Dataset	337,564

For the random forest algorithm, the "randomForest" package is used in R-studio to initiate the running process. To build a random forest model, several parameters shall be initially defined including the "target variable", "ntree", "mtry", and the "importance". In this case, the target variable are the seed variables: alpha (α), Beta_prime (β'), Delta (δ), Gamma (γ), E_1 , E_2 , E_3 , E_4 , α_{RPCC} , β_{RPCC} , α_R , β_R and h_3 . Each variable was tested individually using its corresponding testing dataset and therefore, a total of 13 RF models were created. The "ntree" parameter identifies the number of trees required to build the model. As the number of trees increases, the computational or the building time increases. For this reason, the "ntree" value that tend to minimize the OOB error rate was chosen. For example, 450 trees were selected to build the random forest model for the AC master curve sigmoidal function coefficient "Delta (δ)". Choosing a lower count than 450 trees will increase the error (Figure 109). However, a model with a higher count will generate the same result as the model with 450 trees but with a longer computational time. Therefore, 450 trees build the optimal random forest model for the seed variable "Delta (δ)". On the other hand, 200 trees were enough to build an optimal RF model to predict the modulus of elasticity of the subgrade layer "E_3" (Figure 110). The same logic was followed to select the optimal number of trees to build the Random Forest models for each seed variable (Table 4 in discussion doc.).

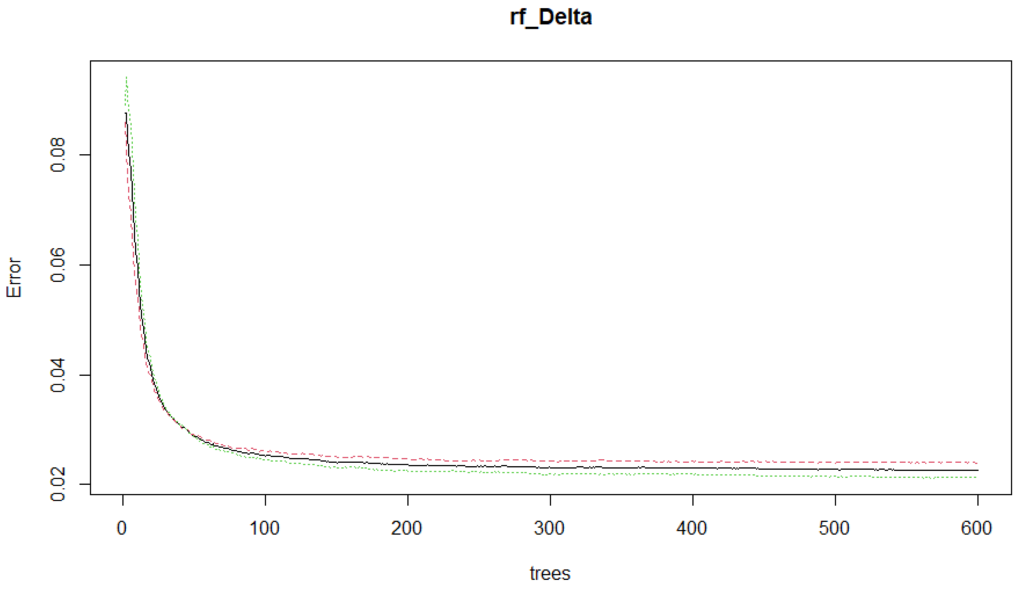

Figure 109: Variation of OOB-Estimate of Error Rate versus Number of Trees for rf_Delta Model

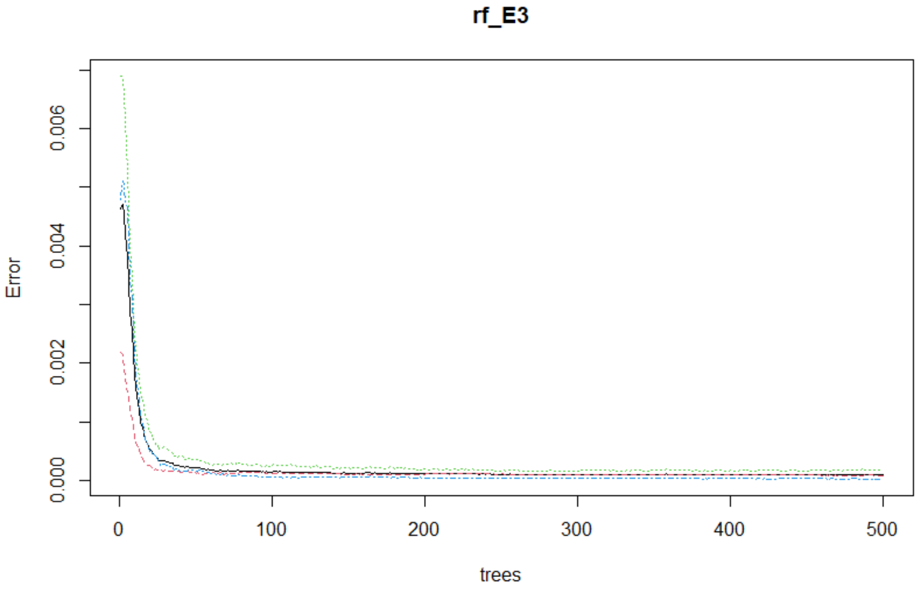

Figure 110: Variation of OOB-Estimate of Error Rate versus Number of Trees for rf_E_3 Model

The “mtry” defines the number of variables used to construct each tree within the model. Such variables are randomly selected by the algorithm. Yet, the default value was considered in this case which is the square root of the number of the variables. Lastly, the “importance” parameter allows the algorithm to compute the variable importance when set as “True”. An example from R-studio is shown in the Figure 111 below for building an RF Model for seed variable “Delta (δ)” denoted by rf_Delta. The same logic was also followed to build the random forest models for the remaining seed variables.

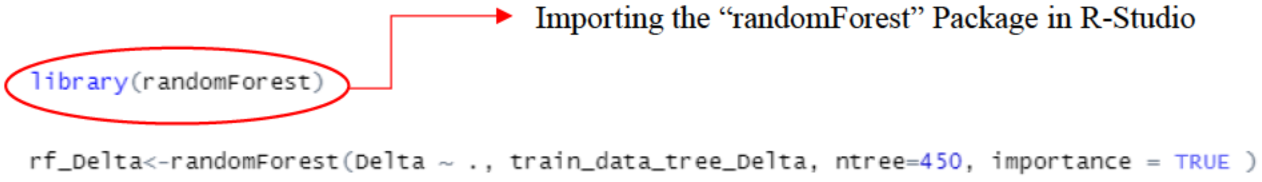

Importing the “randomForest” Package in R-Studio

```
library(randomForest)

rf_Delta<-randomForest(Delta ~ ., train_data_tree_Delta, ntree=450, importance = TRUE )
```

Figure 111: A Sample Code from R-Studio used to Build an RF-Model for “Delta (δ)”

Table 30: The Parameters Defined to Build an RF Model for each Seed Variable

Seed Variable	Ntree	Mtry	Importance
Alpha (α)	300	Default Value	True
Beta_prime (β')	450	Default Value	True
Delta (δ)	450	Default Value	True
Gamma (γ)	500	Default Value	True
E_1	300	Default Value	True
α_{RPCC}	500	Default Value	True
β_{RPCC}	500	Default Value	True
E_2	400	Default Value	True
E_3	200	Default Value	True
E_4	500	Default Value	True
α_R	500	Default Value	True
β_R	500	Default Value	True
h_3	200	Default Value	True

A confusion matrix is a prevalent method for summarizing the findings when dealing with a large count of predictions. For each seed variable, a confusion matrix was generated for each of the testing and training datasets to summarize the results of the RF models built. As shown in Figures (59, 63, 67, 71, 75 ,79 ,83, 87, 91, 95, 99, 103, 107), the number of trees, the number of variables tested at each split and the OOB error rate are listed when calling the RF model. The

OOB error is a valuable measure used to differentiate between the different RF classifiers. It is computed through counting, however, several observations found in the training datasets are misclassified. For example, the off-diagonal items in Figure 67 for the seed variable “Delta (δ)” showed values of 4,291 and 3,882 for a total of 8,173 wrong classifications in the training dataset. Dividing the number of wrong classifications (8,173) by the number of observations in the training dataset (358,231; Table 27), the OOB estimate of error rate is obtained (2.28%) as shown in Figure 67. Therefore, the accuracy of the training dataset is 97.72% (100% - 2.28%) which is slightly lower than the overall accuracy which is 97.86% (Figure 68).

Moving toward the testing data confusion matrix. As previously mentioned, the main objective of a confusion matrix is to provide the comparison between the predictions done from the built model with known outcomes A two-class confusion matrix, that demonstrates the distribution of the predicted and the actual values of the testing dataset, is observed in Figure 68. An example on how to read a confusion matrix in Figure 68 is discussed afterwards.

- 94,282 items are correctly predicted as class “0.5”, thus the predictions match the actual values
- 94,479 items are correctly predicted as class “1”, thus the predictions match the actual values
- 2,207 items are wrongly predicted as class “1”. This indicate that the actual values belong to class “0.5” but they are wrongly predicted as class “1”.
- 1,926 items are wrongly predicted as class “0.5”. This indicate that the actual values belong to class “1” but they are wrongly predicted as class “0.5”.

In other words, the RF model predicted 0.5 as 0.5, 94,282 times, 0.5 as 1, 2,207 times, 1 as 1, 94,479 times as 1 as 0.5, 1,926 times. From these results, one can conclude that a total of 188,761 predictions matched the actual values from the testing dataset that constitute 192,894 observations (Table 27). Thereby, the ratio of the correct predictions over the number of observations gives the overall accuracy of 97.86% (Figure 68). Similarly, a 3-class confusion matrix is observed for the RF-model built to predict the PCC Rayleigh Damping Parameter “β_{RPCC}” (Figure 84). As shown, the off-diagonal items are found to be zero signifying that the predictions match the actual values. This therefore explains the 100% overall accuracy for this RF model.

Normally, a certain threshold should be set to define an acceptable error rate. However, in the case of this research project, all the available predictor variables (a total of 569 variables) were tested to achieve the highest possible accuracy for each seed variable. Note that the latter differ from one seed variable to another. The set that generates the lowest OOB-error rate and the highest overall accuracy while meeting the proper characteristics of the aforementioned statistical measures was selected. This was mainly achieved by testing several trials; each trial includes a different set of predictor variables. Consequently, the chosen set (in Chapter 7: Results) is essential to build the best RF model for its corresponding seed variable. Omitting any variable will lead to an increase in the OOB-error rate and a decrease in the overall accuracy.

The OOB-Estimate of error rate and the overall accuracy values obtained dictate that the predictor variables selected to build the RF models are properly trained and generate accurate predictions. This was the case for all the seed variables under study except for the for the Rayleigh Damping Parameter of the PCC layer "α_{RPCC}" whereby an accuracy of 58.65% was observed. Such results, however, are logical. To visualize the effect of "α_{RPCC}" on the deflection, the combinations that only show a variation in the "α_{RPCC}" variable were selected (Table 31). Their corresponding deflections generated by Pulse_FE are plotted accordingly at different offsets from the applied load (Figure 114).

Table 31: Rigid Pavement Combinations with Varying "α_{RPCC}"

Combination	h_1	h_2	E_1	E_2	E_3	α_{RPCC}	β_{RPCC}	α_R	β_R	FWD Pulse Duration
R000001	9	6	2000	20	5	0	0.002	0	0.002	20
R000082	9	6	2000	20	5	10	0.002	0	0.002	20
R000163	9	6	2000	20	5	20	0.002	0	0.002	20

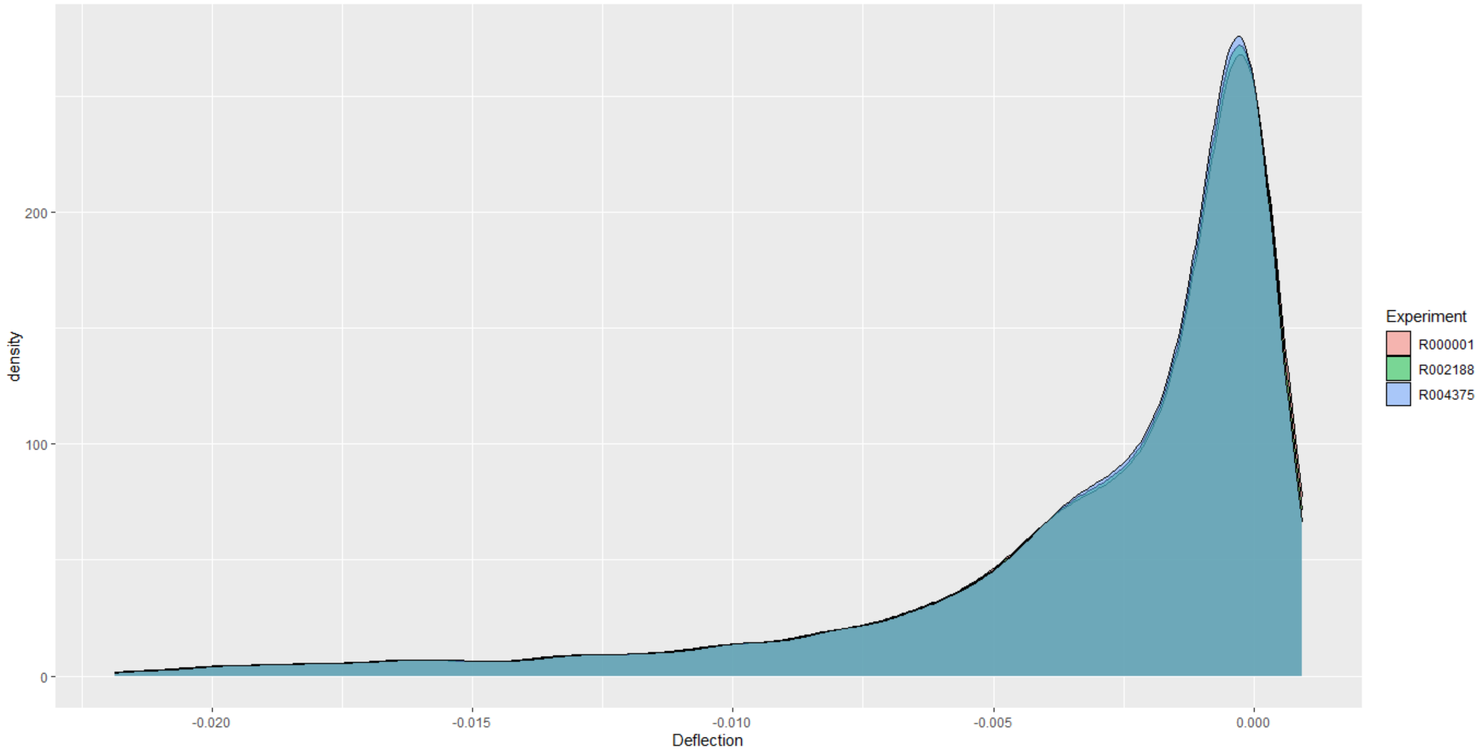

Figure 112: Density Plot for three Combinations

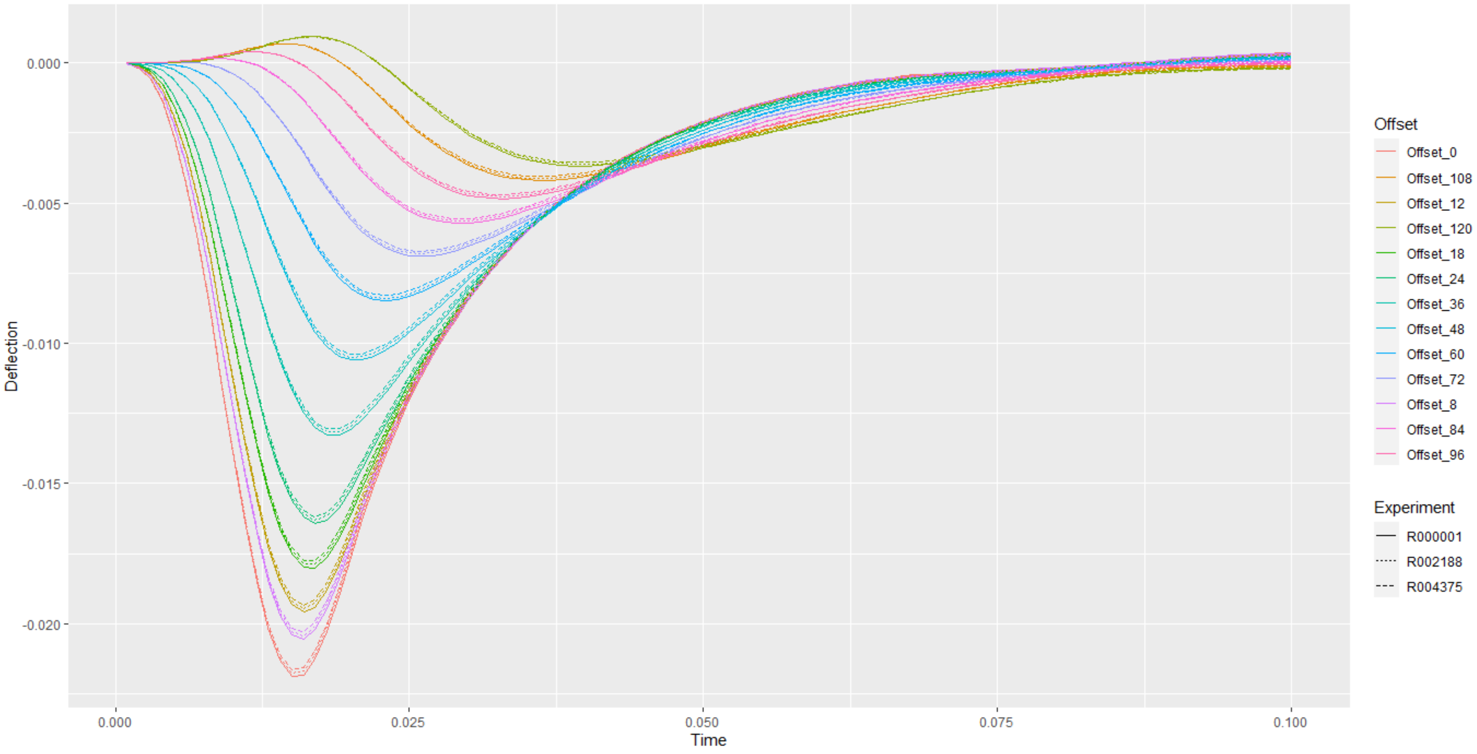

Figure 113: Deflection Plots for three Combinations

At each offset, the deflections showed minimal variations for the three different combinations/experiments. Moreover, the density plot displayed that the distribution of the deflection values formed a cluster at values equal or close to zero. Therefore, one can conclude that the Rayleigh Damping Parameter of the PCC layer “α_{RPCC}” has slight effect on the deflection and consequently on the velocity. Such behavior can be correlated to the low accuracy obtained. This also explains the fact why the “α_{RPCC}” variable is sometimes kept as zero. The latter may also be applied to the Rayleigh Damping Parameter of the unbound layers “α_R”. Unlike other seed variables, “α_R” recorded the highest count of predictor variables needed to achieve an accuracy of 98.48%.

8.3 Validation

For validation purposes, the performance of the random forest models was further tested using new synthetic data of known target values and with real-life deflection data.

8.3.1 Original Combinations

Initially, deflection files were randomly selected from the original combinations and the predictions matched the original values for flexible and rigid pavement structures.

1. Flexible Pavement, h_1= 3 inches, h_2= 6 inches, FWD Pulse Duration = 20 msec. haversine.

Table 32: Prediction Vs. Original for Combination 1 – Flexible Pavement

Comb 1	Delta (δ)	Alpha (α)	Beta_prime (β')	Gamma (γ)	E2	E3	α_R	β_R
Original	0.5	3	-2.11013	-0.46	20	5	0	0.002
Predicted	0.5	3	-2.11013	-0.46	20	5	0	0.002
Time to predict (sec)	2.4	3.1	0.1	2	2.32	0.01	5	3.2

2. Flexible Pavement, h_1= 3 inches, h_2= 12 inches, FWD Pulse Duration = 40 msec. haversine.

Table 33: Prediction Vs. Original for Combination 10,200 – Flexible Pavement

Comb10200	Delta (δ)	Alpha (α)	Beta_prime (β')	Gamma (γ)	E2	E3	α_R	β_R
Original	0.5	3	0.663709	-0.51	200	30	20	0.002
Predicted	0.5	3	0.663709	-0.51	200	30	20	0.002
Time to predict (sec)	1.42	4.5	0.1	1.86	1.48	0.01	3.19	2.56

3. Flexible Pavement, h_1= 6 inches, h_2= 12 inches, FWD Pulse Duration = 30 msec. haversine

Table 34: Prediction Vs. Original for Combination 36,619 – Flexible Pavement

Comb 36,619	Delta (δ)	Alpha (α)	Beta_prime (β')	Gamma (γ)	E2	E3	α_R	β_R
Original	0.5	3.1	-2.11013	-0.46	200	5	0	0.006
Predicted	0.5	3.1	-2.11013	-0.46	200	5	0	0.006
Time to predict (sec)	1.42	2.91	0.1	1.86	1.48	0.01	2.1	1.9

4. Rigid Pavement, h_1= 9 inches, h_2= 6 inches, FWD Pulse Duration = 20 msec. haversine

Table 35:Prediction Vs. Original for Combination 1 – Rigid Pavement

Comb 1	E1	E2	E3	α_{RPCC}	β_{RPCC}	α_R	β_R
Original	2000	20	5	0	0.002	0	0.002
Predicted	2000	200	5	10	0.002	0	0.002
Time to predict (sec)	2	1.2	0.01	2	2.31	4.1	3

5. Rigid Pavement, h_1= 21 inches, h_2= 36 inches, FWD Pulse Duration = 40 msec. haversine

Table 36: Prediction Vs. Original for Combination 413,343 – Rigid Pavement

Comb413343	E1	E2	E3	E4	α_{RPCC}	β_{RPCC}	α_R	β_R	h3
Original	6000	200	30	250	20	0.006	20	0.006	600
Predicted	6000	200	30	250	20	0.006	20	0.006	600
Time to predict (sec)	2	1.2	0.01	2.1	2.3	1.9	3.1	2	1.2

8.3.2 Synthetic Data_2

A new pavement structure was tested using synthetic data that contains deflections up to offset 72-inches. However, the models were built while considering predictor variables that correspond to offsets beyond offset 72- inches. For the models to work, such predictors must be assigned a certain value. Consequently, 4 methods were tested by assigning the predictor variables that correspond to offsets 84-inches through 120-inches as such:

1. Predictor Variables assigned equal to zero (File A10_0)
2. Predictor Variables assigned equal to those at offset 72-inches (File A10_72)
3. Regenerate deflections at offsets 84-inches through 120-inches using Pulse_FE and extract their corresponding parameters (A10_120)

4. Re-build new RF Models that exclude the predictor variables at offsets 84-inches through 120-inches (A10)

Method 4 was tested because in real-life, sensors do not exist beyond offset 72-inches. Therefore, by comparing the predictions obtained from this method to the prediction where all sensors up to 120-inches are included, one can determine if there is any benefit of using additional sensors beyond the 72-inch offset.

As previously mentioned, excluding any predictor variables from the chosen set will cause a slight decrease in the model's accuracy. The predictions, on the other hand, might or might not be affected depending on how important that specific variable is in predicting. As shown below, the accuracy experienced a slight decrease, yet it remained high.

Table 37: New Accuracy Vs. Original Accuracy

Seed Variable	Original Accuracy (%)	New Accuracy (%)
Delta (δ)	97.86	97.84
Alpha (α)	97.38	97.32
Beta_prime (β')	98.14	98.12
Gamma (γ)	97.85	97.65
E2	99.84	99.73
E3	100	99.96
α_R	98.48	98.07
β_R	99.82	99.63
β_{RPCC}	100	99.99
h3	99.99	96.16
E4	99.67	97.9

Table 38: Number of Predictor Variables Corresponding to Offsets 84 through 120-inches in the Optimal Model

Seed Variable	Number of Variables at Offset beyond 72-inches in Optimal Model	Total Number of Predictor Variables in Optimal Model
Delta (δ)	2	20
Alpha (α)	1	12
Beta prime (β')	4	19
Gamma (γ)	4	25
E2	6	24
E3	8	17
α_R	54	175
β_R	40	124
β_{RPCC}	3	11
h3	15	21
E4	39	65

The predictions matched the target values for all the seed variables except for “E2”, “E3” and “α_R” (Table 38). This behavior is related to the fact that around 50% of the predictors used to build their models correspond to predictors at offsets 84 through 120- inches (Table 38); which are mainly experiencing variation from method to method. Note that “E1” and “α_{RPCC}” do not include predictor variables that correspond to offset beyond the 72-inches.

Table 39: Predictions Vs. Target Values for the 4 Methods

Seed Variable	Target	A10_0	A10_72	A10_120	A10
Delta (δ)	1	1	1	1	1
Alpha (α)	2.6	2.6	2.6	2.6	2.6
Beta_prime (β')	-0.7	-0.7	-0.7	-0.7	-0.7
Gamma (γ)	-0.51	-0.51	-0.51	-0.51	-0.51
E2	50	20	20	50	50
E3	5	30	5	5	5
α_R	10	20	0	10	10
β_R	0.006	0.006	0.006	0.006	0.006

The predictions showed that choosing arbitrary values from the predictors at offsets beyond 72-inches will not match the target values (Methods 1 and 2). However, selecting relevant values (Method 3) or excluding those specific predictors (Method 4) will result in correct predictions that match the target values. This proves that the models perform properly based on how they are trained. The deflections in the FE generated A10 file were further tested by including random errors up to 5, 10 and 25% and reported in A15, A20, and A35, respectively. The models that excluded the predictor variables beyond offset 72-inches were used to perform the predictions. For the A35 file, the predictions matched the target values of all the seed variables except for “Gamma (γ)”. The same applies for files A15 and A20 except for the predictions of “Delta (δ)”, and “Alpha (α)” where the predictions did not match the target values.

Table 40: Predictions for A10, A15, A20 & A35 Vs. Target Values

Seed Variable	Target	A10	A15	A20	A35
Delta (δ)	1	1	0.5	0.5	1
Alpha (α)	2.6	2.6	3.2	3	2.6
Beta_prime (β')	-0.7	-0.7	-0.7	-0.7	-0.7
Gamma (γ)	-0.51	-0.51	-0.51	-0.46	-0.46
E2	50	50	50	50	50
E3	5	5	5	5	5
α_R	10	10	10	10	10
β_R	0.006	0.006	0.006	0.006	0.006

8.3.3 Synthetic Data_3 at 3 Different Temperatures (68,104 and 392˚F)

For this set of synthetic data, the target values do not belong to any of the classes or limits initially used. The RF categorical models built will only predict values from the set included in the input data. Hence, being limited to a specific set makes the predictions somehow far from the target values in some cases. Consequently, the predictions made by each individual tree within the random forest model were reported from R-Studio to calculate the average prediction. This step was performed for the purpose of imitating a random forest Regressor while having a random forest classifier. When compared to the classifier, the average prediction is closer to the target values for some seed variables.

Table 41: Predictions Using Classifier & Average Vs. Target for Temp. 68˚F

Seed Variable	Target	Classifier	Average
Delta (δ)	0.6991	1	0.8133
Alpha (α)	2.7761	2.7	2.7507
Beta_prime (β')	-0.72193	-0.7	-0.5778
Gamma (γ)	-0.5887	-0.46	-0.4813
E2	35	20	27.65
E3	7	5	5
α_R	30	20	15.88
β_R	0.003	0.002	0.0039

Table 42: Predictions Using Classifier & Average Vs. Target for Temp. 104˚F

Seed Variable	Target	Classifier	Average
Delta (δ)	0.6991	0.5	0.634444
Alpha (α)	2.7761	3	3.035333
Beta_prime (β')	0.445651	0.530012	0.406001
Gamma (γ)	-0.5887	-0.51	-0.4949
E2	35	20	22.325
E3	7	5	5
α_R	30	20	16.26
β_R	0.003	0.006	0.004032

Table 43: Predictions Using Classifier & Average Vs. Target for Temp. 392˚F

Seed Variable	Target	Classifier	Average
Delta (δ)	0.6991	0.5	0.716667
Alpha (α)	2.7761	3.1	2.879667
Beta_prime (β')	-2.1746	-2.11013	-2.09678
Gamma (γ)	-0.5887	-0.46	-0.474
E2	35	50	40.925
E3	7	5	5
α_R	30	20	15.22
β_R	0.003	0.002	0.003756

8.3.4 Synthetic Data Including Random Errors

The deflection files for the rigid and flexible pavement structures tested in section 8.3.1 are further used while including random errors inside them. The latter was achieved by multiplying the deflection at each offset by an error equal to ($1 + \frac{Random\ Number}{100}$). Note that the random number generator in Microsoft Excel was used to generate the random numbers. Therefore, the effect of such random errors on the predictions can be analyzed.

For comparison purposes, the predictions were generated using RF classifier and RF regressor (average predictions of the trees) models that:

1. Include sensors up to 72-inches
2. Include sensors beyond 72-inches

The predictions are shown below for the Flexible and Rigid Pavement Structures.

8.3.4.1 Flexible Pavement Structure

Table 44: Predictions from RF Classifier Vs. Average Predictions for Combination 1 – Flexible Pavement

Combination 1		RF Classifier		Average Predictions	
Seed Variable	Target	72-inches	120-inches	72-inches	120-inches
Delta (δ)	0.5	1	1	0.782222	0.754444
Alpha (α)	3	2.5	2.5	2.729	2.733
Beta_prime (β')	**-2.11013**	**-2.11013**	**-2.11013**	-1.92307	-1.91009
Gamma (γ)	**-0.46**	**-0.46**	**-0.46**	-0.477	-0.4758
E2	**20**	**20**	**20**	26.75	31.175
E3	**5**	**5**	**5**	5	5
α_R	**0**	**0**	**0**	0.8	1.82
β_R	**0.002**	**0.002**	**0.002**	0.002028	0.002004

Table 45: Predictions from RF Classifier Vs. Average Predictions for Combination 36,619

Combination 36,619		RF Classifier		Average Predictions	
Seed Variable	Target	72-inches	120-inches	72-inches	120-inches
Delta (δ)	0.5	1	1	0.816667	0.794444
Alpha (α)	3.1	3	3	2.841667	2.818667
Beta prime (β')	**-2.11013**	**-2.11013**	**-2.11013**	-2.15816	-2.14958
Gamma (γ)	**-0.46**	**-0.46**	**-0.46**	-0.4811	-0.4824
E2	**200**	**200**	**200**	154.025	152.525
E3	**5**	**5**	**5**	5	5.04
α_R	**0**	**0**	**0**	1.68	0.9
β_R	**0.006**	**0.006**	**0.006**	0.00584	0.005856

8.3.4.2 Rigid Pavement Structure

Table 46: Predictions from RF Classifier Vs. Average Predictions for Combination 1 – Rigid Pavement

Combination 1		RF Classifier		Average Predictions	
Seed Variable	Target	72-inches	120-inches	72-inches	120-inches
E1	2000	6000	NA	4080	NA
E2	20	200	200	160.925	148.625
E3	**5**	**5**	**5**	10.7	9.07
α_{RPCC}	0	20	NA	10.14	NA
β_{RPCC}	0.002	0.006	0.006	0.005656	0.005656
α_R	**0**	20	**0**	14.56	8.78
β_R	**0.002**	**0.002**	**0.002**	0.002848	0.002748

Table 47: Predictions from RF Classifier Vs. Average Predictions for Combination 413,343

Combination 413,343		RF Classifier		Average Predictions	
Seed Variable	Target	72-inches	120-inches	72-inches	120-inches
E1	6000	2000	NA	3733.333	NA
E2	**200**	**200**	**200**	142.775	118.325
E3	30	5	5	8.1	15.5
E4	**250**	**250**	**250**	196	182.9
α_{RPCC}	20	0	NA	3.86	NA
β_{RPCC}	**0.006**	**0.006**	**0.006**	0.005652	0.00562
α_R	**20**	**20**	**20**	16.14	17.26
β_R	0.006	0.002	0.004	0.002632	0.003688
h3	600	120	120	96.8	103.8

Including random errors in the deflection files has affected the predictions for the rigid pavement more than that of the flexible pavement where some values were far from the target. Yet the average predictions of all trees generated a value that is closer to the target. The predictions for the flexible pavement matched the target values for all seed variables except for “Delta (δ)” and “Alpha (α)”.

8.3.5 Real-Life Data

The FWD data for a testing performed on an LTPP section was used. The section consisted of 7.1-inch AC layer ($h_1 = 7.1$ inch) and a 12-inch unbound granular base layer ($h_2 = 12$ inch) built over an untreated silty clayey subgrade. The section is subject to six different peak loadings, hence a total of 6 deflection files were used. The deflections are further normalized to account for the 27 kips load that is originally used in the analysis. Note that the files included deflections measured at offsets 0, 8, 12, 18, 24, 36 and 60 inches from the center. Hence, to account for deflections at offsets 48 and 72 inches, interpolations and extrapolations were done. While using the RF classifier and the average predictions, two strategies were followed:

1. Interpolating and extrapolating the deflections
2. Interpolating and extrapolating the FWD Parameters

The predictions of the sigmoidal coefficients are then used in the sigmoidal function to determine the dynamic modulus “E_1”.

By following the first strategy, the predictions and the “E_1” values are as follows:

Table 48: RF Classifier Predictions using Strategy 1

Data Set	**RF Classifier**							
	Delta (δ)	Alpha (α)	Beta_prime (β')	Gamma (γ)	E2	E3	α_R	β_R
199406080909	0.5	2.7	-0.7	-0.46	20	5	0	0.006
199407141004	0.5	3.2	-0.7	-0.46	20	5	20	0.004
199407150812	0.5	3.2	-0.7	-0.51	20	5	10	0.004
199407151014	1	3	0.53001232	-0.51	20	5	20	0.006
199407151156	0.5	2.6	0.53001232	-0.46	20	5	0	0.006
199407151329	0.5	3	0.53001232	-0.51	20	5	0	0.006

Table 49: “E_1” Values from Sigmoidal Coefficients predicted by RF Classifier in Strategy 1

Data Set	E1 at 17 Hz (ksi)
199406080909	403.792
199407141004	991.258
199407150812	1069.99
199407151014	374.179
199407151156	66.5877
199407151329	118.326

Table 50: Average Predictions using Strategy 1

Data Set	**Average Predictions**							
	Delta (δ)	Alpha (α)	Beta_prime (β')	Gamma (γ)	E2	E3	α_R	β_R
199406080909	0.5955556	2.815	-0.8837606	-0.4834	32.225	5.15	8.38	0.004552
199407141004	0.6988889	2.985667	-0.8046465	-0.4817	28.55	5.2	12.24	0.004344
199407150812	0.67	2.970667	-0.8887981	-0.4854	29.15	5.15	9.88	0.004252
199407151014	0.7944444	2.917	-0.2284067	-0.4852	29.675	5.15	13.26	0.00442
199407151156	0.7455556	2.821333	0.2459763	-0.4847	27.2	5.05	8.18	0.004428
199407151329	0.5511111	2.877333	0.4815562	-0.4882	26.825	5.05	8.88	0.004772

Table 51: “E_1” Values from Sigmoidal Coefficients using Average Predictions in Strategy 1

Data Set	E1 at 17 Hz (ksi)
199406080909	772.618
199407141004	1237.91
199407150812	1237.48
199407151014	665.096
199407151156	251.703
199407151329	118.955

By following the second strategy, the predictions and the “E_1” values are as follows:

Table 52: RF Classifier Predictions using Strategy 2

Data Set	**RF Classifier**							
	Delta (δ)	Alpha (α)	Beta_prime (β')	Gamma (γ)	E2	E3	α_R	β_R
199406080909	0.5	2.7	-0.7	-0.46	20	5	0	0.006
199407141004	0.5	3.2	-0.7	-0.46	20	5	20	0.006
199407150812	0.5	3.2	-0.7	-0.51	20	5	10	0.004
199407151014	1	3	0.53001232	-0.51	20	5	20	0.006
199407151156	0.5	2.6	0.53001232	-0.51	20	5	0	0.006
199407151329	0.5	3	0.53001232	-0.51	20	5	0	0.006

Table 53: “E_1” Values from Sigmoidal Coefficients predicted by RF Classifier in Strategy 2

Data Set	E1 at 17 Hz (ksi)
199406080909	403.792
199407141004	991.258
199407150812	1069.99
199407151014	374.179
199407151156	73.0021
199407151329	118.326

Table 54: Average Predictions using Strategy 2

Data Set	**Average Predictions**							
	Delta (δ)	Alpha (α)	Beta_prime (β')	Gamma (γ)	E2	E3	α_R	β_R
199406080909	0.5911111	2.837	-0.8680412	-0.4831	32	6	9.18	0.004688
199407141004	0.6955556	2.979	-0.8344	-0.4808	27.875	6.6	11.94	0.004396
199407150812	0.6677778	2.977333	-0.9112826	-0.4854	28.4	6.05	9.44	0.004404
199407151014	0.7955556	2.907	-0.2735121	-0.4851	28.4	6	13.46	0.004436
199407151156	0.7477778	2.820667	0.2485083	-0.4851	25.85	5.4	7.68	0.004452
199407151329	0.5544444	2.884667	0.4650529	-0.487	24.65	5.35	8.76	0.004772

Table 55: "E_1" Values from Sigmoidal Coefficients using Average Predictions in Strategy 2

Data Set	E1 at 17 Hz (ksi)
199406080909	784.333
199407141004	1251.57
199407150812	1275.71
199407151014	699.029
199407151156	251.956
199407151329	123.993

The RF Classifier generated the same predictions while following the two strategies, while the average predictions showed variations.

The actual values for "E_1", "E_2" and "E_3" are provided in Table 56. After comparison, the predictions for "E_1"and "E_2" are relatively close to the actual values. However, the predictions for the subgrade modulus "E_3" were far from the actual values.

Table 56: Actual Values for the Moduli of Elasticity

Data Set	E1	E2	E3
199406080909	580	39.2	13
199407141004	314	31.4	13.2
199407150812	338	34.5	13.4
199407151014	244	28.8	13.1
199407151156	156	29.3	12.7
199407151329	107	30.4	12.6

8.3.6 General Observations and Deductions

8.3.6.1 RF Classifier vs. Average Predictions of all Trees

Using models that include sensors up to 72-inches and beyond the 72-inches:

- When the target values belong to the classes that are used to build the RF models, the predictions from the RF classifier match the target values.
- When the target values do not belong to the classes that are used to build the RF models, the average predictions of the trees within the RF model are closer to the target than the ones from the classifier.

This proves that the models are properly trained and have significant performance knowing that they are built on the categorical level. The predictions are further improved when considering the outcome from the individual trees. Therefore, generating more accurate predictions when analyzing existing pavement structures.

8.3.6.2 Predictions with Synthetic Data including Random Errors

Using models that include sensors up to 72-inches and beyond the 72-inches:

- Including random errors in the deflection files affected the predictions for the rigid pavement more than that of the flexible pavements.
- The average predictions of all trees are sometimes closer to the target when compared to the RF classifier.

The same behaviour was encountered when including the sensors up to and beyond the 72-inch offset. The predictions are even better sometimes when excluding the predictor variables corresponding to offsets 84 through 120-inches. This proves that the sensors located beyond the 72-inch offset did not add any benefit nor did it improve the prediction.

8.3.6.3 Predictions with Real-Life Data

For some seed variables, the predictions generated by the RF models generated close predictions to the actual value. However, for the remaining seed variables, the RF models appeared to be very sensitive and not robust, even if they have a high fit. Consequently, the seed variables shall be further improved using other methods as they largely affect the backcalculation results.

8.4 Summary

As a brief summary, the dynamic approach was adopted in this research project to perform the analysis on 3- to 4-layered rigid and flexible pavement structures. For flexible pavements, the AC layer was modelled as an LVE material. However, the PCC layer and the unbound layers underlying both pavement types were modelled as LE materials while including the damping. The optimal mesh was determined using Gmsh for both pavement structures. Generally, three methods exist to simulate the infinite media, yet, the far boundary method was selected due to its time efficiency. A study was further performed to check and evaluate the impact of certain parameters on the seed variables. Generally, the FWD parameters (also known by deflection parameters) are mainly obtained from FWD time histories based on actual testing. In this research project, the data was simulated (synthetized) by Pulse_FE through running thousands of combinations, simulating the different pavement structures and various properties. The FWD parameters were then extracted by Pulse_Analyzer and were used to calculate the FWD Indices and the Difference Variables. Consequently, and by following a classification strategy, Random Forest models were built using those parameters to predict the seed variables. For robust analysis, the most promising predictor variables that significantly affect the response variables were selected. The variable selection process was mainly based on the Variable Importance Measures, including the MDA and the MDG measures, that the Random Forest models offer.

Random forest models were built for each of the AC master curve sigmoidal function coefficients: alpha (α), Beta_prime (β'), Delta (δ), Gamma (γ), the modulus of elasticity (E_1) and the Rayleigh Damping Parameters (α_{RPCC}) and (β_{RPCC}) of the PCC layer, the moduli of elasticity and the Rayleigh Damping Parameters (α_R) and (β_R) of the unbound layers and lastly for the stiff layer thickness measured from the surface (h_3). The significance of each model was quantified and evaluated based on several statistical measures. The developed models accurately predicted the aforementioned seed variables except for the Rayleigh Damping Parameters (α_{RPCC}) of the PCC layer. The significance and performance of the models were further validated by using new synthetic data as well as real-life data. Models with predictor variables corresponding to sensors up to 72-inches are compared to predictions where all sensors up to 120-inch are included.

8.5 Conclusion

The backcalculation process is not only laborious but also holds several discrepencies associated to the software features and to the user's experience specifically when it comes to selecting seed variables. The chosen algorithm and its corresponding regularization techniques dictates the effectiveness of the analysis. For the backcalculation analysis of multi-layer rigid and flexible pavement structures, the selected seed variables may hold significant consequences on the final backcalculated outcomes and on the software's performance. Additionally, the user also has a substantial impact on the results in terms of choosing seed variables to initiate the analysis, the number of iterations performed and the termination norms.

Previous records showed no valid solutions for estimating seed variables using the deflection time histories for flexible and rigid pavement structures. Using Machine Learning algorithms along with a classification analysis, this research project filled such gaps by developing prediction models for the seed variables within each layer of the pavement structure. The developed models accurately predicted all the seed variables except for the Rayleigh Damping Parameters (α_{RPCC}) of the PCC layer, yet such results were expected. It is important to note that such models do not necessitate the user's subjective decisions and judgments. Due to their high prediction accuracy, creating such models will facilitate the analysis process for pavement engineers while obtaining reliable and reasonable backcalculation results. For the synthetic data, the model validation showed that the predictions done by the RF classifier were good, and are further improved when using the average of all the trees within the RF. The predictions for the real FWD data, however, were not consistent for all the seed variables; some predictions were close while others were far.

It is important to mention that classification models force the response variables to take only one value of a limited set of values. This implies that good predictions are obtained in the training dataset, but bad predictions might be potentially generated in reality. Moreover, and due to the large amount of data used, the lack of sufficient and powerful computing resources had largely affected the work flow and rendered the statistical analysis more challenging. This had also restricted the use of continuous or regression models. It is important to note that considering additional sensors beyond the 72-inches offset did not improve the prediction, hence there is no need to consider them in real life. For future work, the seed variables can be further improved by other methods including the Newton-Raphson Method or the models can be rebuilt on the continuous level using Neural Networks and regression analysis prior to their use in the backcalculation analysis.

References

Anderson, D. (1977). The design of asphalt concrete overlays for flexible highway pavements.

Abd El-Raof, H. S., Abd El-Hakim, R. T., El-Badawy, S. M., & Afify, H. A. (2018). Simplified closed-form procedure for network-level determination of pavement layer moduli from falling weight deflectometer data. *Journal of Transportation Engineering, Part B: Pavements*, *144*(4), 04018052.

Alipour, A., & Zareian, F. (2008, October). Study rayleigh damping in structures; uncertainties and treatments. In *the 14th world conference on earthquake engineering* (pp. 12-17).

Ahmad, M. W., Mourshed, M., & Rezgui, Y. (2017). Trees vs Neurons: Comparison between random forest and ANN for high-resolution prediction of building energy consumption. *Energy and Buildings*, *147*, 77-89.

Box, G. E. (1953). Non-normality and tests on variances. *Biometrika*, *40*(3/4), 318-335.

Breiman, L. (1996). Out-of-bag estimation.

Breiman, L. (2001). Random forests. *Machine learning*, *45*(1), 5-32.

Bauer, E., & Kohavi, R. (1999). An empirical comparison of voting classification algorithms: Bagging, boosting, and variants. *Machine learning*, *36*(1), 105-139.

Bathe, K. J. (2014). Finite element procedures, 2nd edn., Watertown MA, USA.

Berzins, M. (1998). A solution-based triangular and tetrahedral mesh quality indicator. *SIAM Journal on Scientific Computing*, *19*(6), 2051-2060.

Bazi, G., & Assi, T. B. (2020). Asphalt concrete master curve using dynamic backcalculation. *International Journal of Pavement Engineering*, *23*(1), 95-106.

Bazi, G., Brynick, M., Bou Assi, T. and Gagnon, J., (2021). An Improved Model for Predicting Asphalt Concrete Master Curve using FWD Data. Transportation Research Board (TRB) Annual Meeting. Washington, D.C.

Bazi, G., Brynick, M., Bou Assi, T. and Gagnon, J., (2021). Data Mining of FWD Deflection Time Histories for Use in Dynamic Backcalculation. Transportation Research Board (TRB) Annual Meeting. Washington, D.C.

Bazi, G., Gagnon, J., Sebaaly, P., & Ullidtz, P. (2020). Effects of rayleigh damping on the subgrade's apparent nonlinearity. *Journal of Transportation Engineering, Part B: Pavements*, *146*(3), 04020042.

Bazi, G., Mansour, E., Sebaaly, P., Ji, R., & Garg, N. (2019). Instrumented flexible pavement responses under aircraft loading. *International Journal of Pavement Engineering*, 1-13

Cleveland, William S. (1977), "Locally Weighted Regression and Smoothing Scatterplots," Bell Laboratories memorandum

Cleveland, W. S. (1979). Robust locally weighted regression and smoothing scatterplots. *Journal of the American statistical association*, *74*(368), 829-836.

Cook, R. D. (1995). Finite element modeling for stress analysis. *John Wiley & Sons, ISBN: 0-471-10774-3*.

Cleveland, W. S., & Devlin, S. J. (1988). Locally weighted regression: an approach to regression analysis by local fitting. *Journal of the American statistical association*, *83*(403), 596-610.

Chou, Y. J., & Lytton, R. L. (1991). Accuracy and consistency of backcalculated pavement layer moduli. *Transportation Research Record*, *1293*, 72-85.

Claessen, A. I., Valkering, C. P., & Ditmarsch, R. (1976). Pavement evaluation with the falling weight deflectometer. In *Association of Asphalt Paving Technologists Proc* (Vol. 45).

Choi, J. W., Wu, R., Pestana, J. M., & Harvey, J. (2010). New layer-moduli back-calculation method based on the constrained extended Kalman filter. *Journal of Transportation Engineering*, *136*(1), 20-30.

Dehlen, G. L. (1962). Flexure of a road surfacing, its relation to fatigue cracking, and factors determining its severity. *Highway Research Board Bulletin*, (321).

FHWA, 2016. *Pavement structural evaluation at the network level: final report. Federal Highway Administration*. Publication no. FHWA-HRT15/074.

Ford Jr, M. C., & Bissett, J. R. (1962). Flexible Pavement Performance Studies in Arkansas. *Highway Research Board Bulletin*, (321).

Fwa, T. F., & Rani, T. S. (2005). Seed modulus generation algorithm for backcalculation of flexible pavement moduli. *Transportation research record*, *1905*(1), 117-127.

Fwa, T. F., Tan, C. Y., & Chan, W. T. (1997). Backcalculation analysis of pavement-layer moduli using genetic algorithms. *Transportation research record*, *1570*(1), 134-142.

Friedman, J. H. (2017). *The elements of statistical learning: Data mining, inference, and prediction*. springer open.

Fuentes, L., Taborda, K., Hu, X., Horak, E., Bai, T., & Walubita, L. F. (2020). A probabilistic approach to detect structural problems in flexible pavement sections at network level assessment. *International Journal of Pavement Engineering*, 1-14.

Garg, N. and Thompson, M., (1997). *Mechanistic-empirical evaluation of the Mn/ROAD low-volume road test sections*. University of Illinois at Urbana-Champaign.

Geuzaine, C., & Remacle, J. F. (2009). Gmsh: A 3-D finite element mesh generator with built-in pre-and post-processing facilities. *International journal for numerical methods in engineering*, *79*(11), 1309-1331.

Hutton, D. V. (2004). *Fundamentals of finite element analysis*. McGraw-hill.

Horak, E., 1987a. The use of deflection basin measurements in the mechanistic analysis of flexible pavements. *Sixth international conference on the structural design of asphalt pavements, vol. 1*. University of Michigan

Horak, E. (1987b). *Aspects of deflection basin parameters used in a mechanistic rehabilitation design procedure for flexible pavements in South Africa* (Doctoral dissertation, University of Pretoria).

Horak, E. (2008). Benchmarking the structural condition of flexible pavements with deflection bowl parameters. *Journal of the South African Institution of Civil Engineering*, *50*(2), 2-9.

Hveem, F. N. (1955). *Pavement deflections and fatigue failures* (No. 114).

Horak, E., & Emery, S. (2006). Falling weight deflectometer bowl parameters as analysis tool for pavement structural evaluations. In *Research into Practice: 22nd ARRB ConferenceARRB*.

Horak, E., Emery, S., & Maina, J. (2015, August). Review of falling weight deflectometer deflection benchmark analysis on roads and airfields. In *11th conference on asphalt pavements for Southern Africa: CAPSA15* (pp. 16-19).

Hatada, T., Kobori, T., Ishida, M., & Niwa, N. (2000). Dynamic analysis of structures with Maxwell model. *Earthquake engineering & structural dynamics*, *29*(2), 159-176.

Hoffman, M. S., & Thompson, M. R. (1981). Mechanistic Interpretation of Nondestructive Pavement Testing Defections. Transportation Engineering Series No. 32, Illinois Cooperative Highway and Transportation Research Program Series No. 190. University of Illinois. *Urbana*

Hossain, A. S. M., & Zaniewski, J. P. (1991). Characterization of falling weight deflectometer deflection basin. *Transportation Research Record*, (1293).

Joubert, F., 1992. Structural Classification of granular base pavement using measured deflection bowl parameters. ProQuest dissertations. Rand Afrikaans University

Katsikadelis, J. T. (2001). The BEM for Vibration Analysis of Non-Homogeneous Bodies. In *Structural Engineering, Mechanics and Computation* (pp. 99-110). Elsevier Science

Kung, K. Y. (1967, January). A New Method in Correlation Study of Pavement Deflection and Cracking. In *Intl Conf Struct Design Asphalt Pvmts*.

Koole, R. C. (1979). Overlay design based on falling weight deflectometer measurements. *Transportation Research Record*, (700).

Kazimi, S. M. A. (2001). *Solid mechanics*. Tata McGraw-Hill Education.

Kilareski, W. P., & Anani, B. A. (1982). EVALUATION OF IN-SITU MODULI AND PAVEMENT LIFE FROM DEFLECTION BASINS--PROCEEDINGS OF THE FIFTH INTERNATIONAL CONFERENCE ON THE STRUCTURAL DESIGN OF ASPHALT PAVEMENTS HELD DEFLT UNIVERSITY OF TECHNOLOGY, AUGUST 23-26 1982. VOL 1 AND 2.--NETHERLANDS. *Publication of: INTERNAT EXE COMM. STUDY CENTRE FOR ROAD CONSTR.*

Kareem, A., & Gurley, K. (1996). Damping in structures: its evaluation and treatment of uncertainty. *Journal of wind engineering and industrial aerodynamics*, *59*(2-3), 131-157.

Kim, Y. R., Lee, Y. C., & Ranjithan, S. R. (2000). Flexible pavement condition evaluation using deflection basin parameters and dynamic finite element analysis implemented by artificial neural networks. In *Nondestructive testing of pavements and backcalculation of moduli: Third volume*. ASTM International

Kim, Y. R., & Park, H. (2002). *Use of falling weight deflectometer multi-load data for pavement strength estimation* (No. FHWA/NC/2002-006). North Carolina. Dept. of Transportation.

Kim, Y. R., Underwood, B., Far, M. S., Jackson, N., Puccinelli, J., & Engineers, N. C. (2011). *LTPP computed parameter: dynamic modulus* (No. FHWA-HRT-10-035). United States. Federal Highway Administration.

Kaliske, M., & Rothert, H. (1997). Formulation and implementation of three-dimensional viscoelasticity at small and finite strains. *Computational Mechanics*, *19*(3), 228-239.

Kutay, M. E., Chatti, K., & Lei, L. (2011). Backcalculation of dynamic modulus mastercurve from falling weight deflectometer surface deflections. *Transportation research record*, *2227*(1), 87-96.

Liu, G. R., & Quek, S. S. (2013). *The finite element method: a practical course*. Butterworth-Heinemann.

Logan, D.L. (2017). A First Course in the Finite Element Method. Cengage Learning, Boston, MA.

Liu, Y., & Glass, G. (2013). *Effects of mesh density on finite element analysis* (No. 2013-01-1375). SAE Technical Paper.

Li, M., & Wang, H. (2019). Development of ANN-GA program for backcalculation of pavement moduli under FWD testing with viscoelastic and nonlinear parameters. *International Journal of Pavement Engineering*, *20*(4), 490-498.

Macauley, Frederick R. (1931), The Smoothing of Time Series, New York: National Bureau of Economic Research.

Miura, Y., & Tobe, T. (1977, January). Evaluation of Existing pavement based on deflection and radius of curvature and overlay design. In *Volume I of proceedings of 4th International Conference on Structural Design of Asphalt Pavements, Ann Arbor, Michigan, August 22-26, 1977.* (No. Proceeding).

Matsui, K., Hachiya, Y., Maina, J. W., Kikuta, Y., & Nagae, T. (2006). Influence of seed layer moduli on FEM based modulus backcalculation results.

Mehta, Y., & Roque, R. (2003). Evaluation of FWD data for determination of layer moduli of pavements. *Journal of Materials in Civil Engineering*, *15*(1), 25-31.

Newmark, N. M. (1959). A method of computation for structural dynamics. *Journal of the engineering mechanics division*, *85*(3), 67-94.

Noureldin, A. S. (1993). New scenario for backcalculation of layer moduli of flexible pavements. *Transportation Research Record*, (1384).

Oñate, E. (2009*). Structural Analysis with the Finite Element Method. Linear Statics: Volume 1: Basis and Solids.* Springer Science & Business Media.

Patel, N., & Upadhyay, S. (2012). Study of various decision tree pruning methods with their empirical comparison in WEKA. *International journal of computer applications*, *60*(12).

Pierce, L. M., Bruinsma, J. E., Smith, K. D., Wade, M. J., Chatti, K., & Vandenbossche, J. (2017). *Using falling weight deflectometer data with mechanistic-empirical design and analysis, volume III: Guidelines for deflection testing, analysis, and interpretation* (No. FHWA-HRT-16-011). United States. Federal Highway Administration

Plati, C., Georgouli, K., Cliatt, B., & Loizos, A. (2017). Incorporation of GPR data into genetic algorithms for assessing recycled pavements. *Construction and Building Materials*, *154*, 1263-1271.

Park, S. W., & Schapery, R. (1999). Methods of interconversion between linear viscoelastic material functions. Part I—A numerical method based on Prony series. *International journal of solids and structures*, *36*(11), 1653-1675.

Pellinen, T. K., Witczak, M. W., & Bonaquist, R. F. (2004). Asphalt mix master curve construction using sigmoidal fitting function with non-linear least squares optimization. In *Recent advances in materials characterization and modeling of pavement systems* (pp. 83-101).

Qu, Z. Q. (2004). *Model Order Reduction Techniques with Applications in Finite Element Analysis: With Applications in Finite Element Analysis*. Springer Science & Business Media.

Rayleigh, L. (1877). *Theory of Sound (two volumes), 1954th ed.*, Dover Publications, New York.

Rohde, G. T., & Van Wijk, A. J. (1996). A mechanistic procedure to determine basin parameter criteria. In *Southern African Transportation Conference, Pretoria*.

Sarle, W. S. (1994). Neural networks and statistical models.

SAANOUNI, K. (2003). Universite deTechnologie deTroyes, GSM/LASMIS, France and JL CHABOCHE Universite deTechnologie deTroyes, GSM/LASMIS, France. *Comprehensive Structural Integrity*, 321.

Shahin, M. (2005). Pavement Management for Aiports Roads and Parkink Lots", 572p.

Saleh, M. (2015). *Multi-scale criteria for structural capacity evaluation of flexible pavements at network level* (No. 15-2397).

Saleh, M. (2016). Utilisation of the deflectograph data to evaluate pavement structural condition of the highway network. *Road Materials and Pavement Design*, *17*(1), 136-152.

Saleh, M. (2016). A mechanistic empirical approach for the evaluation of the structural capacity and remaining service life of flexible pavements at the network level. *Canadian Journal of Civil Engineering*, *43*(8), 749-758.

Song, Y. Y., & Ying, L. U. (2015). Decision tree methods: applications for classification and prediction. *Shanghai archives of psychiatry*, *27*(2), 130.

Seeds, S., Alavi, S., Ott, W., Mikhail, M., & Mactutis, J. (2000). Evaluation of laboratory determined and nondestructive test based resilient modulus values from WesTrack experiment. In *Nondestructive Testing of Pavements and Backcalculation of Moduli: Third Volume*. ASTM International.

Stubstad, R., & Connor, B. I. L. L. Y. (1983). Use of the falling weight deflectometer to predict damage potential on Alaskan highways during spring thaw. *Transportation Research Record: Journal of the Transportation Research Board*, *930*, 46-51.

Sebaaly, B., Davis, T. G., & Mamlouk, M. S. (1985). Dynamics of falling weight deflectometer. *Journal of Transportation Engineering*, *111*(6), 618-632.

Saba, N., Jawaid, M., Alothman, O. Y., & Paridah, M. T. (2016). A review on dynamic mechanical properties of natural fibre reinforced polymer composites. *Construction and Building Materials*, *106*, 149-159.

Solanki, U. J., Gundalia, P. J., & Barasara, M. D. (2014). A review on structural evaluation of flexible pavements using falling weight deflectometer. *Trends in Transport Engineering and Applications (STM) Journals*.

Schmidt, J., Janda, T., Zemanová, A., Zeman, J., & Šejnoha, M. (2019). Newmark algorithm for dynamic analysis with Maxwell chain model. *arXiv preprint arXiv:1911.03255*.

Schwartz, C. W. (2005, January). Evaluation of the Witczak dynamic modulus prediction model. In *Proceedings of the 84th Annual Meeting of the Transportation Research Board, Washington, DC* (No. 05-2112).

Talvik, O. (2007). FWD mõõtmistulemuste alusel arvutatud parameetrite SCI, BDI ja BCI kasutamine teekatendi seisukorra hindamisel (Use of FWD deflection basin parameters (SCI, BDI, BCI) for pavement condition assessment). *Magistritoo [Master thesis]. Tallinn: TTU Teedeinstituut [Tallinn University of Technology, Dept of Transportation]*.

Tapia-Romero, M. A., Dehonor-Gómez, M., & Lugo-Uribe, L. E. (2020). Prony series calculation for viscoelastic behavior modeling of structural adhesives from DMA data. *Ingeniería, investigación y tecnología*, *21*(2).

Tombari, A., Zentner, I., & Cacciola, P. (2014, June). Sensitivity of the Stochastic Response of Structures Protected by the Vibrating Barrier Control Device. In *Computational Stochastic Mechanics* (pp. 705-716). Research Publishing.

UNIVERSITY OF DUNDEE, DEPARTMENT OF CIVIL ENGINEERING. (1980). Pavement evaluation based on surface deflection. Dundee.

Uzan, J. (1994). Advanced backcalculation techniques. In *Nondestructive Testing of Pavements and Backcalculation of Moduli: Second Volume*. ASTM International.

Vaswani, N. K. (1971). Method for separately evaluating structural performance of subgrades and overlying flexible pavements. *Highway Research Record,* (362).

Whitcomb, W., 1982. Surface deflections and pavement evaluation equipment and analysis techniques. Transportation Engineering Report 82-4. Cornwallis, OR: Oregon State University

Wood, W. L. (1984). A further look at Newmark, Houbolt, etc., time-stepping formulae. *International Journal for Numerical Methods in Engineering*, *20*(6), 1009-1017.

Washington State Department of Transportation. (2001) FWD-AREA Program. Washington State Department of Transportation, Olympia, WA.

Zhang, W., Cui, B., Gu, X., & Dong, Q. (2018). Comparison of relaxation modulus converted from frequency-and time-dependent viscoelastic functions through numerical methods. *Applied Sciences*, *8*(12), 2447.

Zienkiewicz, O. C., Watson, M., & King, I. P. (1968). A numerical method of visco-elastic stress analysis. *International Journal of Mechanical Sciences*, *10*(10), 807-827.

Zhao, Y., Ni, Y., & Zeng, W. (2014). A consistent approach for characterising asphalt concrete based on generalised Maxwell or Kelvin model. *Road Materials and Pavement Design*, *15*(3), 674-690.